Near InfraRed (NIR) Nanoemitters for Bioimaging Applications



Dissertation

Zur Erlangung des Doktorgrades Dr. rer. nat.

der Falkutät für Naturwissenschaften

der Universität Ulm

vorgelegt

von **Goutam Pramanik**

aus Kharisha, India

Ulm, 2013

Near InfraRed (NIR) Nanoemitters for Bioimaging Applications



Dissertation

submitted in partial fulfilment of the requirements for the degree

Doctor of Philosophy (Dr. rer. nat.)

to

Faculty of Natural Sciences, University of Ulm

by

Goutam Pramanik

from Kharisha, India

Ulm, 2013

Dissertation der Universität Ulm

Amtierender Dekan: Prof. Dr. Joachim Ankerhold

1. Gutachterin: Prof. Dr. Tanja Weil

2. Gutachter: Prof. Dr. Mika Lindén

Tag der Promotion:

12.12.2013

Universität Ulm, Fakultät für Naturwissenschaften, **2013**

Dedicated to my parents

Abstract of the Dissertation

Fluorophores emitting in the "Near infrared (NIR) optical window" (650-900 nm) is ideally suited for *in vitro* and *in vivo* imaging of cells and tissues. NIR emitting fluorophore allows high signal-to-background imaging due to minimal autofluorescence from biological samples, reduced light scattering, and high tissue penetration. Nanoparticle-based NIR emitters are very attractive for biolabelling and bioimaging applications because their photostability, large surface area and favourable pharmokinetic properties. The preparation of highly stable multifunctional, biocompatible, nontoxic NIR emitting probes, with the ability to deliver large payloads, and incorporation of targeting groups, is highly attractive and desirable. This thesis focuses on the preparation of two types of multifunctional NIR emitting fluorescent nanoprobes, ultrasmall gold nanoparticles and fluorescent nanodiamonds (FNDs).

The large surface of nanoparticles can be functionalised with variety of bioactive molecules. Fluorescent nanoparticles have the high capacity to ferry cargo and loads onto them and serve as both contrast and delivery agent. For these applications, the nanoparticles must have combined properties of biocompatibility and interactive multiple functions at the surface. The surfaces of these particles could be modified through the creation of multifunctional, biocompatible polymer coating suitable for further functionalization for the attachment of various bioactive molecules. To stabilise the NIR emitting nanoparticles by polymer coating, multifunctional biocompatible polypeptide copolymers with different lengths, different charge of the polypeptide backbone chains have been prepared from native proteins or modified globular proteins using "denaturation and pegylation" strategy. These polypeptide copolymers have several attractive features, such as monodispersity, biocompatibility, non toxicity and most importantly the protein backbone contain various functional groups (-COOH, $-NH_2$, -OH) along the polymer backbone which allow the attachment of biomolecules to the polymer using very simple conjugation chemistry.

Thioctic acid (TA) functionalised polypeptide copolymers were used to stabilise NIR emitting ultrasmall AuNPs by following a one step synthetic procedure. Optical properties and the stability of the AuNPs were found to be dependent on the characteristics of the copolymers. Highly cationised copolymer with longer backbone, dcBSA-PEO$(5000)_{28}$-

$(TA)_{26}$, is the most efficient in stabilising the NIR emitting AuNPs. dcBSA-PEO$(5000)_{28}$-$(TA)_{26}$ stabilised AuNPs are well uptaken by the A549 cell line and they were located at the perinuclear region. Further nuclear localised signal (NLS) functionalised NIR emitting AuNPs were developed that can not only cross the cell membrane but also can penetrate through the cell nucleus membrane. Cell nucleus staining ability of NLS functionalised AuNPs were demonstrated by confocal microscopy.

This thesis also deals with another type of NIR fluorescent nanoparticles, called fluorescent nanodiamonds (FNDs). In addition to optical properties, the negatively charged lattice defects NV^- in FNDs show attractive spin properties. The high tendency of FNDs to form aggregates and colloidal instability after chemical modification, were overcomed by coating the FNDs with cationised bovine serum albumin (cBSA) derived copolymer by non-covalent interactions. The cell uptake behaviour copolymer coated FNDs has also been demonstrated. Finally, the magneto metric sensing of biologically important external spins using FNDs has been demonstrated. Iron storage protein ferritin has been introduced at the FNDs surface by non-covalent interactions and detected by measuring changes in the relaxation time (T_1) and decoherence rate (T_2) of FNDs. The large numbers of iron (S = 5/2 Fe^{3+}spins) present in the ferritin core decreases both T_1 and T_2 seven times compared to FNDs without ferritin. These results confirm the feasibility of FNDs as nano-scale magnetic field sensors. The multifunctional NIR emitting nanoparticles developed in this thesis will definitely find much broader *in vivo* applications in biosensing, drug and gene delivery.

Table of Contents

	Page numbers
Abstract of the Dissertation…….....	iii
Table of Contents…….....	v
Amino Acid Symbols……	vii
List of Tables……	vii
List of Figures……	viii
List of Schemes……..	xvi
List of Abbreviations……	xvii
Chapter 1. Introduction……..	1
1.1. Introduction into Near Infrared (NIR) Imaging.....	2
1.1.1. Near infrared (NIR) window……...	2
1.1.2. Near infrared fluorescent (NIRF) molecules……	4
1.1.3. Near infrared fluorescent (NIRF) nanomaterials…….	5
1.1.4. History of fluorescence probes in medical imaging……..	6
1.2. Comparison of Nanoparticles and Organic Dyes as Fluorescent Labels……	8
1.3. Gold Nanoparticles (AuNPs) for Bioimaging Applications……..	10
1.3.1. Synthesis and surface functionalisation of AuNPs.....	11
1.3.2. Size-dependent optical properties of gold nanoparticles……..	12
1.4. Overview of Fluorescent Nanodiamonds (FNDs).....	14
1.4.1. Preparation of nanodiamonds.....	14
1.4.2. Creation of NV centers at the diamond surface……	15
1.4.3. Surface functionalisation of nanodiamonds……...	15
1.4.4. Optical properties of fluorescent nanodiamonds (FNDs)……..	16
1.4.4. Spin properties of FNDs……...…….	17
1.5. References.....	19
Aims and Motivations……..	26
Chapter 2. Preparation of Monodisperse, Multifunctional Polypeptide Copolymers……...	29
2.1. Introduction……..	29
2.2. Results & Discussion…….	30
2.3. Conclusions……	51

2.4. References…….. 51
Chapter 3. 54
3.1. Highly Stable, Ultra Small, Multifunctional Near Infrared (NIR) Gold Nanoemitters for Bioimaging Application……. 54
3.1.1. Introduction…….. 54
3.1.2. Results and Discussion…… 56
3.1.3. Conclusions…….. 68
3.2. Translocation of Near InfraRed (NIR) emitting Gold nanoparticles into the Cell Nucleus……. 69
3.2.1. Introduction……... 69
3.2.2. Results and Discussion…….. 71
3.2.3. Conclusions…… 78
3.3. References…….. 80
Chapter 4. 83
4.1. Stabilization of Fluorescent Nanodiamonds for Cell Studies by a Polypeptide Polymer Coating…….. 83
4.1.1. Introduction…… 83
4.1.2. Results and Discussion…….. 87
4.1.3. Conclusions…… 99
4.2. Detection of the Metallo-Protein Ferritin Using Color Centers in FNDs…… 100
4.2.1. Introduction…… 100
4.2.2. Results and Discussion…….. 103
4.1.3. Conclusions…… 113
4.3. References…….. 113
Chapter 5. Summary and Outlook……. 120
Experimental details…… 123
Declaration of Cooperations……... 137
Erklärung / Declaration of Originality…….. 138
Acknowledgements……..... 139
Curriculum Vitae……. 140
List of Publications…….. 141

Amino Acid Symbols

	Amino Acid (AA)	One letter Symbol	Three Letter Symbol
Natural Amino Acids	Arginine	R	Arg
	Asparagine	N	Asn
	Aspartic acid	D	Asp
	Cysteine	C	Cys
	Glutamic acid	E	Glu
	Glutamine	Q	Gln
	Glycine	G	Gly
	Histidine	H	His
	Isoleucine	I	Ile
	Leucine	L	Leu
	Lysine	K	Lys
	Methionine	M	Met
	Phenylalanine	F	Phe
	Proline	P	Pro
	Serine	S	Ser
	Threonine	T	Thr
	Tryptophan	W	Trp
	Tyrosine	Y	Tyr
	Valine	V	Val

List of Tables

Page numbers

Table 2.1. Point of attachment of PEO to the protein backbone…….. 32

Table 2.2. Summary of the conditions used for denaturation of different proteins..... 45

Table 2.3. Summary of the number of PEO5000 attached to protein backbone..... 48

Table 2.4. Summary of the results of the zeta potential of the native protein and corresponding PP-PEOs and the correlation with the positively and negatively charged amino acids of the protein. Unless mentioned the numbers of positively and negatively charged amino acids were obtained from Expasy (http://web.expasy.org/protparam/)..... 49

Table 3.1.1. Summary of number of thioctic acids attached to different copolymers according to DPS test..... 57

Table 3.1.2. Overview of the sizes and optical properties of AuNPs **2a-f**, **4a-f** and **6a-f** coated with copolymers **1, 3** and **5** by applying different ratios of Au^{3+}/TA as given in the first row..... 60

Table3.1. 3. Calculated sizes of AuNPs **4** at different $HAuCl_4$/TA ratio according to FCS measurements..... 62

Table 3.1.4. Calculation for FQY of AuNPs solution in water..... 63

Table 4.1.1. FCS data for 6 in solutions at different pH..... 95

Table 4.2.1. Summary of the effect of ferritin on NV center..... 112

Table 5.1. Absorption at 325 nm for different concentrations of thioctic acid and PP-PEOs..... 129

Table 5.2. Absorption at 325 nm for different PP-PEOs..... 129

List of Figures

Figure 1.1. Definition of the near-infrared (NIR) optical window. 3

Figure 1.2. Extinction coefficient value of water and oxy- and deoxyhemoglobin plotted ranging from the visible to the near-infrared wavelength. (a) Immediately after sacrifice, the viscera of a hairless, athymic nu/nu mouse have been exposed. Arrows mark the location of the gallbladder (GB), small intestine (SI) and bladder (Bl). Tissue autofluorescence has been imaged using three different excitation/emission filter sets: (b) blue/green (460–500 nm/505–560 nm); (c) green/red (525–555 nm/590–650 nm); and (d) NIR (725–775 nm/790–830 nm). Fluorescence images have identical normalization. 4

Figure 1.3. Basic chemical structures of NIR emitting dye..... 5

Figure 1.4. Near infrared fluorescent dyes that have been used for clinical trials..... 7

Figure 1.5. A simple energy diagram of photoluminescence in AuNPs. Absorption of a photon excites an electron from the d band to the sp band above the Fermi level. Radiative recombination between an electron and the excited hole, results in the emission..... 13

Figure 1.6. Surface functional groups of detonation diamond and its oxidation to carboxylated nanodiamond..... 14

Figure 1.7. Surface chemistry with carboxylic groups terminated nanodiamond..... 15

Figure 1.8. (a) Structure of the nitrogen-vacancy (NV) defect in diamond. (b) Emission spectra of fluorescent nanodiamond. Excitation wavelength of 532 nm..... 17

Figure 1.9. Multiplet structure of the NV^{-1} center in diamond. A 1.945-eV in conserving optical transition exists between the ground- ($^3A_2$) and excited-(^3E) state triplets. Transitions from the $m_s = \pm 1$ sublevels of ^3E to an intermediate spin singlet ($^1A_1$) are much stronger than those from the $m_s=0$ sublevel. The spin-selective nature of this decay path can be used in conjunction with the 1.945 eV transition to optically polarize and measure the spin state of $^3A_2$..... 18

Figure 2.1. Crystal structure of HSA and the locations of domain-binding sites. The locations of hydrophobic binding sites (Sudlow I and Sudlow II) are indicated. The position of the tryptophan residue (Trp-214) in the middle of helix H2 in subdomain IIA is shown. The structure was obtained from the Protein Data Bank (ID code 1ha2)..... 35

Figure 2.2. Purification and characterisation of dHSA-PEO$(5000)_{27}$. (a) FPLC purification chromatograms of an AKTÄ explorer after application of a reaction mixture consisting of the dHSA-PEO$(5000)_{27}$ (**4**) (blue) and AKTÄ explorer chromatogram of native HSA (brown). (b) Gel permeation chromatogram of dHSA-PEO$(5000)_{27}$ (c) MALDI-TOF spectrum for dHSA-PEO$(5000)_{27}$. The molecular mass is 197kDa according to this spectrum and the peak at 106kDa corresponds to the half molecular mass peak. (d) SDS-PAGE analysis of dHSA-PEO$(5000)_{27}$ (**4**)..... 36

Figure 2.3. Crystal structure of BSA. The structure has been obtained from the Protein Data Bank (http://www.pdb.org/pdb/explore/explore.do?structureId=4F5S). 37

Figure 2.4. Purification and characterisation of dcBSA-PEO$(5000)_{28}$. (a) FPLC purification chromatograms of an AKTÄ explorer after application of a reaction mixture consisting of the dcBSA-PEO$(5000)_{28}$ (**2**) (blue) and AKTÄ explorer chromatogram of cBSA (brown). (b) Gel permeation chromatogram of dcBSA-PEO$(5000)_{28}$. (c) SDS-PAGE analysis of dcBSA-PEO$(5000)_{28}$ (**2**)..... 38

Figure 2.5. Crystal structure of hen egg white lysozyme. The structure has been obtained from the Protein Data Bank (http://www.rcsb.org/pdb/explore/explore.do?structureId=2EPE). The ribbon arrows represent regions of the peptide backbone in β-sheet conformation..... 38

Figure 2.6. Purification and characterisation of dLY-PEO$(5000)_8$ (**8**). (a) FPLC purification chromatograms of an AKTÄ explorer after application of a reaction mixture consisting of the dLY-PEO$(5000)_8$ (**8**) (blue) and AKTÄ explorer chromatogram of

native Lysozyme (brown). (b) Gel permeation chromatogram of dLY-PEO(5000)$_8$ (c) MALDI-TOF spectrum for dLY-PEO(5000)$_8$. The molecular mass is ~54.5 kDa according to this spectrum and the peak at 27 kDa corresponds to the half molecular mass peak. (d) SDS-PAGE (NuPAGE Bis-Tris 4-12%) analysis of dLY-PEO(5000)$_8$ (**8**)..... 40

Figure 2.7. Crystal structure of Ovomucoid. The structure has been obtained from the Protein Data Bank (http://www.rcsb.org/pdb/explore/explore.do?structureId=1OVO). The ribbon arrows represent regions of the peptide backbone in β-sheet conformation..... 41

Figure 2.8. Purification and characterisation of dOvomucoid-PEO(5000)$_{18}$ (**10**). (a) FPLC purification chromatograms of an AKTÄ explorer after application of a reaction mixture consisting of the dOvomucoid-PEO(5000)$_{18}$ (**10**) (blue) and AKTÄ explorer chromatogram of native Ovomucoid (brown). (b) Gel permeation chromatogram of dOvomucoid-PEO(5000)$_{18}$ (c) MALDI-TOF spectrum for dOvomucoid-PEO(5000)$_{18}$. The molecular mass is ~115 kDa according to this spectrum and the peak at ~57 kDa corresponds to the half molecular mass peak. (d) SDS-PAGE analysis of dOvomucoid-PEO(5000)$_{18}$ (**10**)..... 42

Figure 2.9. Crystal structure of Kunitz. The structure has been obtained from the Protein Data Bank. (http://www.rcsb.org/pdb/explore/explore.do?structureId=1BA7) The ribbon arrows represent regions of the peptide backbone in β-sheet conformation..... 43

Figure 2.10. Purification and characterisation of dKunitz-PEO(5000)$_4$ (**6**). (a) FPLC purification chromatograms of an AKTÄ explorer after application of a reaction mixture consisting of the dKunitz-PEO(5000)$_4$ (**6**) (blue) and AKTÄ explorer chromatogram of native Kunitz (brown). (b) Gel permeation chromatogram of dKunitz-PEO(5000)$_4$ (c) MALDI-TOF spectrum for dKunitz-PEO(5000)$_4$. The molecular mass is ~40 kDa according to this spectrum. (d) SDS-PAGE analysis of dKunitz-PEO(5000)$_4$ (**6**).... 44

Figure 2.11. Corelation between the secondary structure of the protein and denaturation conditions..... 47

Figure 2.12. Zeta potential of all the polypeptide polyethylene oxide (PP-PEOs)..... 49

Figure 2.13. Secondary structure of all the polypeptide polyethylene oxide (PP-PEOs)..... 50

Figure 3.1.1. SDS-PAGE of dHSA-PEO(5000)$_{27}$-(TA)$_{22}$ (**1**), dcBSA-PEO(5000)$_{28}$-(TA)$_{26}$ (**3**), and dLY-PEO(5000)$_8$-(TA)$_8$ (**5**)……. 56

Figure 3.1.2. MALDI-ToF MS of dLY-PEO$(5000)_8$-$(TA)_8$ (**5**, calcd. MW = 56.6kDa); Matrix: Sinapinic acid…… 57

Figure 3.1.3. (A) Absorption spectra of AuNPs (**2a-f**) prepared by using $HAuCl_4$/TA ratios from 20:1 (**2a**) to 1:5 (**2f**) of copolymer dHSA-PEO$(5000)_{27}$-$(TA)_{22}$. (B) Absorption spectra of AuNPs prepared by using $HAuCl_4$/TA ratios from 20:1 (**4a**) to 1:5 (**4f**) of copolymer dcBSA-PEO$(5000)_{28}$-$(TA)_{26}$. (C) Absorption spectra of AuNPs prepared by using $HAuCl_4$/TA ratios from 20:1 (**6a**) to 1:5 (**6f**) of copolymer of dLY-PEO$(5000)_8$-$(TA)_8$…….. 59

Figure 3.1.4. (A) Emission spectra of AuNPs (**2a**-**2f**) coated with dHSA-PEO$(5000)_{27}$-$(TA)_{22}$ prepared using different $HAuCl_4$/TA ratios from 20:1 (**2a**) to 1:5 (**2f**). (B) Emission spectra of AuNPs (**4a**-**4f**) coated with dcBSA-PEO$(5000)_{28}$-$(TA)_{26}$ prepared using different $HAuCl_4$/TA ratios from 20:1 (**6a**) to 1:5 (**6f**). (C) Emission spectra of AuNPs (**6a**-**6e**) coated with dLY-PEO$(5000)_8$-$(TA)_8$ prepared using different ratios 20:1 (**6a**) to 1:5 (**6f**)…… 60

Figure 3.1.5. a) Representative electron micrographs of AuNPs (**4f**) coated with dcBSA-PEO$(5000)_{28}$-$(TA)_{26}$ prepared using $HAuCl_4$/TA = 1:5. Micrograph showing a cluster of deposited AuNPs on graphene. (b) HRTEM image of (**4f**) deposited on graphene. (c) Scaled cut out of a AuNP with diameter 0.8 nm where the gold atoms of the NP are resolved, the red dotted line indicates the trajectory taken for the line profile shown in d. Each of the gold(d) Line profile showing 0.27 nm Au-Au bond distance in the AuNP corresponding to the reported investigations on the contraction of bond distances for gold particles with size < 1nm. (e) Particle size distribution of AuNPs (**4f**) coated with dcBSA-PEO$(5000)_{28}$-$(TA)_{26}$ for the of $HAuCl_4$/TA (1:5) ratio. (f) Emission spectra of AuNPs coated with **2f** (blue), **4f** (red) and **6f** (green) for a $HAuCl_4$/TA ratio of 1:5 upon excitation at 365 nm... 61

Figure 3.1.6. Determination of diameter of dcBSA-AuNPs (**4**) by fluorescence correlation spectroscopy (FCS) measurements…….. 62

Figure 3.1.7. Absorption spectra of dcBSA-AuNPs (**4a**) in different solutions: (a) 10 mM phosphate buffer pH 7.4 +2% glucose solution. (b) 1M NaCl. (c) 0.5M DTT. (d) pH 4. (e) pH 10.(f) 0.1 mg/mL Trypsin solution. After 24 h the absorption intensity of the AuNPs remained almost unchanged and no precipitation of the AuNPs have been observed. These experimental data suggest high colloidal stability of the AuNPs coated with dcBSA-PEO$(5000)_{28}$-$(TA)_{26}$…… 64

Figure 3.1.8. Emission spectra of dcBSA-AuNPs (**4f**) in different solutions: (a) 10mM phosphate buffer pH 7.4 +2% glucose solution. (b) 1M NaCl. (c) 0.5M DTT. (d) pH 4. (e) pH 10. (f) 0.1 mg/mL trypsin. Excitation wavelength of 365 nm was chosen. Even after 24 h, the emission intensity of the AuNPs remained almost unchanged and no precipitation observed. These results suggest high colloidal stability of the AuNPs coated with dcBSA-PEO$(5000)_{28}$-$(TA)_{26}$…….. 64

Figure 3.1.9. Absorption spectra of dHSA-AuNPs (**2a**) in different solutions: (a) 10 mM phosphate buffer pH 7.4 +2% glucose solution. (b) 1M NaCl. (c) 0.5M DTT. (d) pH 4. (e) pH 10.(f) 0.1 mg/mL trypsin solution. Even after 24 h, the absorption intensity of the AuNPs remained almost unchanged except in the presence of DTT (c). AuNPs coated with dHSA-PEO$(5000)_{27}$-$(TA)_{22}$ shows a significant decrease in surface plasmon resonance band in DTT solution, which indicates the particle are unstable in DTT solution…… 65

Figure 3.1.10. Emission spectra of dHSA-AuNPs (**2f**) in different solutions. (a) 10 mM phosphate buffer pH 7.4 +2% glucose solution. (b) 1M NaCl. (c) 0.5 M DTT. (d) pH 4. (e) pH 10.(f) 0.1 mg/mL trypsin solution. Excitation wavelength 365 nm. After 24 h the emission intensity of the AuNPs remained almost unchanged and no precipitation of AuNPs has been observed……..... 65

Figure 3.1.11. Absorption spectra of dLY-AuNPs (**6a**) in different solutions: (a) 10 mM phosphate buffer pH 7.4 +2% glucose solution. (b) 1M NaCl. (c) 0.5M DTT. (d) pH 4. (e) pH 10.(f) 0.1 mg/mL trypsin solution. After 24 h, the absorbance intensity of the AuNPs remained almost unchanged except in the presence of trypsin (f). In trypsin solution, there is a significant decrease of the surface plasmon band, indicating proteolytic instability of AuNPs coated with dLY-PEO$(5000)_{8}$-$(TA)_{8}$…….. 66

Figure 3.1.12. Emission spectra of dLY-AuNPs (**6f**) in different solutions. (a) 10 mM phosphate buffer pH 7.4 +2% glucose solution. (b) 1M NaCl. (c) 0.5 M DTT. (d) pH 4. (e) pH 10.(f) 0.1 mg/mL trypsin solution. Excitation wavelength 365 nm. After 24 h the emission intensity of the AuNPs remained almost unchanged and no precipitation of AuNPs have been observed……... 66

Figure 3.1.13. a) Viability of A549 cells after 24 h of incubation with 50 µL of 1 µM dcBSA-AuNPs (**4f**) in cell medium as determined by a Cell-Titer Glo (Promega) cell viability assay. The error bars represent variations among three independent measurements. 96% cells are still viable after 24 h of incubation with dcBSA-AuNPs. b) Imaging of dcBSA-AuNPs (**4a**) on the surface of A549 cells by the Scanning Electron Microscope**.** The surface is

covered with many microvilli. Clusters of gold nanoparticles can be imaged with the material dependent backscattered electron signal that is overlaid in red onto the (black and white) secondary electron signal. Some gold aggregates are sharply imaged (white arrow), which indicates that they are still on the cell surface. Some gold aggregates are blurred (black arrow), which indicates that they are already incorporated into the cell. The blurring is caused by the widening of the primary beam as an effect of beam specimen interaction. The framed arrow depicts a gold aggregate that is imaged sharp at the left hand side and blurred at the right hand side since it is, there, covered by a cell protrusion. c) Thin section of 50 µL of 1 µM AuNPs (**4a**) incubated A549 cells after incubation for 24 h imaged in the transmission electron microscope. Clusters of gold particles (arrows) can be easily seen in the cytoplasm, but not in the nucleus (N). They are usually found in vesicles. (G: Golgi apparatus, M: Mitochondrion). d) Confocal images of A549 cells incubated with 50 µL of 1 µM AuNPs (**4f**) incubated for 24 h. NIR fluorescent gold nanoparticle is visible in perinucleur region. DIC image (e) All panels show fluorescence and (f) overlay. Images were acquired on a confocal microscope equipped with fluorophore-appropriate filter sets and an environmental chamber in which cells remained at 37 °C + CO_2 throughout imaging..... 67

Figure 3.2.1. (a) Absorbance (b) fluorescence of AuNPs. Blue –TA coated AuNPs and red is TA coated AuNPs conjugated with NLS…….. 73

Figure 3.2.2a. DLS size distribution of TA-AuNPs (**1**)…… 74

Figure 3.2.2b. DLS size distribution of TA-AuNPs-NLS (**2**)…… 74

Figure 3.2.3a. XPS spectra of TA-AuNPs (**1**)…… 75

Figure 3.2.3b. XPS spectra of TA-AuNPs conjugated to NLS (**2**)…… 76

Figure 3.2.4. Confocal microscopy images of A549 cells incubated with AuNPs **2**. a) Red represents data acquired by the gold channel. (b) DIC image. (c) Blue represents data acquired by the DAPI channel. (d) Overlay. Image scanned using simultaneous scanning. 77

Figure 3.2.5a. *z*-stack imaging data of AuNPs channel of A549 cells, incubated with AuNPs **2**. Scale bar 50 µm…….. 78

Figure 3.2.5b. z-stack imaging data of DAPI channel of A549 cells, incubated

with AuNPs **2**. Scale bar 50 μm..... 78

Figure 4.1.1. The surface of nanodiamond can be oxidized with various methods. All result in coverage with mainly COOH groups…….. 84

Figure 4.1.2. Schematic reaction of carboxylated FNDs with amines and alcohols……... 85

Figure 4.1.3. Infrared spectra of (a) FNDs, (b) FNDs coated with Rho-dcBSA-PEO$(5000)_{27}$ (**6**)…….. 89

Figure 4.1.4. (a) Autocorrelation functions of **6** in solutions at different pH ranging from pH 2 to 8. (b) Autocorrelation function of **6** in 50mM NaCl solution. Lines are experimental data, symbols represent the exponential fit…… 90

Figure 4.1.5. Number size distribution of only FNDs by DLS. The average hydrodynamic diameter of FND is 30.1±1.2 nm. The results were obtained after three independent measurements and each measurement consisting of ten individual runs……... 90

Figure 4.1.6. Number size distributions of Rho-dcBSA-PEO$(5000)_{27}$ coated FNDs (**6**) by DLS. The average hydrodynamic diameter of Rho-dcBSA-PEO$(5000)_{27}$ coated FNDs (**6**) is 84.5±3.8 nm. The results were obtained after three independent measurements and each measurement consisting of ten individual runs…….. 91

Figure 4.1.7. The TEM image of FNDs coated with Rho-dcBSA-PEO$(5000)_{27}$ (**6**). Scale bar 200nm……... 92

Figure 4.1.8. XPS S 2p core level spectrum of Rho-dcBSA-PEO$(5000)_{27}$ coated FNDs (**6**)…….. 92

Figure 4.1.9. The sample solution was deposited on a glass coverslip and observed with the confocal microscope. (a) Green represents data acquired by the Rhodamine channel. (b) DIC image. (c) Red represents data acquired by the FNDs channel. (d) Overlay..... 93

Figure 4.1.10. A) Photograph of FNDs solution in 5 mM NaCl. (B) Photograph of Rho-dcBSA-PEO$(5000)_{27}$ coated FNDs in 5 mM NaCl solution. (C) Photograph of Rho-dcBSA-PEO$(5000)_{27}$ coated FNDs in 1 M NaCl solution…… 94

Figure 4.1.11. Confocal microscopy image of Hela cells incubated with Rho-dcBSA-PEO$(5000)_{27}$ coated FNDs (**6**). (a) Green represents data acquired by the Rhodamine channel. (b) DIC image. (c) Red represents data acquired by the FNDs channel. (d) Overlay. Image scanned using simultaneous scanning. The green and red spots overlap to such an extent that only yellow spots are visible in overlay…… 95

Figure 4.1.12. Confocal microscopy image of HeLa cells incubated with FITC labeled dcBSA-PEO$(5000)_{27}$ coated FNDs. (a) Green represents data acquired by the FITC channel. (b) Red represents data acquired by the FNDs channel. (c) DIC image. (d) Overlay. Image scanned using simultaneous scanning.……. 98

Figure 4.1.13. Confocal microscopy image of HeLa cells incubated with Atto 520 labeled dcBSA-PEO$(5000)_{27}$ coated FNDs. (a) Green represents data acquired by the Atto520 channel. (b) Red represents data acquired by the FNDs channel. (c) DIC image. (d) Overlay. Image scanned using simultaneous scanning……. 98

Figure 4.2.1. Structure of Nitrogen Vacancy (NV) center in diamond…… 101

Figure 4.2.2a. TEM image of unpurified ferritin adsorbed FNDs……. 105

Figure 4.2.2b. TEM image of purified ferritin adsorbed FNDs……. 106

Figure 4.2.3. FTIR spectra of FND-ferritin complex……... 107

Figure 4.2.4a. Number size distributions of FNDs by DLS. The average hydrodynamic diameter of the FNDs is 30.1±1.2 nm. The results were obtained after three independent measurements…… 107

Figure 4.2.4b. Number size distributions of ferritin adsorbed FNDs by DLS. The average hydrodynamic diameter is 83.8±2.7. The results were obtained after three independent measurements. …….. 108

Figure 4.2.5. XPS spectra of FND-ferritin complex, showing the presence of Fe……. 109

Figure 4.2.6. HRTEM images of ferritin molecules (right) and FNDs covered with ferritin (left). The red arrows indicate the position of the metalloprotein on the surface…….. 110

Figure 4.1.7. Measurement of the electron spin-lattice relaxation time T_1 of NV covered by FNDs from group 1 (left) and in FNDs from group 2 (left, inset). Statistical distribution of the T_1 for "free" FNDs (right, blue bars) and for coated FNDs (right, red bars). Decrease of T_1 for group 2 is clearly visible. The black dotted curve is a theoretical model using the fluctuation dynamics of the iron ions…….. 111

Figure 4.2.8. Electron spin Hahn echo decay for FNDs in group 1 (left) and group 2 (left, Inset). Again a decrease of T_2 for group is observed. The dotted line is a theoretical model……. 111

Figure 5.1. Calibration curve of DPS assay based on thioctic acid standard… 128

List of Schemes

Scheme 2.1. Preparation of dcBSA-PEO(5000)$_{28}$ and dHSA-PEO(5000)$_{27}$…….. 31

Scheme 2.2. (A) Preparation of dKunitz-PEO(5000)$_4$. (B) One letter amino acid sequence of Kunitz and the site of PEO attachment to the protein backbone…… 33

Scheme 2.3. (A) Preparation of dLY-PEO(5000)$_{8.}$ (B) One letter amino acid sequence of Lysozyme and the site of PEO attachment to the protein backbone……. 33

Scheme 2.4. (A) Preparation of dOvomucoid-PEO(5000)$_{18}$. (B) One letter amino acid sequence of Ovomucoid and the site of PEO attachment to the protein backbone…….. 34

Scheme 3.1.1. Chemical structures of HSA-, cBSA- and LY-derived copolymers (**1, 3, 5**) and stabilization of AuNPs in the presence of these copolymers……..... 55

Scheme 3.2.1. Scheme of preparation of NLS sequence labeled NIR emitting fluorescent AuNPs……. 71

Scheme 4.1.1. Schematic representation of preparation of Rho-dcBSA-PEO(5000)$_{27}$ and coating of FNDs with Rho-dcBSA-PEO(5000)$_{27}$…….. 88

Scheme 4.1.2. Schematic representation of multifunctionality of dcBSA-PEO(5000)$_{27}$ coated FNDs…… 97

Scheme 4.2.1. Schematic diagram of the interaction between NV center and ferritin. The NV spin is represented in blue and the spin of ferritin in red. The yellow beam represents microwave radiation…….. 103

List of Abbreviations

AFM	Atomic force microscopy
AuNPs	Gold nanoparticles
BI	Bladder
BODIPY	Boron-dipyrromethene
br	Broad
BSA	Bovine serum albumin
cBSA	Cationised bovine serum albumin
CD	Circular dichroism
CLSM	Confocal laser scanning microscopy
cm	Centimeter
CVD	Chemical vapor deposition
Da	Dalton
DAPI	4´, 6-diamino-2-phenylindole
DHLA	Dihydrolipoic Acid
DIC	Differential interference contrast
DLS	Dynamic light scattering
DPS	4,4´-dithiodipyridine
DTT	Dithiothreitol
EDC	1-ethyl-3-(3-dimethylamino-propyl)-carbodiimide hydrochloride
EPR	Enhanced permeability and retention
eV	Electron volt
FCS	Fluorescence correlation spectroscopy
FDA	Food and Drug Administration
FITC	Fluorescein isothiocyanate
FND	Fluorescent nanodiamond
FPLC	Fast protein liquid chromatography
FTIR	Fourier transform infrared spectroscopy
GB	Gallbladder
GHz	Giga hertz
GPC	Gel permeation chromatography
Gu.HCl	Guanidine. HCl
HRP	Horseradish peroxidase

HSA	Human serum albumin
Hb	Deoxyhemoglobin
HBO_2	Oxyhemoglobin
HRTEM	High-resolution transmission electron microscopy
HTHP	High temperature high pressure
ICG	Indocyanine green
kDA	Kilo dalton
Kunitz	Trypsin inhibitor from glycine max
LY	Lysozyme
MALDI	Matrix-assisted laser desorption ionization
m_s	Magnetic quantum number
MS	Mass spectrometry
MWCO	Molecular weight cut off
mV	Millivolt
NPs	Nanoparticles
NHS	N-hydroxysuccinimide
NF	Non-fluorescent
NIR	Near infrared
NIRF	Near infraRed fluorescent
NLS	Nucleus localisation signal
nm	Nanometer
ns	Nano second
NV	Nitrogen vacancy
ODMR	Optically detected magnetic resonance
Ovomucoid	Trypsin inhibitor from chicken egg white
PEO	Polyethylene oxide
PP-PEO	Polypeptide-polyethylene (oxide)
QDs	Quantum dots
QY	Quantum yield
Ref	Reference
Rho	Tetramethylrhodamine-5-maleimide
Rpm	Revolutions per minute
SDS-PAGE	Sodiumdodecyl sulfate polyacrylamide gel electrophoresis

SI	Small intestine
SPR	Surface plasmon resonance
SOD	Superoxide dismutase
SWNTs	Single-walled carbon nanotubes
TA	Thioctic Acid
TCEP	Tris(2-carboxyethyl)phosphine)
TEM	Transmission electron microscopy
Tof	Time of flight
UV	Ultraviolet
XPS	X-ray photo electron spectroscopy

Chapter 1. Introduction

Fluorescence microscopy is among the most widely used techniques for high resolution, non-invasive imaging of live organisms.[1] Fluorescence-based live cell imaging allows visualization of biological processes in an intact and native physiological state and is very important for gaining a better understanding of dynamic biochemical processes.[2] It has helped significantly in improving our understanding of fundamental cellular processes. During the last decade, fluorescent nanoparticles have emerged as versatile tools in the area of biomedical imaging.[3] The recent advances in nanotechnology and nanomaterials have enabled the preparation of nanoparticle-based fluorescent chemical and biological probes, based on various metal cores.[3] Diverse surface chemistries, unique magnetic properties, tunable absorption and emission properties, and recent advances in the synthesis and engineering of these nanoparticles suggest their potential as probes for early detection of diseases, such as cancer.[3] Most commonly used fluorescent NPs are noble metal (Au, Ag), metal oxide (Fe_3O_4), semiconductor nanocrystals {e.g., quantum dots (QDs)}, carbon-based NPs (e.g., nanodiamonds), insulator nanoparticles (e.g., dye-labelled silica nanoparticles) and up-converting nanoparticles (e.g., solid-state materials, doped with rare-earth ions).

However, limitations discussed for these NPs for diagnostic or therapeutic administration to the human body is their biosafety.[4] Nanomaterials are regulated by the Food and Drug Administration (FDA), like any other new diagnostic or therapeutic agent.[4] However, many NPs contain elements, such as lanthanide, cadmium, selenium, tellurium, arsenic, lead and the complexes thereof, which are known to induce acute or chronic toxicity in vertebrates.[5] Therefore, there is an emerging interest in the preparation of alternative fluorescent nanoparticles, based on more bio-inert cores that could be applied for *in vivo* imaging. In this respect, the noble metal gold as well as nanodiamonds, which contain carbon-based diamond at the core, might be particularly suitable for biomedical applications.[6,7] In addition, gold nanoparticles (AuNPs) and fluorescent nanodiamonds (FNDs) have favorable optical and spin properties.[6,8] In particular, surface chemistry of nanodiamonds is still not well-understood and there is an increasing interest to stabilize these nanoparticles in aqueous solution and impart biologically active functionalities. An ultimate goal would be to access multifunctional near-infrared (NIR) emitting AuNPs and FNDs that are stable under various biological conditions to allow bioimaging and sensing applications. In the following section, NIR emitting nanoparticles will be compared with small molecule NIR emitters as well as

UV or visible light-emitting nanoparticles with particular focus on bioimaging applications. Thereafter, the surface chemistry of AuNPs and FNDs will be introduced, that serves as basis for this thesis.

1.1. Introduction into Near InfraRed (NIR) Imaging

1.1.1. The near infrared (NIR) window

Molecular imaging is defined as the *in vivo* characterization and measurement of biological processes at the cellular and molecular level.[9] It serves as a powerful technique to monitor and record cellular processes which is of great interest for diagnostic and therapeutic applications.[10] Currently, the predominant modalities for clinical detection and diagnosis of cancer are lack of specificity and sensitivity (such as magnetic resonance imaging, positron emission tomography, computerized tomography, X-ray, radiography, ultrasound), and this also includes radioactive risks.[11] Optical imaging is emerging as a simple, highly sensitive, non-invasive and safe detection method using readily available instruments. Fluorescent probes are indispensable tools in molecular imaging, as they provide dynamic information of the localization and quantity of the molecules of interest. Optical-based *in vivo* imaging is based on the detection of photons, emitted by fluorescent probes upon reacting specifically with biological molecules that induce a concomitant change of their photochemical properties (fluorescence intensity, excitation/emission wavelength, and so forth).[12] In the past two decades, a large number of fluorescent probes have been developed and the majority of them fluoresce in the UV and visible region of the spectrum.[13,14] However, the interfering background signal in the UV and visible region comes from autofluorescence of biological targets, such as tissues, proteins or other biomarkers that fluoresce naturally.[15] Endogenous biological chromophores, in particular oxy- and deoxyhemoglobin (HbO_2 and Hb), respectively (**Figure 1.1.**), strongly absorb visible light, thereby limiting the penetration depth at short wavelength.[15] Other biological components, such as water and lipids, are optically transparent from the visible to the NIR, but strongly absorb light in the infrared.[15] Autofluorescence from intrinsic fluorophores, such as elastin,[16] collagen[17] and other biological fluorophores, ocurrs in the visible region (<600 nm). *In vivo* imaging is therefore limited by the scattering and absorption of light by intrinsic fluorophores and water. In order to study the molecules of interest by simple optical observation, the desired biomolecules need to be distinguished from the background. One of the ways to achieve high signal-to-background imaging in deep tissues is the use of probes emitting in the NIR region. NIR probes emit in a narrow 'optical window' between 650 and 900 nm (**Figure 1.1.**), where light

can penetrate deeper, typically a few centimeter[18] depth, where the absorption coefficient, light scattering and autofluorescence of tissue remain at a minimum. Therefore, NIRF imaging probes provide high signal-to-background ratio and thereby allow to access low detection limits.

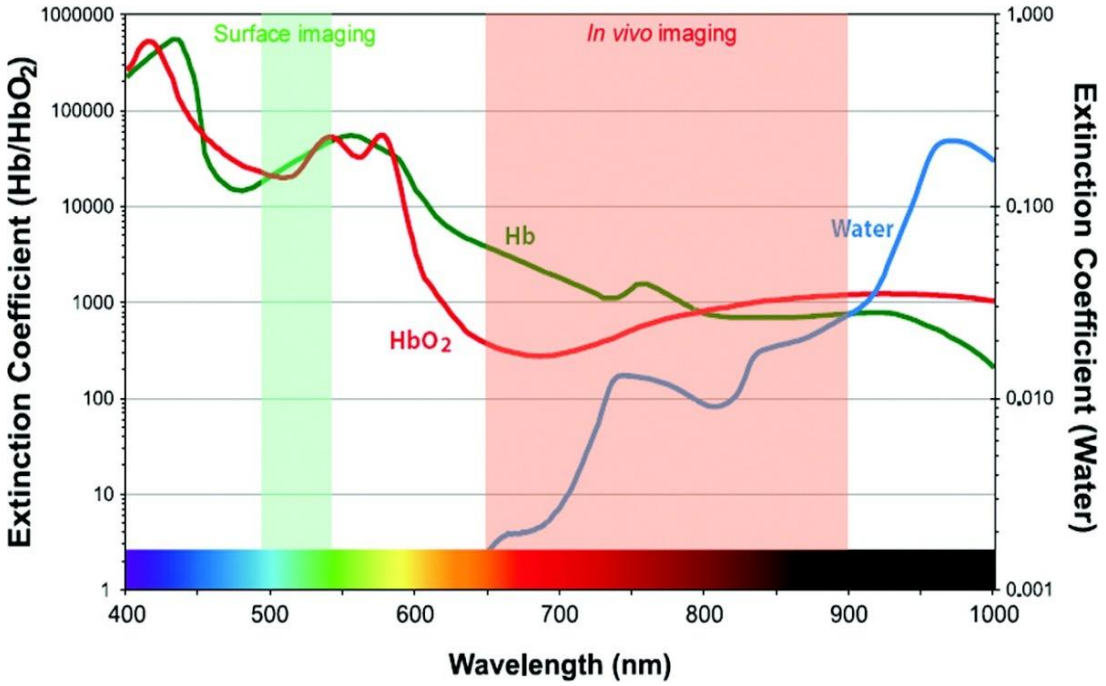

Figure 1.1. Definition of the near-infrared (NIR) optical window. Extinction coefficient value of water and oxy- and deoxyhemoglobin plotted ranging from the visible to the near-infrared wavelength. (Image Ref.)[15] "Reprinted with permission.[15] Copyright 2010 American Chemical Society."

Frangioni's research group has explored the wavelength-dependent autofluorescence of vital organs and body fluids, using different filter sets (**Figure 1.2**.).[19] When the viscera of a killed athymic mouse has been excited with blue light, green autofluorescence of the skin and the viscera, especially the gall bladder, the intestine, and the bladder, can be clearly seen (**Figure 1.2.b**). The use of red filter sets, green light emission, reduces the autofluorescence of the gallbladder and intestine significantly, but donot eliminate the autofluorescence (**Figure 1.2.c**). Only after the use of NIR filter sets, the autofluorescence has been totally eliminated (**Figure 1.2.d**). These results clearly demonstrated that the NIR region of the spectra, "the optical window", offers the unique opportunity to detect fluorescent probes with high contrast from deep tissue.

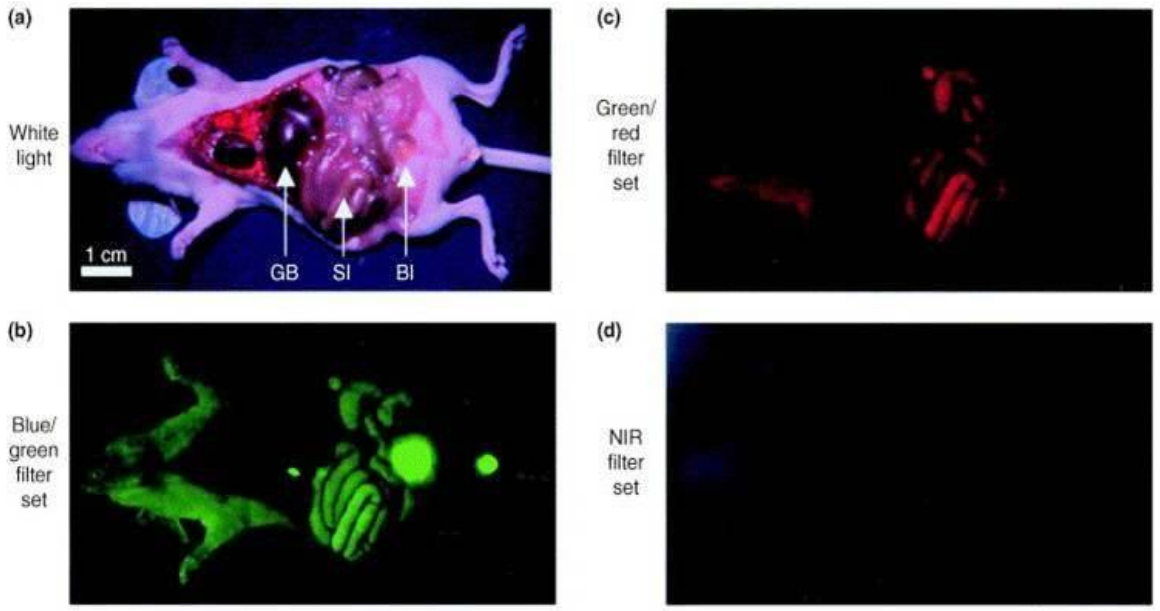

Figure 1.2. (a) Immediately after sacrifice, the viscera of a hairless, athymic *nu/nu* mouse have been exposed. Arrows mark the location of the gallbladder (GB), small intestine (SI) and bladder (Bl). Tissue autofluorescence has been imaged using three different excitation/emission filter sets: **(b)** blue/green (460–500 nm/505–560 nm); **(c)** green/red (525–555 nm/590–650 nm); and **(d)** NIR (725–775 nm/790–830 nm). Fluorescence images have identical normalization. (Image Ref.)[19] "Reprinted with permission. Copyright © 2003, Elsevier"

1.1.2. Near infrared fluorescent (NIRF) molecules

Small molecule fluorescent NIR dyes (NIRF) are currently the most widely used tracers. A huge library of NIR dyes with well-defined chemical structures, tailored optical and chemical properties are nowadays commercially available (e.g. www.atto-tec.com). The most common NIR organic fluorophore families include rhodamines,[20] BODIPY,[21] indocyanines,[22] porphyrines[23] and phthalocyanines[24]. Each of the chromophore scaffolds (**Figure 1.3.**) have been modified by functional groups in order to adjust emission wavelengths, enhance photostability, to tune the hydrophobic/hydrophilic features or to enable conjugation with targeting moieties. For instance, solubility of these polycyclic, hydrophobic NIR dyes has been improved by attaching sulphonate groups to the dye[25,26] or the fluorescence lifetimes of these dye molecules have been increased by introducing different heavy atom (e. g., halogen) substitutions near the center of the dye or excitation and emission wavelength can be tuned by altering the substituent groups of the dye.[27]

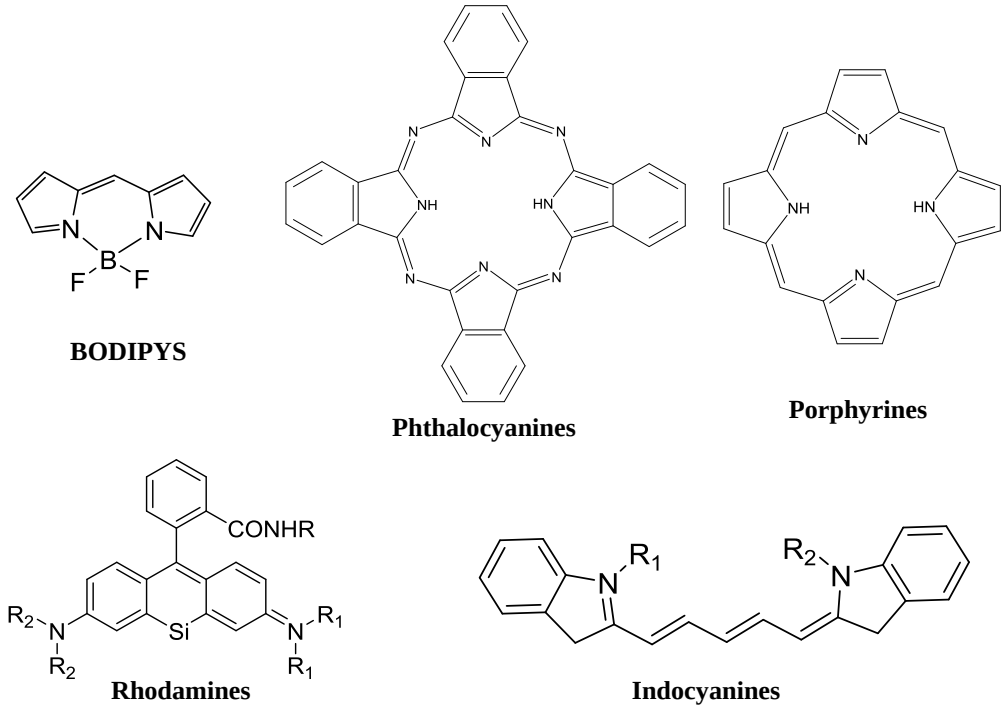

Figure 1.3. Basic chemical structures of NIR emitting dyes.[28,29]

The recent trend is to encapsulate the NIRF dyes inside polymers or within inorganic matrices to use these nanoprobes for tumor imaging via the enhanced permeability and retention (EPR) effect.[30-32] Compared to free NIRF, there are several distinctive features in the NIRF dye-containing nanoprobes. The polymer or inorganic matrix encapsulation protects the dye by reducing their exposure to oxygen, increases the photostability, biocompatibility and most importantly, NIRF signal is enhanced due to their higher local concentration at the targeted site, which results in much higher sensitivity compared to free NIRF.[30] Notable, the use of nanotemplates for fluorescent dye encapsulation prevents dye water solubility issues, aggregation and changes the pharmacokinetic properties of the NIRF dye.[30] Here, the use of nanotechnology has helped designing more efficient and cell or tissue-specific nanoprobes, suitable for high contrast fluorescence imaging.

1.1.3. Near infrared fluorescent (NIRF) nanomaterials

NIR emitting metallic nanoparticles, for *in vitro* and *in vivo* molecular imaging, have received much attention because of their unique features.[33] Semi-conducting quantum dots (QDs) are the most widely used NIR fluorescent nanoprobes. In addition, there exist single-walled carbon nanotubes (SWNTs), noble metal (Au, Ag) clusters and fluorescent nanodiamonds.[17] QDs are made of elements from the II and VI periodic groups (*i.e.*, ZnS,

CdSe or CdTe compositions for instance), or more recently from the III / V periodic groups (InP) as well as the IV / VI periodic groups (PbS, PbSe, PbTe).[28] They are chemically grown and their optical properties display tunable, narrow and symmetric emission bands, long luminescence lifetime and they are highly photostable.[34-36] Cadmium-free nano-crystals emitting in the near-infrared region have also been developed that are particularly attractive for *in vivo* applications.[37-41]

Single-walled carbon nanotubes (CNTs) are explored as potential imaging tools.[42] CNTs are promising NIRF nanomaterials for molecular imaging, due to their NIR excitation and emission as well as large Stokes shift, photostability and high surface areas.[43]

Emission from small noble metal (Au, Ag) nanoparticles, with sizes below 2 nm, has gained significant attention in the field of bio-imaging.[44] Nanoparticles with a small number of atoms, in sizes comparable to the Fermi wavelength, display size-dependent emission.[45] These nanoparticles are attractive for bio-imaging applications due to their low cytotoxicity and their ultrasmall sizes.[46] Recently, the preparation of NIR AuNPs & AgNPs with reasonable quantum yields, has been described and it opened the possibility for many *in vivo* imaging applications.[47-51]

In addition to the NIRF materials mentioned above, fluorescent nanodiamonds (FNDs) have drawn much attention in recent years as a promising fluorescent nanoprobe for bioimaging applications.[52] Type Ib nanodiamonds emit bright fluorescence at 550–800 nm from nitrogen-vacancy point defects, $(NV)^0$ and $(NV)^-$, and together with their bio-inertness, lack of cytotoxicity, high photostability makes nano-sized diamonds a promising fluorescent probe for single-particle tracking in heterogeneous environments.[53] The detailed overview about the optical properties, spin properties and surface functionalisation of nanodiamonds are described in section 1.4.

1.1.4. History of fluorescence probes in medical imaging

There is a long history of fluorescence imaging in medicine. For human treatment, only the NIR fluorophore indocyanine green (ICG) has been approved by the US Food and Drug Administration (FDA).[28] Since 1970s, ICG has been used for retinal angiography, cardiac output and hepatic function assessment,[54] as an intra-operative staining fluorophore in surgery to image vascular network,[55] bile ducts,[56] and the demarcations of liver segments and sub-segments.[57]

The first clinical trials in the field of oncology using fluorescence as an image-guiding intra-operative method for sentinel lymph node resection have been published in 2008/2009 by

Frangioni's and Sevick-Muraca's groups,[58,59] and also by three Japanese teams using the "Photodynamic Eye" developed by Hamamatsu.[60-62] Precious insights about the possibility of metastatic progression have been obtained by removing the sentinel lymph node, first lymph node draining the tumour, and analysing it to determine the presence or absence of malignant cells.[63] Methylene blue (emission ≈ 700 nm, **Figure 1.4**.), another dye mainly used until now for its colour staining properties, is also slightly fluorescent in the near infrared domain.[64] Methylene blue recently allowed the identification of bile ducts and ureters during fluorescence-guided surgery.[56,65]

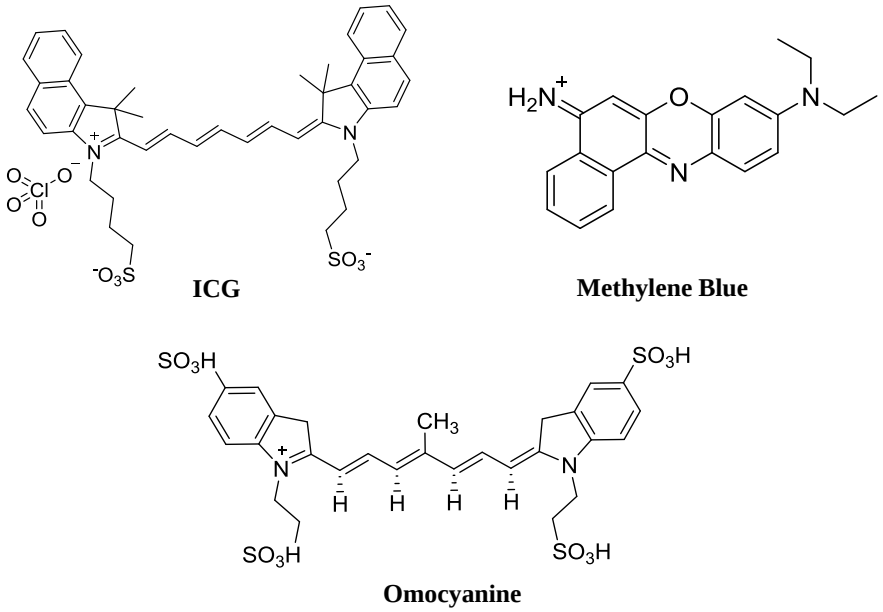

Figure 1.4. Near Infrared fluorescent dyes that have been used for clinical trials.

Another fluorescent dye, Omocianine (emission > 750 nm, Figure 1.4.), has been applied for the detection of malignant breast lesions in women suspected of breast cancer.[66,67] All these very recent studies (<4 years) demonstrate that clinical fluorescence imaging is exponentially growing, and will soon be used in more surgery and other applications. However, there is also evidence of the poor availability of approved near infrared probes (only ICG is validated by the FDA for fluorescence imaging, whereas Methylene blue and Omocyanine have been accepted in selected clinical trials).[28] Hence, there is a large avenue for the development of more efficient NIRF probes.

1.2. Comparison of Nanoparticles and Organic Dyes as Fluorescent Labels

The success of an imaging method, to a great extent, is determined by the physicochemical properties of the chromophore used.[68,69] These include its chemical nature, size, biocompatibility and the interaction between the fluorophore and biological system. Fluorophore properties affect the detection limit and the reliability of the readout for a particular target or event, and the suitability for multiplexing, that is, parallel detection of different targets. Broadly there are two different kinds of fluorophores: (i) small molecule organic dye molecular systems with a defined structure, (ii) nanocrystal chromophores with size-dependent optical and physicochemical properties. While these fluorescent probes exhibit varying levels of sensitivity, each offers advantages as well as disadvantages in terms of biological imaging applications.

Organic fluorescent dyes have well-defined chemical structures, which can be tailored according to the desired optical and chemical properties, and they are mostly commercially available also in larger quantities. The optical properties of organic dyes depend on the electronic transition (s) involved and can be fine-tuned by elaborate design strategies if the structure-property relationship is known for the given class of dye.[68,70] The emission of organic dyes typically originates either from an optical transition delocalized over the entire chromophore or from intramolecular charge transfer transitions.[68] The photoluminescence of nanoparticles has a very different origin, depending on the type of nanomaterial: semiconductor QDs luminescence by recombination of excitons,[35] rare-earth doped nanoparticles photoluminescence by atom orbital (AO) transitions within the rare-earth ions acting as luminescent centers,[71] electron transition from d band to sp band in novel metal clusters[44] or NV center in fluorescent nanodiamonds[6]. Optical properties of luminescent nanoparticles are very different, depending on the material they consist of.

The common fluorophores in the near-infrared domain (600–900 nm), mainly rhodamines, cyanine, bodipy, porphyrine and phtalocyanine - are resonant dyes that are characterized by slightly structured, comparatively narrow absorption and emission bands that often mirror each other, a small stokes shift.[11] The poor separation of the absorption and emission spectrum favors cross-talk between different dye molecules. In comparison to organic dyes, the spectral position of absorption and emission are tunable by the particle size (quantum size effect) and depend on the individual nanomaterial.

In general, the molar absorption coefficient of nanoparticles is larger than organic dyes.[72] Typical molar absorption coefficients are 100,000 – 1,000,000 $M^{-1}cm^{-1}$, whereas for dyes, molar absorption coefficients at the main (long-wavelength) absorption maximum are about 25,000–250,000 $M^{-1}cm^{-1}$.[68] Fluorescence quantum yield of nanoparticles (e.g., QDs) is high in the visible range (400–700 nm) as well as in the NIR (≥700 nm) region.[73-75] In contrast, the more red-shifted the emission of organic dye is, the lower its fluorescence quantum yield.[76,77] As compared to organic dyes, another favorable feature of nanoparticles is the typically very large two-photon absorption cross-section.[77,78] For this reason nanoparticles are very suitable for multiphoton microscopy, which enables deep imaging of a variety of biological samples with less overall photobleaching than with wide-field or confocal microscopy.

The fluorescence lifetime of organic dyes is about 5 ns in the visible light and 1 ns in the NIR wavelengths.[79] In the case of nanoparticles, the comparatively long lifetimes (typically five to hundreds of nanoseconds) enable straightforward temporal discrimination of the signal from cellular autofluorescence and scattered excitation light by time-gated measurements, thereby enhancing the sensitivity.[80] However, in contrast to the monoexponential decay of organic dyes, nanoparticles show complicated size, surface, wavelength and time dependent, bi- or multiexponential decay behavior[81,82] which renders species identification from time-resolved fluorescence measurements very challenging. This is an inherent disadvantage of these materials.

Organic fluorophores are prone to photobleaching. The best organic dyes undergo approximately ~10^7 excitation cycles before permanent photobleaching as a result of highly reactive triplet dark states.[83-85] The long triplet state increases the probability of a covalent modification of the dye which makes the dye permanently nonfluorescent.[85] Photobleaching leads to a steady decrease in the emission.[86] Higher excitation intensities are needed to increase emission rates, which lead to more rapid photobleaching and phototoxicity.[87] Higher excitation intensities result in both increased background and the contrast decreases significantly. Lack of the photostability consequently does not allow the tracking of cellular events that happen over minutes to days. Imaging applications need to balance between sufficiently high emission intensities on the one hand and low enough excitation intensities at the other hand. This is particularly evident for imaging smaller sub-cellular structures, which utilize fewer fluorescent labels so that higher excitation intensities are needed to generate sufficient emission. In addition, many NIR dyes, such as the clinically approved indocyanine

green (ICG), suffer from poor thermal stability in aqueous solution.[88] In contrast, nanoparticles display excellent thermal, photochemical stability and photo-oxidation is almost completely suppressed for relevant time intervals.[82,89] This is a considerable advantage over organic fluorophores for single molecule spectroscopy applications where intense laser excitation sources are used.[90]

Labeling of biomolecules, such as peptides, proteins or oligonucleotides with a fluorophore requires suitable functional groups for covalent binding or for noncovalent attachment of the fluorophore. The advantage of organic dyes in this regard are the already well established protocols and commercial availability of a toolbox of functionalized dyes.[69] Furthermore, the small size of organic dye labels minimizes possible steric hindrance, which can interfere with biomolecule function, and allows the attachment of several fluorophores to a single biomolecule to maximize the fluorescence signal. In contrast, several biomolecules are typically attached to a single nanoparticle, and it is difficult to control biomolecule orientation.

Nanoparticles are very well suited for *in vivo* imaging due to their tunable pharmacokinetics, ability to deliver large payloads, and incorporation of targeting groups. Due to the "enhanced permeability and retention" (EPR) effect, nanoparticles passively accumulate in tumours more efficiently than in healthy tissues.[91] The tumor accumulation can also be enhanced by the decoration of the nanoparticle surface with targeting ligands, which is able to specifically bind to receptors overexpressed by many tumour cells. The tumour accumulation leads to increased signal-to-background ratio. However, this is not the case for small organic fluorescent dyes, which undergoes fast body clearance.

1.3. Gold Nanoparticles (AuNPs) for Bioimaging Applications

Atom clusters with sizes in the range of 1-100 nm are denoted nanoparticles.[92] Nanoparticles consist of different numbers of atoms or molecules bound together and they are usually of intermediate sizes ranging between individual atoms and bulk material.[92] Since nanoparticles are larger than individual atoms and molecules but smaller than the bulk solid, materials in the nanometer size regime reveal a number of particular features that are somewhat in between a macroscopic solid and an atomic or molecular system.[92] There are three major reasons that explain these differences: the existence of a high surface-to-volume ratio,[93-95] quantum size effects,[96] and electrodynamic interactions.[97] Nanometer-scale metal particles exhibit optical properties of great aesthetic, technological, and economic value. Colloidal solutions of the noble metals, particularly gold nanoparticles (AuNPs), have

received considerable attention due to their ease of synthesis, unique optoelectronic properties, readily tunable sizes, shapes and facile surface functionalisation thus offering an attractive platform for diagnostics and therapeutics application.[98]

1.3.1. Synthesis and surface functionalisation of AuNPs

During the past two decades, numerous methods for preparing AuNPs have been developed, mainly focusing on controling their size, shape, solubility, stability, and surface functionality. The scientific synthesis of colloidal gold reports back to the work of Michael Faraday in 1857.[99] He prepared gold hydrosols by reduction of an aqueous solution of chloroaurate with phosphorus dissolved in carbon disulfide.[99] Later in 1951, Turkevich developed the synthesis of AuNPs, using citrate reduction of $HAuCl_4$ and in 1973, G. Frens demonstrated procedures to control AuNPs size by varying the ratio of gold salt to sodium citrate.[100,101] A significant breakthrough in AuNPs synthesis has been achieved by Brust and Schiffrin in 1994.[102] They reported the stabilisation of AuNPs utilizing strong thiol−gold interactions (the Brust−Schiffrin method).[102] These thiol-protected AuNPs displayed superior stability due to strong thiol−gold interactions and they can be easily functionalized.[102] Nowadays, the particle sizes of AuNPs can be tuned by varying the reaction conditions, such as the gold/thiol ratio, temperature and reduction rate.[103] In general, the reduction of metal ions in aqueous solution results in the formation of large nanoparticles due the high tendency of NPs to aggregate.[104] In order to prepare fluorescent AuNPs with dimensions smaller than 2 nm, the aggregation of nanoparticles needs to be prevented. In addition, the nature of the ligands used for capping the particle surface, can markedly affect their emission properties.[105] Therefore, choosing suitable agents capable of stabilizing clusters from aggregation to enhance their stability is of key importance for obtaining small, highly fluorescent AuNPs.[106,107] Even though first fluorescent noble metal nanoparticles report back to 1969, they have not received much interest due to their extremely low quantum yield (QY) of 10^{-10}.[108] Recently, however, researchers have developed various approaches to synthesize water-soluble, fluorescent metal NPs with much enhanced QYs in the range of 56 %.[109] Thiol-containing small molecules are the most commonly adopted stabilizers in metal nanoparticle synthesis due to the strong interaction between thiols and Au.[110] The facile one pot synthesis of AuNPs has been developed by simply reducing Au^{3+} with $NaBH_4$.[48] In addition, glutathione,[111-113] tiopronin,[114] mercaptopropionic acid,[115] thioctic acid,[48] have shown to be excellent stabilizers for the synthesis of AuNPs with visible-NIR luminescence. Based on their capability of sequestering

metal ions from solution, PAMAM dendrimers have also been utilized as templates to prepare small metal NPs.[44,116,117] There are also several recent reports on the synthesis of polymer-stabilized fluorescent AuNPs. For instance, AuNPs capped with polyethylenimine (PEI),[118] poly(N-vinylpyrrolidone) (PVP)[119] amino-terminated poly(1,2-butadiene)[120] water-soluble polymethacrylic acid,[121] have been reported with reseaonable quantum yield. Proteins also offer excellent scaffolds for template-driven formation of small metal NPs. Many proteins, such as, bovine serum albumin (BSA),[7] lysozyme,[122] transferrin,[123,124] horseradish peroxidase (HRP),[125] have been reported to sequester and reduce Au^{3+} to Au^{0} *in situ*, and thereby producing a simple, green synthetic route for the preparation of fluorescent AuNPs.[7, 116-119]

Regardless of the synthetic strategy used, successful integration of luminicent nanocrystals into a biological environment requires stability over a broad range of conditions, such as at pH ranges between 2-9, at high ionic strength or in the presence of cellular proteases.[126] One step facile synthesis of highly stable AuNPs with different functional end groups (biotin, amino, and carboxyl groups) has been developed.[127] The availability of different kinds of reactive groups will allow covalent reaction schemes to attach AuNPs to a variety of bioreceptors.[128] The attachment of specific biomolecules (e.g., peptides and proteins) at the nanocrystal surfaces offers access to a NP-based technology for sensing, imaging, and *in vivo* tracking.[129]

1.3.2. Size-dependent optical properties of AuNPs

AuNPs possess unique optical and electronic properties mainly due to the surface plasmon resonance (SPR), which results from the resonance between the incident photon frequency and the collective oscillation of the conduction band electrons.[92] AuNPs with dimensions smaller than the electron mean free path (ca. 20 nm), exhibit SPR absorption at around 520 nm, corresponding to the frequency of coherent oscillation of the conduction band electrons induced by the interacting electromagnetic field.[130] The resonance frequency of this SPR is strongly dependent on the size, shape, interparticle interactions, dielectric properties and the local environment of the nanoparticle.[131] With increasing nanoparticle sizes, a red shift of the SPR is observed due to electromagnetic retardation in larger particles.[131] The aggregation of AuNPs results in significant red-shifting (from ~520 to ~650 nm) and broadening in the SPR, changing the solution color from red to blue due to the interparticle plasmon coupling.[132,133] This phenomenon is very attractive for colorimetric sensing.[98] Metal nanoparticles exhibit a continuous density of states due to the overlapping atomic orbitals as described by the band

theory.[134] As a result of the overlapping atomic orbitals, valence and conduction bands are so close in energy for a metal that there is no band gap. Hence larger (>2 nm) gold nanoparticle donot fluoresce anymore. However, as the nanoparticle gets smaller in size the number of atoms as well as the number of orbitals is reduced. As a result, small nanoparticles or quantum clusters no longer allow the plasmon excitation unlike their larger counterpart.[135-137] In nanoclusters, the conduction and valence bands become discrete leading to an energy gap that increases with decreasing size.[138] This becomes particularly relevant to the electronic properties of the metal cluster when the size approaches that of the deBroglie wavelength of electrons at the Fermi energy level, at which point the system clearly exhibits molecular states.[139] Thus, clusters of these size exhibit molecular properties such as a separation between electronic states analogous to HOMO and LUMO of molecule. At this small size regime, the excited state gets sufficiently populated for light emission. The AuNPs emit from the blue to the near-IR region and the emission wavelength depends on the number of atom within the cluster due to the transitions between electrons in the sp conduction band and holes in the d-band generated by optical excitation (**Figure 1.5.**).[106,116] Upon decreasing the sizes of homologous stabilizer-protected AuNPs, the emission wavelength undergoes a blue shift.[116] The emission wavelength of AuNPs can be tuned by changing the capping molecules, and a single light source is needed for simultaneous excitation of all different-emissive nanoclusters, which is similar to semiconductor quantum dots.

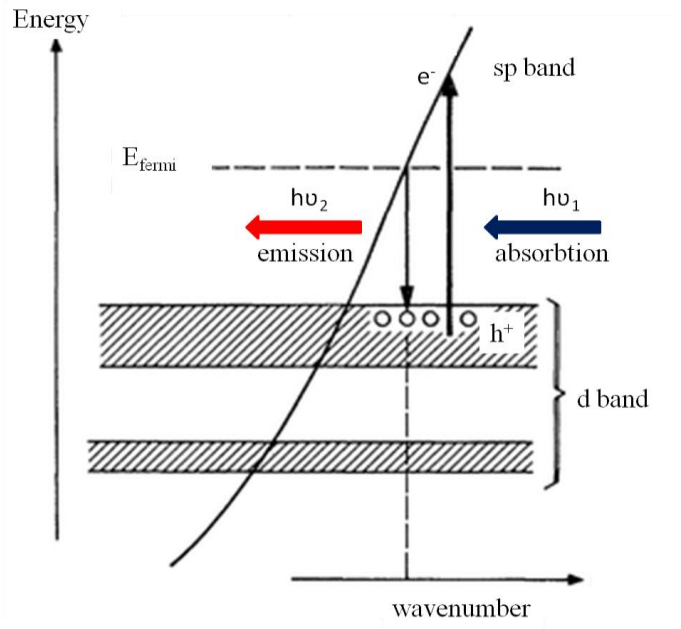

Figure 1.5. A simple energy diagram of photoluminescence in AuNPs. Absorption of a photon excites an electron from the d band to the sp band above the Fermi level. Radiative recombination between an electron and the excited hole, results in the emission. (Image Ref[44])

In this dissertation work, in addition to NIR emitting fluorescent AuNPs, NIR emitting fluorescent nanodiamonds (FNDs) have been used for bioimaging and sensing applications. Unlike AuNPs, fluorescent nanodiamonds exhibit size independent optical properties. In addition to optical properties, the negatively charged lattice defects in FNDs, is of particular interest because of its spin properties. The optical and magnetic properties of FNDs promise to be the foundation of a variety of biomedical, magnetic and quantum applications. The detailed overview of nanodiamond is the following.

1.4. Overview of fluorescent nanodiamonds (FNDs)

1.4.1. Preparation of nanodiamonds

In 1960s nanodiamonds were first prepared by detonation or shockwave synthesis methods.[140] The soot of the detonation of certain explosives, for example, TNT–hexogene mixtures contains nanoscale diamond.[140] This so-called detonation diamond consists of tiny diamond crystallites of about 5 nm in size.[141] For large industrial scale production of nanodiamonds, commonly used methods are HTHP (high temperature high pressure synthesis) and CVD (chemical vapor deposition). The size and surface property highly depends on the method used for their production.[142] The main surface groups that are found on diamond nanoparticles include -COOH and C=O groups in addition to different alcohol functions (tertiary, secondary, primary) and ether groups.[143] However, other structural elements, such as areas with sp^2 carbon of different nature (isolated double bonds, extended areas with π-conjugation up to graphene-like or graphitic structures) are also detectable on nanodiamond (**Figure 1.6**). Additionally, the purification of nanodiamonds is most often carried out using oxidizing mineral acids and/or air oxidation[144,145] which leads to carboxyl groups on the diamond surface. However, nanodiamond prepared by CVD method would carry hydrogenated surface.[146]

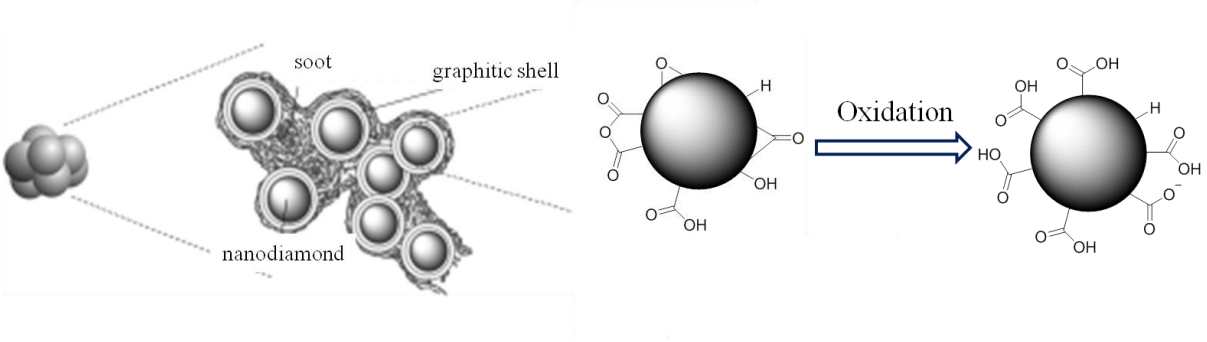

Figure 1.6. Surface functional groups of detonation diamond and its oxidation to carboxylated nanodiamond.[147,148]

1.4.2. Creation of NV centers at the diamond surface

In order to controllably create NV centers, highly sofisticated techniques have been developed.[142-144] Diamonds are firstly irradiated by high-energy particles such as electrons, protons, neutrons, ions and gamma particles, which produce lattice vacancies.[149,150] Then the sample is annealed at temperatures around 800^0C, in order to mobile the vacancies. At this temperature, substitutional nitrogen produces strain in the diamond lattice and efficiently captures moving vacancies, then forms the NV color center.[151] Another approach of creating NV color centers is nitrogen implantation in a very pure type IIa diamond.[152] In this approach, nitrogen atoms are implanted by focusing a nitrogen ion beam on the diamond surface by focusing a nitrogen ion beam on the diamond surface. The CVD-grown diamond, NV centers can be created during the synthesis process. The NV color center incorporated diamond film can be grown with 0-0.1% N_2, 0.7% CH_4, 99.2% H_2 gas mixture, at about 800^0C substrate temperature and low pressure.[153] The NV center concentration varies with the nitrogen doping levels. Single defects can be created by optimizing the nitrogen doping levels. Moreover, it is perfectly photostable, showing no sign of photobleaching even under high-power excitation at the single molecule level.[154]

1.4.3. Surface functionalisation of nanodiamond

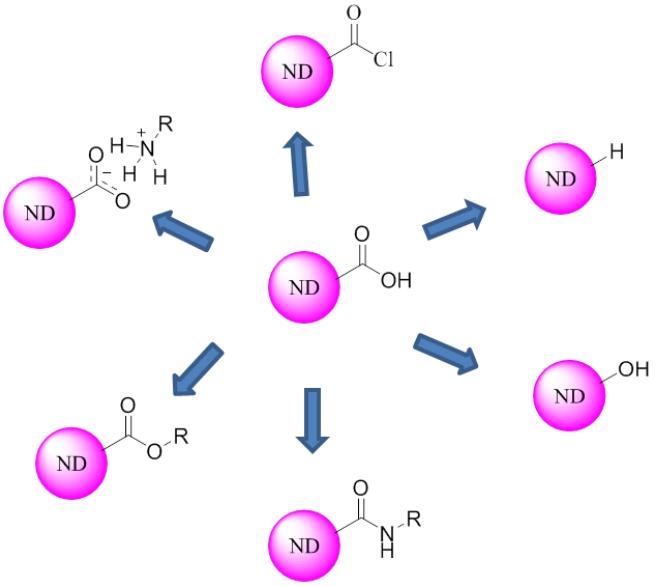

Figure 1.7. Surface chemistry with carboxylic groups terminated nanodiamond.

Nanodiamond surfaces are typically covered by a variety of oxygen-rich functional groups, including esters, hydroxyls and carboxylic acids.[155] The process for nanodiamond

functionalisation usually begins with nitric and/or sulphuric acid treatment, which removes the surface graphite and uniformly terminates the diamond surface with carboxylic acid groups.[156] Hydroxyl group terminated nanodiamonds can be prepared by treating nanodiamonds with reducing agent.[157]Carboxylated nanodiamonds can be covalently functionalised via carbodiimide chemistry.[158,159] Ligands with free amino or hydroxyl groups have been covalently coupled to nanodiamonds via amide or ester linkage.[53,147,159-162] Nanodiamonds can also be modified through the chemistry of graphitic carbon on the surface by means of Diels–Alder reactions[163] and diazonium chemistry.[164-166]

In addition to covalent surface modification, oxidised nanodiamond surfaces can be functionalised non-covalently by adsorbing bio-active molecules via hydrogen bonding, electrostatic or other polar interactions (physisorption).[167] Diamonds have been used to adsorb small organic molecule drugs[168,169] or macromolecules such as proteins,[170-173] hormones,[174] antibodies,[175] DNA,[176] colagen[177] or fibrinogen[178] for the production of sensing devices, purification of proteins or the delivery of therapeutic agents. A distinct feature of nanodiamonds is that many different functional groups can be attached to their surface without compromising the optical and spin properties of the diamond core.[179]

1.4.4. Optical properties of fluorescent nanodiamonds (FNDs)

Type Ib diamonds emit bright fluorescence at 550–800 nm due to imperfections called nitrogen-vacancy (NV) centers or color centers — a nitrogen atom next to a vacancy (**Figure 1.8**). FNDs do not blink like quantum dots or bleach like organic dyes. Their "perfect photostability" makes FNDs useful for long-term tracking inside cells, such as following molecular motors.[180] The photostability also means nanodiamond could be used to monitor cell processes at the nanometer scale by super-resolution microscopy.[181]

The NV color center exhibits two charge states: neutrally charged NV^0, with a zero-phonon line at 575 nm (2.156 eV)[182] and negatively charged NV^-, with a zero-phonon line at 637 nm (1.945 eV)[149]. The bound states of this deep NV^- center are multiparticle states composed of six electrons: five contributed by the four atoms surrounding the vacancy, and one captured from the bulk.[183] The NV^- color center has a long lifetime metastable level. When excited with a strong laser power, the electron will be populated to the metastable level and results in the bunching effect.[184] In contrast, all the observations on single NV^0 color centers showed no

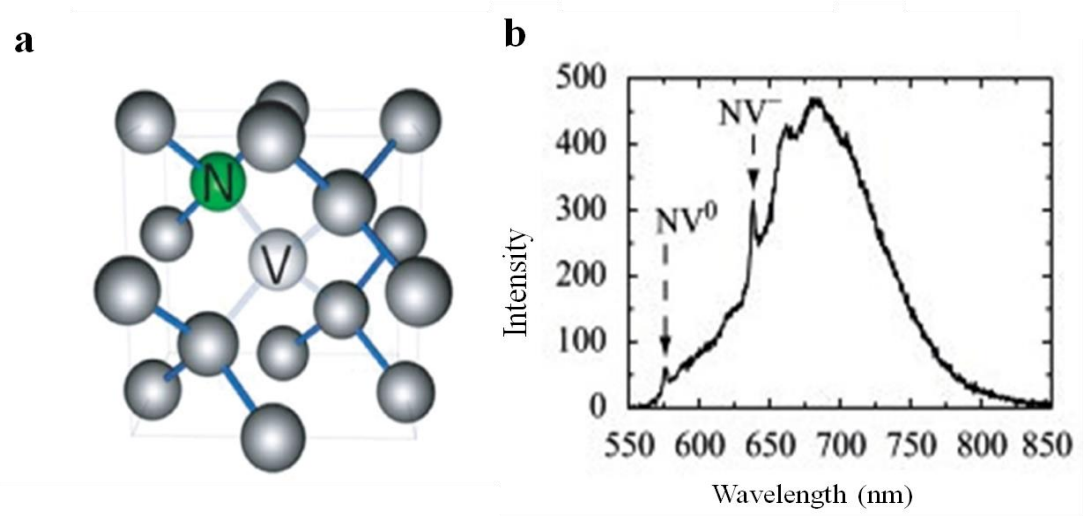

Figure 1.8. (a) Structure of the nitrogen-vacancy (NV) defect in diamond. (Image Ref[189]) **(b)** Emission spectra of fluorescent nanodiamond. Excitation wavelength of 532 nm.

bunching effect. When the NV center is present in a diamond crystal, a single charge state often dominates but both charge states can co-exist.[185] The NV color center is able to switch between different charge states. These two charge states could be created independently but also can be transformed from one to the other by applying different kinds of excitations.[186] This transformation is called photochromic effect since it changes the band gaps between two charge states.[186] Photochromic effects of an ensemble of NV color centers, and verified the proportion of the NV^- and NV^0 color centers as a function of the excitation wavelength and excitation time.[186] All these observations were generally attributed to electron excitation and capture dynamics between nearby nitrogen donors and NV centers. The high excitation power converts NV^0 to NV^-, which leads to red shifts of the optical spectra. This photochromic effect is reversible.[152] After decreasing the excitation power to the centers, it returns to the NV^0 form. The quantum yield of NV center is 70% and the luminescence decay time of the 1.945 eV centre in type Ib diamond is 11ns.[187]

1.4.5. Spin Properties of FNDs

The NV^- centre is of particular interest because it has an S = 1 spin ground state that can be spin-polarized by optical pumping and manipulated using electron paramagnetic resonance.[188] Two out of six electrons of the centre are unpaired, forming an electron spin triplet in the electronic ground and first excited state. Hyperfine coupling constants to the nitrogen nuclear spin and carbon spins in the first coordination shell show that roughly 70%

of the unpaired electron spin density is found at the three nearest neighbouring carbon atoms, whereas the spin density at the nitrogen is only 2%.[188] The electrons spend most of their time at the three carbons next to the vacancy. Broadband optical excitation of the centre polarizes it by optical pumping into the m_s=0 spin sublevel. Laser-assisted detection of the spin state of a single nitrogen-vacancy centre makes use of differences in the absorption and emission properties of the spin sublevels. Specifically, the spin sublevel with a magnetic quantum number of m_s=0 (bright state) scatters, 30% more photons than m_s=±1 states. Hence, when a resonant microwave field induces magnetic dipole transitions between these electronic spin sublevels, it destroys the optically pumped spin polarization, resulting in a significant decrease of the nitrogen-vacancy centre fluorescence.[189]

As shown in **Figure 1.9.** the lowest energy bound state is a spin triplet ($^3A_2$) whose spin sublevels differ slightly in energy. A spin-conserving optical transition exists between the $^3A_2$ state and an excited-state triplet (^3E) 1.945 eV higher in energy. In addition, there exists a spin-selective decay path between these two states that includes a nonradiative transition from ^3E to an intermediate spin singlet ($^1A_1$). In combination, these transitions allow the

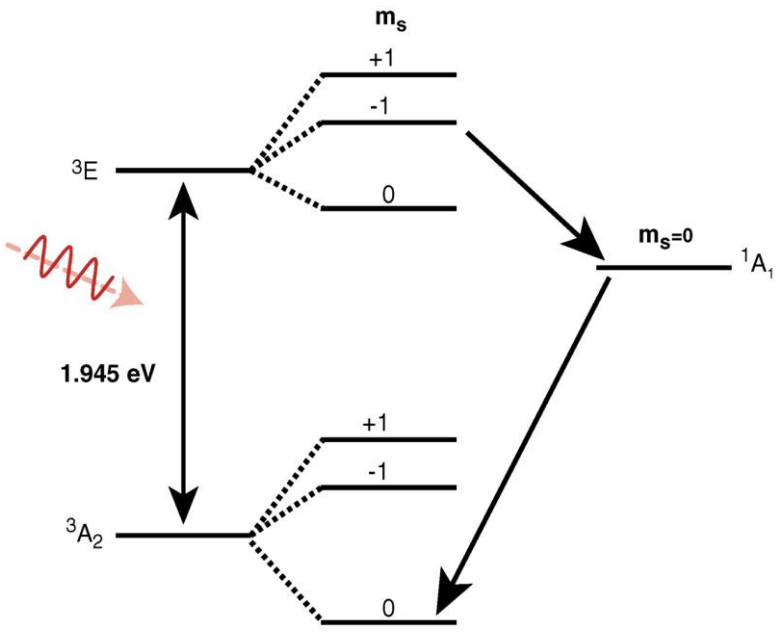

Figure 1.9. Multiplet structure of the NV^- center in diamond. A 1.945-eV in conserving optical transition exists between the ground- ($^3A_2$) and excited-(^3E) state triplets. Transitions from the ms =±1 sublevels of ^3E to an intermediate spin singlet ($^1A_1$) are much stronger than those from the m_s=0 sublevel. The spin-selective nature of this decay path can be used in conjunctionwith the 1.945 eV transition to optically polarize and measure the spin state of $^3A_2$. (Image Reference)[190]

center to be optically initialized and measured. That is, they allow the defect to be optically pumped into the m_s=0 sublevel of $^3A_2$, and they cause the fluorescence intensity between ^3E and $^3A_2$ to be spin-dependent.[191] Spin dependent optical property makes NV centre a promising candidate for nanoscale magnetometry and imaging with extraordinary spatial resolution, field precision, linearity and directional sensitivity.[189]

1.5. References

(1) Stephens, D. J.; Allan, V. J. *Science* **2003**, *300*, 82.
(2) Emptage, N. J. *Curr. Opin. Pharmcol.* **2001**, *1*, 521.
(3) Nune, S. K.; Gunda, P.; Thallapally, P. K.; Lin, Y.-Y.; Laird Forrest, M.; Berkland, C. J. *Expert Opin. Drug Deliv.* **2009**, *6*, 1175.
(4) Frangioni, J, V.; Choi, H. S. *Mol. Imaging* **2010**, *9*, 291.
(5) Klaassen, C. D. *Casarett & Doull's Toxicology: The Basic Science of Poisons*; McGraw-Hill: New York, 2001.
(6) Mochalin, V. N.; Shenderova, O.; Ho, D.; Gogotsi, Y. *Nat. Nanotechnol.* **2012**, *7*, 11.
(7) Xie, J.; Zheng, Y.; Ying, J. Y. *J. Am.Chem. Soc.***2009**, *131*, 888.
(8) Jain, P. K.; Huang, X.; El-Sayed, I. H.; El-Sayed, M. A. *Acc. Chem. Res.* **2008**, *41*, 1578.
(9) Weissleder, R.; Mahmood, U. *Radiology* **2001**, *219*, 316.
(10) Thakur, M.; Lentle, B. C. *Radiology* **2005**, *236*, 753.
(11) Luo, S.; Zhang, E.; Su, Y.; Cheng, T.; Shi, C. *Biomaterials* **2011**, *32*, 7127.
(12) Becker, A.; Hessenius, C.; Licha, K.; Ebert, B.; Sukowski, U.; Semmler, W.; Wiedenmann, B.; Grotzinger, C. *Nat. Biotechnol.* **2001**, *19*, 327.
(13) De Silva, A. P.; Gunaratne, H. Q. N.; Gunnlaugsson, T.; Huxley, A. J. M.; McCoy, C. P.; Rademacher, J. T.; Rice, T. E. *Chem. Rev.* **1997**, *97*, 1515.
(14) Callan, J. F.; de Silva, A. P.; Magri, D. C. *Tetrahedron* **2005**, *61*, 8551.
(15) Kobayashi, H.; Ogawa, M.; Alford, R.; Choyke, P. L.; Urano, Y. *Chem. Rev.* **2010**, *110*, 2620.
(16) Boumaza, S.; Arribas, S. M.; Osborne-Pellegrin, M.; McGrath, J. C.; Laurent, S. P.; Lacolley, P.; Challande, P. *Hypertension* **2001**, *37*, 1101.
(17) Lee, W. K.; Bell, J.; Kilpatrick, E.; Hayes, M.; Lindop, G. B. M.; Dominiczak, M. H. *Atherosclerosis* **1993**, *98*, 219.
(18) Mérian, J.; Gravier, J.; Navarro, F.; Texier, I. *Molecules* **2012**, *17*, 5564.
(19) Frangioni, J. V. *Curr.Opin.Chem.Biol.* **2003**, *7*, 626.
(20) Koide, Y.; Urano, Y.; Hanaoka, K.; Terai, T.; Nagano, T. *J. Am.Chem. Soc.* **2011**, *133*, 5680.
(21) Zhao, W.; Carreira, E. M. *Chem. Eur. J.* **2006**, *12*, 7254.
(22) Leevy, W. M.; Gammon, S. T.; Jiang, H.; Johnson, J. R.; Maxwell, D. J.; Jackson, E. N.; Marquez, M.; Piwnica-Worms, D.; Smith, B. D. *J. Am. Chem.Soc.* **2006**, *128*, 16476.
(23) Kamat, N. P.; Liao, Z.; Moses, L. E.; Rawson, J.; Therien, M. J.; Dmochowski, I. J.; Hammer, D. A. *Proc. Natl. Acad. Sci. USA* **2011**, *108*, 13984.
(24) Nesterova, I. V.; Verdree, V. T.; Pakhomov, S.; Strickler, K. L.; Allen, M. W.; Hammer, R. P.; Soper, S. A. *Bioconjugate Chem.* **2007**, *18*, 2159.
(25) Kiyose, K.; Kojima, H.; Urano, Y.; Nagano, T. *J. Am. Chem. Soc.***2006**, *128*, 6548.
(26) Cheng, Z.; Wu, Y.; Xiong, Z.; Gambhir, S. S.; Chen, X. *Bioconjugate Chem.* **2005**, *16*, 1433.

(27) Peng, X.; Song, F.; Lu, E.; Wang, Y.; Zhou, W.; Fan, J.; Gao, Y. *J.Am.Chem. Soc.* **2005**, *127*, 4170.
(28) Mérian, J.; Gravier, J.; Navarro, F.; Texier, I. *Molecules* **2012**, *17*, 5564.
(29) Escobedo, J. O.; Rusin, O.; Lim, S.; Strongin, R. M. *Curr. Opin. Chem. Biol.* **2010**, *14*, 64.
(30) Yang, Z.; Zheng, S.; Harrison, W. J.; Harder, J.; Wen, X.; Gelovani, J. G.; Qiao, A.; Li, C. *Biomacromolecules* **2007**, *8*, 3422.
(31) Zhi, Y.; Jeffrey, L.; Mike, M.; John, W. H.; Rui, Z.; Dong, L.; Wei, L.; Mei, T.; Juri, G. G.; Alex, Q.; Chun, L. *Nanotechnology* **2009**, *20*, 165101.
(32) Mulder, W. J. M.; Strijkers, G. J.; Tilborg, G. A. F.; Cormode, D. P.; Fayad, Z. A.; Nicolay, K. *Acc. Chem. Res.* **2009**, *42*, 904.
(33) LaManna, J. C.; Puchowicz, M. A.; Xu, K.; Harrison, D. K.; Bruley, D. F.; Wang, J.; O'Toole, M.; Massey, A.; Biswas, S.; Nantz, M.; Achilefu, S.; Kang, K. *In Oxygen Transport to Tissue XXXII*; Springer US; Vol. 701, p 149.
(34) Smith, A. M.; Duan, H.; Mohs, A. M.; Nie, S. *Adv. Drug Deliver. Rev.* **2008**, *60*, 1226.
(35) Zrazhevskiy, P.; Sena, M.; Gao, X. *Chem. Soc. Rev.* **2010**, *39*, 4326.
(36) Xing, Y.; Rao, J. *Cancer Biomark.* **2008**, *4*, 307.
(37) Li, L.; Daou, T. J.; Texier, I.; Kim Chi, T. T.; Liem, N. Q.; Reiss, P. *Chem.Mater.* **2009**, *21*, 2422.
(38) Li, L.; Reiss, P. *J. Am.Chem.Soc.* **2008**, *130*, 11588.
(39) Gao, J.; Chen, K.; Xie, R.; Xie, J.; Lee, S.; Cheng, Z.; Peng, X.; Chen, X. *Small* **2010**, *6*, 256.
(40) Pons, T.; Pic, E.; Lequeux, N.; Cassette, E.; Bezdetnaya, L.; Guillemin, F. O.; Marchal, F. D. R.; Dubertret, B. *ACS Nano* **2010**, *4*, 2531.
(41) Yong, K.-T.; Roy, I.; Ding, H.; Bergey, E. J.; Prasad, P. N. *Small* **2009**, *5*, 1997.
(42) O'Connell, M. J.; Bachilo, S. M.; Huffman, C. B.; Moore, V. C.; Strano, M. S.; Haroz, E. H.; Rialon, K. L.; Boul, P. J.; Noon, W. H.; Kittrell, C.; Ma, J.; Hauge, R. H.; Weisman, R. B.; Smalley, R. E. *Science* **2002**, *297*, 593.
(43) Hong, H.; Gao, T.; Cai, W. *Nano Today* **2009**, *4*, 252.
(44) Zheng, J.; Zhou, C.; Yu, M.; Liu, J. *Nanoscale* **2012**, *4*, 4073.
(45) Zheng, J.; Nicovich, P. R.; Dickson, R. M. *Annu. Rev. Phys. Chem.* **2007**, *58*, 409.
(46) Shang, L.; Dong, S.; Nienhaus, G. U. *Nano Today* **2011**, *6*, 401.
(47) Lin, C.-A. J.; Yang, T.-Y.; Lee, C.-H.; Huang, S. H.; Sperling, R. A.; Zanella, M.; Li, J. K.; Shen, J.-L.; Wang, H.-H.; Yeh, H.-I.; Parak, W. J.; Chang, W. H. *ACS Nano* **2009**, *3*, 395.
(48) Shang, L.; Azadfar, N.; Stockmar, F.; Send, W.; Trouillet, V.; Bruns, M.; Gerthsen, D.; Nienhaus, G. U. *Small* **2011**, *7*, 2614.
(49) Richards, C. I.; Choi, S.; Hsiang, J.-C.; Antoku, Y.; Vosch, T.; Bongiorno, A.; Tzeng, Y.-L.; Dickson, R. M. *J. Am.Chem. Soc.* **2008**, *130*, 5038.
(50) Vosch, T.; Antoku, Y.; Hsiang, J.-C.; Richards, C. I.; Gonzalez, J. I.; Dickson, R. M. *Proc. Natl. Acad. Sci. U.S.A* **2007**, *104*, 12616.
(51) Guo, W.; Yuan, J.; Wang, E. *Chem. Commun.* **2009**, *45*, 3395.
(52) Mohan, N.; Chen, C.-S.; Hsieh, H.-H.; Wu, Y.-C.; Chang, H.-C. *Nano Lett.* **2010**, *10*, 3692.
(53) Fu, C.-C.; Lee, H.-Y.; Chen, K.; Lim, T.-S.; Wu, H.-Y.; Lin, P.-K.; Wei, P.-K.; Tsao, P.-H.; Chang, H.-C.; Fann, W. *Proc. Natl. Acad. Sci. U.S.A* **2007**, *104*, 727.
(54) Benson, R. C.; Kues, H. A. *Phys. Med. Biol.* **1978**, *23*, 159.
(55) Lee, B. T.; Matsui, A.; Hutteman, M.; Lin, S. J.; Winer, J. H.; Laurence, R. G.; Frangioni, J. V. *J. Reconstr. Microsurg.* **2010**, *26*, 59.
(56) Matsui, A.; Tanaka, E.; Choi, H. S.; Kianzad, V.; Gioux, S.; Lomnes, S. J.; Frangioni, J. V. *Surgery* **2010**, *148*, 78.

(57) Aoki, T.; Yasuda, D.; Shimizu, Y.; Odaira, M.; Niiya, T.; Kusano, T.; Mitamura, K.; Hayashi, K.; Murai, N.; Koizumi, T.; Kato, H.; Enami, Y.; Miwa, M.; Kusano, M. *World J. Surg.* **2008**, *32*, 1763.
(58) Sevick-Muraca, E. M.; Sharma, R.; Rasmussen, J. C.; Marshall, M. V.; Wendt, J. A.; Pham, H. Q.; Bonefas, E.; Houston, J. P.; Sampath, L.; Adams, K. E.; Blanchard, D. K.; Fisher, R. E.; Chiang, S. B.; Elledge, R.; Mawad, M. E. *Radiology* **2008**, *246*, 734.
(59) Troyan, S.; Kianzad, V.; Gibbs-Strauss, S.; Gioux, S.; Matsui, A.; Oketokoun, R.; Ngo, L.; Khamene, A.; Azar, F.; Frangioni, J. *Ann. Surg. Oncol.* **2009**, *16*, 2943.
(60) Miyashiro, I.; Miyoshi, N.; Hiratsuka, M.; Kishi, K.; Yamada, T.; Ohue, M.; Ohigashi, H.; Yano, M.; Ishikawa, O.; Imaoka, S. *Ann. Surg.Oncol.* **2008**, *15*, 1640.
(61) Ogasawara, Y.; Ikeda, H.; Takahashi, M.; Kawasaki, K.; Doihara, H. *World J. Surg.* **2008**, *32*, 1924.
(62) Tagaya, N.; Yamazaki, R.; Nakagawa, A.; Abe, A.; Hamada, K.; Kubota, K.; Oyama, T. *Am. J. Surg.* **2008**, *195*, 850.
(63) Velde, E. A.; Veerman, T.; Subramaniam, V.; Ruers, T. *Eur. J. Surg.Oncol.* **2010**, *36*, 6.
(64) Gioux, S. C., H.S.; Frangioni, J.V. *Mol. Imaging* **2010**, *9*, 237.
(65) Matsui, A.; Tanaka, E.; Choi, H. S.; Winer, J. H.; Kianzad, V.; Gioux, S.; Laurence, R. G.; Frangioni, J. V. *Surgery*, **2010**, *148*, 87.
(66) Poellinger, A.; Persigehl, T.; Mahler, M.; Bahner, M.; Ponder, S. L.; Diekmann, F.; Bremer, C.; Moesta, T. *Invest. Radiol.* **2011**, *46*, 697.
(67) Ven, S.; Wiethoff, A.; Nielsen, T.; Brendel, B.; Voort, M.; Nachabe, R.; Mark, M.; Beek, M.; Bakker, L.; Fels, L.; Elias, S.; Luijten, P.; Mali, W. *Mol. Imaging Biol.* **2010**, *12*, 343.
(68) Mason, W. T. *Fluorescent and luminescent probes for biological activity*; Academic Press: London, 1999.
(69) Waggoner, A. *Curr. Opin.Chem.Biol.* **2006**, *10*, 62.
(70) Dähne, S.; Resch-Genger, U.; Wolfbeis, O.S., eds. *Near-infrared dyes for high technology applications.*; Kluwer Academic Publishers, Dordrecht, The Netherlands: Dordrecht, 1998; Vol. 52.
(71) Demchenko, A. P.; Resch-Genger, U.; Grabolle, M.; Nitschke, R.; Nann, T. *In Advanced Fluorescence Reporters in Chemistry and Biology II*; Springer Berlin Heidelberg; Vol. 9, p 3.
(72) Yu, W. W.; Qu, L.; Guo, W.; Peng, X. *Chem.Mater.* **2003**, *15*, 2854.
(73) Hinds, S.; Myrskog, S.; Levina, L.; Koleilat, G.; Yang, J.; Kelley, S. O.; Sargent, E. H. *J. Am.Chem.Soc.* **2007**, *129*, 7218.
(74) Jiang, W.; Singhal, A.; Zheng, J.; Wang, C.; Chan, W. C. W. *Chem. Mater.* **2006**, *18*, 4845.
(75) Shavel, A.; Gaponik, N.; Eychmüller, A. *J. Phys. Chem. B* **2006**, *110*, 19280.
(76) Soper, S. A.; Nutter, H. L.; Keller, R. A.; Davis, L. M.; Shera, E. B. *Photochem. Photobio.* **1993**, *57*, 972.
(77) Larson, D. R.; Zipfel, W. R.; Williams, R. M.; Clark, S. W.; Bruchez, M. P.; Wise, F. W.; Webb, W. W. *Science* **2003**, *300*, 1434.
(78) Padilha, L.; Fu, J.; Hagan, D.; Van Stryland, E.; Cesar, C.; Barbosa, L.; Cruz, C. *Opt. Express* **2005**, *13*, 6460.
(79) Mihindukulasuriya, S. H.; Morcone, T. K.; McGown, L. B. *Electrophoresis* **2003**, *24*, 20.
(80) Dahan, M.; Laurence, T.; Pinaud, F.; Chemla, D. S.; Alivisatos, A. P.; Sauer, M.; Weiss, S. *Opt. Lett.* **2001**, *26*, 825.
(81) Schlegel, G.; Bohnenberger, J.; Potapova, I.; Mews, A. *Phys. Rev. Lett.* **2002**, *88*, 137401.

(82) Sun, Y. H.; Liu, Y. S.; Vernier, P. T.; Liang, C. H.; Chong, S. Y.; Marcu, L.; Gundersen, M. A. *Nanotechnology* **2006**, *17*, 4469.
(83) Eggeling, C.; Widengren, J.; Rigler, R.; Seidel, C. A. M. *Anal. Chem.* **1998**, *70*, 2651.
(84) Zhang, K.; Chang, H.; Fu, A.; Alivisatos, A. P.; Yang, H. *Nano Lett.* **2006**, *6*, 843.
(85) Vogelsang, J.; Cordes, T.; Tinnefeld, P. *Photoch. Photobio. Sci.* **2009**, *8*, 486.
(86) Bernas, T.; Zarebski, M.; Cook, R. R.; Dobrucki, J. W. *J. Microsc.* **2004**, *215*, 281.
(87) Hoebe, R. A.; Van Oven, C. H.; Gadella, T. W. J.; Dhonukshe, P. B.; Van Noorden, C. J. F.; Manders, E. M. M. *Nat. Biotechnol.* **2007**, 25, 249.
(88) Soper, S. A.; Mattingly, Q. L. *J. Am. Chem. Soc.* **1994**, *116*, 3744.
(89) Ziegler, J.; Merkulov, A.; Grabolle, M.; Resch-Genger, U.; Nann, T. *Langmuir* **2007**, *23*, 7751.
(90) Mason, J. N.; Farmer, H.; Tomlinson, I. D.; Schwartz, J. W.; Savchenko, V.; DeFelice, L. J.; Rosenthal, S. J.; Blakely, R. D. *J. Neurosci. Meth.***2005**, *143*, 3.
(91) Maeda, H.; Wu, J.; Sawa, T.; Matsumura, Y.; Hori, K. *J. Control. Release* **2000**, *65*, 271.
(92) Ghosh, S. K.; Pal, T. *Chem. Rev.* **2007**, *107*, 4797.
(93) Ghosh, S. K.; Kundu, S.; Mandal, M.; Pal, T. *Langmuir* **2002**, *18*, 8756.
(94) Ghosh, S. K.; Pal, A.; Kundu, S.; Nath, S.; Pal, T. *Chem. Phys. Lett.* **2004**, *395*, 366.
(95) Ghosh, S. K.; Pal, A.; Nath, S.; Kundu, S.; Panigrahi, S.; Pal, T. *Chem. Phys. Lett.* **2005**, *412*, 5.
(96) Kubo, R. *J. Phys. Soc. Jpn.* **1962**, *17*, 975.
(97) Jackson, J. D. *Classical Electrodynamics*; Wiley: New York, 1975.
(98) Saha, K.; Agasti, S. S.; Kim, C.; Li, X.; Rotello, V. M. *Chem. Rev.* **2012**, *112*, 2739.
(99) Faraday, M. *Philos. Trans. R. Soc. London* **1857**, *147*, 145.
(100) Turkevich, J.; Stevenson, P. C.; Hillier, J. *Discuss. Faraday Soc.* **1951**, *11*, 55.
(101) Frens, G. *Nat. Phys. Sci.* **1973**, *241*, 20.
(102) Brust, M.; Walker, M.; Bethell, D.; Schiffrin, D. J.; Whyman, R. *J. Chem. Soc., Chem. Commun.***1994**, 801.
(103) Hostetler, M. J.; Wingate, J. E.; Zhong, C.-J.; Harris, J. E.; Vachet, R. W.; Clark, M. R.; Londono, J. D.; Green, S. J.; Stokes, J. J.; Wignall, G. D.; Glish, G. L.; Porter, M. D.; Evans, N. D.; Murray, R. W. *Langmuir* **1998**, *14*, 17.
(104) Ji, G.; Ding, B.; Sha, Z.; Wu, J.; Ma, Y.; Lee, J. Y. *Nanoscale*, **2013**, *5*, 5965.
(105) Wu, Z.; Jin, R. *Nano Lett.* **2010**, *10*, 2568.
(106) Huang, C.-C.; Yang, Z.; Lee, K.-H.; Chang, H.-T. *Angew.Chem. Int. Ed.* **2007**, *46*, 6824.
(107) Zhang, G.; Yang, Z.; Lu, W.; Zhang, R.; Huang, Q.; Tian, M.; Li, L.; Liang, D.; Li, C. *Biomaterials* **2009**, *30*, 1928.
(108) Mooradian, A. *Phys. Rev. Lett.* **1969**, *22*, 185.
(109) Chen, T.-H.; Tseng, W.-L. *Small* **2012**, *8*, 1912.
(110) Jin, R. *Nanoscale* **2010**, *2*, 343.
(111) Link, S.; Beeby, A.; FitzGerald, S.; El-Sayed, M. A.; Schaaff, T. G.; Whetten, R. L. *J. Phys. Chem. B* **2002**, *106*, 3410.
(112) Negishi, Y.; Takasugi, Y.; Sato, S.; Yao, H.; Kimura, K.; Tsukuda, T. *J. Am. Chem. Soc.* **2004**, *126*, 6518.
(113) Negishi, Y.; Nobusada, K.; Tsukuda, T. *J. Am. Chem. Soc.* **2005**, *127*, 5261.
(114) Huang, T.; Murray, R. W. *J. Phys. Chem. B* **2001**, *105*, 12498.
(115) Wang, Z.; Cai, W.; Sui, J. *ChemPhysChem* **2009**, *10*, 2012.
(116) Zheng, J.; Zhang, C.; Dickson, R. M. *Phys. Rev. Lett.* **2004**, *93*, 077402.
(117) Bao, Y.; Zhong, C.; Vu, D. M.; Temirov, J. P.; Dyer, R. B.; Martinez, J. S. *J. Phys. Chem. C* **2007**, *111*, 12194.
(118) Duan, H.; Nie, S. *J. Am. Chem. Soc.***2007**, *129*, 2412.

(119) Santiago GonzaÌlez, B.; RodriÌguez, M. A. J.; Blanco, C.; Rivas, J.; LoÌpez-Quintela, M. A.; Martinho, J. M. G. *Nano Lett.* **2010**, *10*, 4217.
(120) Yabu, H. *Chem.Commun.* **2011**, *47*, 1196.
(121) Schaeffer, N.; Tan, B.; Dickinson, C.; Rosseinsky, M. J.; Laromaine, A.; McComb, D. W.; Stevens, M. M.; Wang, Y.; Petit, L.; Barentin, C.; Spiller, D. G.; Cooper, A. I.; Levy, R. *Chem. Commun.* **2008**, *44*, 3986.
(122) Wei, H.; Wang, Z.; Yang, L.; Tian, S.; Hou, C.; Lu, Y. *Analyst* **2010**, *135*, 1406.
(123) Xavier, P. L.; Chaudhari, K.; Verma, P. K.; Pal, S. K.; Pradeep, T. *Nanoscale*, **2010**, *2*, 2769.
(124) Xavier Le, G. V.; Nicole, D.; Marc, S. *Nanotechnology*, **2011**, *22*, 275103.
(125) Wen, F.; Dong, Y.; Feng, L.; Wang, S.; Zhang, S.; Zhang, X. *Anal. Chem.* **2011**, *83*, 1193.
(126) Susumu, K.; Uyeda, H. T.; Medintz, I. L.; Pons, T.; Delehanty, J. B.; Mattoussi, H. *J. Am. Chem. Soc*.**2007**, *129*, 13987.
(127) Oh, E.; Susumu, K.; Goswami, R.; Mattoussi, H. *Langmuir*, **2010**, *26*, 7604.
(128) Hermanson, G. T. *Bioconjugate Techniques*; Academic Press San Diego, 1996.
(129) Chenjie, X.; Luye, M.; Isaac, R.; David, M.-N.; Matthias, N.; James, A. A.; Weian, Z.; Jeffrey, M. K. *Nanotechnology*, **2011**, *22*, 494001.
(130) Link, S.; El-Sayed, M. A. *Annu. Rev. Phys. Chem.* **2003**, *54*, 331.
(131) Efrima, S.; Metiu, H. *J. Chem. Phys.* **1979**, *70*, 1602.
(132) Srivastava, S.; Frankamp, B. L.; Rotello, V. M. *Chem. Mater.* **2005**, *17*, 487.
(133) Su, K. H.; Wei, Q. H.; Zhang, X.; Mock, J. J.; Smith, D. R.; Schultz, S. *Nano Lett.* **2003**, *3*, 1087.
(134) Kreibig, U. V., M. *Optical Properties of Metal Clusters*; Springer: Berlin, 1995; Vol. 25.
(135) Chen, S.; Ingram, R. S.; Hostetler, M. J.; Pietron, J. J.; Murray, R. W.; Schaaff, T. G.; Khoury, J. T.; Alvarez, M. M.; Whetten, R. L. *Science* **1998**, *280*, 2098.
(136) Lee, D.; Donkers, R. L.; Wang, G.; Harper, A. S.; Murray, R. W. *J. Am. Chem. Soc.* **2004**, *126*, 6193.
(137) Lin, Z.; Kanters, R. P. F.; Mingos, D. M. P. *Inorg. Chem.***1991**, *30*, 91.
(138) Dupree, R.; Smithard, M. A. *J. Phys. C Solid State* **1972**, *5*, 408.
(139) Johnston, R. L. *Atomic and Molecular Clusters*; Taylor & Francis: London and New York, 2002.
(140) Yu. Dolmatov, V. *Russ. Chem. Rev.* **2001**, *70*, 607.
(141) Shenderova, O. A.; Zhirnov, V. V.; Brenner, D. W. *Crit. Rev. Solid State Mater. Sci.* **2002**, *27*, 227.
(142) Cheng, C. L.; Chen, C. F.; Shaio, W. C.; Tsai, D. S.; Chen, K. H. *Diamond Relat. Mater.* **2005**, *14*, 1455.
(143) Mochalin, V.; Osswald, S.; Gogotsi, Y. *Chem. Mater.* **2008**, *21*, 273.
(144) Pichot, V.; Comet, M.; Fousson, E.; Baras, C.; Senger, A.; Le Normand, F.; Spitzer, D. *Diamond Relat. Mater.* **2008**, *17*, 13.
(145) Mitev, D.; Dimitrova, R.; Spassova, M.; Minchev, C.; Stavrev, S. *Diamond Relat. Mater.* **2007**, *16*, 776.
(146) Landstrass, M. I.; Ravi, K. V. *Appl. Phys. Lett.* **1989**, *55*, 975.
(147) Krueger, A.; Lang, D. *Adv. Func. Mater.* **2012**, *22*, 890.
(148) Krueger, A. *J. Mater. Chem.* **2011**, *21*, 12571.
(149) Davies, G.; Hamer, M. F. *Proc. R. Soc. A* **1976**, *348*, 285.
(150) Lang, A. R.; Moore, M.; Makepeace, A. P. W.; Wierzchowski, W.; Welbourn, C. M. *Phil. Trans. R. Soc. A* **1991**, *337*, 497.
(151) Konstantin, I.; Guy, J. A. *J. Phys.: Condens. Matter* **2001**, *13*, 6015.

(152) Gaebel, T.; Domhan, M.; Wittmann, C.; Popa, I.; Jelezko, F.; Rabeau, J.; Greentree, A.; Prawer, S.; Trajkov, E.; Hemmer, P. R.; Wrachtrup, J. *Appl. Phys. B* **2006**, *82*, 243.
(153) Rabeau, J. R.; Huntington, S. T.; Greentree, A. D.; Prawer, S. *Appl. Phys. Lett.* **2005**, *86*, 134104.
(154) Gruber, A.; Dräbenstedt, A.; Tietz, C.; Fleury, L.; Wrachtrup, J.; Borczyskowski, C. *Science* **1997**, *276*, 2012.
(155) Schrand, A. M.; Hens, S. A. C.; Shenderova, O. A. *Crit. Rev. Solid State Mater. Sci.* **2009**, *34*, 18.
(156) Ando, T.; Tanaka, J.; Ishii, M.; Kamo, M.; Sato, Y.; Ohashi, N.; Shimosaki, S. *J. Chem. Soc. Faraday Trans.* **1993**, *89*, 3105.
(157) Kruger, A.; Liang, Y.; Jarre, G.; Stegk, J. *J. Mater. Chem.* **2006**, *16*, 2322.
(158) Huang, L. C. L.; Chang, H.-C. *Langmuir* **2004**, *20*, 5879.
(159) Manus, L. M.; Mastarone, D. J.; Waters, E. A.; Zhang, X.-Q.; Schultz-Sikma, E. A.; MacRenaris, K. W.; Ho, D.; Meade, T. J. *Nano Lett.* **2009**, *10*, 484.
(160) Mochalin, V. N.; Gogotsi, Y. *J. Am.Chem.Soc.* **2009**, *131*, 4594.
(161) Park, C.-L.; Jee, A. Y.; Lee, M.; Lee, S. G. *Chem. Commun.* **2009**, *45*, 5576.
(162) Weng, M.-F.; Chiang, S.-Y.; Wang, N.-S.; Niu, H. *Diamond Relat. Mater.* **2009**, *18*, 587.
(163) Jarre, G.; Liang, Y.; Betz, P.; Lang, D.; Krueger, A. *Chem. Commun.* **2011**, *47*, 544.
(164) Yeap, W. S.; Chen, S.; Loh, K. P. *Langmuir* **2008**, *25*, 185.
(165) Liang, Y.; Meinhardt, T.; Jarre, G.; Ozawa, M.; Vrdoljak, P.; Schöll, A.; Reinert, F.; Krueger, A. *J. Colloid Interface Sci.* **2011**, *354*, 23.
(166) Liang, Y.; Ozawa, M.; Krueger, A. *ACS Nano* **2009**, *3*, 2288.
(167) Say, J.; Vreden, C.; Reilly, D.; Brown, L.; Rabeau, J.; King, N. C. *Biophys. Rev.* **2011**, *3*, 171.
(168) Huang, H.; Pierstorff, E.; Osawa, E.; Ho, D. *Nano Lett.* **2007**, *7*, 3305.
(169) Chen, M.; Pierstorff, E. D.; Lam, R.; Li, S.-Y.; Huang, H.; Osawa, E.; Ho, D. *ACS Nano* **2009**, *3*, 2016.
(170) Bondar', V. S.; Pozdnyakova, I. O.; Puzyr', A. P. *Phys. Solid State* **2004**, *46*, 758.
(171) Puzyr, A. P.; Baron, A. V.; Purtov, K. V.; Bortnikov, E. V.; Skobelev, N. N.; Mogilnaya, O. A.; Bondar, V. S. *Diamond Relat. Mater.* **2007**, *16*, 2124.
(172) Kong, X. L.; Huang, L. C. L.; Hsu, C. M.; Chen, W. H.; Han, C. C.; Chang, H. C. *Anal. Chem.* **2004**, *77*, 259.
(173) Puzyr', A. P.; Purtov, K. V.; Shenderova, O. A.; Luo, M.; Brenner, D. W.; Bondar, V. S. *Dokl. Biochem. Biophys.* **2007**, *417*, 299.
(174) Shimkunas, R. A.; Robinson, E.; Lam, R.; Lu, S.; Xu, X.; Zhang, X.-Q.; Huang, H.; Osawa, E.; Ho, D. *Biomaterials* **2009**, *30*, 5720.
(175) Purtov, K. V.; Petunin, A. I.; Burov, A. E.; Puzyr, A. P.; Bondar, V. S. *Nanoscale Res. Lett.* **2010**, *5*, 631.
(176) Wenmackers, S.; Vermeeren, V.; vandeVen, M.; Ameloot, M.; Bijnens, N.; Haenen, K.; Michiels, L.; Wagner, P. *Phys. Status Solidi A* **2009**, *206*, 391.
(177) Huang, H.; Chen, M.; Bruno, P.; Lam, R.; Robinson, E.; Gruen, D.; Ho, D. *J. Phys.Chem. B* **2009**, *113*, 2966.
(178) Garguilo, J. M.; Davis, B. A.; Buddie, M.; Köck, F. A. M.; Nemanich, R. J. *Diamond Relat. Mater.* **2004**, *13*, 595.
(179) Meinhardt, T.; Lang, D.; Dill, H.; Krueger, A. *Adv. Func. Mater.* **2011**, *21*, 494.
(180) Börsch, M.; Reuter, R.; Balasubramanian, G.; Erdmann, R.; Jelezko, F.; Wrachtrup, J. *Proc. SPIE*, **2009**, 71832N.
(181) Han, K. Y.; Willig, K. I.; Rittweger, E.; Jelezko, F.; Eggeling, C.; Hell, S. W. *Nano Lett.* **2009**, *9*, 3323.

(182) Mita, Y. *Phys. Rev. B* **1996**, *53*, 11360.
(183) Loubser, J. H. N.; Van Wyk, J. A. *Diamond Res.* **1977**, *1*, 11.
(184) A. Beveratos, R. B., J. -P. Poizat, P. Grangier *arXiv:quant-ph/0010044v1* **2000**.
(185) Lawson, S. C.; Fischer, D.; Hunt, D. C.; Newton M. E. *J. Phys.: Condens. Matter.* **1998**, *10*.
(186) Manson, N. B.; Harrison, J. P. *Diamond Relat. Mater.* **2005**, *14*, 1705.
(187) Collins, A. T.; Thomaz, M. F.; Jorge, M. I. B. *J. Phys. C: Solid State Phys.* **1983**, *16*, 2177.
(188) Jelezko, F.; Wrachtrup, J. *Phys. Status Solidi A* **2006**, *203*, 3207.
(189) Balasubramanian, G.; Chan, I. Y.; Kolesov, R.; Al-Hmoud, M.; Tisler, J.; Shin, C.; Kim, C.; Wojcik, A.; Hemmer, P. R.; Krueger, A.; Hanke, T.; Leitenstorfer, A.; Bratschitsch, R.; Jelezko, F.; Wrachtrup, J. *Nature* **2008**, *455*, 648.
(190) Weber, J. R.; Koehl, W. F.; Varley, J. B.; Janotti, A.; Buckley, B. B.; Van de Walle, C. G.; Awschalom, D. D. *Proc. Natl. Acad. Sci. U.S.A* **2010**, *107*, 8513.
(191) Manson, N. B.; Harrison, J. P.; Sellars, M. J. *Phys. Rev. B* **2006**, *74*, 104303.

Aims and Motivations

Over the past decade, concepts and tools derived from nanotechnology have been applied to further improve imaging techniques and diagnosis methods. Fluorescent nanoparticles (NPs), especially those emitting in the near infrared (NIR), are one of the most promising and highly sensitive tools for diagnosis of diseases at the cellular and animal level. In particular, the development of multi-functional NPs, which allow the conjugation of several functional groups including cell targeting moieties or therapeutic agents, provides new avenues for clinical therapies and diagnostics.

Recently, luminescent gold NPs (AuNPs) and fluorescent nanodiamonds (FNDs) have emerged that hold great promise for many applications such as luminescence imaging, drug delivery or quantum engineering. However, to address these applications, the surface of these nanoparticles needs to be functionalized with a variety of ligands such as small molecules, surfactants, polymers or biomolecules. In addition, for biological applications, e.g. in a cellular environment, colloidal stability is crucial. In this context, polymer coatings offering multiple stabilizing anchor groups seem particularly appealing to achieve manoparticles with high colloidal stability in water. The polymeric coatings not only impart water solubility but they also serve as a versatile platform for further chemical modifications or bioconjugation reactions since biomolecules can be covalently linked to the polymer surface. There are several synthetic polymers that have been used for the coating of NPs, for example poly(acrylic acid), poly(maleic anhydride), polylysine or dextran among others. Although many polymer coated non-fluorescent nanoparticles have been reported, only limited attempts have been made to prepare multifunctional polymer coated NPs emitting in the NIR. In most cases, the synthetic polymers used are polydisperse and contain only one or a very limited set of chemically reactive repeat units. It is therefopre highly desirable to prepare AuNPs and FNDs coated with a hydrophilic polymer that efficiently stabilizes these nanoparticles but that also contains multiple functional groups that offer the attachment of drug molecules, cell targeting groups. In addition, biocomaptibilty, reduced non-specific adsorbtion and low immunogenic responses represent additional key features.

This thesis aims to develop multifunctional, highly stable, nontoxic nanoemitters emitting in the near infrared (NIR) region such as gold nanoparticles (AuNPs) and fluorescent nanodiamonds (FNDs) that can be easily functionalized. Such particles would be very attractive for bioimaging and sensing applications. The synthesis of an optimal coating of

these NPs represents a key step to achieve this goal. Protein derived polypeptide copolymers have been selected due to the availability of multiple reactive groups along the backbone of these biopolymers.

Chapter 2 deals with the synthesis of these multifunctional, narrowly dispersed polypeptide copolymers. Some known copolymers containing long polypeptides chains have been resynthesized to assess their suitability for the stabilization of NPs. In addition, novel polypeptide copolymers based on shorter main chains and a higher degree of structural perfection will be prepared from protein precursor using the established "denaturation-pegylation" strategy. The backbone lengths, net charges, as well as the secondary structural elements have been varied to assess the impact of these features on copolymer formation and particle stabilization. One attractive feature of these copolymers is the presence of various functional groups at precise positions, such as primary amines of lysine residues, carboxylic groups of aspartic and glutamic acids, hydroxyl groups of serine, tyrosine and guanidine groups of arginine residues, which in principle allow additional functionalization with biomolecules. The semi-synthetic method for the preparation of multifunctional copolymers from protein precursor presented herein will help to overcome the challenges such as polydispersity, repeated amino acids, sophisticated procedures, low yields and high costs of traditional ring-opening polymerization, solid-phase peptide synthesis or genetically engineered protein expression method for synthesis of polypeptidic materials.

In chapter 3 the multifunctional copolymers prepared in chapter 2 will be further functionalised with e.g. thioctic acid groups that can interact with metal surface. These thioctic acid appended copolymers offer great potential to prepare ultrasmall, highly stable, nontoxic NIR emitting AuNPs *in situ*. These AuNPs will be investigated in view of their possibility to cross biological barriers and traffick into the cytoplasm by sparing out the cell nucleus. The presence of many different functional groups at the surface of AuNPs in principle allows post-modification of the AuNPs with different bioactive molecules such as drug molecule, DNA and deliver the payload inside the cell. After successfully developing multifunctional NIR emitting AuNPs that can enter inside the cell and locate itself in the cytoplasm, fluorescent NIR emitting AuNPs for the visualization of particular cellular organelle will be prepared. A particularly desirable target is the cell nucleus, since the genetic information is located there. Due to the impermeable nature of the nuclear membranes, the translocation efficiency of nanoparticles into the cell nucleus is very low; thus nanoparticle

design, its size and synthesis is a critical factor. Ultrasmall NIR-emitting AuNPs will be decorated with an NLS peptide that targets the cell nuclei as demonstrated by confocal microscopy.

In this thesis work, another type of non-metalic carbon based nanoparticles will be discussed, such as fluorescent nanodiamonds (FNDs) to address bioimaging and sensing applications. In contrast to AuNPs, FNDs reveal size independent optical properties. FNDs emit bright fluorescence in near infrared region (550–800 nm) due to imperfections called nitrogen-vacancy (NV) centers. Their "perfect photostability" and non-blinking makes FNDs useful for long-term tracking inside cells and they could be used to monitor cell processes at the nanometer scale. One of the major callenges of this thesis relates to the high tendency of FNDs to form aggregates and these aggregates can even withstand ultrasonic treatment. In chapter 4 copolymers will be applied to coat the nanodiamonds by non-covalent interactions. Polypeptide copolymer coated nanodiamonds have been applied that showed enhanced stability and resistance towards aggregation. The nitrogen-vacancy centers (NV^-) centre is paramagnetic, has a triplet ground state and its fluorescence depends on the spin state. This allows the optical detection and coherent manipulation of the electron spin from single NV centers even at room temperature. NV centers are very promising for magnetic field sensors. We have applied FNDs towards the implementation as magnetic sensor of biologically important metalloprotein, such as ferritin by investigating the influence of ferritin on the spin properties of single NV centers in FNDs.

Chapter 2. Preparation of Monodisperse, Multifunctional Polypeptide Copolymers

Declaration

This chapter contains experimental results published previously in *Biomacromolecules* **2012**,*13*,1890 written by Wu, Y.; Pramanik, G.; Eisele, K.; Weil, T. "Reprinted with permission.[19] Copyright 2012 American Chemical Society." The preparation and characterization of dcBSA-PEO$(5000)_{28}$ and dHSA-PEO$(5000)_{27}$ have been developed by Ms. Wu Yuzhou, Institute of Organic Chemistry III–Macromolecular Chemistry and Organic Materials, Universität Ulm and are part of her thesis and the synthesis have been repeated in this chapter. Experiments with Ovomucoid and Kunitz have been accomplished together with Ms. Ayse Guenay under my supervision and based on my synthetic protocols and they were partly also included in her master's thesis, Institute of Organic Chemistry III–Macromolecular Chemistry and Organic Materials, Universität Ulm.

2.1. Introduction

The use of nanoparticles (NPs) in biomedicine, in particular in the field of diagnosis and therapy of human diseases, has rapidly grown in the last decade.[1] Much effort has been made towards surface modification of nanoparticles (NPs) by various organic compounds in order to develop new building blocks for biomedical applications.[2] In the past decade, the design and preparation of polymer-functionalized NPs have attracted great interest.[3,4] Strategies have been developed to tailor NPs surfaces by various polymers, e.g. thermo-responsive Poly(N-isopropylacrylamide) (PNIPAM),[5] poly(methyl methacrylate) (PMMA),[6] diblock copolymers,[7] dendrimers,[8] poly-(ethylene glycol)-based glycopolymers,[9] polystyrene[10] etc. The commonly followed strategies towards functionalization of NPs with polymers are (i) direct encapsulation of the NPs by polymers, (ii) ligand exchange of the original surfactant with polymers.[11] The thiol groups on the polymer backbone provide strong chemisorption to the NPs surface, and the carboxyl or amine groups impart water solubility for further functionalization.[1] Most of the polymers used for coating of NPs are synthetic. Generally, the well-defined synthetic polymers exhibit well-defined and fine-tunable degradation kinetic as well as mechanical properties.[12] In comparison, polypeptide based materials offer several advantages over traditional synthetic polymers towards biomedical applications.[13] In this chapter, I present new methods to prepare highly monodisperse, multifunctional polypeptide

copolymers with different lengths of the main chains, which have later (Chapter 3 & 4) been used for stabilization of fluorescent nanoparticles. I have used native proteins or modified globular proteins as starting materials. The application of proteins as a starting material for the preparation of polypeptide copolymers offers many potential advantages over synthetic polymers. First, proteins are known to be perfectly monodisperse and they can be modified to prepare perfectly monodisperse polypeptide copolymers.[14] Second, polypeptide-based materials are biocompatible because polypeptides are composed of building blocks that are native to all organisms. Third, polypeptide-based copolymers prepared from proteins are easily metabolizable by digestive enzymes into innocuous peptides whereas synthetic polymers may accumulate in the body and result in toxic degradation product.[15] Fourth, proteins contain various functional groups (-COOH, $-NH_2$, -OH) along the polymer backbone which allows the attachment of biomolecules to the polymer using very simple conjugation chemistry.[14,16] Fifth, polypeptides can also be prepared by ring-opening polymerization, solid-phase peptide synthesis or genetically engineered protein expression.[17] But polymerization reactions are only able to prepare optically impure polypeptides with repeated amino acid sequences and without the sequence specificity of natural proteins, and other techniques, such as solid-phase peptide synthesis and protein engineering are limited by sophisticated procedures, low yields and high costs.[17] In this thesis work, multifunctional and structurally defined polypeptide-polyethylene (oxide) copolymers (PP-PEOs) have been prepared using five different native globular or modified globular proteins as a starting material.

2.2. Results & Discussion

Serum albumins (BSA, HSA) are readily available, single chain, high molecular weight (~ 66 kD) proteins with very high numbers (~583-585) of amino acids in the primary structure. The primary structure of the albumins contain a large number of functional groups, such as~ 100 carboxylic acid groups,~ 60 amino groups and in addition 35 cysteine residues in the sequence forming 17 disulfide bridges. The high numbers of functional groups are very attractive for chemical modifications and preparation high molecular weight polypeptide copolymers. Therefore, serum albumin proteins were selected for preparation of high molecular weight polypeptide copolymers. The preparation of dcBSA-PEO$(5000)_{28}$ and dHSA-PEO$(5000)_{27}$ have been reproduced from protocols developed by Dr. Wu Yuzhou previously.[18,19] In this method, the proteins cationised bovine serum albumin (cBSA) and human serum albumin (HSA) were denatured by 5M urea and the disulphide bonds are

reduced by tris(2-carboxyethyl)phosphine (TCEP) followed by an *in situ* stabilization with polyethylene (oxide) chains which yields polypeptide side chain copolymers of precisely defined backbone lengths as described in Scheme 2.1.

However it is very difficult to reduce all 34 disulphide bond of the HSA and cBSA and cap them with PEO5000-maleimide to get a complete mono disperse polymer. Even though the number of PEO attached to the protein backbone is highly reproducible, the PEO substituents might not be located at the same cysteine residue. It is also very challenging to characterize the copolymer dcBSA-PEO(5000)$_{28}$ (2) and dHSA-PEO(5000)$_{27}$ (4) via MALDI-TOF, most likely due to their high molecular weights. However, to understand the fundamental interactions of functional polymers and complex biological systems, such as cells, tissues,

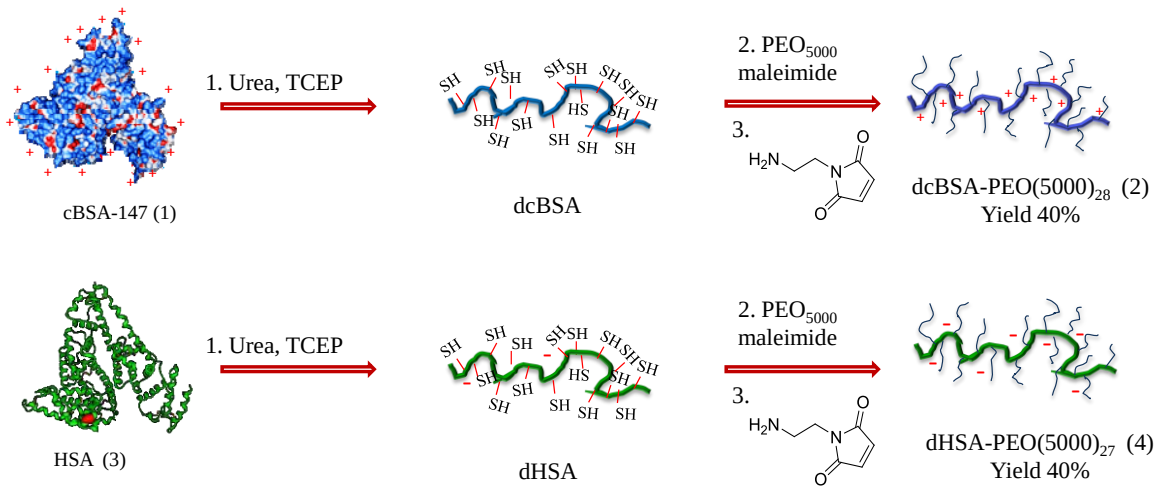

Scheme 2.1. Preparation of dcBSA-PEO(5000)$_{28}$ and dHSA-PEO(5000)$_{27}$.
(The preparation of dcBSA-PEO(5000)$_{28}$ and dHSA-PEO(5000)$_{27}$ have been reproduced as developed by Ms. Wu Yuzhou previously and is part of her PhD thesis).

specific organs, and entire organisms, it is also necessary to know the exact sequence of the polymers. In my goal to create a protein based copolymer with well defined as well as exactly known sequence of attachment of PEO to the backbone, three smaller native protein hen egg white lysozyme, Trypsin inhibitor from *Glycine max* (Kunitz)**,** Trypsin inhibitor from chicken egg white (Ovomucoid) have been used. These three proteins have been completely denatured and all the disulfide bonds of the respective proteins have been reduced and capped with PEO5000. Following this "denaturation-pegylation" strategy I have created three new precisely defined polymer systems, referred to as ''Precision Polymers''.[20] These polymers are as precise as natural proteins. The exact number and the point of the attachment of the

PEO to the polypeptide backbone are precisely determined as given in **table 2.1.** The three new copolymers are denoted as dKunitz-PEO(5000)$_4$ (**Scheme 2.2.**), dLY-PEO(5000)$_8$ (**Scheme 2.3**.), dOvomucoid-PEO(5000)$_{18}$ (**Scheme 2.4.**) "d" refers to the denatured protein and the subscript after PEO(5000) refers to the number of PEO grafted onto the protein polypeptide backbone. The polymers have been characterized by MALDI-ToF mass spectrometry, SDS Page gel, dynamic light scattering (DLS) and zeta potential. Their monodispersity was demonstrated using GPC and their secondary structure has been studied using CD spectroscopy.

Table 2.1. Point of attachment of PEO to the protein backbone.

Polypeptide copolymers	**sequence number cysteine of the PEO attachment to the polypeptide backbone**
dKunitz-PEO(5000)$_4$	39, 86, 138 and 145. Ref[21]
dLY-PEO(5000)$_8$	6, 30 ,64, 76, 80, 94, 115, 127 Ref-http://www.uniprot.org/uniprot/P00698
dOvomucoid-PEO(5000)$_{18}$	5, 22, 30, 41, 44, 62, 70, 87, 96, 106, 109, 127, 138, 146, 154, 165, 168, 186 Ref-http://www.uniprot.org/uniprot/P01005

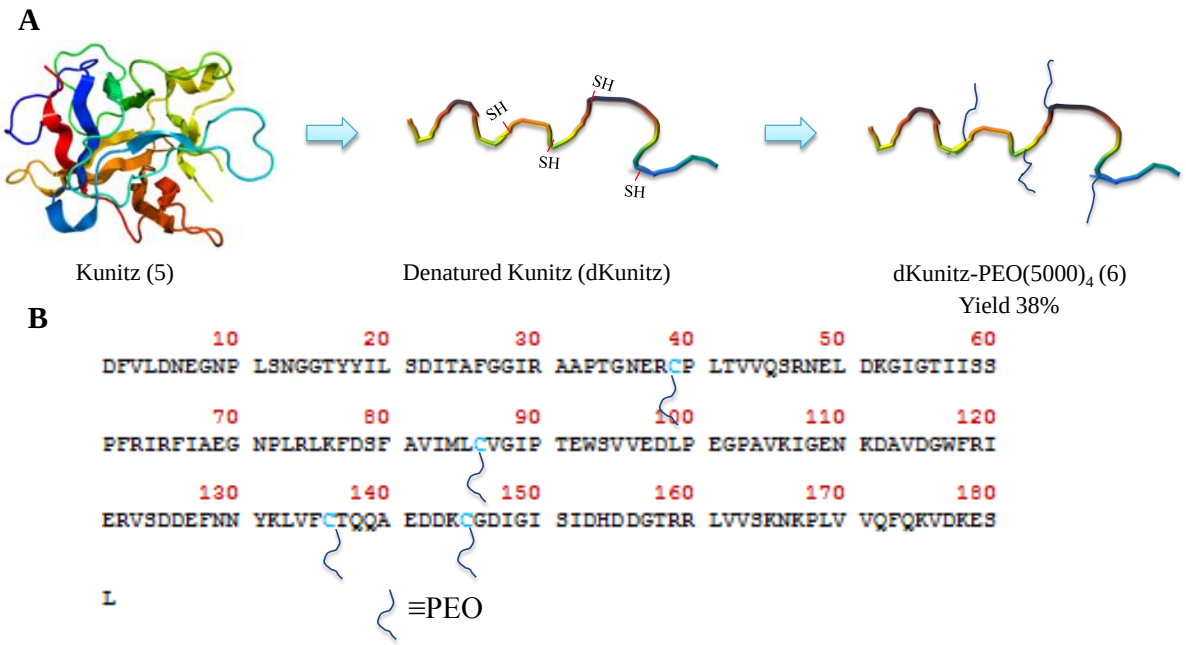

Scheme 2.2. (A) Preparation of dKunitz-PEO(5000)$_4$. (B) One letter amino acid sequence of Kunitz and the site of PEO attachment to the protein backbone.

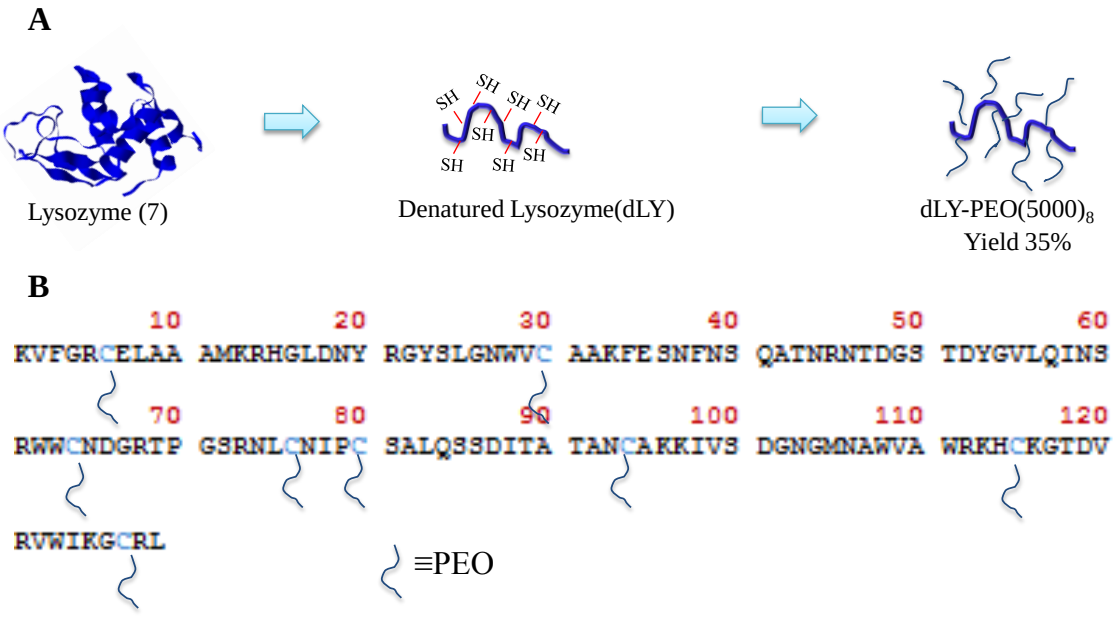

Scheme 2.3. (A) Preparation of dLY-PEO(5000)$_8$. (B) One letter amino acid sequence of Lysozyme and the site of PEO attachment to the protein backbone.

A

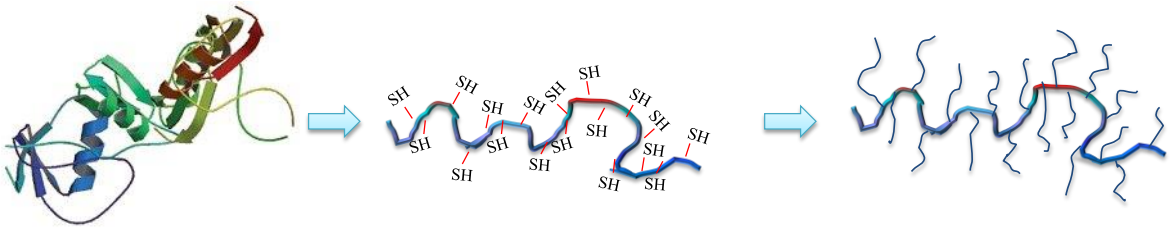

Ovomucoid (9) | Denatured Ovomucoid (dOvomucoid) | dOvomucoid-PEO(5000)$_{18}$ (10) Yield 42%

B

```
        10         20         30         40         50         60
VEVDCSRFPN TTNEEGKDEV VCPDELRLIC GTDGVTYNHE CMLCFYNKEY GTNISKEQDG

        70         80         90        100        110        120
ECGETVPMDC SRYPNTTSED GKVTILCTKD FSFVCGTDGV TYDNECMLCA HNVVQGTSVG

       130        140        150        160        170        180
KKHDGECRKE LAAVSVDCSE YPKPACPKDY RPVCGSDNKT YSNKCNFCNA VVESNGTLTL

NHFGKC
```

≡PEO

Scheme 2.4. (A) Preparation of dOvomucoid-PEO(5000)$_{18}$. (B) One letter amino acid sequence of Ovomucoid and the site of PEO attachment to the protein backbone.

2.2.1. Conditions for denaturation of different proteins

Conditions for the preparation of five different proteins polypeptide polyethylene oxide (PP-PEO) copolymers have been screened. The proteins are Human Serum Albumin (HSA), cationised Bovine Serum Albumin (cBSA), Lysozyme, Ovomucoid and Kunitz. The brief descriptions of the proteins, the denaturing condition used to prepare the PP-PEOs and the characterizations are described below.

Human Serum Albumin (HSA)

Human serum albumin (HSA) is the most abundant protein circulating in blood and it transports a wide variety of ligands like fatty acids, L-tryptophan, hormones, bilirubin, as well as many drugs.[22-24] The protein has a folded three-dimensional structure,[25] which allows it to carry out this transport function very efficiently. This protein of 585 residues is composed of a single polypeptide chain with molecular weight of 66.4 kDa,[26-28] with three α-helical domains I-III, each containing two subdomains A and B (**Figure 2.1.**). It contains 17 intrachain disulfide bonds and a free cysteine residue at position 34 in domain I and a lone

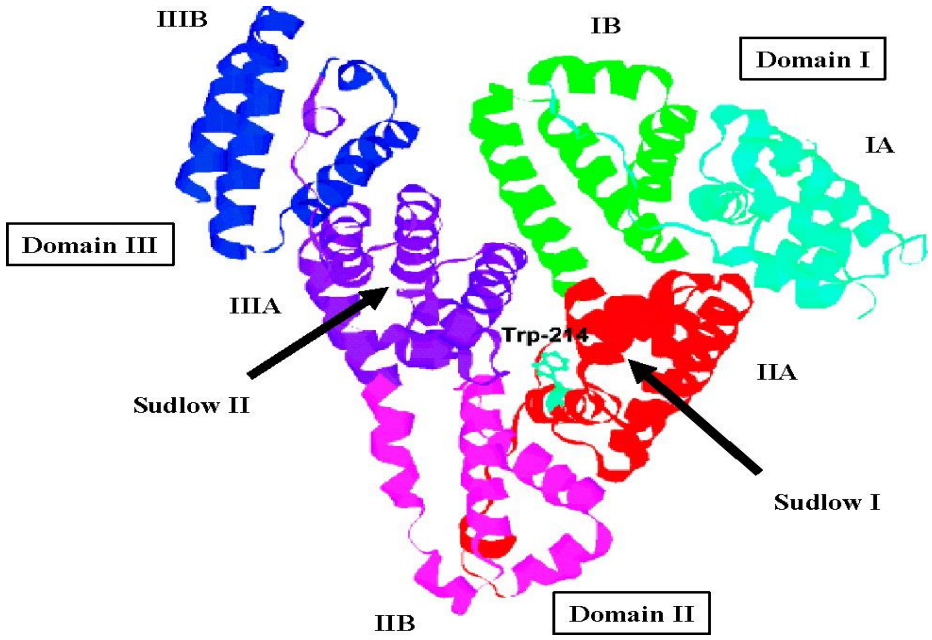

Figure 2.1: Crystal structure of HSA and the locations of domain-binding sites. The locations of hydrophobic binding sites (Sudlow I and Sudlow II) are indicated. The position of the tryptophan residue (Trp-214) in the middle of helix H2 in subdomain IIA is shown. The structure was obtained from the Protein Data Bank (ID code 1ha2).

tryptophan residue at position 214 in domain II.[26,29] Urea denatures HSA in a single step involving the unfolding of domain II of the protein.[30] To obtain the high-molecular-weight polypeptide copolymer dHSA-PEO(5000)$_{27}$(**4**) 5M urea/phosphate buffer (pH 7.4) was used. Urea destabilizes the tertiary protein structure by diminishing secondary interactions and the reducing agent, tris(2-carboxyethyl)phosphine (TCEP) reduces the disulfide bridges. The reduced thiol groups were capped with O-(2-maleimidoethyl)-O′-methylpolyethylene(oxide)-5000 (PEO(5000)-MI) (**Scheme 2.1.**).[18] Because the presence of remaining free sulfhydryl groups has a negative impact on the long-term stability of the copolymer, N-(2-aminoethyl)maleimide has been added after the pegylation step to increase the shelf life of the copolymer. This procedure of preparation of HSA-based copolymer (4) has been reported previously.[18] In this thesis, the preparation of dHSA-PEO(5000)$_{27}$ has been repeated and characterised accordingly. dHSA-PEO(5000)$_{27}$ has been purified by FPLC (**Figure 2.2.a**). The molecular weight of (4) has been assessed by SDS-PAGE (**Figure 2.2.d**) and Maldi-Tof mass spectrometry (**Figure 2.2.c**), suggesting that the molecular-weight of the biopolymer is ~200 kDa. The high molecular weight of 4 indicates that dHSA-PEO(5000)$_{27}$ carrys about 27

PEO(5000) chains.[18] Furthermore, the polymer dispersity of 4 has been investigated by gel permeation chromatography (GPC). A sharp signal indicates a narrow size distribution and low dispersity (PDI-1.07) (**Figure 2.2.b**).

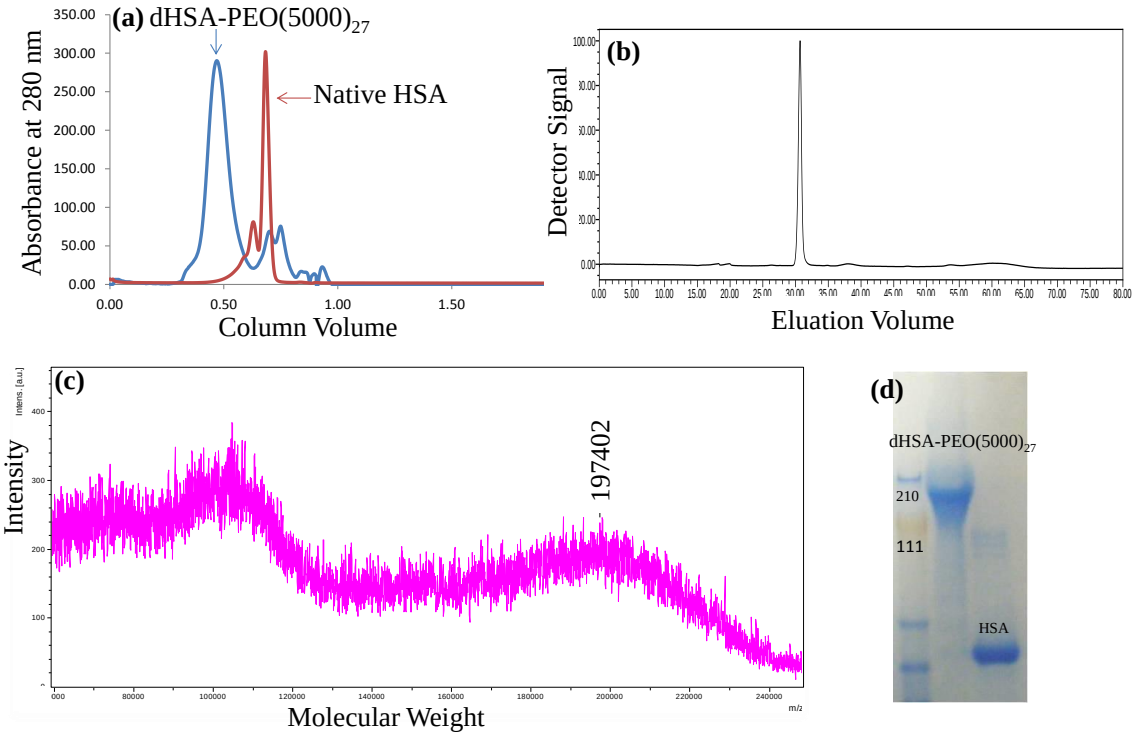

Figure 2.2. Purification and characterisation of dHSA-PEO(5000)$_{27}$. (a) FPLC purification chromatograms of an AKTÄ explorer after application of a reaction mixture consisting of the dHSA-PEO(5000)$_{27}$ (**4**) (blue) and AKTÄ explorer chromatogram of native HSA (brown). (b) Gel permeation chromatogram of dHSA-PEO(5000)$_{27}$ (c) MALDI-TOF spectrum for dHSA-PEO(5000)$_{27}$. The molecular mass is 197kDa according to this spectrum and the peak at 106kDa corresponds to the half molecular mass peak. (d) SDS-PAGE analysis of dHSA-PEO(5000)$_{27}$ (**4**).[18] This image is "Adapted with permission.[18] Copyright 2010 American Chemical Society."

Bovine Serum Albumin (BSA)

BSA has similar conformation as HSA due to 76% of amino acid sequence homology.[31] BSA contains a single polypeptide chain of 583 amino acids with a molecular mass of 66.5 kDa. It is folded into tertiary globular conformation forming three domains.[32] The native BSA has a larger proportion of hydrophobic interior and less non-polar surface at the exterior than HSA.[33] The folding of BSA is characterized by a unique arrangement of nine disulphide loops created by 17-disulphide bonds and one free cysteine.[34] BSA possesses two tryptophan residues, Trp-134 located in domain I and Trp-212 in domain II.[35] The unfolding of BSA is a

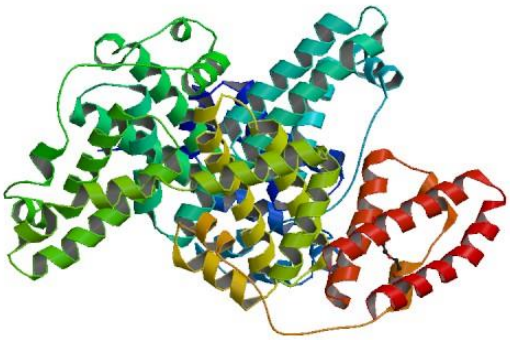

Figure 2.3. Crystal structure of BSA. The structure has been obtained from the Protein Data Bank (http://www.pdb.org/pdb/explore/explore.do?structureId=4F5S).

complex process of the independent unfolding behavior of all the three domains. BSA also contains a high content of Asp, Glu resulting in a negative zeta potential of bovine serum albumin at pH 7.[36] BSA has been cationised (cBSA-147) by reacting the carboxylic acid groups of aspartate and glutamate residues of BSA with ethylenediamine in the presence of 125 equivalents of 1-ethyl-3-(30-dimethylamino-propyl)-carbodiimide hydrochloride (EDC) by following the reported procedure.[37] cBSA-147 contains about 147 primary amino groups and on average only thirteen negatively charged amino acid residues.[37] Polypeptide copolymer dcBSA-PEO$(5000)_{28}$ has been achieved from cBSA-147 or cBSA by applying a similar "denaturation-pegylation" strategy as HSA.[19] dcBSA-PEO$(5000)_{28}$ was purified by FPLC (**Figure 2.4.a**). The Molecular weight of dcBSA-PEO$(5000)_{28}$ (**2**) has been found to be of about 200kD as analysed by SDS page gel, which is in agreement with previous reports (**Figure 2.4.c**).[19] The molecular weight of (**2**) indicates that about 28 PEO have been attached to the cBSA-backbone. The sharp GPC peak also indicates low polydispersity (PDI-1.07) of dcBSA-PEO$(5000)_{28}$ (**figure 2.4.b**).

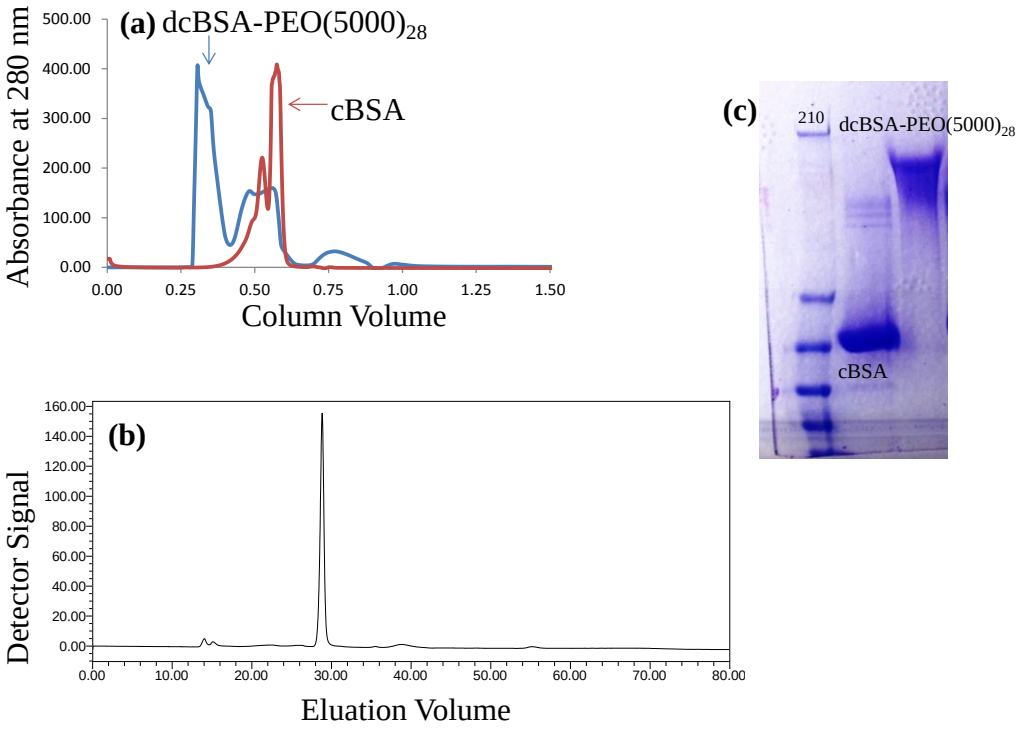

Figure 2.4. Purification and characterisation of dcBSA-PEO(5000)$_{28}$. (a) FPLC purification chromatograms of an AKTÄ explorer after application of a reaction mixture consisting of the dcBSA-PEO(5000)$_{28}$ (**2**) (blue) and AKTÄ explorer chromatogram of cBSA (brown). (b) Gel permeation chromatogram of dcBSA-PEO(5000)$_{28}$. (c) SDS-PAGE analysis of dcBSA-PEO(5000)$_{28}$ (**2**). Image 2.4.b is "Adapted with permission.[19] Copyright 2012 American Chemical Society."

Hen Egg White Lysozyme

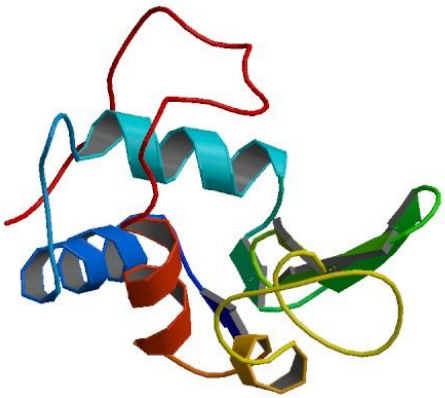

Figure 2.5. Crystal structure of Hen egg white lysozyme. The structure has been obtained from the Protein Data Bank (http://www.rcsb.org/pdb/explore/explore.do?structureId=2EPE).

The ribbon arrows represent regions of the peptide backbone in β-sheet conformation.

Lysozyme is a 14.3 kDa protein that consists of 129 amino acids, with 4 cross-linked disulfide bridges, found in animal tissues, organs and serum as well as in tears, milk, saliva, nasal secretions and cervical mucus.[38,39] The major source of commercial lysozyme, in particular for pharmaceutical use, is extraction and purification of hen egg albumen. Lysozyme concentration in egg albumen is about 0.5%.[40] Lysozyme is heat-stable (80 °C for 2 minutes) but gets inactivated at lower temperatures with increased pH.[40] The optimum temperature for activity is 55 °C to 60 °C.[40] It is known from the literature that guanidine. HCl (GuHCl) is more effective in denaturing lysozyme than urea.[41] Urea transforms lysozyme's tertiary structure corresponding to a molten globule state without unfolding of α-helix structures, in contrast GuHCl clearly induces conformational changes, associated with a loss of activity.[42] Upon addition of guanidine to the lysozyme solution, lysozyme undergoes a two state denaturation process.[41] The denaturation of lysozyme is represented as

$$\mathbf{N} \rightleftharpoons \mathbf{X} \rightleftharpoons \mathbf{D}$$

where D represents the truly denatured state reached only in concentrated guanidine hydrochloride and **X** is a distinct but only partially denatured state.[43] GuHCl denaturation leads to randomly coiled conformations. [43] To denature the Lysozyme I have used 8M guanidine.HCl in 100 mM Tris.HCl buffer pH 8.4. For the reduction of the 4 disulphide bridges, dithiothreitol (DTT) was more effective than TCEP. According to MALDI-ToF MS, the use of TCEP results in incomplete dissociation of disulphide bonds. TCEP can reduce only one disulphide bridge, which is exposed to the solvent.[44] DTT is more reactive reducing agent than TCEP and smaller in size, which enables it to access and cleave all disulphide bonds.[45] After the denaturation is complete, the excess DTT is removed from reaction mixture by "HiTrap Desalting Columns" from gelifesciences. Then the denatured and reduced lysozyme has been reacted with PEO5000-maleimide in phosphate buffer pH 7.4 for overnight. The formed white solid has been purified by FPLC (**Figure 2.6.a**) and characterised by Maldi-Tof MS (**Figure 2.6.c**) and SDS-PAGE (**Figure 2.6.d**). Both of the technique shows similar molecular masses. dLY-PEO$(5000)_8$ has a molecular weight of 54.6 kD, which indicates all of the four disulphide bonds have been reduced and successfully capped by PEO5000-maleimide. The monodispersivity of dLY-PEO$(5000)_8$ has been confirmed by GPC analysis (**Figure 2.6.b**).

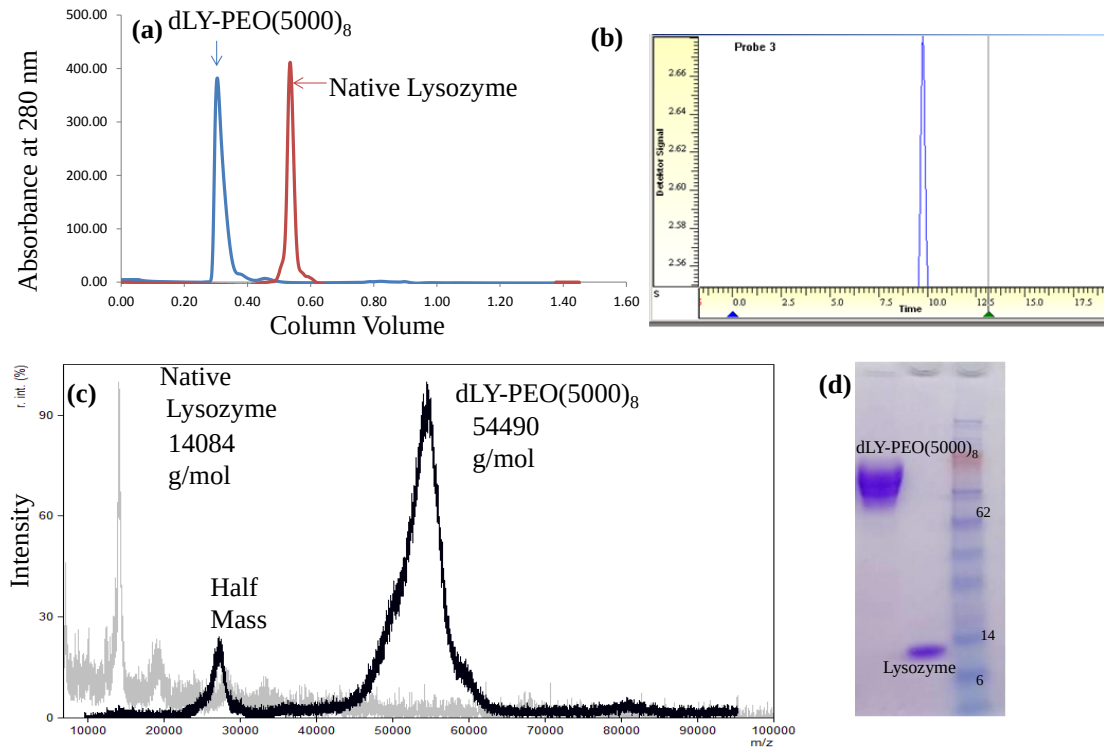

Figure 2.6. Purification and characterisation of dLY-PEO(5000)$_8$ (**8**). (a) FPLC purification chromatograms of an AKTÄ explorer after application of a reaction mixture consisting of the dLY-PEO(5000)$_8$ (8) (blue) and AKTÄ explorer chromatogram of native Lysozyme (brown). (b) Gel permeation chromatogram of dLY-PEO(5000)$_8$ (c) MALDI-TOF spectrum for dLY-PEO(5000)$_8$. The molecular mass is ~54.5 kDa according to this spectrum and the peak at 27 kDa corresponds to the half molecular mass peak. (d) SDS-PAGE (NuPAGE Bis-Tris 4-12%) analysis of dLY-PEO(5000)$_8$ (**8**).[19] Image 2.6 is "Adapted with permission.[19] Copyright 2012 American Chemical Society."

Ovomucoid

Chicken ovomucoid, the major glycoprotein of egg-white, is a single chain inhibitor of trypsin. Ovomucoid comprises 10% of total egg white protein and is a highly glycosylated protein and comprises 186 amino acids.[46] It consists of three tandem, homologous structural domains.[47] Each domain contains three disulphide bonds, two tyrosine residues, and one active site. Nine disulfide bridges and a high content of helical and β-sheet structures severely limit conformational fluctuations and greatly stabilize the native structure.[48] Its native conformation is resistant to extreme values of pH, temperature (e.g., 100 °C for 1 h), concentrated chemical denaturants, such as urea and also resistant to protease digestion.[49,50] Guanidine hydrochloride induces biphasic transitions to Ovomucoid.[51] However, in presence

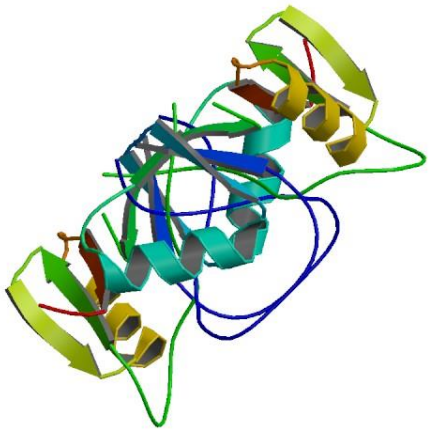

Figure 2.7. Crystal structure of Ovomucoid. The structure has been obtained from the Protein Data Bank (http://www.rcsb.org/pdb/explore/explore.do?structureId=1OVO). The ribbon arrows represent regions of the peptide backbone in β-sheet conformation.

of polyol (sorbitol), ovomucoid shows the three stable conformational states which were involved in the overall unfolding process.[52] Here polyol acts as osmolytes. The osmolytes exert a dramatic effect on protein folding reactions, without making or breaking covalent bonds.[52] Osmolytes stabilize proteins, not by interacting with them but by altering the solvent properties of the surrounding water and hence protein-solvent interaction.[53] When a protein is present in the polyol solution, two types of interactions are observed, namely the osmophobic effect (i.e., the unfavorable interaction between peptide units and polyols) and solvophobic effect (i.e., the unfavorable interaction between side chains and polyols).[54] Both of these effects will be larger in guanidinium chloride-induced denatured proteins than that in heat denatured protein samples.[54] 10 M Guanidine have been used as denaturing conditions for Ovomucoid. I also varied the amount of guanidine to be used. 6 M or 8M guanidine have been found to be insufficient for complete denaturation of Ovomucoid, 10 M guanidine was needed. Instead of guanidine hydrochloride, guanidine thiocyante was used, since it is known that guanidine thiocyanate is better denaturing agent than guanidine hydrochloride.[55] To denature ovomucoid, urea has been also investigated as chaotropic agent, but these attempts were unsuccessful. Only guanidine was not sufficient for complete denaturation and 15% sorbitol was needed in addition. Here sorbitol acts as osmolyte as discussed above. 15% sorbitol was the optimum for complete denaturation and reduction of all nine disulphide bonds. dOvomucoid-PEO$(5000)_{18}$ has been purified by FPLC (**Figure 2.8.a**) and characterized by Maldi-Tof MS (**Figure 2.8.c**) and SDS Page (**Figure 2.8.d**). The mass of dOvomucoid-PEO$(5000)_{18}$ has been found to be 115 kDa, which indicates all the 9 disulphides of Ovomucoid have been reduced and capped with PEO5000. The

monodispersivity of dOvomucoid-PEO(5000)$_{18}$ has been further confirmed by GPC analysis (**Figure 2.8.b**).

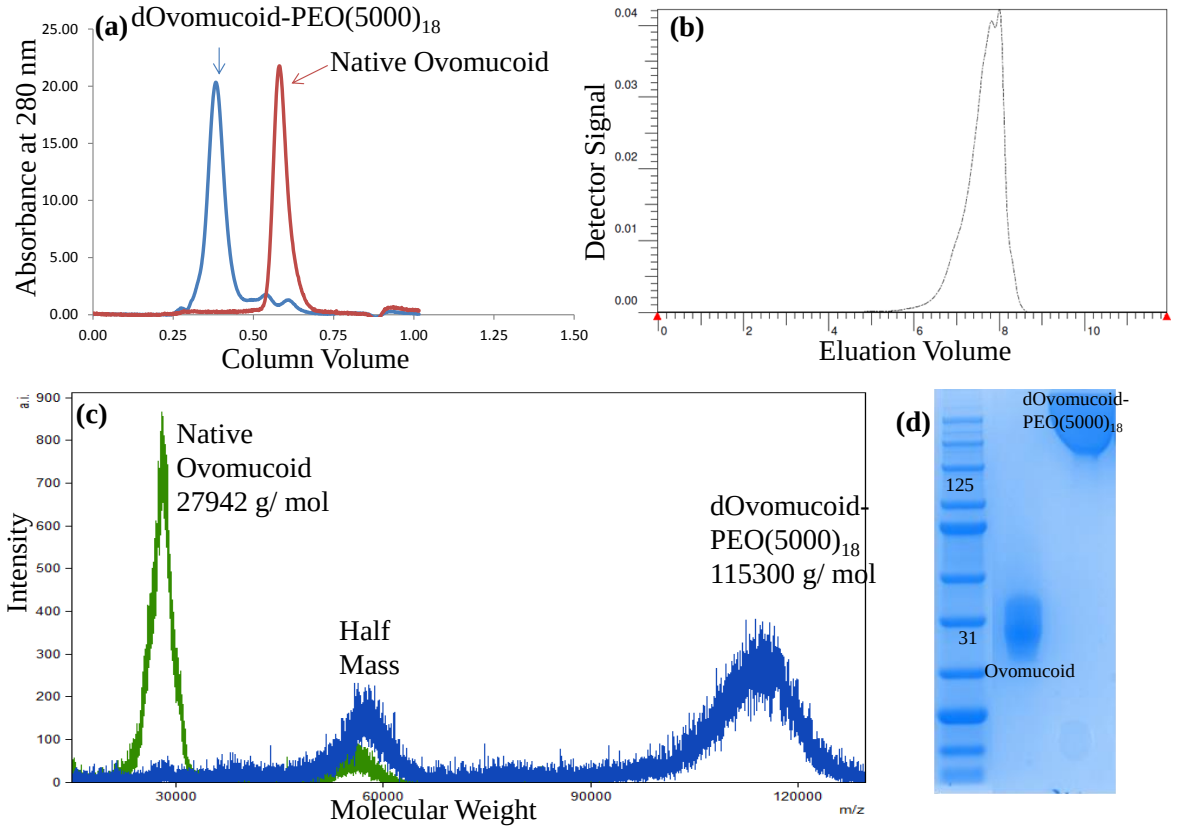

Figure 2.8. Purification and Characterisation of dOvomucoid-PEO(5000)$_{18}$ (10). (a) FPLC purification chromatograms of an AKTÄ explorer after application of a reaction mixture consisting of the dOvomucoid-PEO(5000)$_{18}$ (10) (blue) and AKTÄ explorer chromatogram of native Ovomucoid (brown). (b) Gel permeation chromatogram of dOvomucoid-PEO(5000)$_{18}$ (c) MALDI-TOF spectrum for dOvomucoid-PEO(5000)$_{18}$. The molecular mass is ~115 kDa according to this spectrum and the peak at ~57 kDa corresponds to the half molecular mass peak. (d) SDS-PAGE analysis of dOvomucoid-PEO(5000)$_{18}$ (10).

Kunitz

Soybean trypsin inhibitor is a 21.5 kDa monomeric, nonglycosylated protein first isolated from soybean seeds.[56] It comprises 181 residues and has two disulfide bridges, involving Cys 39–Cys 86 and Cys 138–Cys 145, that are solvent exposed and critical for its inhibitory function.[57-59] The overall structure of Kunitz is that of a sphere of about 3–5 nm in diameter, consisting of 12 criss-crossing antiparallel β-strands, largely stabilized by hydrophobic side chains.[60,61] The soybean Kunitz trypsin inhibitor has unusual stability to chemical and thermal denaturation. It is presumably because of its compact antiparallel β-sheets.[62] Upon

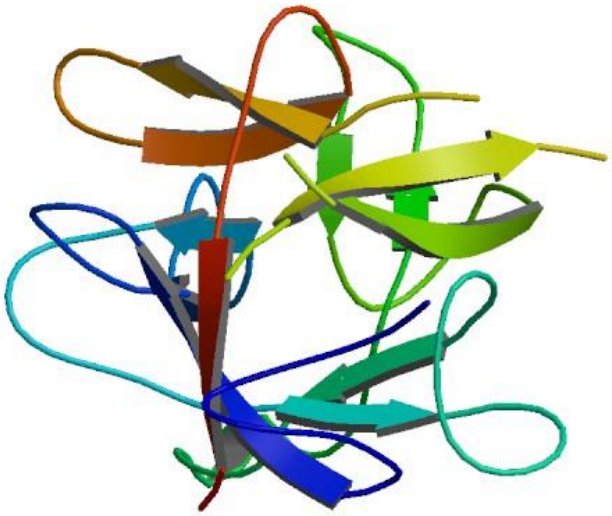

Figure 2.9. Crystal structure of Kunitz. The structure has been obtained from the Protein Data Bank (http://www.rcsb.org/pdb/explore/explore.do?structureId=1BA7). The ribbon arrows represent regions of the peptide backbone in β-sheet conformation.

heating it undergoes a two-state transition with the midpoint at approximately 65^0C. Between 60 and 70 ^{0}C, a transition of the native inhibitor to an alternate conformation with a more molten state occurs.[21] With increase in temperature, there is a progressive decrease in side chain interactions between the aromatic residues in the hydrophobic core of the Kunitz.[21] At 65^0C, most of the tertiary structural interactions get lost, and at 75^0C, there is a further loss.[21] The thermal denaturation of Kunitz is readily reversible.[21] Following the literature results, Kunitz has been denatured by heating and the 2 disulphide bonds have been reduced with TCEP and caped with PEO5000-maleimide. For denaturation, very harsh condition like 10 M guanidinium thiocynate pH 7.4 and 100^0C temperature have been used. However, the denaturation of Kunitz in 10M guanidine at room temperature has still not run to completion. Heating at higher temperature such as at 100^0C, complete denaturation occurs. The resulting dKunitz-PEO$(5000)_4$ has been characterised by Maldi-Tof, SDS Page gel, GPC. The dKunitz-PEO$(5000)_4$ has been purified by FPLC (**Figure 2.10.a**). The molecular weight of dKunitz-PEO$(5000)_4$ has been found to be 40kD by Maldi-tof MS (**Figure 2.10.c**) and SDS PAGE gel, (**Figure 2.10.d**) which reflects the fact that all two disulphide bridges have been cleaved and the resulting 4 thiol have been capped with PEO(5000). The monodispersivity of dKunitz-PEO$(5000)_4$ has been confirmed by GPC analysis (**Figure 2.8.b**).

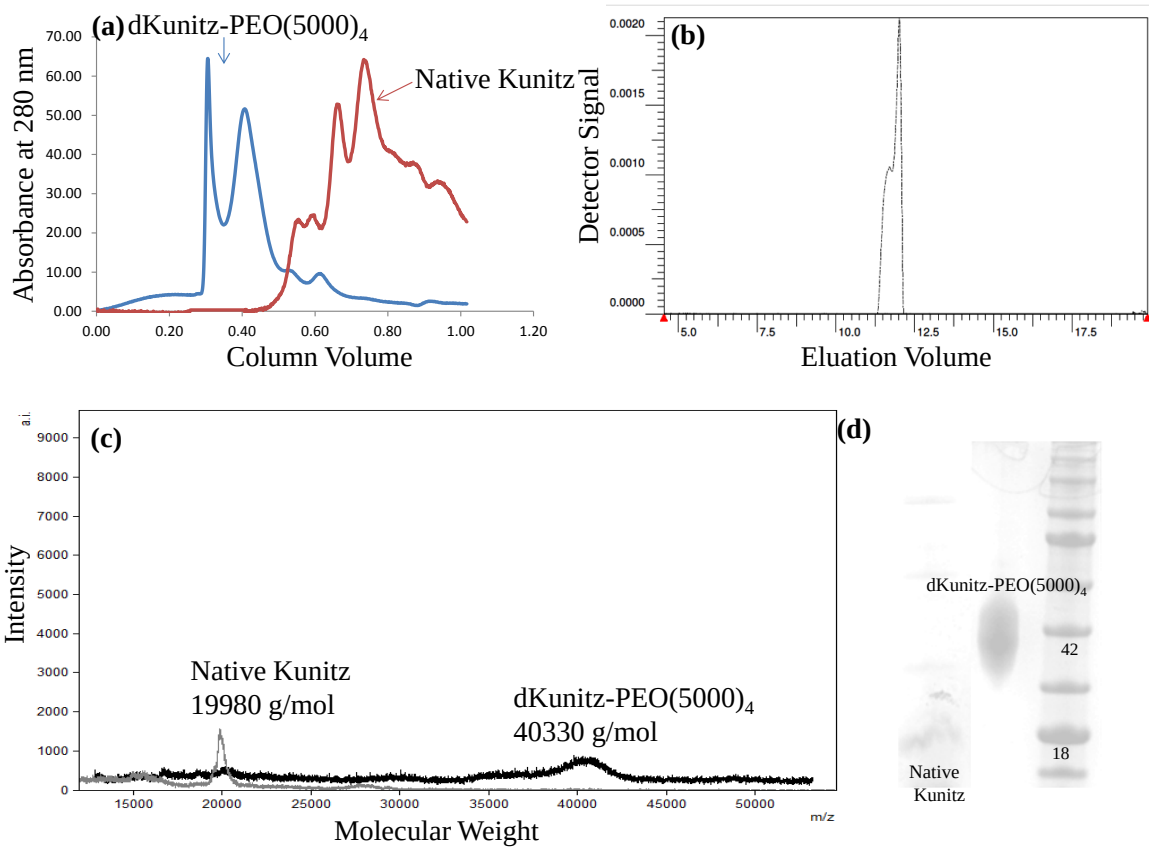

Figure 2.10. Purification and characterisation of dKunitz-PEO(5000)$_4$ (**6**). (a) FPLC purification chromatograms of an AKTÄ explorer after application of a reaction mixture consisting of the dKunitz-PEO(5000)$_4$ (6) (blue) and AKTÄ explorer chromatogram of native Kunitz (brown). (b) Gel permeation chromatogram of dKunitz-PEO(5000)$_4$ (c) MALDI-TOF spectrum for dKunitz-PEO(5000)$_4$. The molecular mass is ~40 kDa according to this spectrum. (d) SDS-PAGE analysis of dKunitz-PEO(5000)$_4$ (**6**).

Table2.2. Summary of the conditions used for denaturation of different proteins.

Proteins	**Denaturating Conditions**				
	Chaotropic agent	**Buffer**	**Reducing agent**	**Temperature**	**Time**
Human Serum Albumin (HSA)	5M Urea	pH 7.4, 100 mM phosphate buffer.	TCEP	Room Temperature	6 h
Bovine Serum Albumin (BSA)	5M Urea	pH 7.4, 100 mM phosphate buffer.	TCEP	Room Temperature	6 h
Kunitz	10M Gu.SCN.	pH 7.4, 100 mM tris HCl buffer.	TCEP	100^0C	Total 8 h
Lysozyme (LY)	8M Gu.HCl.	pH 7.4, 100 mM tris.HCl buffer.	DTT	Room Temperature	24 h
Ovomucoid	10 M Gu.SCN, 15% Sorbitol.	pH 7.4, 100 mM tris HCl buffer.	TCEP	Room Temperature	Total 8 h

2.2.2. General observation about the denaturation conditions needed for different proteins

In the denaturation procedure, chemical denaturants, such as urea or guanidine have been used. The chemical denaturants bind to the protein and stabilize the denatured state, thereby favouring unfolding. As it is clear from the above discussion, different proteins need different denaturing conditions. HSA and BSA need mild denaturing condition, such as 5M urea/TCEP, while the smaller proteins like lysozyme and ovomucoid require stronger denaturing agents i.e. guanidine in 8M and 10M concentration, respectively. Kunitz requires the harshest conditions like 10M guanidine and 100^0C for complete denaturation.

It is known that proteins with high α-helix unfold very rapidly.[63] However, β-sheet proteins appear to be more robust.[63] Oligomeric β-sheet proteins are particularly resistant to unfolding, possibly due to the higher content of hydrogen bonding interactions between the β-strands; in addition, there might be a general selection for kinetically stable β-structures since partially unfolded β-sheet proteins are particularly susceptible to aggregation.[64] HSA and BSA, which contains 67% α-helix and no β-sheet, unfold easily in 5M urea. As the amount of β-sheet structures increases in the protein, harsher conditions are essential to achieve complete denaturation. Lysozyme has about 13% beta sheets and it needs the stronger denaturing agent guanidine.HCl in much higher concentration of 8M for denaturation, while Ovomucoid which contains 26% beta sheet structures requires 10M guanidine thiocyanate and 10% sorbitol for full denaturation. For all beta sheet proteins, Kunitz has been the most difficult to denature and the procedure has been only successful under harsh conditions like 10M guanidine thiocyante and 100^0C for complete denaturation. From the experimental results and above discussion it is evident that denaturing conditions required for complete denaturation of protein is correlated to the secondary structure of the protein. Higher the β-sheet content of the protein, more harsh conditions are needed for denaturation of the protein. The correlation between denaturing condition and the secondary structure is shown in **Figure 2.11**.

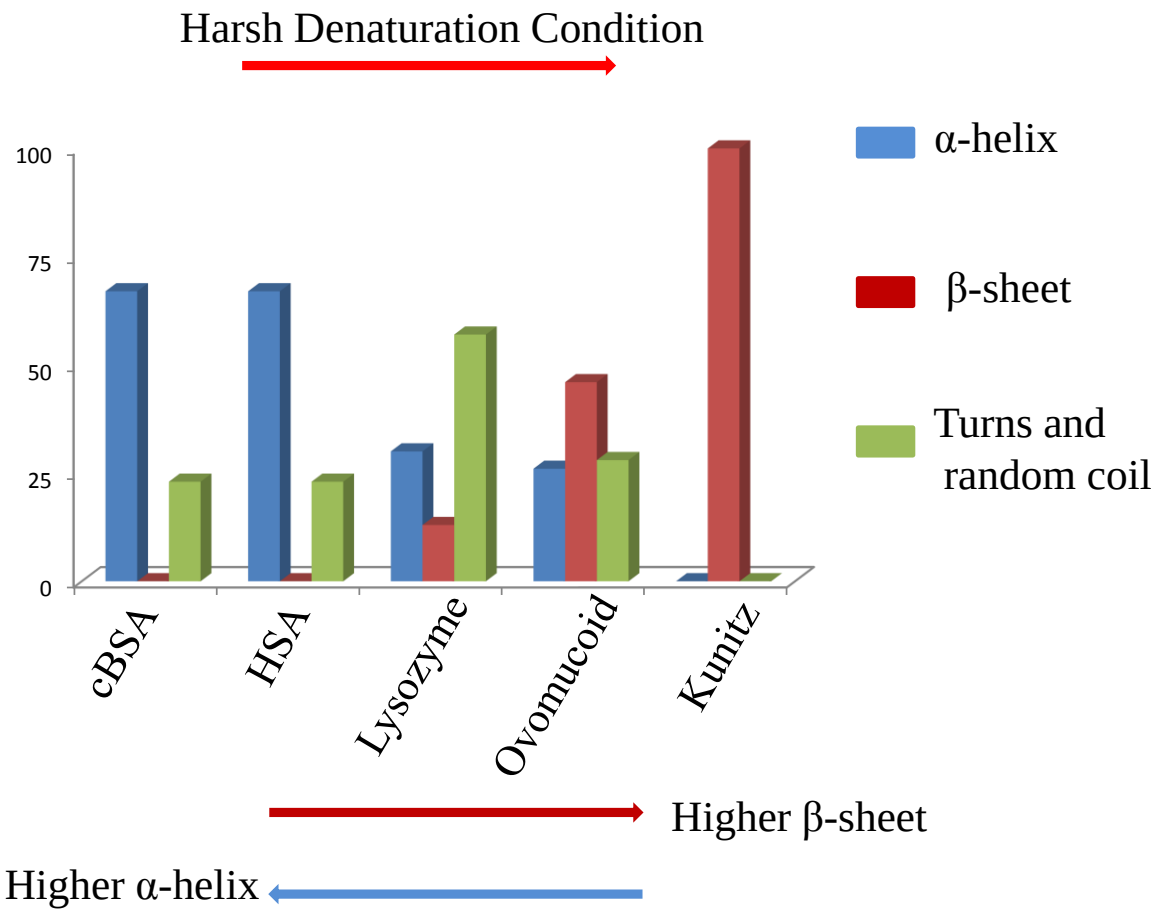

Figure 2.11. Corelation between the secondary structure of the protein and denaturation conditions.

2.2.3. Properties of the polypeptide copolymers.

Five polypeptide copolymers (**2**), (**4**), (**6**), (**8**), and (**10**) derived from macromolecular but structurally distinct precursor proteins have revealed excellent water solubility (>20 mg/mL) and long shelf lives (>6 months) at 4 °C. Five different protein precursors have been chosen to prepare polypeptide copolymers to demonstrate that following the strategy of "denaturation-pegylation" the copolymers with different backbone lengths, different numbers of PEO grafted to the polypeptide backbone (**Table 2.3**), different sizes, different charge and different secondary structures can be prepared. dcBSA-PEO(5000)$_{28}$ (**2**) and dHSA-PEO(5000)$_{27}$ (**4**) have backbone lengths of about 583 and 585 amino acids in their extended conformation, respectively. While dKunitz-PEO(5000)$_4$(**6**) and dOvomucoid-PEO(5000)$_{18}$ (**10**) have backbone polypeptide length of 181 and 186 residues respectively. dLY-PEO(5000)$_8$ has even shorter backbone of only 129 amino acids. The number of PEO attached to the copolymers 2, 4, 6, 8 and 10 are 28, 27, 4, 8 and 18, respectively.

Table 2.3. Summary of the number of PEO5000 attached to protein backbone.

PP-PEOs	**Number of amino acids at protein back bone**	**Number of PEO attached to the protein back bone**
dcBSA-PEO(5000)$_{28}$ (2)	583	28
dHSA-PEO(5000)$_{27}$ (4)	585	27
dKunitz-PEO(5000)$_4$ (6)	181	4
dLY-PEO(5000)$_8$ (8)	129	8
dOvomucoid-PEO(5000)$_{18}$ (10)	186	18

Zeta Potential

Surface charges of PP-PEOs provide an effective way to control the interface between PP-PEOs and the biological systems. A thorough knowledge of surface charge of these PP-PEOs is essential for using them as drug delivery agents, gene transfection agents or coating of NPs. The surface charges of all polypeptide copolymers have been characterized by zeta potential measurements, and the results are summarized in **Figure 2.12** and **Table 2.4**. A high positive zeta potential of 21.6 ± 1.5 mV has been obtained for dcBSA-PEO(5000)$_{28}$ (2), which reflects the presence of large number of primary amino groups (147) on the protein backbone.[37] A negative zeta potential of -20.8±1.49 mV and -28.9±0.85 mV have been found for dOvomucoid-PEO(5000)$_{18}$ (10) and dKunitz-PEO(5000)$_4$ (6) respectively. Native Kunitz contains 31 negatively charged (Asp + Glu) and 23 positively charged (Arg + Lys) amino acids in its primary structure. Ovomucoid has 30 negatively charged (Asp + Glu) and 18 (Arg + Lys) positively charged amino acids. The zeta potential of 6 and 10 is in accordance with the presence of higher numbers of negatively charged amino acids (Asp + Glu) on the protein backbone compared to the positively charged residues (Arg + Lys). dHSA-PEO(5000)$_{27}$ (2) reveals slightly negative zeta potential of −0.7 ± 1.7 mV, similar to the net charges of native HSA. dLY-PEO(5000)$_8$ (8) revealed negative zeta potential of −8.4 ± 2.8 mV. Even though the precursor protein lysozyme has 18 positively charged residues (Arg + Lys) and only 9 negatively charged amino acids (Asp + Glu), the negative zeta potential of dLY-PEO(5000)$_8$ (8) is surprising. The change in the suface charges of 8 from native LY may indicate to the formation of the intermolecular interactions between the dLY-PEO(5000)$_8$. These findings underline that polypeptide with tunable charges have been achieved. Polypeptides that allow fine-tuning of their surface charges are highly attractive to achieve biopolymers with tunable cell and tissue penetration properties.

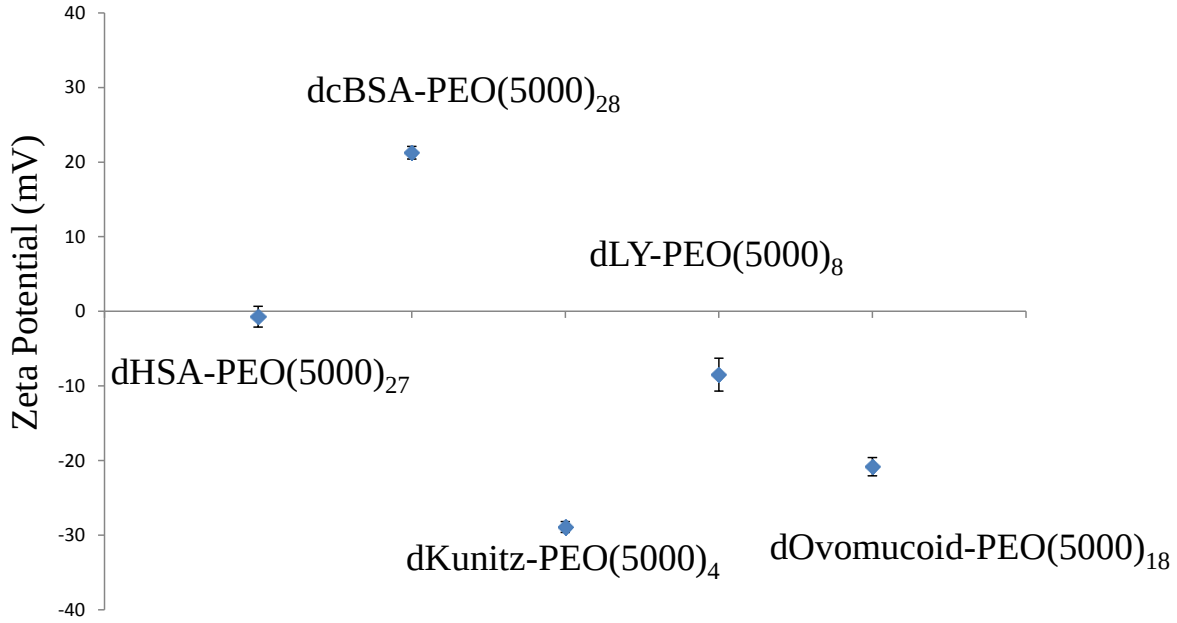

Figure 2.12. Zeta Potential of all the polypeptide polyethylene oxide (PP-PEOs).

Table 2.4. Summary of the results of the zeta potential of the native protein and corresponding PP-PEOs and the correlation with the positively and negatively charged amino acids of the protein. Unless mentioned the numbers of positively and negatively charged amino acids were obtained from Expasy (http://web.expasy.org/protparam/).

Proteins	**Number of total positively charged amino acids in the sequence**	**Number of total negatively charged amino acids in the sequence**	**Zeta potential of globular protein at pH 7.4**	**Zeta potential of coreesponding PP-PEOs at pH 7.4**
cBSA	147[37]	13[37]	22.7 ± 3.0 mV (1)	21.6 ± 1.5 mV (2)
HSA	86 (27 Arg + 59 Lys)	98 (36 Asp+62 Glu)	−3.1 ± 1.3 mV (3)	−0.7 ± 1.7 mV (4)
Kunitz	23 (10 Arg+13 Lys)	31(17 Asp +14 Glu)	-26.6± 0.6mV (5)	-28.9±0.85 mV (6)
Lysozyme	18(10 Arg +8 Lys)	9 (7Asp +2 Glu)	4.9 ± 0.6 mV (7)	−8.4 ± 2.8 mV (8)
Ovomucoid	18 (5 Arg +13 Lys)	30 (14 Asp+16 Glu)	-10.2±1.3 mV (9)	-20.8±1.49 mV (10)

Secondary structure of PP-PEOs

The primary amino acid sequence of the protein backbone contributes to the formation of the secondary structure, for example, helical and β sheet structures, due to noncovalent interactions among the amino acid residues. The presence of regular structural elements in polymers is highly attractive because secondary interactions could yield additional features such as self-assembly into ordered supra-structures such as amyloid fiber formation[65] due to

the presence of β-sheet structures. According to CD studies, the predominant secondary structure elements of the precursor proteins are partially conserved for all protein-derived polypeptide copolymers (**Figure 2.13**.). For instance, HSA, cBSA reveals a high content of α-helix (~ 67%) and the corresponding polypeptide copolymer (**4** and **2**) contains mainly α-helix (~ 42-43%) structures. For Lysozyme and Ovomucoid a similar trend of decrease in α-helix were observed after preparation of polypeptide polyethylene oxide. dLY-PEO(5000)$_8$ (**8**) contains 21% α-helix structure compared with 30% of native Lysozyme (**7**). dOvomucoid-PEO(5000)$_{18}$ (**10**) contains 20% α-helix structure compared with 26% of native Ovomucoid (**9**). However, for Kunitz (**5**) an opposite trend has been observed. Kunitz is a complete beta sheet protein.[60] dKunitz-PEO(5000)$_4$ (**6**) contains only 12% β-sheet and the α-helix content increases significantly to 60% compared with no α-helix on native Kunitz. Probably, the β-strands of Kunitz protein that are formed by a long-range hydrogen bonds and hydrophobic interactions between residues on neighboring strands,[21] are mostly destroyed by the high concentration of denaturing agent and heating. Instead, preferential stabilization of isolated structural elements with independent hydrogen binding abilities has been observed upon denaturation of Kunitz. However, in all cases, the polypeptide copolymers reveal an increase in random structures elements, most likely due to the denaturation and pegylation steps.

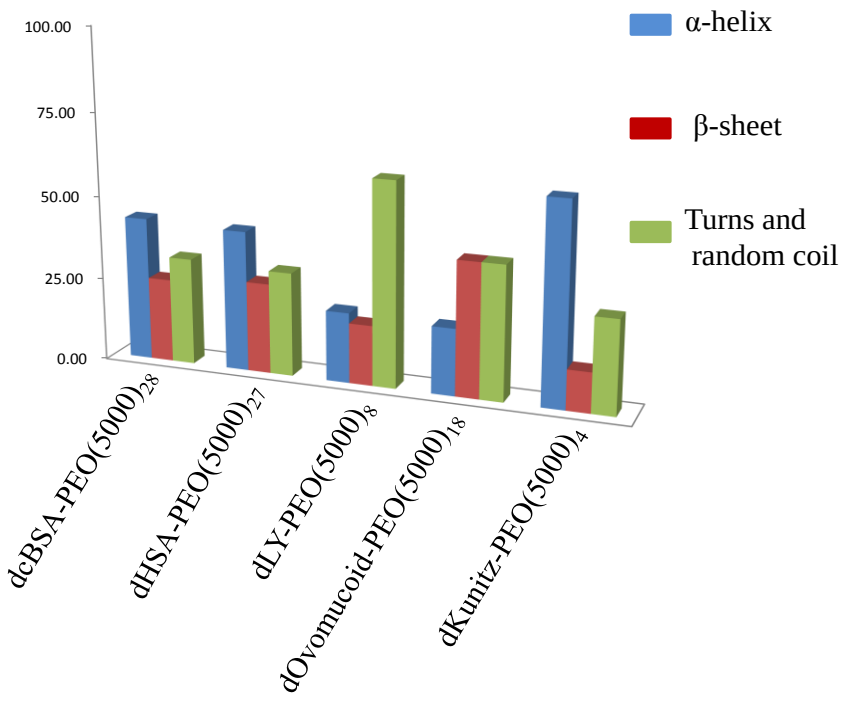

Figure 2.13. Secondary structure of all the polypeptide polyethylene oxide (PP-PEOs).

2.3. Conclusions

In conclusion, in this chapter reaction schemes towards narrowly dispersed polypeptide copolymers with defined structures and molecular weights as well as attractive physical properties have been described. The denaturation of the globular proteins followed by stabilization with polyethylene (oxide) chains yields polypeptide copolymers of precisely defined backbone lengths. In this way, polypeptides with different backbone lengths, {e.g. dHSA-PEO(5000)$_{27}$, dcBSA-PEO(5000)$_{28}$, dLY-PEO(5000)$_{8}$, dOvomucoid-PEO(5000)$_{18}$ and dKunitz-PEO(5000)$_{4}$ have (calculated) backbone length of 0.2515, 0.25, 0.0554, 0.08 and 0.0778 micrometer respectively}[66] varying net charges, as well as the presence of ordered secondary structural elements have been achieved successfully. Interestingly, different proteins required different denaturing conditions and reagents to achieve narrowly dispersed polypeptide copolymers. Proteins with higher β-sheet content required more harsh denaturing conditions than proteins with more α-helix elements. This result is in consistence with fact that β-sheet proteins tend to be more robust due to the higher content of nonlocal interactions; and inherent kinetic stability of β-structures since partially unfolded β-sheet proteins are particularly susceptible to aggregation.[64] All of these copolymers reveal excellent solubility and stability in aqueous media. The protein backbone offers a wide range of functional groups at precise positions, such as primary amine from lysine, carboxylic groups from aspartic and glutamic acids, hydroxyl groups of serine, tyrosine and guanidine group of arginine, which can be easily further functionalized with bioactive molecules. In chapter 3, these tailored multifunctional copolymers have been applied for the multivalent stabilization of NIR emitting fluorescent gold nanoparticles and the effect of the length of the polymer length have been discussed.

2.4. References

(1) Quarta, A.; Curcio, A.; Kakwere, H.; Pellegrino, T. *Nanoscale* **2012**, *4*, 3319.
(2) Erathodiyil, N.; Ying, J. Y. *Acc. Chem. Res.* **2011**, *44*, 925.
(3) Li, D.; He, Q.; Li, J. *Adv. Colloid Interfac.* **2009**, *149*, 28.
(4) Shan, J.; Tenhu, H. *Chem.Commun.***2007**, *47*, 4580.
(5) Shan, J.; Nuopponen, M.; Jiang, H.; Kauppinen, E.; Tenhu, H. *Macromolecules* **2003**, *36*, 4526.
(6) Kotal, A.; Mandal, T. K.; Walt, D. R. *J. Polym. Sci. A1* **2005**, *43*, 3631.
(7) Youk, J. H.; Park, M.-K.; Locklin, J.; Advincula, R.; Yang, J.; Mays, J. *Langmuir* **2002**, *18*, 2455.
(8) Hermes, J. P.; Sander, F.; Fluch, U.; Peterle, T.; Thompson, D.; Urbani, R.; Pfohl, T.; Mayor, M. *J. Am. Chem. Soc.***2012**, *134*, 14674.
(9) Otsuka, H.; Akiyama, Y.; Nagasaki, Y.; Kataoka, K. *J. Am. Chem. Soc.* **2001**, *123*, 8226.

(10) Corbierre, M. K.; Cameron, N. S.; Sutton, M.; Mochrie, S. G. J.; Lurio, L. B.; Rühm, A.; Lennox, R. B. *J. Am. Chem. Soc.***2001**, *123*, 10411.
(11) Aldana, J.; Lavelle, N.; Wang, Y.; Peng, X. *J. Am. Chem. Soc.* **2005**, *127*, 2496.
(12) Hamidi, M.; Azadi, A.; Rafiei, P. *Adv. Drug Deliver. Rev.* **2008**, *60*, 1638.
(13) Nitta, S.; Numata, K. *Int. J. Mol. Sci.* **2013**, *14*, 1629.
(14) Yang, J.; Gitlin, I.; Krishnamurthy, V. M.; Vazquez, J. A.; Costello, C. E.; Whitesides, G. M. *J. Am. Chem. Soc.* **2003**, *125*, 12392.
(15) Elzoghby, A. O.; Samy, W. M.; Elgindy, N. A. *J. Control Release* **2012**, *161*, 38.
(16) Barron, A. E.; Zuckerman, R. N. *Curr.Opin. Chem. Biol.***1999**, *3*, 681.
(17) Klok, H.A. *Angew.Chem.Int.Ed.* **2002**, *41*, 1509.
(18) Wu, Y.; Chakrabortty, S.; Gropeanu, R. A.; Wilhelmi, J.; Xu, Y.; Er, K. S.; Kuan, S. L.; Koynov, K.; Chan, Y.; Weil, T. *J. Am. Chem. Soc.* **2010**, *132*, 5012.
(19) Wu, Y.; Pramanik, G.; Eisele, K.; Weil, T. *Biomacromolecules* **2012**, *13*, 1890.
(20) Hartmann, L.; Börner, H. G. *Adv. Mater.***2009**, *21*, 3425.
(21) Roychaudhuri, R.; Sarath, G.; Zeece, M.; Markwell, J. *Arch. Biochem. Biophys.* **2003**, *412*, 20.
(22) Brown, K. F.; Crooks, M. J. *Biochem. Pharmacol.* **1976**, *25*, 1175.
(23) Kragh-Hansen, U. *Pharmacol. Rev.***1981**, *33*, 17.
(24) Gonzalez-Jimenez, J.; Frutos, G.; Cayre, I.; Cortijo, M. *Biochimie* **1991**, *73*, 551.
(25) Creighton, T. E. *Biochem. J.* **1990**, *270*, 1.
(26) He, X. M.; Carter, D. C. *Nature* **1992**, *358*, 209.
(27) Dugaiczyk, A.; Law, S. W.; Dennison, O. E. *Proc. Natl. Acad. Sci. U S A* **1982**, *79*, 71.
(28) Curry, S.; Brick, P.; Franks, N. P. *BBA - Mol.Cell Biol. L.* **1999**, *1441*, 131.
(29) Carter, D. C.; He, X. M. *Science* **1990**, *249*, 302.
(30) González-Jiménez, J.; Cortijo, M. *J. Protein Chem.***2002**, *21*, 75.
(31) Weijers, R. N. *Clin.Chem.* **1977**, *23*, 1361.
(32) Murayama, K.; Tomida, M. *Biochemistry* **2004**, *43*, 11526.
(33) Petersen, H. A.; Foster, J. F. *J.Biol. Chem.* **1965**, *240*, 2503.
(34) Carter, D. C.; Ho, J. X.; C.B. Anfinsen, J. T. E. F. M. R.; David, S. E. *In Advances in Protein Chemistry*; Academic Press: 1994; Vol. Volume 45, p 153.
(35) Tanaka, N.; Nishizawa, H.; Kunugi, S. *BBA - Protein Struct. M.* **1997**, *1338*, 13.
(36) Rezwan, K.; Meier, L. P.; Gauckler, L. J. *Biomaterials* **2005**, *26*, 4351.
(37) Eisele, K.; Gropeanu, R. A.; Zehendner, C. M.; Rouhanipour, A.; Ramanathan, A.; Mihov, G.; Koynov, K.; Kuhlmann, C. R. W.; Vasudevan, S. G.; Luhmann, H. J.; Weil, T. *Biomaterials* **2010**, *31*, 8789.
(38) Canfield, R. E. *J. Biol. Chem.* **1963**, *238*, 2698.
(39) Xu, M.; Shashilov, V. A.; Ermolenkov, V. V.; Fredriksen, L.; Zagorevski, D.; Lednev, I. K. *Protein Sci.* **2007**, *16*, 815.
(40) Proctor, V. A.; Cunningham, F. E.; Fung, D. Y. C. *C R C Cr. Rev. Food Sci.* **1988**, *26*, 359.
(41) Greene, R. F.; Pace, C. N. *J. Biol.Chem.* **1974**, *249*, 5388.
(42) Hedoux, A.; Krenzlin, S.; Paccou, L.; Guinet, Y.; Flament, M.-P.; Siepmann, J. *Phys.Chem.Chem. Phys.***2010**, *12*, 13189.
(43) McDonald, C. C.; Phillips, W. D.; Glickson, J. D. *J. Am.Chem. Soc.***1971**, *93*, 235.
(44) David, C.; Foley, S.; Enescu, M. *Phys. Chem. Chem.Phys.* **2009**, *11*, 2532.
(45) Cline, D.J.; Redding, S. E.; Brohawn, S. G.; Psathas, J. N.; Schneider, J. P.; Thorpe, C. *Biochemistry* **2004**, *43*, 15195.
(46) Cooke, S. K.; Sampson, H. A. *J. Immunol.* **1997**, *159*, 2026.
(47) Laskowski, M.; Kato, I. *Ann. Rev. Biochem.* **1980**, *49*, 593.
(48) Watanabe, K.; Matsuda, T.; Sato, Y. *Biochim. Biophys. Acta* **1981**, *667*, 242.

(49) Matsuda, T.; Watanabe, K.; Nakamura, R. *BBA - Protein Struct. M.* **1982**, *707*, 121.
(50) Leduc, V.; Demeulemester, C.; Guizard, C.; Le Guern, L.; Polack, B.; Peltre, G. *Allergy* **1999**, *54*, 464.
(51) Salahuddin, A.; Sibghatullah; Baig, M. A. *Proc. Int. Symp. Biomol. Struct. Interactions, Suppl. J. Biosci.* **1985**, *8*, 67.
(52) Mustafa, M.G.; Dar, T. A.; Ali, S. A. *Int. J. Biol. Chem.* **2011**, *5*, 327.
(53) Timasheff, S. N. *Ann. Rev. Bioph. Biom.***1993**, *22*, 67.
(54) Ahmad, F.; Contaxis, C. C.; Bigelow, C. C. *J. Biol. Chem.***1983**, *258*, 7960.
(55) Castellino, F. J.; Barker, R. *Biochemistry* **1968**, *7*, 4135.
(56) Kunitz, M. *Science* **1945**, *101*, 668.
(57) Tetenbaum, J.; Miller, L. M. *Biochemistry* **2001**, *40*, 12215.
(58) Steiner, R. F. *BBA - Gen. Subjects* **1965**, *100*, 111.
(59) Lehle, K.; Wrba, A.; Jaenicke, R. *J. Mol. Biol.* **1994**, *239*, 276.
(60) Sweet, R. M.; Wright, H. T.; Janin, J.; Chothia, C. H.; Blow, D. M. *Biochemistry* **1974**, *13*, 4212.
(61) Song, H. K.; Suh, S. W. *J. Mol. Biol.* **1998**, *275*, 347.
(62) Chou, K. C., Pottle, M., Nemethy, G., Ueda, Y., and Scheraga, H.A. *J. Mol. Biol.* **1982**, *162*, 89.
(63) Nielsen, M. M.; Andersen, K. K.; Westh, P.; Otzen, D. E. *Biophys. J.* **2007**, *92*, 3674.
(64) Manning, M.; Colón, W. *Biochemistry* **2004**, *43*, 11248.
(65) Dong, H.; Hartgerink, J. D. *Biomacromolecules* **2007**, *8*, 617.
(66) Marsh, R. E.; Donohue, J.; C.B. Anfinsen, A. L. A. J. T. E.; Frederic, M. R. *In Advances in Protein Chemistry*; Academic Press: 1967; Vol. Volume 22, p 235.

Chapter3.

3.1. Highly Stable, Ultra Small, Multifunctional Near Infrared (NIR) Gold Nanoemitters for Bioimaging Applications

3.1.1. Introduction

Fluorophores, emitting in the near infrared (NIR) region have attracted ongoing attention because of their applications in biomedical, materials, and related fields. NIR-probes are attractive for imaging due to their low interfering absorption and fluorescence from biological samples, inexpensive laser diode excitation, reduced scattering, and enhanced tissue penetration depth.[1,2] Most organic NIR dyes reveal only low photochemical stabilities, rapid photobleaching, and little water solubility.[3,4] Unlike organic fluorophores, nanoparticle-based NIR emitters are very attractive for biolabelling and bioimaging applications because they allow long-term, sensitive tracking of signals with minimal photobleaching. AuNPs exhibit size dependent optical properties.[5-9] Small gold nanoparticles (<3 nm) lose their bulk-like electronic properties; for example, they no longer support the plasmon excitation characteristics of relatively large gold nanocrystals (3-100 nm) and below 2 nm, they emit bright fluorescence ranging from the visible to the infrared depending on the number of Au atoms in the cluster.[6,9] It is highly desirable to prepare water soluble, stable NIR AuNPs for bioimaging applications. Recently, few NIR AuNPs have been reported, such as monolayer-protected NIR-emitting AuNPs (NIR-AuNPs),[10,11] multistep etching-based time consuming synthesis of fluorescent AuNPs.[12] One step protein directed synthesis, dihydrolipoic acid (DHLA) capped NIR emitting AuNPs have also been published.[13, 14] But these AuNPs are very unstable, especially at low pH (<5) and DHLA also has the tendency to adsorb biomolecules nonspecifically onto the nanoparticle surface.[15] A nanoparticle platform with great potential for use in biomedical applications needs to promote biocompatibility and reduce nonspecific interactions, must exhibit long term stability over a broad pH range, in the presence of high concentrations of electrolytes and in biological media and also offers multiple functional groups to which biomolecules can be attached.[16] To implement this new approach, the copolymers,[17] dcBSA-PEO$(5000)_{28}$, dHSA-PEO$(5000)_{27}$ and dLY-PEO$(5000)_{8}$ were used and thioctic acid (TA) attached at the protein backbone, acts as anchoring group to

metal surfaces. Then the TA attached copolymers dcBSA-PEO(5000)$_{28}$-(TA)$_{26}$, dHSA-PEO(5000)$_{27}$-(TA)$_{22}$ and dLY-PEO(5000)$_{8}$-(TA)$_{8}$ have been used to prepare AuNPs following a facile one pot synthesis method by reducing the Au^{3+} to Au^{0}.[14] It was found that the dcBSA-PEO(5000)$_{28}$-(TA)$_{26}$ coated nanoparticles exhibit high colloidal stability over a broad pH range, in the presence of excess electrolytes (NaCl), DTT, phosphate buffer, trypsin without any significant cytotoxicity. dcBSA-PEO(5000)$_{28}$-(TA)$_{26}$, coated AuNPs were further imaged inside A549 cells by the confocal laser scanning microscopy (CLSM). These results indicate that dcBSA-PEO(5000)$_{28}$-(TA)$_{26}$, coated AuNPs have great potential as robust fluorophores in biomedical applications.

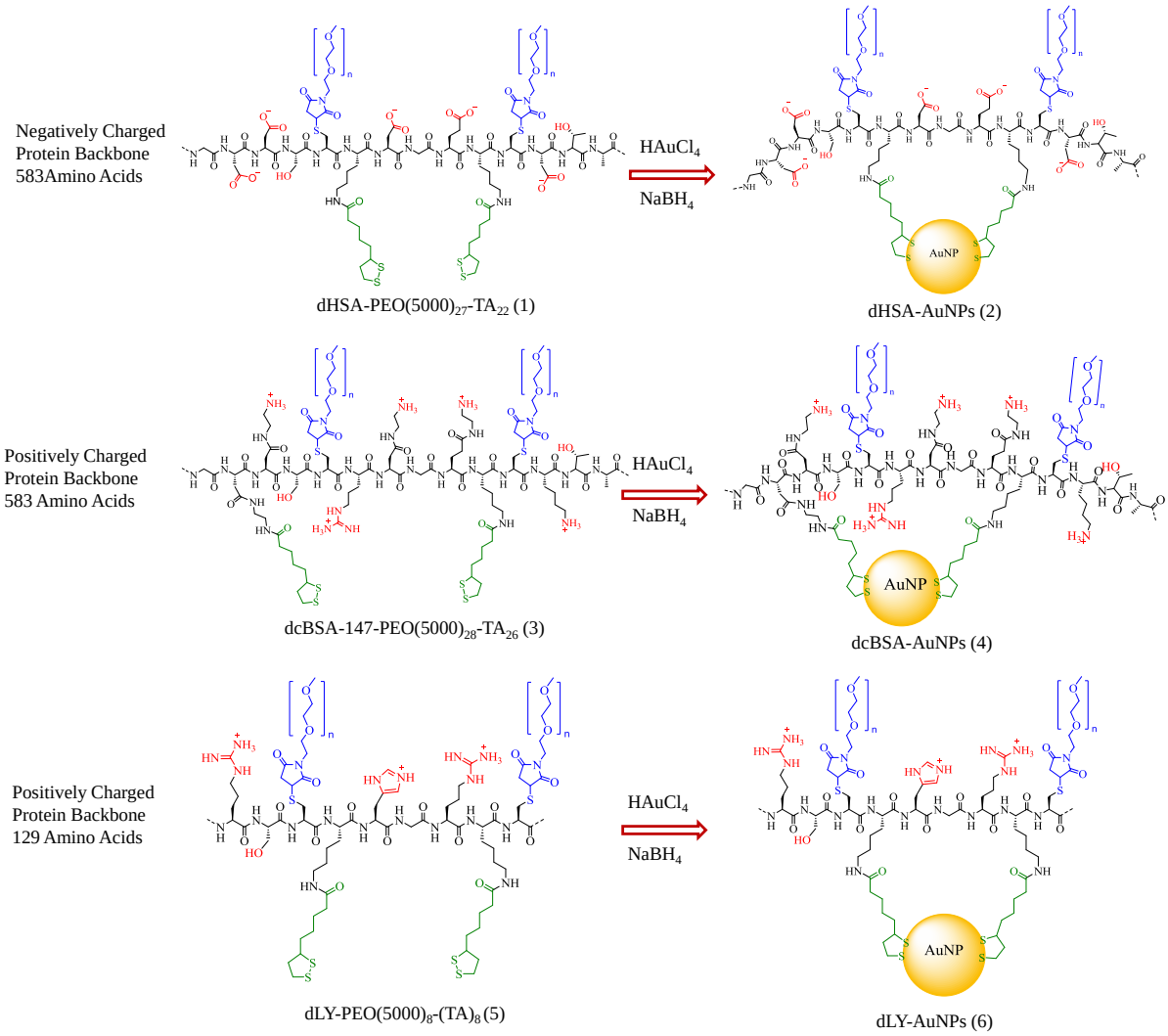

Scheme 3.1.1. Chemical structures of HSA-, cBSA- and LY-derived copolymers (**1, 3, 5**) and stabilization of AuNPs in the presence of these copolymers.

3.1.2. Results and Discussion

Preparation and characterization of TA-containing polypeptide copolymers

Copolymers dcHSA-PEO(5000)$_{27}$, dcBSA-PEO(5000)$_{28}$ and dLY-PEO(5000)$_8$ provide several reactive primary amino groups that allow the attachment of multiple lipophilic thioctic acid (TA) groups. After reaction of copolymers dcHSA-PEO(5000)$_{27}$, dcBSA-PEO(5000)$_{28}$ and dLY-PEO(5000)$_8$ with N-hydroxysuccinimide (NHS)-activated TA, copolymers dcHSA-PEO(5000)$_{27}$-(TA)$_{22}$ (**1**), dcBSA-PEO(5000)$_{28}$-(TA)$_{26}$ (**3**) and dLY-PEO(5000)$_8$-(TA)$_8$ (**5**) have been isolated. According to SDS-PAGE (sodium dodecyl sulfate polyacrylamide gel electrophoresis) (**Figure 3.1.1**) molecular weights of 200kDa for (**1**), 210 kDa for (**3**) and 56.6 kDa for (**5**) have been obtained indicating that about 27 to 28 of 35 available thiol groups of the precursor proteins HSA and cBSA-147 have been pegylated and about 22±4 and 26±3 TA groups have been attached as quantified by the 4,4´-dithiodipyridine (DPS) test (**Table 3.1.1**).[18] In case of (**5**), 8±3 TA groups were attached to the backbone.

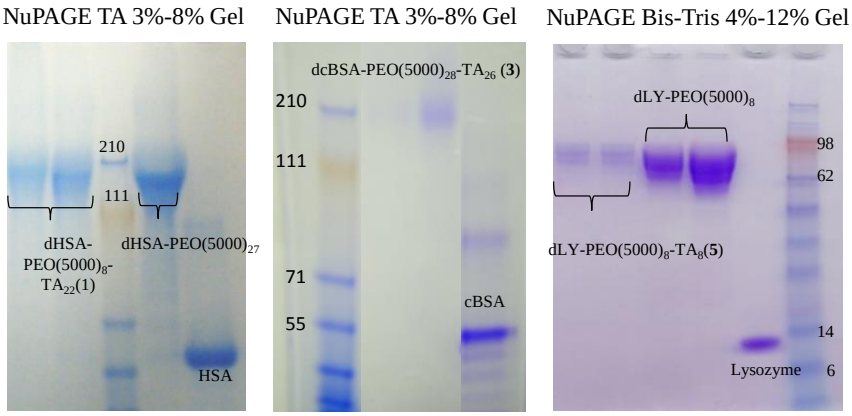

Figure 3.1.1. SDS-PAGE of dHSA-PEO(5000)$_{27}$-(TA)$_{22}$ (**1**), dcBSA-PEO(5000)$_{28}$-(TA)$_{26}$ (**3**), and dLY-PEO(5000)$_8$-(TA)$_8$ (**5**).

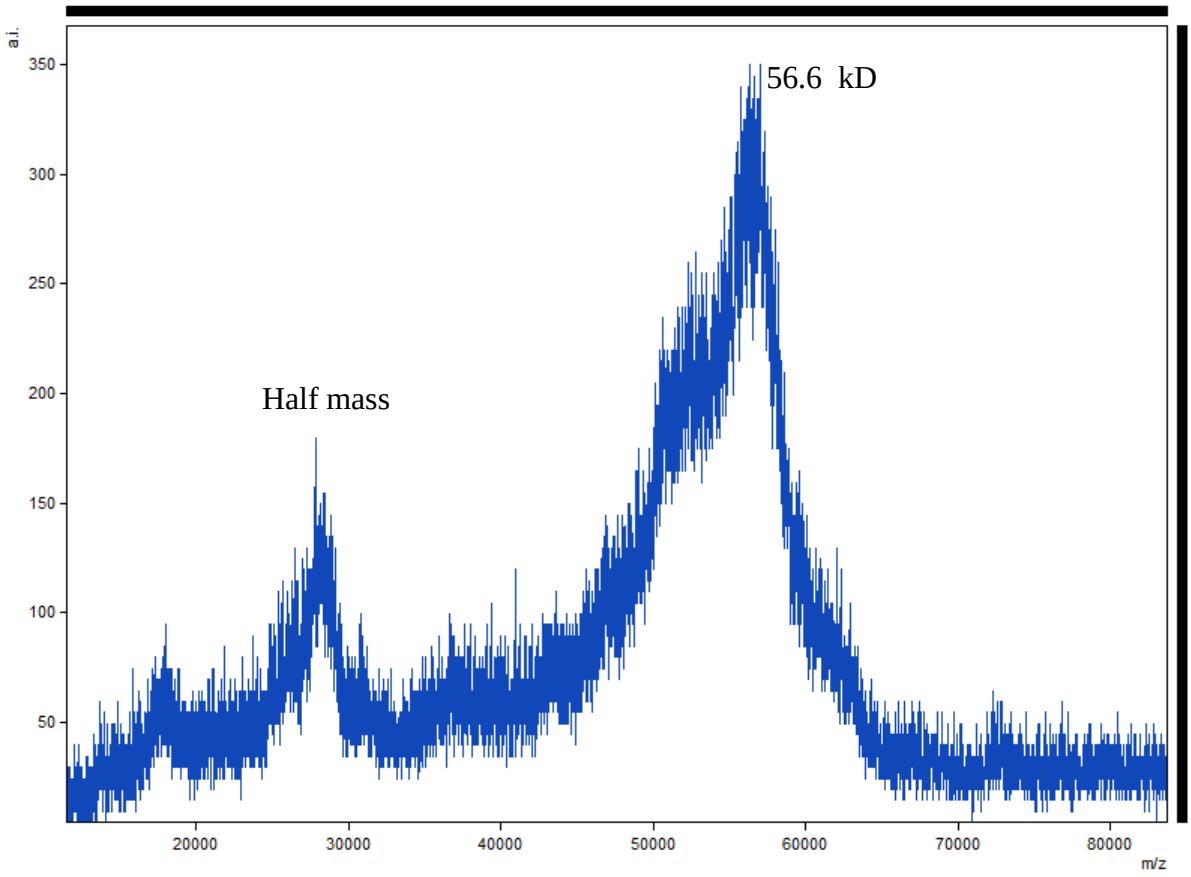

Figure 3.1.2. MALDI-TOF MS of dLY-PEO(5000)$_8$-(TA)$_8$ (**5**, calcd. MW = 56.6kD); Matrix: Sinapinic acid.

4,4′-Dithiodipyridine (DPS) test Results

The numbers of thioctic acid (TA) attached to each copolymer have been estimated by the DPS Test (for details see experimental section). The results for different copolymer materials are listed below.

Table 3.1.1. Summary of number of thioctic acids attached to different copolymers according to DPS test.

Name of the copolymers	**Number of thioctic acids (TA) attached to each copolymer**
dHSA-PEO(5000)$_{27}$-(TA)$_{22}$ (**1**)	22±3
dcBSA-PEO(5000)$_{28}$-(TA)$_{26}$ (**3**)	26±3
dLY-PEO(5000)$_8$-(TA)$_8$ (**5**)	8±3

Characterization of AuNPs

In situ preparation and characterization of NIR-AuNPs

In situ synthesis of AuNPs have been accomplished at room-temperature in water following a one pot synthetic procedure.[19] First, precursors have been prepared in solution by reacting the TA groups of the copolymers with tetrachloroauric(III) acid ($HAuCl_4.3H_2O$), followed by the growth of the AuNPs in the presence of the reducing agent $NaBH_4$. The sizes of the AuNPs have been adjusted by varying the Au^{3+}/TA ratio as well as the copolymer lengths at low Au^{3+} concentrations (**Table 3.1.2**). By decreasing the Au^{3+}/TA ratio from (a) 20:1; (b) 10:1; (c) 5:1, (d) 3:1, (e) 1:1 to (f) 1:5 , successively smaller AuNPs have been stabilized *in situ*. With decreasing AuNPs sizes, the peak amplitude of the surface plasmon resonance band at around 530 nm also declines (**Figure 3.1.3.**), which is in accordance to the literature.[20] dHSA-AuNPs **2d, 2e, 2f** and dcBSA-AuNPs **4d, 4e, 4f** displayed well-detectable emission envelopes with emission maxima in the NIR at about 720 nm after excitation at 365 nm. In contrast, only dLY-AuNPs **6f** shows a broad emission with a maximum at around 680 nm (**Figure 3.1.4**). No Plasmon bands have been observed in the corresponding absorption spectra (**Figure 3.1.3**) already indicating average particle diameters below 2 nm.[27] For the dHSA-AuNPs (**2f**) and dcBSA-AuNPs (**4f**), fluorescence quantum yields (FQYs) of 1.6% and 1.8%, respectively, have been calculated by applying tris(2,2'-bipyridyl) ruthenium hexahydrate (II) as reference chromophore (**Table 3.1.4**). Interestingly, at similar concentrations and 3:1 Au^{3+}/TA ratio, stabilization with (**5**) only yielded non-fluorescent dLY-AuNPs (**6d**) with sizes larger than 2 nm. Only after decreasing the Au^{3+}/TA ratio to 1:5, fluorescent dLY-AuNPs (**6f**) have been obtained. Fluorescent dLY-AuNPs (**6f**) showed very weak emission and a broad emission spectrum with a maximum at around 680 nm (**Figure 3.1.4.C**). Even at Au^{3+}/TA ratio of 1:5, a significantly reduced quantum yield of 0.3% was calculated for **6f** compared to 1.6-1.7% for **2f** and 1.8-2% for **4f**. Since the same experimental conditions as well as a similar (1:1) ratio of the Au^{3+}/TA anchoring groups of 5 have been selected thus indicating that the length of the polymer backbone might have an important impact on the potential to stabilize ultra-small AuNPs. dcBSA-AuNPs (**4f**) with dimensions smaller than 2 nm have been investigated via Atomic Force Microscopy (AFM), FCS as well as high resolution transmission electron microscopy (HRTEM) on graphene. **4f** has been deposited on a graphene substrate and studied by 80 kV aberration-corrected high-resolution transmission electron microscopy (AC-HRTEM) (**Figure 3.1.5 a, b, c**). Interestingly, dcBSA-AuNPs with sizes smaller than 1 nm and the Au-Au bond contracts from 2.8 to 0.27 nm (**Figure 3.1.5 d**) was detected, which is consistent with previously reported results.[21] Due to

the low intensity contribution of the graphene substrate and the high resolution achieved at 80 kV TEM, each coated AuNPs have been atomically described while remaining unaffected by the electron beam. Slightly larger dimensions of about 3 nm diameter have been found with AFM on mica surfaces, which also reflect the contribution of the protein-copolymer shell on the surface (**Figure 3.1.5 e**). In solution, diffusion times of **4d-f** were recorded by FCS measurements and the corresponding hydrodynamic diameters have been calculated in the range of 2 nm (**Table 3.1.3**). Noteworthy, by applying polypeptide copolymers (**1**) and (**3**), exclusively small, narrowly dispersed, stable and fluorescent particles have been formed under mild conditions in a one pot synthesis scheme. In contrast to alternative procedures, neither separation of larger non-fluorescent nanoparticles nor extreme pH values during preparation and purification or multistep synthetic procedures have been required for obtaining water soluble AuNPs or NIR-AuNPs.[13,22,23, 12,14] For similar ratios of $HAuCl_4$/TA, AuNPs coated with dLY-PEO$(5000)_8$-$(TA)_8$ (**5**) reveals a surface plasmon band indicating the existence of particle sizes larger than 2 nm (**Table 3.1.2**).

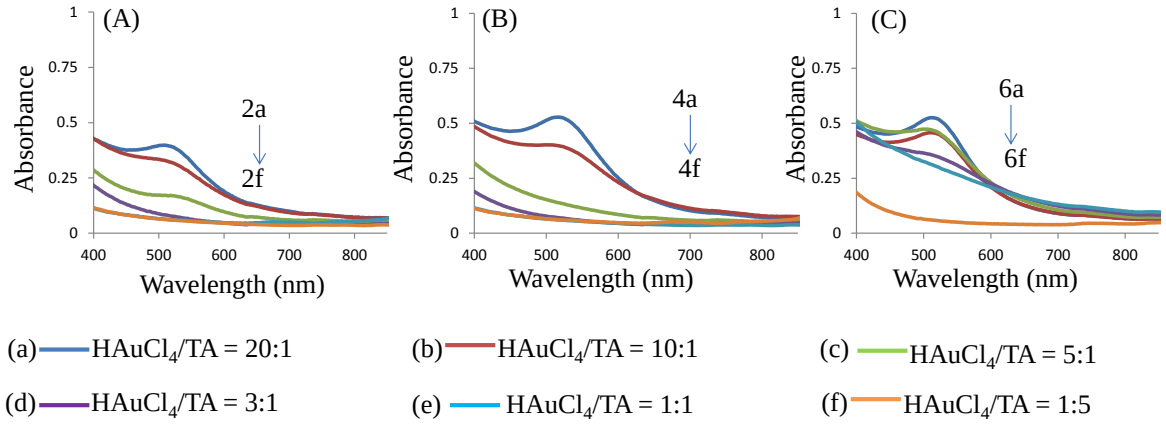

Figure 3.1.3. (a) Absorption spectra of AuNPs (**2a-f**) prepared by using $HAuCl_4$/TA ratios from 20:1 (**2a**) to 1:5 (**2f**) of copolymer dHSA-PEO$(5000)_{27}$-$(TA)_{22}$. (b) Absorption spectra of AuNPs prepared by using $HAuCl_4$/TA ratios from 20:1 (**4a**) to 1:5 (**4f**) of copolymer dcBSA-PEO$(5000)_{28}$-$(TA)_{26}$. (c) Absorption spectra of AuNPs prepared by using $HAuCl_4$/TA ratios from 20:1 (**6a**) to 1:5 (**6f**) of copolymer of dLY-PEO$(5000)_8$-$(TA)_8$.

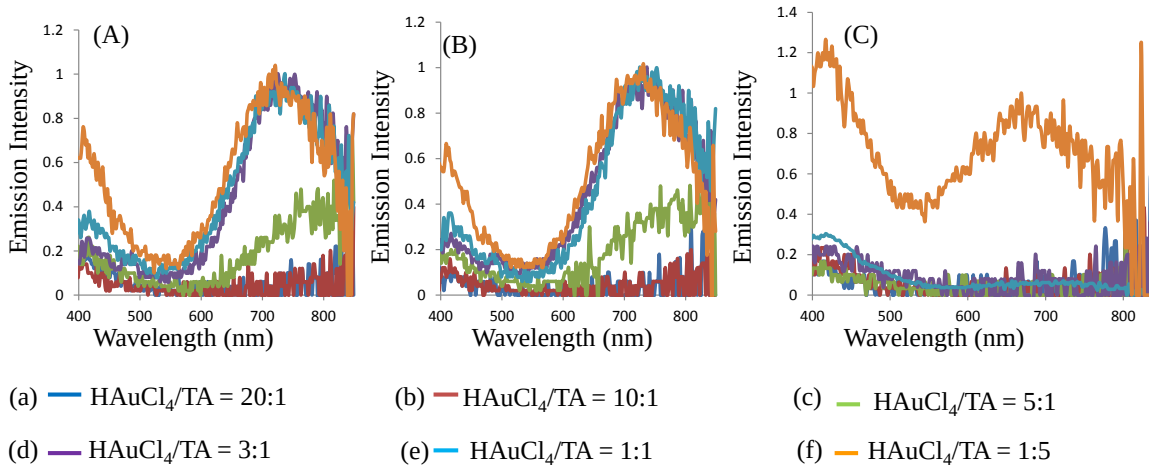

Figure 3.1.4. (a) Emission spectra of AuNPs (**2a-2f**) coated with dHSA-PEO(5000)$_{27}$-(TA)$_{22}$ prepared using different HAuCl$_4$/TA ratios from 20:1 (**2a**) to 1:5 (**2f**). (b) Emission spectra of AuNPs (**4a-4f**) coated with dcBSA-PEO(5000)$_{28}$-(TA)$_{26}$ prepared using different HAuCl$_4$/TA ratios from 20:1 (**6a**) to 1:5 (**6f**). (c) Emission spectra of AuNPs (**6a-6f**) coated with dLY-PEO(5000)$_8$-(TA)$_8$ prepared using different ratios 20:1 (**6a**) to 1:5 (**6f**).

Table 3.1.2: Overview of the sizes and optical properties of AuNPs **2a-f**, **4a-f** and **6a-f** coated with copolymers **1**, **3** and **5** by applying different ratios of Au^{3+}/TA as given in the first row. AuNPs **2a, 2b, 2c, 2d, 2e, 2f** have been coated with dHSA-PEO(5000)$_{27}$-(TA)$_{22}$, AuNPs **4a, 4b, 4c, 4d, 4e, 4f** have been coated with dcBSA-PEO(5000)$_{28}$-(TA)$_{26}$ and **6a, 6b, 6c, 6d, 6e, 6f** have been coated with dLY-PEO(5000)$_8$-(TA)$_8$. NF = non fluorescent, br = broad emission maximum.

Au^{3+}/TA ratio	**2a** 20:1	**2b** 10:1	**2c** 5:1	**2d** 3:1	**2e** 1:1	**2f** 1:5
Emission λ_{max} (nm)	NF	NF	br ~750-800	720	720	720
FQY (%)	NF	NF	0.05	1.6-1.7	1.6-1.7	1.6-1.7
Diameter TEM (nm)	9.4	8.9	< 2	< 2	< 2	< 2

Au^{3+}/TA ratio	**4a** 20:1	**4b** 10:1	**4c** 5:1	**4d** 3:1	**4e** 1:1	**4f** 1:5
Emission λ_{max} (nm)	NF	NF	br ~750-800	730	730	730
FQY %	NF	NF	0.057	1.8-2	1.8-2	1.8-2
Diameter TEM (nm)	10	8.3	< 2	< 2	< 2	< 2

Au^{3+}/TA ratio	**6a** 20:1	**6b** 10:1	**6c** 5:1	**6d** 3:1	**6e** 1:1	**6f** 1:5
Emission λ_{max} (nm)	NF	NF	NF	NF	NF	br 680
FQY %	NF	NF	NF	NF	NF	0.3
Diameter TEM (nm)	15	13.5	10.8	7.8	3.4	< 2

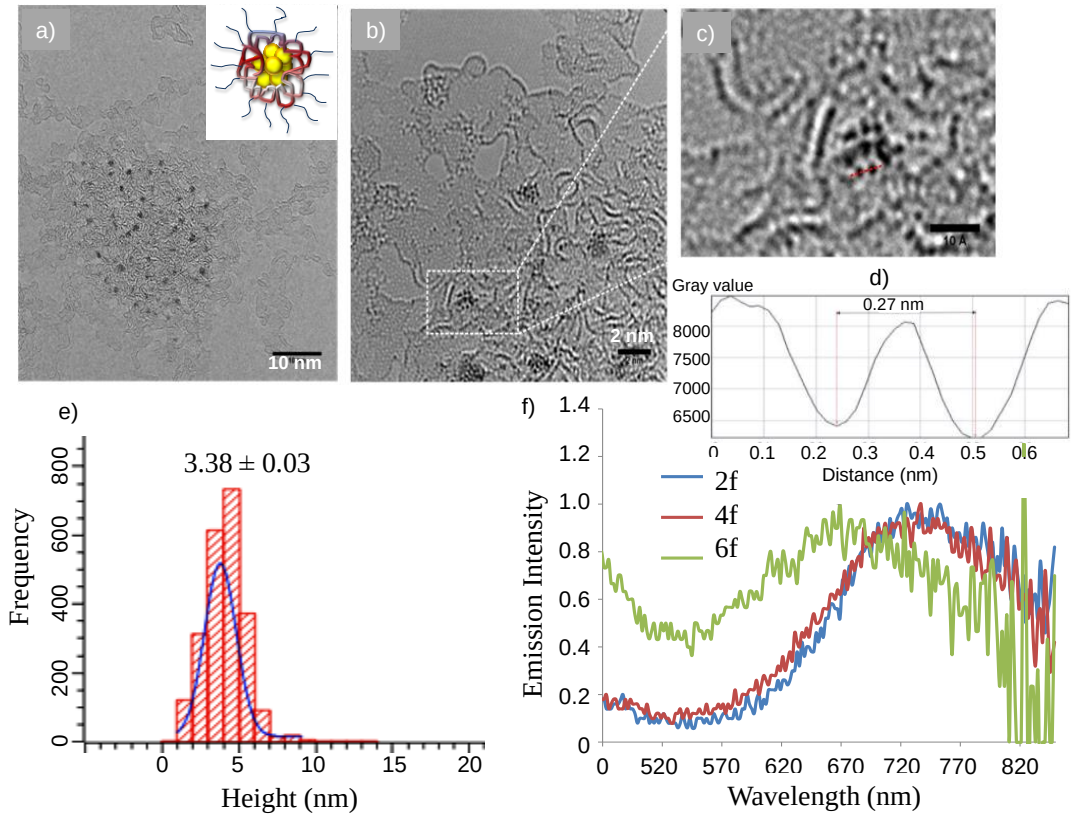

Figure 3.1.5 a) Representative electron micrographs of AuNPs (**4f**) coated with dcBSA-PEO(5000)$_{28}$-(TA)$_{26}$ prepared using $HAuCl_4$/TA = 1:5. Micrograph showing a cluster of deposited AuNPs on graphene. (b) HRTEM image of (**4f**) deposited on graphene. (c) Scaled cut out of a AuNP with diameter 0.8 nm where the gold atoms of the NP are resolved, the red dotted line indicates the trajectory taken for the line profile shown in d. Each of the gold(d) Line profile showing 0.27 nm Au-Au bond distance in the AuNP corresponding to the reported investigations on the contraction of bond distances for gold particles with size < 1nm. (e) Particle size distribution of AuNPs (**4f**) coated with dcBSA-PEO(5000)$_{28}$-(TA)$_{26}$ for the of $HAuCl_4$/TA (1:5) ratio. (f) Emission spectra of AuNPs coated with **2f** (blue), **4f** (red) and **6f** (green) for a $HAuCl_4$/TA ratio of 1:5 upon excitation at 365 nm.

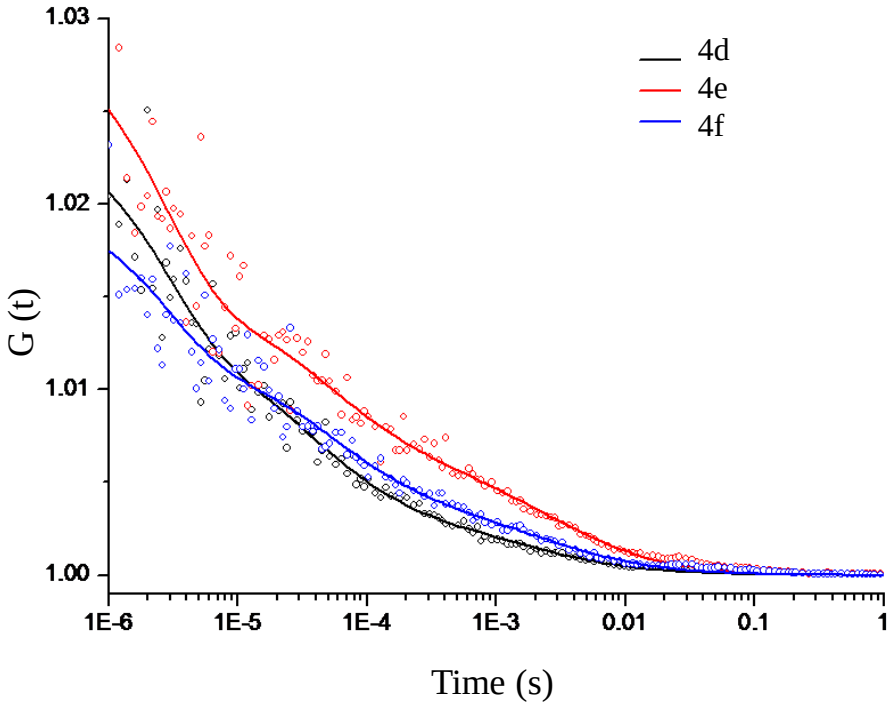

Figure 3.1.6. Determination of diameter of AuNPs coated with dcBSA-PEO(5000)$_{28}$-(TA)$_{26}$ (**4**) by fluorescence correlation spectroscopy (FCS) measurements.

Table 3.1. 3. Calculated sizes of AuNPs **4** at different $HAuCl_4$/TA ratio according to FCS measurements.

AuNPs	R_H [24]	Concentration [μm]
4d	1.5	0.8
4e	1.3	0.6
4f	1.0	0.7

Fluorescence Quantum Yield (FQY, Φ) Calculations. FQY of AuNPs at room temperature have been determined relative to Tris(2,2'-bipyridyl) ruthenium hexahydrate (II) as fluorescent standard and calculated using the following equation.

$$\Phi_f(s) = \Phi_f(r).\{(\int I_s(\bar{\upsilon})d\bar{\upsilon})/(\int I_r(\bar{\upsilon})d\bar{\upsilon})\}.(D_r/D_s).(n_s^2/n_r^2)$$

Indices "s" and "r" denote "sample" and "reference", respectively. The integrals of *I* represent areas of the corrected emission spectra and *D* corresponds to the optical density at

the wavelength of excitation (365 nm). Refractive index of the reference n_r and the sample solutions n_s are the same since the emission have been measured for both reference and sample in water. Different parameters for the calculation of the FQY (**Φ**) of AuNPs (**2f**, **4f** and **6f**) coated with dcHSA-PEO$(5000)_{27}$-$(TA)_{22}$, dcBSA-PEO$(5000)_{28}$-$(TA)_{26}$ and dLY-PEO$(5000)_8$-$(TA)_8$ at $HAuCl_4$: TA=1:5 ratio are listed in **Table 3.1.4**.

Table 3.1.4. Calculation for FQY of AuNPs solution in water.

AuNPs	$\Phi_f(r)$=0.04	$\int I_s(\bar{\upsilon})d\bar{\upsilon}$	$\int I_r(\bar{\upsilon})d\bar{\upsilon}$	D_r	D_s	$\Phi_f(s)$
dHSA-AuNPs (**2f**)	0.04	6159	14775	0.147	0.140	~0.016
dcBSA-AuNPs (**4f**)	0.04	6098	14775	0.147	0.156	~0.018
dLY-AuNPs (**6f**)	0.04	980	14775	0.147	0.130	~0.003

High Stability of AuNPs under various conditions

For bioimaging applications, the colloidal stability and ligand chemistry of AuNPs is very crucial, undisered aggregation, loss of ligand may result in cytotoxicity.[25] Colloidal stability of AuNPs has been investigated via optical spectroscopy in the presence of different cell culture conditions such as (a) phosphate buffer pH 7.4 and 2% glucose solution, (b) effects of excess salt concentration such as 1M NaCl, (c) competition by dithiothreitol (DTT, 0.5 M) since thiol-rich molecules such as glutathione are abundant in the cytoplasm, (d) pH 4 to (e) pH 10 as well as resistance against (f) the protease trypsin (**Figure 3.1.7, 3.1.8, 3.1.9, 3.1.10, 3.1.11, 3.1.12**). Interestingly, the absorption (**Figure 3.1.7**) and emission (**Figure 3.1.8**) spectra of dcBSA-AuNPs (**4a**) and (**4f**), respectively, remained unchanged for all the conditions after incubation for one day. In contrast, dHSA- and dLY-AuNPs revealed a significant decrease of the surface plasmon resonance band in the presence of 0.5 M DTT (**Figure 3.1.9c**) and 0.1 mg/mL trypsin (**Figure 3.1.11f**) respectively. Most likely, the presence of high numbers of primary amino groups of (**4a**) and (**4f**) contributes to the high stablilty of AuNPs due to the electrostatic repulsion between the multiple primary amino groups on the surface of dcBSA-AuNPs (**4**).

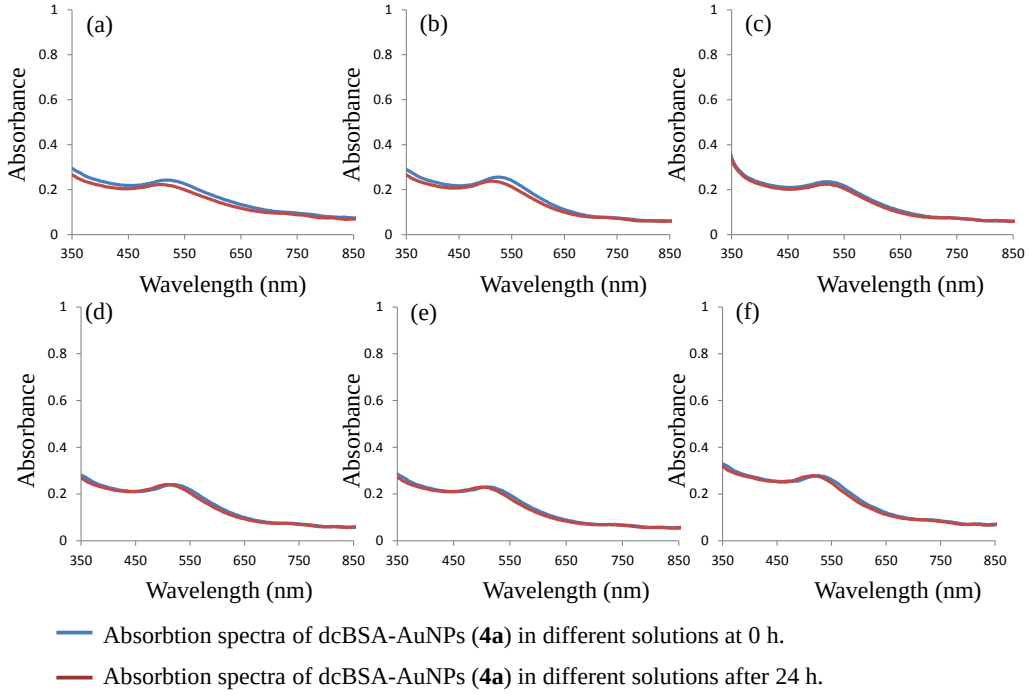

Figure 3.1.7. Absorption spectra of dcBSA-AuNPs (**4a**) in different solutions: (a) 10 mM phosphate buffer pH 7.4 +2% glucose solution. (b) 1M NaCl. (c) 0.5M DTT. (d) pH 4. (e) pH 10.(f) 0.1 mg/mL Trypsin solution. After 24 h the absorption intensity of the AuNPs remained almost unchanged and no precipitation of the AuNPs have been observed.

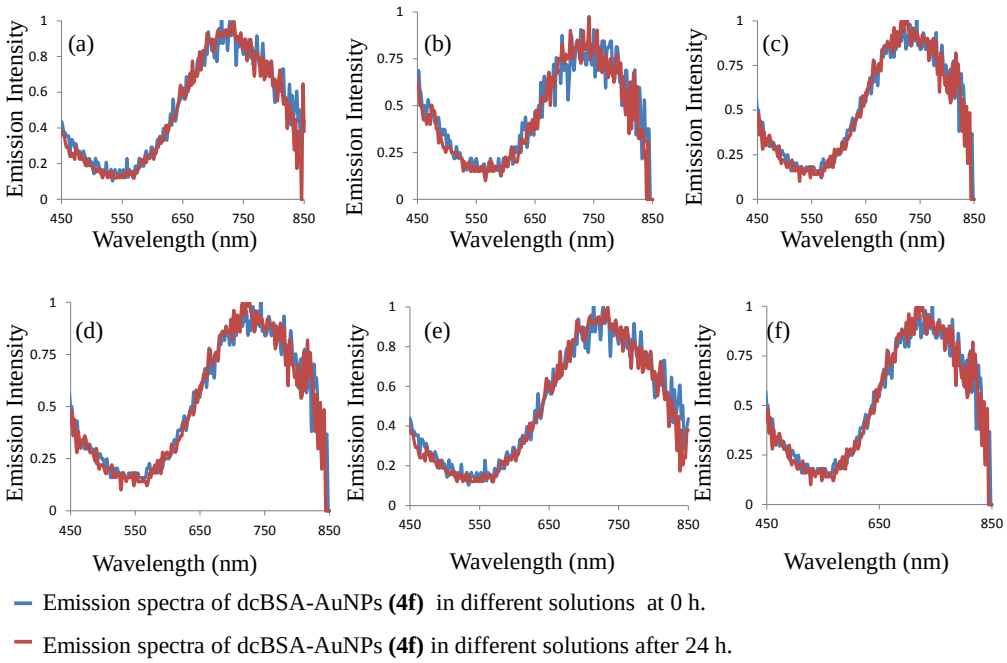

Figure 3.1.8. Emission spectra of dcBSA-AuNPs (**4f**) in different solutions: (a) 10mM Phosphate buffer pH 7.4 +2% glucose solution. (b) 1M NaCl. (c) 0.5M DTT. (d) pH 4. (e) pH 10. (f) 0.1 mg/mL trypsin. Excitation wavelength of 365 nm was chosen. Even after 24 h, the emission intensity of the AuNPs remained almost unchanged and no precipitation observed.

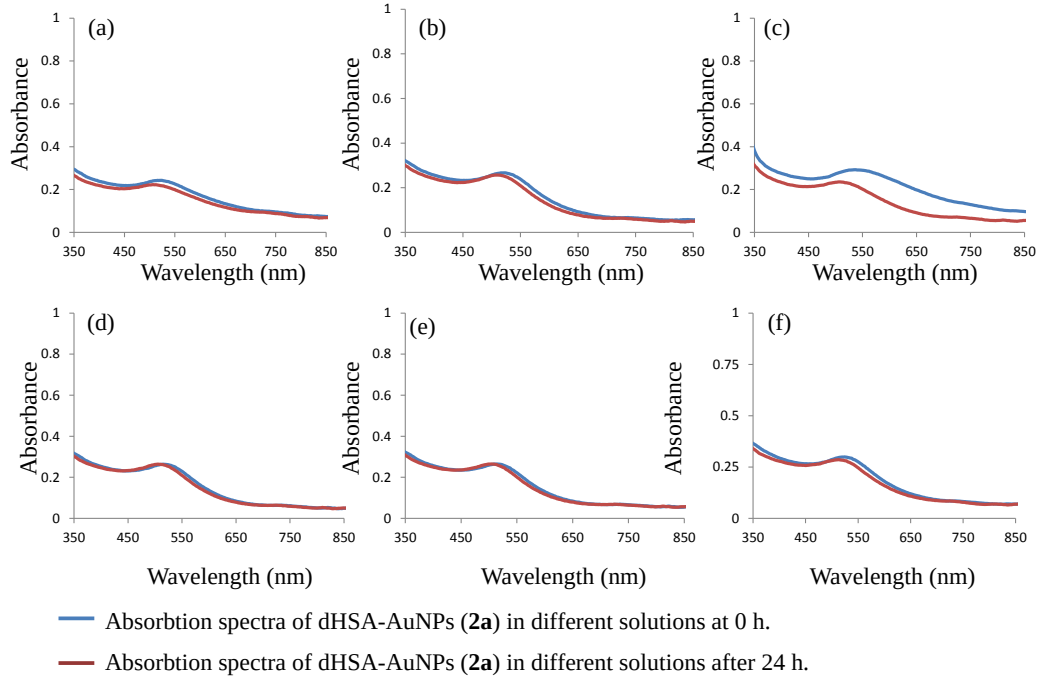

Figure 3.1.9. Absorption spectra of dHSA-AuNPs (**2a**) in different solutions: (a) 10 mM phosphate buffer pH 7.4 +2% glucose solution. (b) 1M NaCl. (c) 0.5M DTT. (d) pH 4. (e) pH 10.(f) 0.1 mg/mL trypsin solution. Even after 24 h, the absorption intensity of the AuNPs remained almost unchanged except in the presence of DTT (c). dHSA-AuNPs (**2a**) show a significant decrease in surface plasmon resonance band in DTT solution, which indicates the particle are unstable in DTT solution.

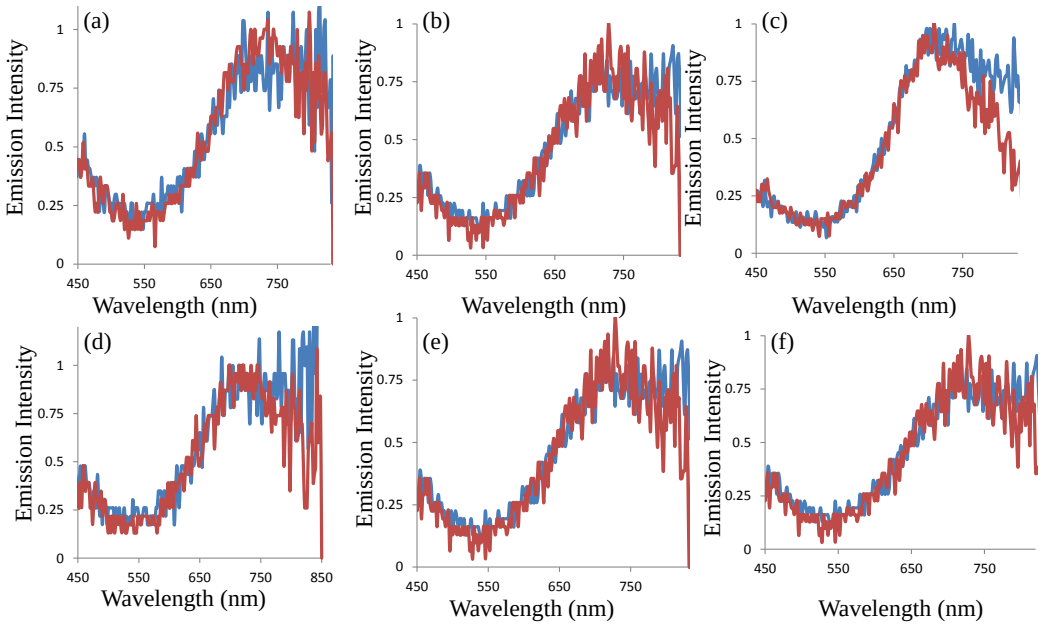

Figure 3.1.10. Emission spectra of dHSA-AuNPs (**2f**) in different solutions. (a) 10 mM phosphate buffer pH 7.4 +2% glucose solution. (b) 1M NaCl. (c) 0.5 M DTT. (d) pH 4. (e) pH 10.(f) 0.1 mg/mL trypsin solution. Excitation wavelength 365 nm. After 24 h the emission intensity of the AuNPs remained almost unchanged and no precipitation of AuNPs have been observed.

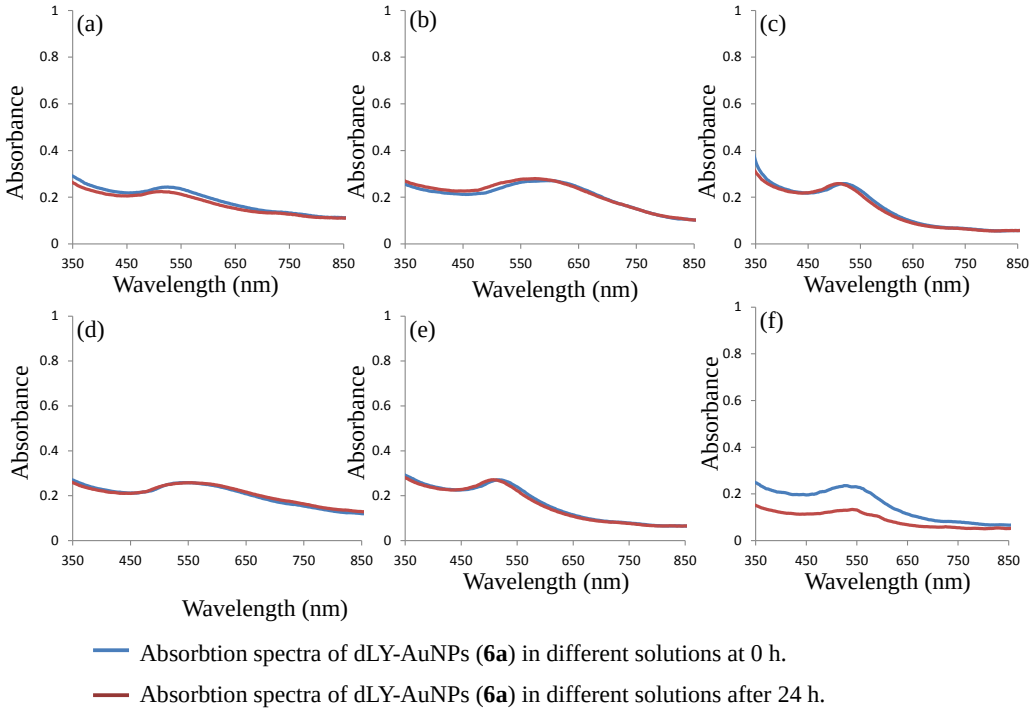

Figure 3.1.11. Absorption spectra of dLY-AuNPs (**6a**) in different solutions: (a) 10 mM Phosphate buffer pH 7.4 +2% glucose solution. (b) 1M NaCl. (c) 0.5M DTT. (d) pH 4. (e) pH 10.(f) 0.1 mg/mL trypsin solution. After 24 h, the absorbance intensity of the AuNPs remained almost unchanged except in the presence of trypsin (f). In trypsin solution, there is a significant decrease of the surface plasmon band, indicating proteolytic instability of dLY-AuNPs (**6a**).

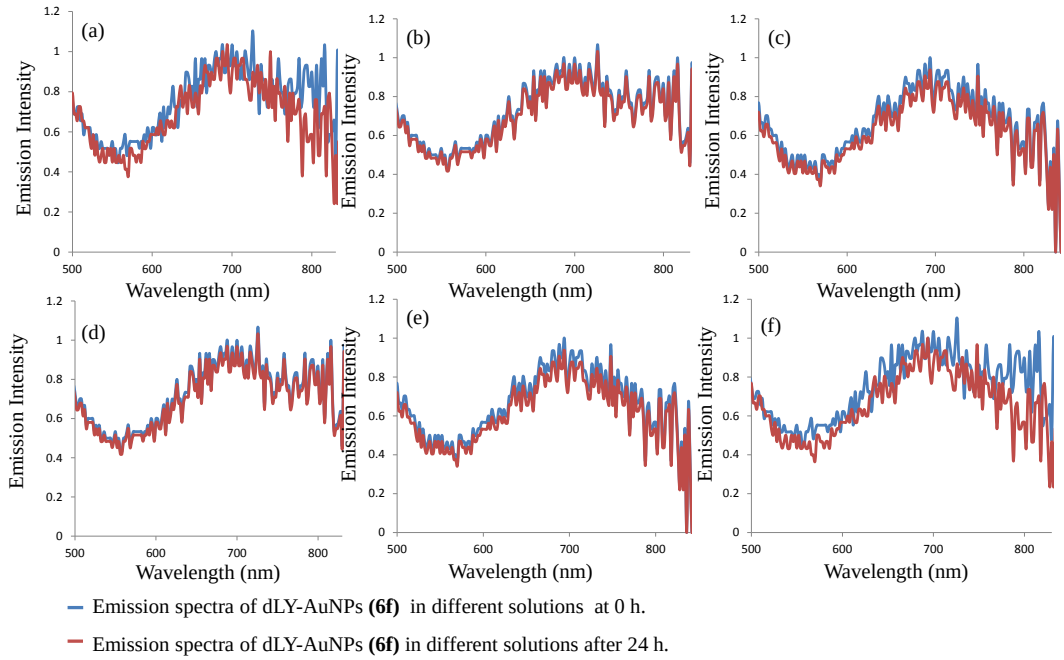

Figure 3.1.12. Stability test of AuNPs (**6f**) coated with dLY-PEO(5000)$_8$-(TA)$_8$ in different solutions. (a) 10 mM phosphate buffer pH 7.4 +2% glucose solution. (b) 1M NaCl. (c) 0.5 M DTT. (d) pH 4. (e) pH 10.(f) 0.1 mg/mL trypsin solution. Excitation wavelength 365 nm. After 24 h the emission intensity of the AuNPs remained almost unchanged and no precipitation of AuNPs have been observed.

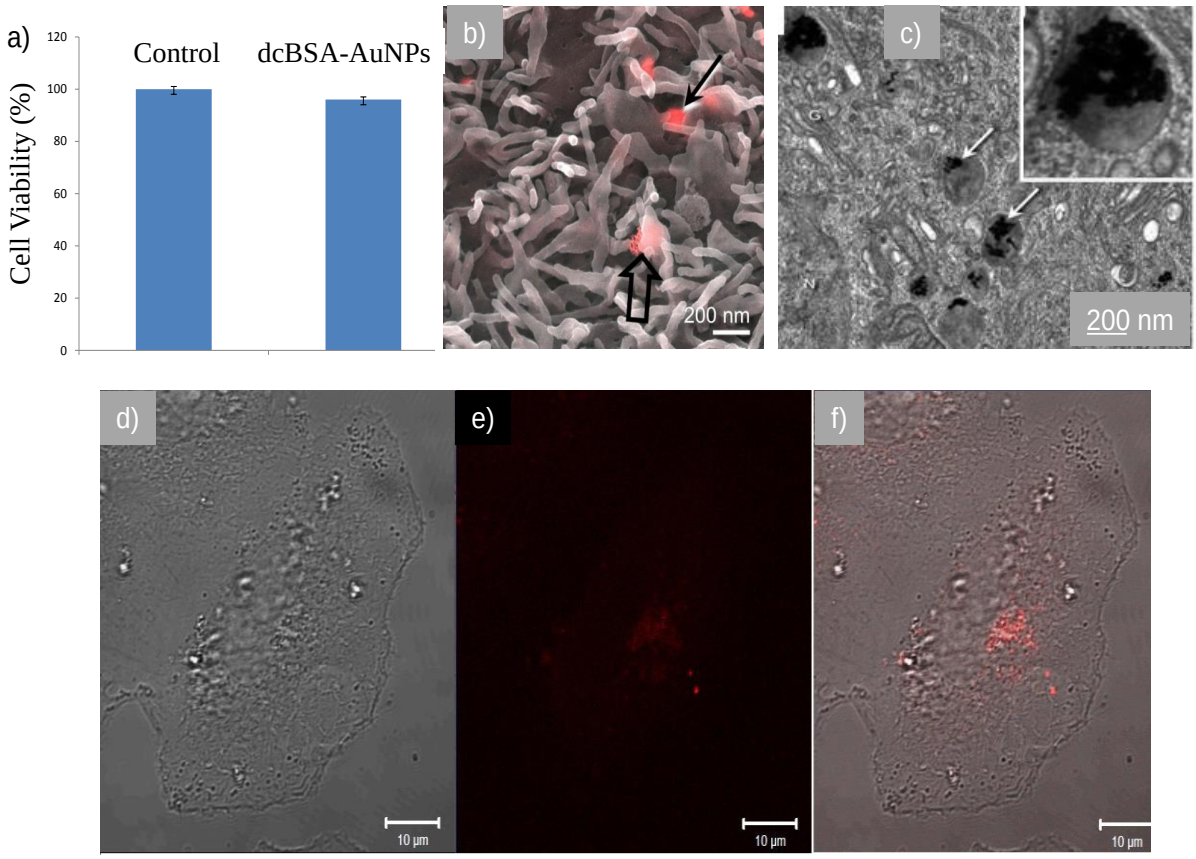

Figure 3.1.13. a) Viability of A549 cells after 24 h of incubation with 50 µL of 1 µM dcBSA-AuNPs (**4f**) in cell medium as determined by a Cell-Titer Glo (Promega) cell viability assay. The error bars represent variations among three independent measurements. 96% cells are still viable after 24 h of incubation with dcBSA-AuNPs. b) Imaging of dcBSA-AuNPs (**4a**) on the surface of A549 cells by the Scanning Electron Microscope**.** The surface is covered with many microvilli. Clusters of gold nanoparticles can be imaged with the material dependent backscattered electron signal that is overlaid in red onto the (black and white) secondary electron signal. Some gold aggregates are sharply imaged (white arrow), which indicates that they are still on the cell surface. Some gold aggregates are blurred (black arrow), which indicates that they are already incorporated into the cell. The blurring is caused by the widening of the primary beam as an effect of beam specimen interaction. The framed arrow depicts a gold aggregate that is imaged sharp at the left hand side and blurred at the right hand side since it is, there, covered by a cell protrusion. c) Thin section of 50 µL of 1 µM AuNPs (**4a**) incubated A549 cells after incubation for 24 h imaged in the transmission electron microscope. Clusters of gold particles (arrows) can be easily seen in the cytoplasm, but not in the nucleus (N). They are usually found in vesicles. (G: Golgi apparatus, M: Mitochondrion). d) Confocal images of A549 cells incubated with 50 µL of 1 µM AuNPs (**4f**) incubated for 24 h. NIR fluorescent gold nanoparticle is visible in perinucleur region. DIC image (e) fluorescence channel and (f) overlay. Images were acquired on a confocal microscope equipped with fluorophore-appropriate filter sets and an environmental chamber in which cells remained at 37 °C + CO_2 throughout imaging.

***In vitro* characterization of AuNPs**

All dcBSA-AuNPs (**4**) revealed no significant cytotoxicity in a cell viability assay at relevant concentrations (**Figure 3.1.13a**) and 96% viable cells were found after 24h incubation time. Cell uptake of (**4a**) into A549 cells was investigated by TEM based on cryo-preparation as well as fluorescence microscopy. Only dcBSA-AuNPs (**4a**) were selected for cryo-TEM since detection of ultra-small AuNPs **4f** with dimensions of about 1 nm is very challenging compared with slightly larger AuNPs. After incubation of the cells with (**4a**) for 24 h, a thin section of the cells was imaged and clusters of AuNPs (arrows) were found in vesicles, in the cytoplasm (**Figure 3.1.13c**), but not in the nucleus. These particles have mainly been localized in vesicles but also free AuNPs have been found. The subcellular localization in the perinuclear region as well as trafficking of dcBSA-AuNPs (**4a**) in vesicles reveals remarkable similarities with the precursor protein cBSA-147[26] which has also been found in vesicles and released in the periplasm.[26] Ultra-small fluorescent AuNPs (**4f)** have been detected by confocal laser scanning microscopy (CLSM) inside the cell (**Figure 3.1.13d, e, f**). Most likely, the high uptake efficiency of (**4f**) facilitated their direct recognition due to high numbers of AuNPs present inside the cells. Here, direct detection of the emission of **4f** inside cells has been successful and without the requirement of additional charomophores.

3.1.3. Conclusions

In summary, multifunctional, highly stable and nontoxic AuNPs of tunable sizes from 1-15 nm have been prepared that are attractive for bioimaging applications. Different polypeptide copolymer coatings with multiple TA anchor groups have been applied; very long albumin-derived polypeptides are more efficient stabilizing extremely small, sub nanometer AuNPs. Such AuNPs have been characterized by HRTEM, AFM and FCS and a well-detectable NIR emission. In particular, dcBSA-AuNPs coated with polypeptides bearing high numbers of primary amino groups such as **4a** and **4f** revealed very high stabilities at high ion strength, extreme pH, in the presence of thiol-containing ligands or in the presence of proteases, thus making them very attractive for cellular studies. Significant cellular uptake and intracellular localization of the larger dcBSA-AuNPs (**4a**) and ultra-small dcBSA-AuNPs (**4f**) have been detected by cryo-TEM and fluorescence microscopy, respectively. As an additional feature, the presence of multiple grafted PEO chains located at the AuNP surface might contribute to reduced immunogenicity as well as non-specific adsorption thus rendering these dcBSA-

AuNPs very attractive for *in vitro* and *in vivo* applications. Noteworthy, the side chains of amino acids in the polypeptide backbone, such as primary amine from lysine, carboxylic groups from aspartic and glutamic acids, hydroxyl groups of serine, tyrosine and guanidine group of arginine offers the possibility of further functionalization of AuNPs with additional bioactive molecules. These tailored highly stable multifunctional NIR emitting nanoparticles will find wide applications in biosensing, diagnostic and other biomedical applications.

3.2. Translocation of Near InfraRed (NIR) emitting Gold Nanoparticles into the Cell Nucleus

3.2.1. Introduction

In eukaryotic cells the nucleus is an organelle that contains the cell's genetic material. The function of the nucleus is to maintain the integrity of genes and to control the activities of the cell by regulating gene expression. In living cells, a double-membrane nuclear envelope separates the cytoplasm from the cell nucleus. The nuclear envelope comprises two lipid bilayers: the outer and inner nuclear membranes.[27] Its outer nuclear membrane is continuous with the endoplasmic reticulum, whereas the inner nuclear membrane contains a unique set of proteins, some of which interact with chromatin.[26] These membranes are separated by a lumen and joined at nuclear pore complexes (NPCs).[28] These nuclear envelope is highly impermeable to most kinds of probes, except through these nuclear pores. The nuclear pore is composed of proteins called nucleoporins (NUPs). Proteomic analyses of the mammalian NPC have estimated 30–50 NUPs.[29,30] The nuclear pore consists of an eightfold symmetric central scaffold, eight cytoplasmic filaments and a nuclear basket.[29,31,32] These pores serve as a gate for the trafficking of proteins and RNAs between the nucleus and cytoplasm.[33-39] Human immunodeficiency virus 1 (HIV-1) and other retroviruses deliver a DNA copy of their genome into the host cell's nucleus through the nuclear pore by active cellular transport mechanisms. They carry karyophilic signals that direct transport across the intact nuclear envelope through NPCs.[40] Karyophilic signals or peptide regions from viruses that show nuclear translocation activity are termed as Nucleus Localisation Signal (NLS). Classical NLSs are characterised by short stretches of basic amino acids. Although different examples of classical NLS sequences exist, the best understood are those that resemble the SV40 large tumour antigen (T-ag), which comprises a single stretch of basic amino acids (PKKKRKV^{132}) [41,42] and the NLS of the Xenopus protein nucleoplasmin (KRPAATKKAGQAKKKK^{170}), which consist of two distinct stretches of basic amino acids separated by a spacer of 10–12

residues.[43] A third, less defined class of NLS consist of charged/polar residues interspersed with non-polar residues, resembling the yeast homeodomain containing protein, MATα2 (NKIPIKDLLNPQ[13] and VRILESWFAKNI[159])[44,45]. Each of these classes are typically recognised by the so-called NLS receptor.[46] This NLS receptor comprises two cytosolic proteins: importin-α (also called α - karyopherin/srp1/NPI1) and importin-β (or β-karyopherin).[47-53] NLS binds to importin-α, which binds to importin-β, which in turn docks the complex to the nuclear pore by binding directly to nucleoporins.[54-56] Then the complex is translocated through the nuclear pore by an energy dependent process involving the small soluble GTPase Ran/TC4[57,58] and p10 (also called NTF2/pp15).[59,60] The RanGTP/GDP gradient across the nuclear envelope promotes the direction of transport. The RanGTPase and its regulators control the rate at which cargo is moved in and out of the nuclear pore, as well as the loading and unloading of cargoes.[38]

The detection of cell nucleus with specific stains is key to nucleus imaging. Nucleus stains can be used as counterstains to help identify the location of specific proteins and targets of interest within the nucleus while detection of antibodies against proteins associated with nucleus can lead to a better understanding of cell nucleus function. It is therefore desirable to design a molecular probe that can help to study non-invasively, the structure, activities and dynamics of the nucleus for longer period of time. As described in the first part (3.1) of this chapter, that the noble metal nanoparticles, particularly gold nanoparticles are very promising for optical imaging and labeling of biological systems due to their non-toxicity, photostability and size dependent optical properties.[61] AuNPs can easily be synthesized routinely in sizes varying from 0.8 to 200 nm and modified with small molecules, peptides, proteins, DNA, and polymers.[62] There are several studies that demonstrate nuclear targeting of peptide functionalized non-fluorescent AuNPs and the AuNPs were imaged by a number of techniques, such as electron microscopy,[63-65] surface-enhanced Raman scattering (SERS),[66] video-enhanced color (VEC) microscopy and differential interference contrast microscopy (DIC)[62,67]. Confocal microscopy has also been used to visualize nuclear trajectories of dye labeled non-fluorescent AuNPs.[68-70] Other studies have also demonstrated the successful entry of NLS AuNPs into the nucleus after their microinjection directly into the cytoplasm.[71,72] However, in those studies the NPs were injected directly into the cytoplasm near the nucleus, thus bypassing cellular membrane entry and endosomal/lysosomal pathways. Recently, nuclear-targeted AuNPs used to distinguish between progenitor and differentiated cell types by surface enhanced Raman spectroscopy (SERS).[73]

Fluorescence based imaging presents a comparatively simple, non-invasive biophysical approach to study the cell organelles, such as nuclei. Fluorescent organic dyes are widely employed in cell life cycle analysis and flow cytometry and as nuclear counterstains in fluorescence microscopy.[74] Despite great advancement in nanotechnology, only few fluorescent nuclear targeting nanoprobes are known.[75-77] In this section, the preparation of nucleus targeting of ultrasmall NIR emitting fluorescent AuNPs have been described. The nuclear translocation of the NIR fluorescent AuNPs to nucleus from outside intact cells has been observed by confocal laser scanning microscopy (CLSM).

3.2.2. Result and Disscussion

Preparation of NIR emitting Nucleaus Targeting AuNPs

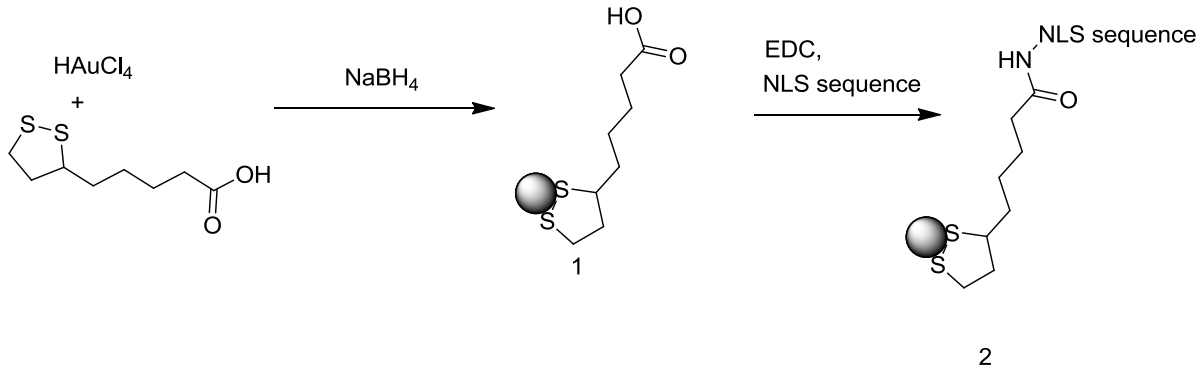

Scheme 3.2.1. Scheme of preparation of NLS sequence labeled NIR emitting fluorescent AuNPs.

Even though macromolecules and supramolecular complexes are frequently required to enter and exit the nucleus during normal cell function, but access is restricted and exchange to and from the nucleus is tightly controlled.[78] The restricted access to nucleus makes the design and preparation of the fluorescent AuNPs targeting cell nucleus, a challenging task. To prepare AuNPs for nuclear targeting mainly three types of designed were followed. Firstly, pre-stabilized non-fluorescent AuNPs were directly conjugated with targeting peptide[63] or amine containing PEG[68] or with BSA-peptide conjugates[62,67] and streptavidin-peptide conjugates[79] for active nuclear targeting. Secondly, citrate or alkylamine stabilized AuNPs were functionalized with mono-thiol modified nuclear targeting peptide or ligand via gold and thiol chemistry.[64,73] Thirdly, BSA directed synthesis of AuNPs and followed by conjugation with nuclear targeting antibody, such as Herceptin.[64]

Initially, In my design of nuclear targeting AuNPs, I functionalized the NIR emitting dcBSA-(PEO)5000_{28}-$(TA)_{26}$ coated AuNPs (described in section 3.1) with NLS peptide. The

NLS peptides were attached to the protein backbone. But unfortunately, NLS peptide functionalized dcBSA-PEO$(5000)_{28}$-$(TA)_{26}$ AuNPs donot enter the nucleus, it was found in perinuclear region. Most probably the presence of high number of long PEO5000 on the protein backbone prevents the interaction between the NLS peptide and NLS receptors (importin-α and importin-β). The failure of NLS functionalized dcBSA-AuNPs to translocate into nucleus underscores the importance of the design of AuNPs for effective nuclear targeting. To reach nucleus any probe must satisfy minimally the following requirements: it must (i) enter the cell, via receptor-mediated endocytosis; (ii) escape endosomal/lysosomal pathways; (iii) possess a nuclear localization signal (NLS) to interact with the NLS receptors, (importin-α and importin-β); and (iv) be small enough (<30 nm) to cross the nuclear membrane.

In my modified design (**Scheme 3.2.1.**) of nuclear targeting NIR fluorescent AuNPs, I decided to first prepare NIR fluorescent AuNPs stabilized by thioctic acid (TA) and followed by conjugation of NLS peptide. TA has several inherent advantages in stabilizing NIR fluorescent AuNPs. Fluorescent AuNPs smaller than 2 nm have larger surface curvature compared to larger nanoparticles. Larger surface curvature reduces the protecting ligands packing density. For stabilization of smaller AuNPs a higher coordination number ligand is clearly beneficial.[80] TA has two closely spaced sulfur groups (constrained by the five-membered ring structure), which provide better coordination to the NP surface compared to monothiol-terminated ligands. Peptides and biomolecules can be conjugated to the AuNPs using the reactivity of the free carboxyl group of the TA. Thioctic acid (TA) protected NIR emitting fluorescent AuNPs (**1**) have readily been synthesized by reducing both TA and the gold salt with $NaBH_4$ in aqueous solution following the similar procedure reported previously.[81] Mixing $HAuCl_4$ with TA in basic solution led to a gradual light yellow coloured solution, indicating the formation of Au(I) complexes due to the interaction of gold ions with the disulfides of TA.[82] Upon adding the reductant $NaBH_4$, the colourless solution slowly turned pale brown. It is very important to control the molar ratio of TA to Au as well as the amount of $NaBH_4$ during the reaction to obtain brightly luminescent AuNPs. Au(I)–thiol complexes have also been suggested for the luminescence of AuNPs due to ligand–metal charge transfer and Au(I)–Au(I) interactions.[81-85] Usually 10 times more $NaBH_4$ was used to assure complete reduction of Au^{3+} to Au^0.

The nanoparticles were purified by dialysis and characterized by UV/vis and fluorescence spectroscopy, DLS, zeta potential. The absence of surface plasmon band around 520 nm indicates that the AuNPs are smaller than 2 nm (**Figure 3.2.1 (a)** blue line). Unlike large Au

nanoparticles, ultrasmall AuNPs exhibit a strong fluorescence with emission maxima centered on 680 nm in the near-infrared region in aqueous solution upon excitation at 365 nm (**Figure 3.2.1 (b),** blue line) and the fluorescence arises from mixed intraband (sp to sp) and interband (d to sp) transitions as explained in chapter 1 (section 1.3.2) .[86] The emission maxima of these AuNPs are independent of the excitation wavelength and can be excited by a wide range of wavelengths below 600 nm. The quantum yield of AuNPs 1 and 2 was measured in aqueous solution (pH 9.0) and was determined as 0.7% and 0.76% using Rhodamine B (QY = 0.95 in ethanol) as a reference. Probably, high number of electron donating amino groups present in NLS peptide increases the QY of the NLS conjugated AuNPs. The increase in quantum yield upon conjugation with NLS demonstrates the fact that the ligand plays an important role for the luminescence efficiency of AuNPs.[87]

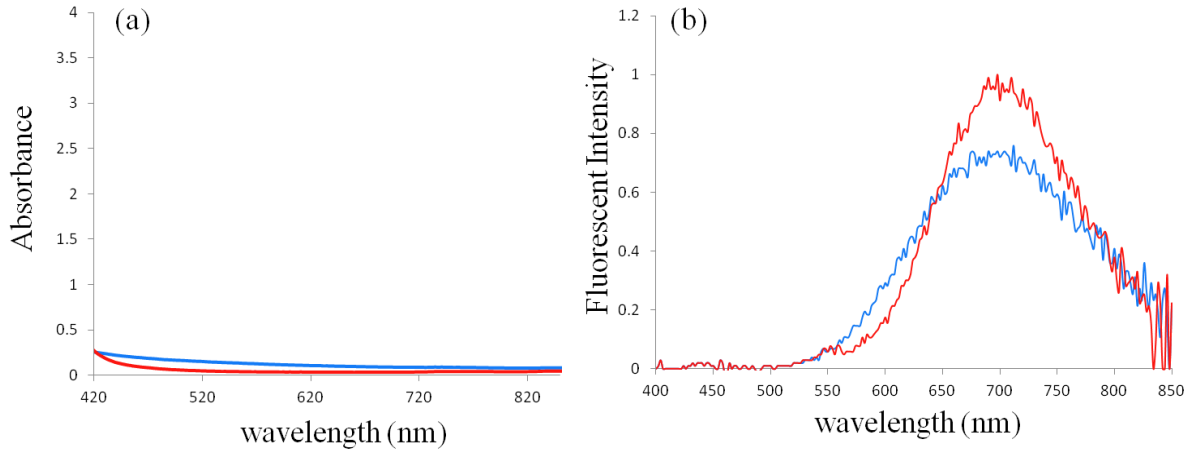

Figure 3.2.1. (a) Absorbance (b) fluorescence of AuNPs. Blue –TA coated AuNPs and red is TA coated AuNPs conjugated with NLS.

The functionalization of TA-AuNPs with the NLS peptide (PKKKRKVEDPYC) has been carried out via EDC coupling using the reactivity of the free carboxyl group of the thioctic acid (**Scheme 3.2.1**). EDC reacts with the carboxyl group on the modified nanoparticles, forming an amine-reactive O-acylisourea intermediate. This intermediate reacts with an amine on the peptide, yielding a conjugate of the two molecules joined by a stable amide bond. After the conjugation reaction, the AuNP-NLS conjugate has been purified by dialysis.

The purified nanoparticles have been analyzed by UV/VIS, fluorescence spectroscopy, X-ray photo electron spectroscopy (XPS), dynamic light scattering (DLS) and zeta potential.

Dynamic light scattering measurement (DLS)

Dynamic light scattering (DLS) has been used to determine the hydrodynamic diameters of the AuNPs. To test if the conjugation of NLS to the TA-AuNPs have any deleterious effects on the AuNPs stability, the nanoparticles were examined by dynamic light scattering (DLS) before and after conjugation with NLS peptide. The DLS experiment results are shown in **Figure 3.2.2a** and **3.2.2b**. The average hydrodynamic diameter measured for the TA-AuNP-NLS (**2**) is 2.2±0.1 nm (**Figure 3.2.2b**) compared to that for the TA-AuNP (**1**) 1.69±0.1 nm (**Figure 3.2.2a**). The increase in the hydrodynamic diameters after the conjugation of the NLS peptide with TA-AuNPs (**1**) indicates the contribution of NLS peptide to the hydrodynamic diameter. The TA-NLS ligand has a larger lateral extension and results in a slightly larger contribution compared to the thioctic acid functions. The functionalization with NLS contributed to the increase in the diameter of the AuNPs.

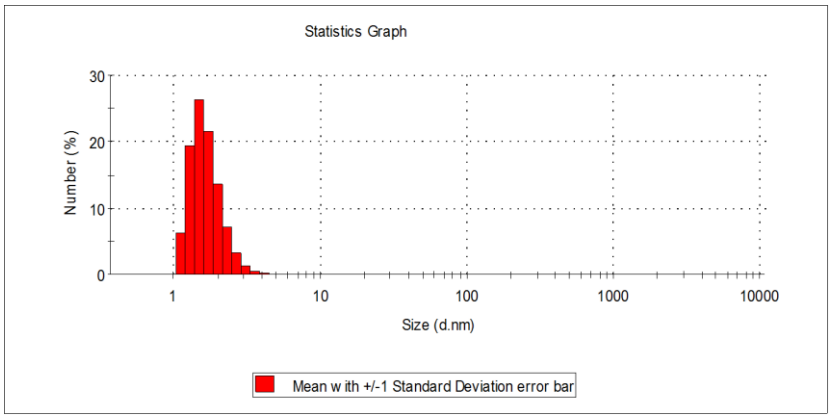

Figure 3.2.2a. DLS size distribution of TA-AuNPs (**1**).

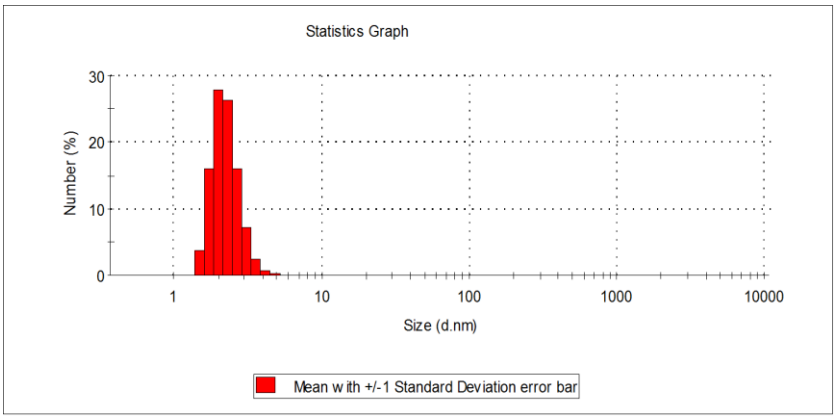

Figure 3.2.2b. DLS size distribution of TA-AuNP-NLS (**2**).

Zeta potential measurement

Zeta potential is an important parameter related to the stability of nanoparticles. A relatively high surface charge may present a repelling force between the particles and then increase the stability of the solution.[88] The zeta potential of the TA–AuNPs (**1**) in 1 mM KCl solution (pH 7.4) was –36.8 ± 2.8 mV. The negative zeta potential is expected because of the carboxylic group of thioctic acid present on the surface of AuNPs. After conjugation with NLS the zeta potential changes drastically to 11.3±1.7 mV. The positive zeta potential of the AuNPs was attributed to the presence of ionized amino groups on the NLS peptide. It is known that the surface of a cell membrane is negatively charged. These positively charged nanoparticles should interact with cells and should in principle be effectively internalized as discussed later.

X-Ray Photoelectron Spectroscopy (XPS) measurement

A survey scan X-ray photoelectron spectroscopy has been carried out to determine all the elements present in TA-AuNPs (**1**) and TA-AuNPs conjugated to NLS (**2**). The peaks of interest in the XPS survey spectra of TA-AuNPs (**1**) (**Figure 3.2.3a**) are the C1s peak at a binding energy of 284.6 eV, the Au 4f peak at 83 eV, the sulpur 2p at 162 eV and the oxygen 1s at 530 eV. It is noteworthy, that there is no nitrogen peak. XPS spectra for NLS conjugated AuNPs (**Figure 3.2.3b**), in addition to C, O, S, Au peak, show a N1s peak at 400 eV which relates to the NLS peptide. The presence of the N peak confirms the successful coupling of NLS to TA-AuNPs.

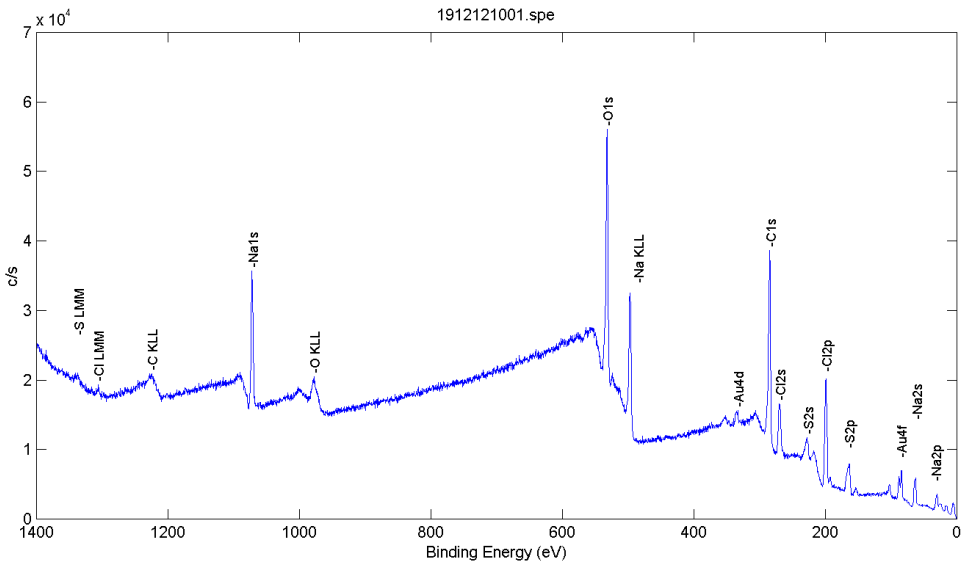

Figure 3.2.3a. XPS spectra of TA-AuNPs (**1**).

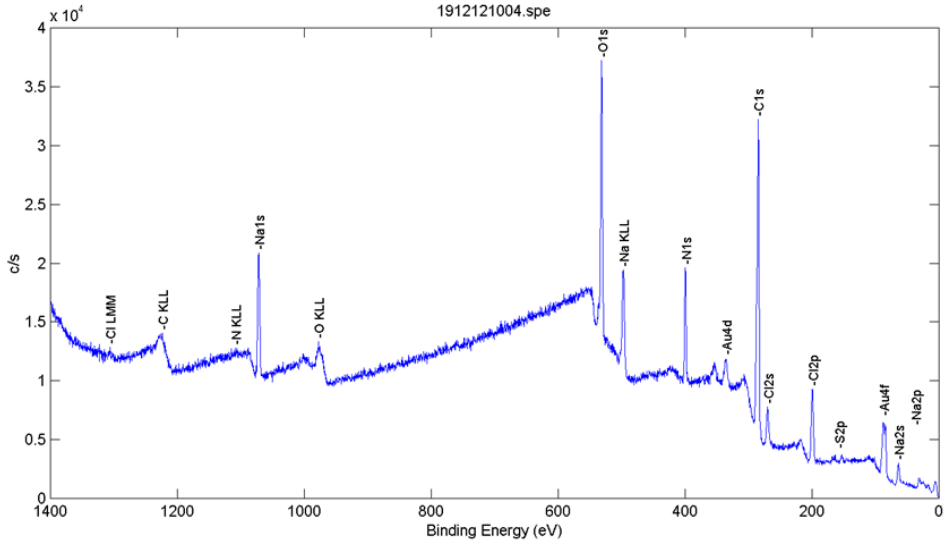

Figure 3.2.3b. XPS spectra of TA-AuNPs conjugated to NLS (**2**).

Bioimaging of NLS conjugated AuNPs in living A549 cells

The nuclear targeting of NLS conjugated AuNPs (**2**) has been investigated after incubation with A549 cells. A549 cells have been exposed to **2** and the fluorescence images of AuNPs labelled cells have been recorded after 24h incubation. NIR light emitting AuNPs have been found internalized by the cells. The confocal images showed that AuNPs have been localized in the cytoplasm as well as in the nuclei of the cells (**Figure 3.2.4**). The emitted fluorescence signals of AuNPs and 4′, 6-diamino-2-phenylindole (DAPI) have been separately collected, and the subcellular localization of AuNPs has been determined by overlapping the fluorescence images of AuNPs with DAPI. A clear pattern of nuclear colocalization of AuNPs and DAPI, as judged from the overlapping of the fluorescent signals of AuNPs (red) (**Figure 3.2.4a**) and the nuclear dye DAPI (blue) (**Figure 3.2.4c**), have been observed (**Figure 3.2.4d**). This transport involves peptidic nuclear localisation signals (NLSs) or import signals that bind to nuclear transport proteins (namely the karyopherins), which mediate their movement in or out of the nucleus. The role of the NLS in nuclear localisation was investigated by using a fluorescent TA AuNPs (**1**) without any NLS peptide. The TA AuNPs (**1**) was unable to reach the nucleus and it was localised in the cytoplasm as reported earlier[14]. The result implies that the NLS amino acid sequence is essential for nuclear distribution of AuNPs and occurs by active karyophilic method not by diffusion through nuclear membrane.

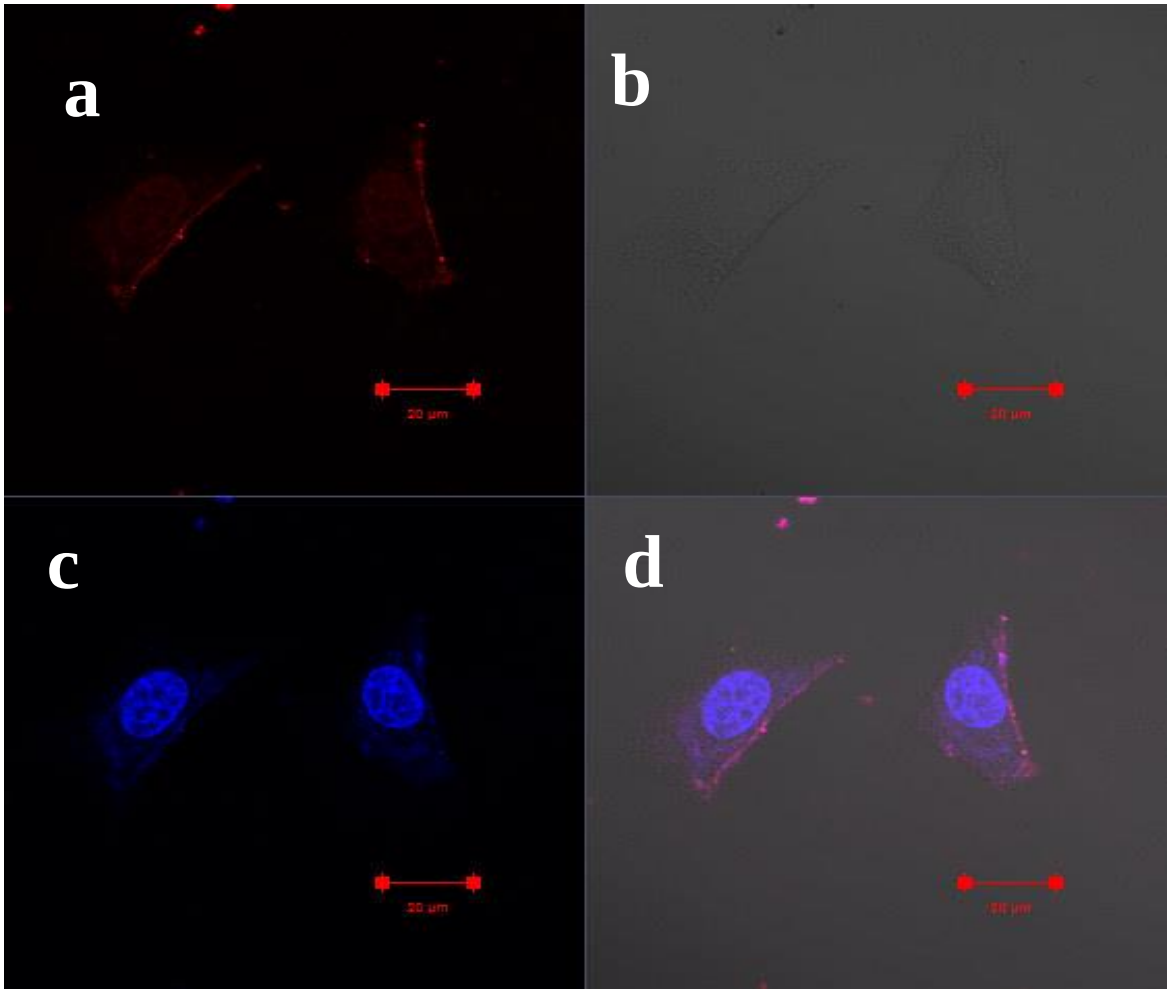

Figure 3.2.4: Confocal microscopy images of A549 cells incubated with AuNPs **2**. a) Red represents data acquired by the gold channel. (b) DIC image. (c) Blue represents data acquired by the DAPI channel. (d) Overlay. Image scanned using simultaneous scanning.

Z-stack Confocal Microscopy Experiemnt

It can also happen that the AuNPs are just sticking to the top of nucleus nonspecifically and not exactly inside the nucleus. To obtain a precise view of AuNPs localization in intact cells, z-stack confocal imaging in live cells was performed. Laser scanning confocal microscopy collects light from a single focal plane. It scans the specimen point-by-point, line by line and assembles the pixel information into a single image. By moving the focal plane in axial (z) dimension, single images can be put together. In our case, the optical sections through A549 cells in axial (z) dimension were spaced by 0.74 μm. A typical *z* stack experiment of A549 cells treated with AuNPs and DAPI is reported in **Figure 3.2.5**. **Figure 3.2.5a** shows the emission from AuNPs channel and **Figure 3.2.5b** shows emission from DAPI channel. The fluorescence of AuNPs were maximal during the images 5-8 confocal slices, which corresponded to the region inside the cell, and well colocalised with the DAPI-stained

nucleus, which also had the strongest intensity in the images 5-8 confocal slices of the confocal z stacks. The images depicted in **Figure 3.2.5a** and **3.2.5b**, clearly establish that AuNPs (**2**) are predominantly localized inside the nucleus.

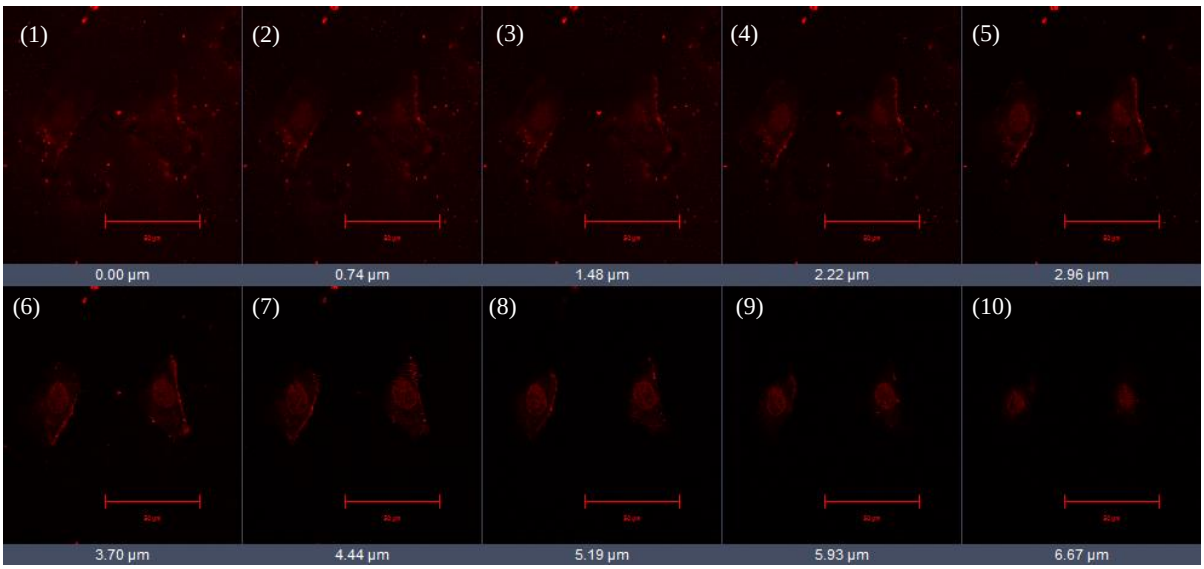

Figure 3.2.5a. *z*-stack imaging data of AuNPs channel of A549 cells, incubated with AuNPs **2**. Scale bar 50 µm.

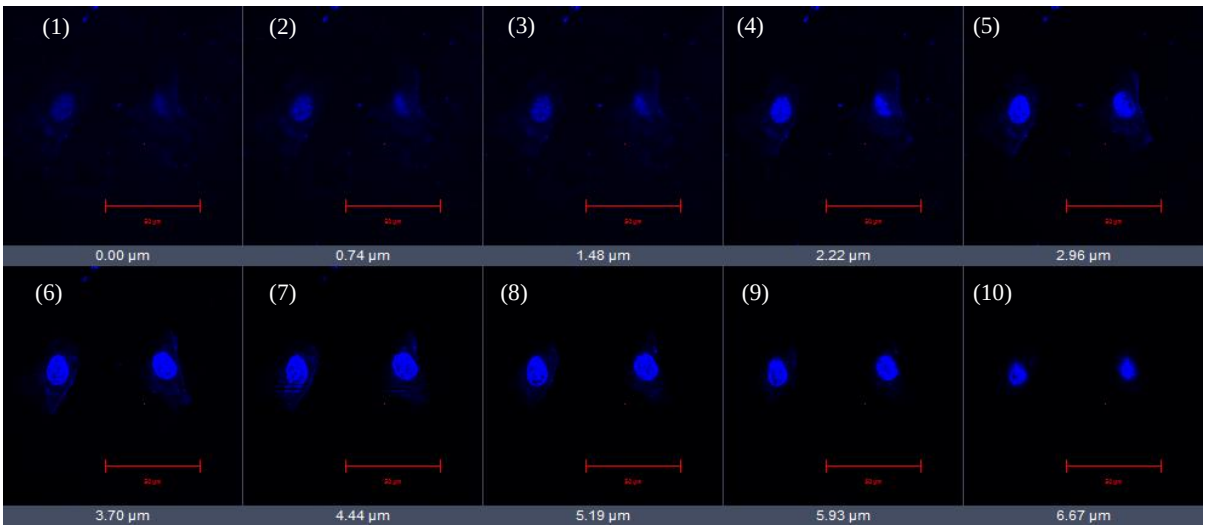

Figure 3.2.5b. z-stack imaging data of DAPI channel of A549 cells, incubated with AuNPs **2**. Scale bar 50 µm.

Conclusions

In summary, ultra-small NIR-emitting NLS peptide conjugated AuNPs were constructed in a two-step facile synthesis that allow targeting cell nuclei. For translocation of nanoparticles into nucleus, the sizes of the AuNPs are a critical factor. The ultra-small (~2 nm) AuNPs

conjugated with the NLS peptide in this study have been proved to be suitable for transport across the nuclear membrane. The presence of NLS peptide facilitates the active nuclear entry of AuNPs through the nuclear pore complexes. The fluorescent AuNPs described here may help to overcome the limitations of traditional nuclear targeting probes and offer several advantages. First, fluorescent AuNPs are inherently photostable, which will allow imaging of nucleus for longer period of time. Second, unlike traditional nuclear probes which have UV or visible emission,[74] the emission of AuNPs described here, is in NIR wavelength, which may be helpful for avoiding autofluorescence and offer the possibility for deep tissue molecular imaging of the nuclear components *in vivo*. Third, the AuNPs have emission maxima at 680 nm with excitation wavelength 365 nm. The large Stokes shift, will prevent the crosstalk between the excitation light and the emitting, which is a problem specially incase of multichannel imaging[89]. Fourth, the design of fluorescent AuNPs requires only one type of peptide unlike others where multiple peptides are needed.[67] Fifth, the studies of nuclear uptake of AuNPs demonstrated here are entirely in live intact cells, unlike other where non-invasive method, such as microinjection, cell permeation or fixation of cells is needed.[71,72,90] The study in live cell also prevents false results which may arise from artificial redistribution of nanoparticles upon fixation. [91]

The nucleus is also the desired target for cancer therapies that involve DNA-drug interactions, genes, short interfering RNA, and antisense strategies that target RNA splicing.[62] These therapeutic agents are often prevented from reaching the cell nucleus because P-glycoproteins pump them out of the cell.[92] It has also been shown that delivery of drugs; antibody directly to nucleus enhances its efficacy significantly.[77,93] Fluorescent AuNPs described here that cross cell and nuclear membrane barriers efficiently and are unaffected by cellular pumping mechanisms, could aid to the enhancement of the efficacy of the therapeutics. The fluorescent AuNPs may help to map drug-loaded nanoparticles and the release of drug, revealing a varying nuclear diffusion pattern of the chemotherapeutics in drug-sensitive and –resistant cells in a live dynamic cellular environment. Currently, single molecule imaging and detection of AuNPs using various optical methods in collaboration with Prof. Theo Lasser, EPFL is in progress and also the studies related to delivery of therapeutics directly to the cell nucleus using nuclear targeting AuNPs are undergoing in our laboratory.

3.3. References

(1) Jobsis, F. *Science* **1977**, *198*, 1264.
(2) Escobedo, J. O.; Rusin, O.; Lim, S.; Strongin, R. M. *Curr. Opin.Chem. Biol.* **2010**, *14*, 64.
(3) Mishra, A.; Behera, R. K.; Behera, P. K.; Mishra, B. K.; Behera, G. B. *Chem. Rev.* **2000**, *100*, 1973.
(4) Ros-Lis, J. V.; García, B.; Jiménez, D.; Martínez-Máñez, R.; Sancenón, F.; Soto, J.; Gonzalvo, F.; Valldecabres, M. C. *J. Am. Chem.Soc.* **2004**, *126*, 4064.
(5) Link, S.; El-Sayed, M. A. *Annu. Rev. Phys. Chem.* **2003**, *54*, 331.
(6) Zheng, J.; Zhang, C.; Dickson, R. M. *Phys. Rev. Lett.* **2004**, *93*, 077402.
(7) Schaeffer, N.; Tan, B.; Dickinson, C.; Rosseinsky, M. J.; Laromaine, A.; McComb, D. W.; Stevens, M. M.; Wang, Y.; Petit, L.; Barentin, C.; Spiller, D. G.; Cooper, A. I.; Levy, R. *Chem.Commun.* **2008**, *4*,3986.
(8) Zheng, J.; Nicovich, P. R.; Dickson, R. M. *Annu. Rev. Phys. Chem.* **2007**, *58*, 409.
(9) Huang, C.-C.; Liao, H.-Y.; Shiang, Y.-C.; Lin, Z.-H.; Yang, Z.; Chang, H.-T. *J.Mater.Chem.* **2009**, *19*, 755.
(10) Wang, G.; Huang, T.; Murray, R. W.; Menard, L.; Nuzzo, R. G. *J. Am. Chem.Soc.***2004**, *127*, 812.
(11) Huang, T.; Murray, R. W. *J. Phys.Chem. B* **2001**, *105*, 12498.
(12) Lin, C.-A. J.; Yang, T.-Y.; Lee, C.-H.; Huang, S. H.; Sperling, R. A.; Zanella, M.; Li, J. K.; Shen, J.-L.; Wang, H.-H.; Yeh, H.-I.; Parak, W. J.; Chang, W. H. *ACS Nano* **2009**, *3*, 395.
(13) Xie, J.; Zheng, Y.; Ying, J. Y. *J. Am. Chem. Soc.* **2009**, *131*, 888.
(14) Shang, L.; Azadfar, N.; Stockmar, F.; Send, W.; Trouillet, V.; Bruns, M.; Gerthsen, D.; Nienhaus, G. U. *Small* **2011**, *7*, 2614.
(15) Maya, L.; Muralidharan, G.; Thundat, T. G.; Kenik, E. A. *Langmuir* **2000**, *16*, 9151.
(16) Na, H. B.; Palui, G.; Rosenberg, J. T.; Ji, X.; Grant, S. C.; Mattoussi, H. *ACS Nano* **2012**, *6*, 389.
(17) Wu, Y.; Pramanik, G.; Eisele, K.; Weil, T. *Biomacromolecules* **2012**, *13*, 1890.
(18) Hansen, R. E.; Østergaard, H.; Nørgaard, P.; Winther, J. R. *Anal. Biochem.* **2007**, *363*, 77.
(19) Oh, E.; Susumu, K.; Goswami, R.; Mattoussi, H. *Langmuir* **2010**, *26*, 7604.
(20) Hussain, I.; Graham, S.; Wang, Z.; Tan, B.; Sherrington, D. C.; Rannard, S. P.; Cooper, A. I.; Brust, M. *J. Am.Chem. Soc.* **2005**, *127*, 16398.
(21) Miller, J. T.; Kropf, A. J.; Zha, Y.; Regalbuto, J. R.; Delannoy, L.; Louis, C.; Bus, E.; van Bokhoven, J. A. *J. Catal.* **2006**, *240*, 222.
(22) Tian, D.; Qian, Z.; Xia, Y.; Zhu, C. *Langmuir* **2012**, *28*, 3945.
(23) Liu, H.; Zhang, X.; Wu, X.; Jiang, L.; Burda, C.; Zhu, J.-J. *Chem. Commun.* **2011**, *47*, 4237.
(24) Wilcoxon, J. P.; Martin, J. E.; Parsapour, F.; Wiedenman, B.; Kelley, D. F. *J. Chem. Phys.* **1998**, *108*, 9137.
(25) Pan, Y.; Leifert, A.; Ruau, D.; Neuss, S.; Bornemann, J.; Schmid, G.; Brandau, W.; Simon, U.; Jahnen-Dechent, W. *Small* **2009**, *5*, 2067.
(26) Eisele, K.; Gropeanu, R. A.; Zehendner, C. M.; Rouhanipour, A.; Ramanathan, A.; Mihov, G.; Koynov, K.; Kuhlmann, C. R. W.; Vasudevan, S. G.; Luhmann, H. J.; Weil, T. *Biomaterials* **2010**, *31*, 8789.
(27) Gruenbaum, Y.; Margalit, A.; Goldman, R. D.; Shumaker, D. K.; Wilson, K. L. *Nat. Rev. Mol. Cell Biol.* **2005**, *6*, 21.
(28) Fahrenkrog, B.; Aebi, U. *Nat. Rev. Mol. Cell Biol.* **2003**, *4*, 757.
(29) Cronshaw, J. M.; Krutchinsky, A. N.; Zhang, W.; Chait, B. T.; Matunis, M. J. *J. Cell Biol.* **2002**, *158*, 915.
(30) Miller, B. R.; Forbes, D. J. *Traffic* **2000**, *1*, 941.

(31) Lim, R. H.; Aebi, U.; Fahrenkrog, B. *Histochem.Cell Biol.* **2008**, *129*, 105.
(32) Rout, M. P.; Aitchison, J. D.; Suprapto, A.; Hjertaas, K.; Zhao, Y.; Chait, B. T. *J.Cell Biol.* **2000**, *148*, 635.
(33) Cook, A.; Bono, F.; Jinek, M.; Conti, E. *Annu. Rev. Biochem.* **2007**, *76*, 647.
(34) Pemberton, L. F.; Paschal, B. M. *Traffic* **2005**, *6*, 187.
(35) Görlich, D.; Kutay, U. *Annu. Rev. Cell Dev.Biol.***1999**, *15*, 607.
(36) Strom, A.-C.; Weis, K. *Genome Biol.* **2001**, *2*, 3008.1.
(37) Fahrenkrog, B.; Köser, J.; Aebi, U. *Trends Biochem. Sci.* **2004**, *29*, 175.
(38) Kau, T. R.; Way, J. C.; Silver, P. A. *Nat. Rev. Cancer* **2004**, *4*, 106.
(39) Peters, R. *Traffic* **2005**, *6*, 421.
(40) Fouchier, R. A. M.; Malim, M. H.; Karl Rlaramorosch, F. A. M.; Aaron, J. S. In *Advances in Virus Research*; Academic Press: 1999; Vol. Volume 52, p 275-299.
(41) Kalderon, D.; Richardson, W. D.; Markham, A. F.; Smith, A. E. *Nature* **1984**, *311*, 33.
(42) Kalderon, D.; Roberts, B. L.; Richardson, W. D.; Smith, A. E. *Cell* **1984**, *39*, 499.
(43) Robbins, J.; Dilwortht, S. M.; Laskey, R. A.; Dingwall, C. *Cell* **1991**, *64*, 615.
(44) Hall, M. N.; Craik, C.; Hiraoka, Y. *Proc. Natl. Acad. Sci. USA* **1990**, *87*, 6954.
(45) Hall, M. N.; Hereford, L.; Herskowitz, I. *Cell* **1984**, *36*, 1057.
(46) Dingwall, C.; Laskey, R. A. *Trends Biochem. Sci.* **1991**, *16*, 478.
(47) Chi, N. C.; Adam, E. J.; Adam, S. A. *J. Cell Biol.* **1995**, *130*, 265.
(48) Görlich, D.; Prehn, S.; Laskey, R. A.; Hartmann, E. *Cell* **1994**, *79*, 767.
(49) Görlich, D.; Kostka, S.; Kraft, R.; Dingwall, C.; Laskey, R. A.; Hartmann, E.; Prehn, S. *Curr. Biol.* **1995**, *5*, 383.
(50) Naoko, I.; Takuya, S.; Shingo, K.; Toshifumi, T.; Taro, T.; Masami, M.; Toshihiro, S.; Yasutsugu, S.; Yoshihiro, Y. *FEBS Lett.* **1995**, *368*, 415.
(51) Radu, A.; Blobel, G.; Moore, M. S. *Proc. Natl. Acad. Sci.USA* **1995**, *92*, 1769.
(52) Görlich, D.; Mattaj, I. W. *Science* **1996**, *271*, 1513.
(53) Nigg, E. A. *Nature* **1997**, *386*, 779.
(54) Gorlich, D.; Vogel, F.; Mills, A. D.; Hartmann, E.; Laskey, R. A. *Nature* **1995**, *377*, 246.
(55) Moroianu, J.; Hijikata, M.; Blobel, G.; Radu, A. *Proc. Natl. Acad. Sci. USA* **1995**, *92*, 6532.
(56) Weis, K.; Mattaj, I. W.; Lamond, A. I. *Science* **1995**, *268*, 1049.
(57) Melchior, F.; Paschal, B.; Evans, J.; Gerace, L. *J.Cell Biol.* **1993**, *123*, 1649.
(58) Moore, M. S.; Blobel, G. *Nature* **1993**, *365*, 661.
(59) Moore, M. S.; Blobel, G. *Proc. Natl. Acad.Sci. USA* **1994**, *91*, 10212.
(60) Paschal, B. M.; Delphin, C.; Gerace, L. *Proc. Natl. Acad. Sci. USA* **1996**, *93*, 7679.
(61) Xie, X.; Xu, W.; Liu, X. *Acc. Chem. Res.* **2012**, *45*, 1511.
(62) Tkachenko, A. G.; Xie, H.; Liu, Y.; Coleman, D.; Ryan, J.; Glomm, W. R.; Shipton, M. K.; Franzen, S.; Feldheim, D. L. *Bioconjugate Chem.* **2004**, *15*, 482.
(63) de la Fuente, J. M.; Berry, C. C. *Bioconjugate Chem.* **2005**, *16*, 1176.
(64) Ojea-Jiménez, I.; García-Fernández, L.; Lorenzo, J.; Puntes, V. F. *ACS Nano*, **2012**, *6*, 7692.
(65) Krpetić, Ž.; Saleemi, S.; Prior, I. A.; Sée, V.; Qureshi, R.; Brust, M. *ACS Nano*, **2011**, *5*, 5195.
(66) Xie, W.; Wang, L.; Zhang, Y.; Su, L.; Shen, A.; Tan, J.; Hu, J. *Bioconjugate Chem.* **2009**, *20*, 768.
(67) Tkachenko, A. G.; Xie, H.; Coleman, D.; Glomm, W.; Ryan, J.; Anderson, M. F.; Franzen, S.; Feldheim, D. L. *J. Am. Chem. Soc.* **2003**, *125*, 4700.
(68) Gu, Y.-J.; Cheng, J.; Lin, C.-C.; Lam, Y. W.; Cheng, S. H.; Wong, W.-T. *Toxicol. Appl. Pharm.* **2009**, *237*, 196.

(69) Wang, H.-Y.; Li, C.; Yi, W.-J.; Sun, Y.-X.; Cheng, S.-X.; Zhuo, R.-X.; Zhang, X.-Z. *Bioconjugate Chem.* **2011**, *22*, 1567.
(70) Kang, B.; Mackey, M. A.; El-Sayed, M. A. *J. Am. Chem. Soc.* **2010**, *132*, 1517.
(71) Feldherr, C. M.; Lanford, R. E.; Akin, D. *Proc. Natl.Acad. Sci.USA* **1992**, *89*, 11002.
(72) Feldherr, C. M.; Akin, D. *Exp. Cell Res.***1993**, *205*, 179.
(73) Huefner, A.; Kuan, W.-L.; Barker, R. A.; Mahajan, S. *Nano Lett.* **2013**, *13*, 2463.
(74) Pitter, D. R. G.; Wigenius, J.; Brown, A. S.; Baker, J. D.; Westerlund, F.; Wilson, J. N. *Org. Lett.* **2013**, *15*, 1330.
(75) Shen, R.; Shen, X.; Zhang, Z.; Li, Y.; Liu, S.; Liu, H. *J. Am. Chem.Soc.* **2010**, *132*, 8627.
(76) Chen, F.; Gerion, D. *Nano Lett.* **2004**, *4*, 1827.
(77) Wang, Y.; Chen, J.; Irudayaraj, J. *ACS Nano* **2011**, *5*, 9718.
(78) Pouton, C. W.; Wagstaff, K. M.; Roth, D. M.; Moseley, G. W.; Jans, D. A. *Adv. Drug Deliver.Rev.* **2007**, *59*, 698.
(79) Liu, Y.; Franzen, S. *Bioconjugate Chem.* **2008**, *19*, 1009.
(80) Mei, B. C.; Oh, E.; Susumu, K.; Farrell, D.; Mountziaris, T. J.; Mattoussi, H. *Langmuir* **2009**, *25*, 10604.
(81) Shang, L.; Azadfar, N.; Stockmar, F.; Send, W.; Trouillet, V.; Bruns, M.; Gerthsen, D.; Nienhaus, G. U. *Small* **2011**, *7*, 2614.
(82) Zhou, C.; Sun, C.; Yu, M.; Qin, Y.; Wang, J.; Kim, M.; Zheng, J. *J. Phys. Chem. C* **2010**, *114*, 7727.
(83) Yam, V. W.-W.; Cheng, E. C.-C. *Chem. Soc. Rev.* **2008**, *37*, 1806.
(84) Huang, C.-C.; Hung, Y.-L.; Shiang, Y.-C.; Lin, T.-Y.; Lin, Y.-S.; Chen, C.-T.; Chang, H.-T. *Asian J. Chem.* **2010**, *5*, 334.
(85) Vogler, A.; Kunkely, H. *Coordin. Chem. Rev.* **2000**, *208*, 321.
(86) Muhammed, M. A. H.; Verma, P. K.; Pal, S. K.; Kumar, R. C. A.; Paul, S.; Omkumar, R. V.; Pradeep, T. *Chem. Eur. J.* **2009**, *15*, 10110.
(87) Wu, Z.; Jin, R. *Nano Lett.* **2010**, *10*, 2568.
(88) Liang, N.; Sun, S.; Li, X.; Piao, H.; Piao, H.; Cui, F.; Fang, L. *Int. J. Pharm.***2012**, *423*, 480.
(89) He, X.; Wang, Y.; Wang, K.; Chen, M.; Chen, S. *Anal. Chem.* **2012**, *84*, 9056.
(90) Bink, K.; Walch, A.; Feuchtinger, A.; Eisenmann, H.; Hutzler, P.; Höfler, H.; Werner, M. *Histochem. Cell Biol.***2001**, *115*, 293.
(91) Richard, J. P.; Melikov, K.; Vives, E.; Ramos, C.; Verbeure, B.; Gait, M. J.; Chernomordik, L. V.; Lebleu, B. *J. Biol. Chem.* **2003**, *278*, 585.
(92) Fox, E.; Bates, S. E. *Expert Rev. Anticanc.* **2007**, *7*, 447.
(93) Pan, L.; He, Q.; Liu, J.; Chen, Y.; Ma, M.; Zhang, L.; Shi, J. *J. Am. Chem. Soc.* **2012**, *134*, 5722.

Chapter 4.

4.1. Stabilization of fluorescent nanodiamonds (FNDs) for cell studies by a polypeptide polymer coating

Declaration

Experiments with nanodiamonds were accomplished in cooperation with Lars Boorberg, Institute of Organic Chemistry III–Macromolecular Chemistry and Organic Materials, Ulm University and they were included also within his master's thesis. The experimental protocols in the Master thesis were based on the intellectual property developed in this thesis. High-resolution transmission electron microscopy (HRTEM) was performed by Gerardo Algara-Siller, Electron Microscopy Group of Materials Science, Universität Ulm. T_1, T_2 and FCS measurements were performed by Anna Ermakova, Institute for Quantum Optics, Universität Ulm and the theoritical calculations were performed by Dr. Jianming Cai, Controlled Quantum Dynamics Group, Universität Ulm. This experimental results in second part 4.2 of this chapter have been published previously in *Nano Lett.* **2013**, *13*, 3305 written by A. Ermakova, G. Pramanik, J.-M. Cai, G. Algara-Siller, U. Kaiser, T. Weil, Y.-K. Tzeng, H. C. Chang, L. P. McGuinness, M. B. Plenio, B. Naydenov, and F. Jelezko. Section 4.2 is "Reprinted (adapted) with permission from *Nano Lett*. **2013**, *13*, 3305. Copyright 2013 American Chemical Society."

4.1.1. Introduction:

Development of new fluorescent markers for fluorescence microscopy has attracted considerable attention during the past decade. Recently developed single molecule detection techniques[1] have the ability to probe fluorescent molecules like single organic molecules or auto fluorescent proteins. However, the photostability of such markers often represents a limiting factor. This drawback is particularly important for superresolution fluorescence microscopy (STED, PALM) and tracking techniques where relatively high excitation intensities are used.[2] In particular the introduction of semiconductor nanocrystals (quantum dots) has contributed to an improved photostability,[3] but toxicity and fluorescence blinking limits their application areas. Colour centers in diamond provide a promising alternative to the conventional fluorescent markers mentioned above owing to the unique combination of physical and chemical properties of the diamond crystal lattice.[4,5] First, the diamond material is biocompatible and fluorescent nanodiamonds (FNDs) are known to be non-toxic.[6] Second,

FNDs possesses more than a few hundred fluorescing defects (colour centers) and some of them show very bright and stable fluorescence emission in the NIR region allowing to detect single impurities in diamond lattice.[7] Third, fluorescence properties of localized defects are defined by their structure and not by the size of the nanocrystal allowing shrinking the size of the marker down to a few nanometers.[8,9] Furthermore, optically assisted spin readout[10,11] can be used to sense the local magnetic and electric fields using single colour centers.[12] This technique allows the use of FNDs containing single color centers as electric[13] and magnetic field sensors[12-14] at the nanoscale. Recently, the unlimited photostability of FNDs was exploited for superresolution optical imaging[15,16] and nanoscale MRI.[17] As the light emission results from defect sites within the core of the FNDs, the surface of the particle can be modified and bioconjugation performed without altering the emission signal.[18] The main surface groups that are found on FNDs include COOH and C=O groups in addition to different alcohol functions (tertiary, secondary, primary) and ether groups.[19-21] Depending on the production method, the surface functionalities of FNDs differ significantly.[22] However, FNDs surfaces also contain varying amounts of removable disordered (sp^2) graphitic carbon on the surface.[22] Several research groups have exploited these graphitic shells around FNDs to functionalize FNDs by means of various reactions, such as Diels–Alder reactions,[23] diazonium chemistry,[24] electrochemical reduction,[25] radical reaction,[26] grafting polymer[27]. However, the presence of the graphitic shell around the FNDs has also undesired detrimental effect on the fluorescence of nanodiamonds. The graphite-shell around FNDs quenches the fluorescence which results in multiexponential decays of the FND emission.[28] These graphitic carbon can be removed by treatment with oxidizing mineral acids and/or air oxidation.[29-31] Both treatments lead to the formation of mainly carboxyl groups at the FND surface (**Figure 4.1.1**).

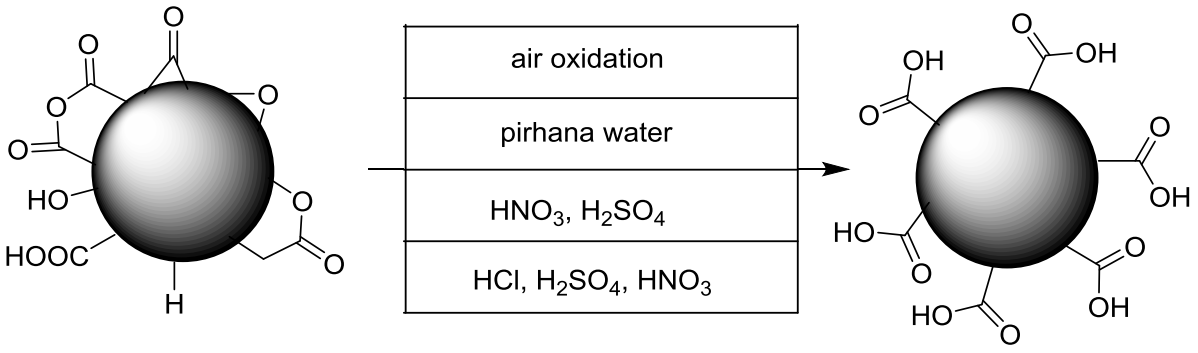

Figure 4.1.1. The surface of nanodiamonds can be oxidized with various methods. All result in coverage with mainly -COOH groups.

One of the ways to functionalize FNDs with biomolecules is to covalently couple amino or hydroxyl groups from biomolecules with carboxyl groups onto the surface of FNDs via carbodiimide chemistry, NHS ester or acid chloride chemistry (**Figure 4.1.2**).[5,32-34]

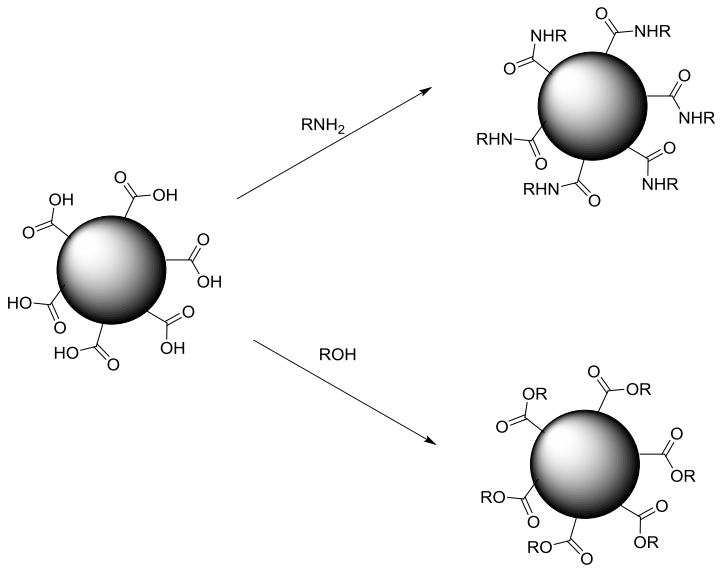

Figure 4.1.2. Schematic reaction of carboxylated FNDs with amines and alcohols.

However, according to my own findings, FNDs form aggregates, which leads to precipitation during carbodiimide coupling of biomolecules as described in greater detail in the main part. Similar ineffective coupling of biomolecules and aggregation of the FNDs were also reported in the literature[35,36,37] and these aggregates of FNDs can even withstand ultrasonic treatment.[37] This aggregation tendency increases with decreasing size of the FNDs.[38-40] Aggregation of FNDs makes homogeneous cell labeling and/or labeling of non-adherent cells (or suspension cells) very difficult, if not impossible.[41] For the use of FNDs as a fluorescent label or marker for imaging in cells, following hurdles regarding the functionalization need to be overcome: (1) After functionalization, FNDs must be soluble in water and exhibit long-term stability over a broad pH range, in the presence of high concentrations of electrolytes and in biological media. (2) The surface coating of the FNDs must promote biocompatibility and reduce non-specific interactions while maintaining an overall compact size. (3) Surface functionalization needs to be effective and controllable, which permits one to adjust the number and nature of biomolecules attached to FNDs, thus facilitating the use of these materials in targeting, sensing, and imaging applications.

In recent years, many papers have reported the covalent and non-covalent surface functionalization of NDs.[37,42-44] For e.g. covalent DNA immobilization,[35] biotinylation,[45] phosphorylation,[46] grafting TEMPO radicals,[47] suzuki coupling,[48] click chemistry,[49] solvent free covalent modification[50] grafting polymers to the nanodiamond surface[51,52] were achieved. Functionalised NDs have been widely used as cellular biomarkers,[5] glycoproteome analysis,[53] detection of pathogenic bacteria,[44] chemotherapeutic drug[52,54-58] and gene[59-62] delivery system. However, only few papers[63-65] have been devoted on improving the nanodiamond dispersion stability and avoiding post modification aggregation of the nanodiamond in biological media.

The motivation for the first part (4.1) of this chapter is to stabilize the FNDs for cell studies by the non-covalent coating with the denatured protein based multifunctional polycationic polypeptide copolymers and motivation for the second part (4.2) of this chapter is to coat the FNDs with native metallo-protein such as ferritin and detect the metallo-protein based on the change in relaxation time (T_1) and coherence time (T_2).

The use of polymer coatings bearing multiple functions is very attractive for nanoparticles stabilization and have been widely used to afford coating materials for inorganic nanoparticles like quantum dots (QDs),[66-68] iron oxide nanoparticles[69,70] and gold (Au) nanoparticles[71,72] as diagnostic imaging probes and drug carriers (nanotheranostics)[73,74]. These polymer coatings play an important role in delivering high drug payloads to specific subcellular targets.[75,76] Carboxylated nanodiamonds are known to adsorb biomolecules like proteins,[36,41,77-79] toxins,[80,81] antibodies,[82] hormones[83] by non-covalent electrostatic interactions, e.g. between the amine groups of biomolecules and carboxylic acid groups of the nanodiamonds. Following the above mentioned principle, an efficient method for the stabilization of FNDs for cell studies will be developed that allows non-covalent coating of FNDs by polypeptide copolymer reported in the previous chapters such as Rho-dcBSA-PEO$(5000)_{27}$ (**5**) (**Scheme 4.1.1**). Rho-dcBSA-PEO$(5000)_{27}$ consists of a single polypeptide chain derived from the protein bovine serum albumin (BSA) bearing about 27 PEO chains, multiple primary amino groups as well as a single chromophore. Unlike, the stabilization of AuNPs (chapter 3), where the gold core is covalently connected to the polypeptide copolymer via thioctic acid, the FNDs are non-covalently attached with Rho-dcBSA-PEO$(5000)_{27}$ (**5**) by the electrostatic interaction between carboxylic acid groups of the FND and primary amine groups of Rho-dcBSA-PEO$(5000)_{27}$ (**5**) (**scheme 4.1.1**). These results are important to achieve highly dispersive FNDs that are resistant to agglomeration in solution in a wide range

of pH and even at high ionic strength. In addition, colocalisation of Rho-dcBSA-PEO(5000)$_{27}$ and FNDs inside the cell will be studied using confocal laser scanning microscopy (CLSM).

4.1.2. Results & Discussion

Development of novel schemes for the coating of FNDs with of Rho-dcBSA-PEO(5000)$_{27}$ (5)

A schematic of the synthesis of Rho-dcBSA-PEO(5000)$_{27}$ and coating of FNDs is depicted in scheme 4.1.1. The synthesis and the structure of Rho-dcBSA-PEO(5000)$_{27}$ (**5**) is very similar to the dcBSA-PEO(5000)$_{27}$, which has been described in chapter 2. The only difference is the attachment of the commercially available tetramethylrhodamine-5-maleimide (Rho) chromophore to native BSA **(scheme 4.1.1**). The attachment Rho allows to visualize the intracellular fate of the Rho-dcBSA-PEO(5000)$_{27}$ (**5**) coating to elucidate whether the polymer coating remains intact or get dissociated from the FNDs during the cell internalization process. Native bovine serum albumin (BSA, **1**) was labeled with a single tetramethylrhodamine-5-maleimide (Rho) chromophore to yield Rho-BSA (**2**), as reported previously, by 1,4-michael addition reaction between the only unpaired and accessible cysteine residue (cys34)[84] of BSA and maleimide group of Rho.[85] Then, high numbers of amino groups were introduced to Rho-BSA by reacting ethylene diamine with the carboxylic acid groups of aspartate and glutamate residues of Rho-BSA (**2**) in the presence of 1-ethyl-3-(3´-dimethylamino-propyl)-carbodiimide hydrochloride (EDC).[85] The cationisation or the introduction of high numbers of primary amines is necessary to facilitate interaction with the carboxylic acids of the FNDs (**scheme 4.1.1**). The high number of primary amino group facilitates coating of the FNDs with the polymer shell by multiple electrostatic interactions with the carboxylic acid of the FNDs. The primary amines remain positively charged at physiological pH, which helps to improve the stability of FNDs in solution by electrostatic repulsion and also the positively charged primary amine groups should enhance the cellular uptake of the FNDs. Unfolding globular Rho-cBSA (**3**) under denaturing conditions in the presence of urea and the reduction reagent TCEP, followed by the addition of PEO5000 maleimide yields copolymer Rho-dcBSA-PEO(5000)$_{27}$ (**5**) as described in chapter 2.[86] The presence of PEO5000 is important given the fact that carboxylated NDs are prone to adsorb proteins non-specifically.[36] Therefore, the addition of PEO5000 should contribute to reduce the non-specific adsorption of proteins to the surface of FNDs. Polyelectrolyte complex formation between FNDs with multiple carboxylic acid groups at the surface and the polypeptide copolymer Rho-dcBSA-PEO(5000)$_{27}$ (**5**) with high numbers of primary amino

groups along the backbone proceeds via electrostatic interactions in boric acid buffer at pH 8.5. At pH 8.5, the primary amino groups of Rho-dcBSA-PEO(5000)$_{27}$ (5) are still positively charged and the surface terminating carboxylic acid remains negatively charged. The multiple electrostatic attraction forces between the surface-terminating anionic groups (-COO^-) and the positively charged amino groups (-NH_3^+) facilitate the coating of FNDs with Rho-dcBSA-PEO(5000)$_{27}$ (**5**).

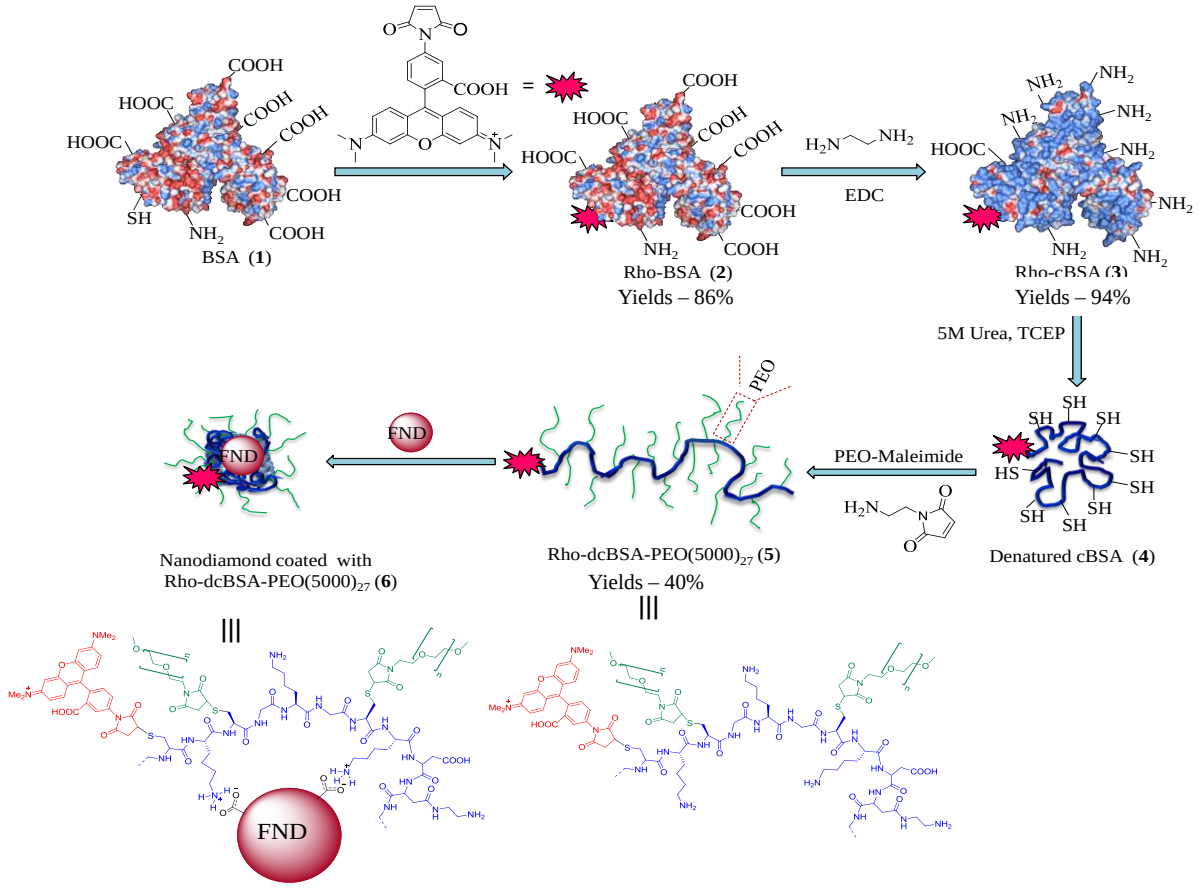

Scheme 4.1.1. Schematic representation of preparation of Rho-dcBSA-PEO(5000)$_{27}$ and coating of FNDs with Rho-dcBSA-PEO(5000)$_{27}$.

Characterization of the coated FNDs surface.

The successful coating of FNDs with Rho-dcBSA-PEO(5000)$_{27}$ has been demonstrated by fourier transform infrared spectroscopy (FTIR), size measurement, zeta Potential, X-ray photoelectron spectroscopy (XPS), transmission electron microscopy (TEM) and confocal colocalisation experiments.

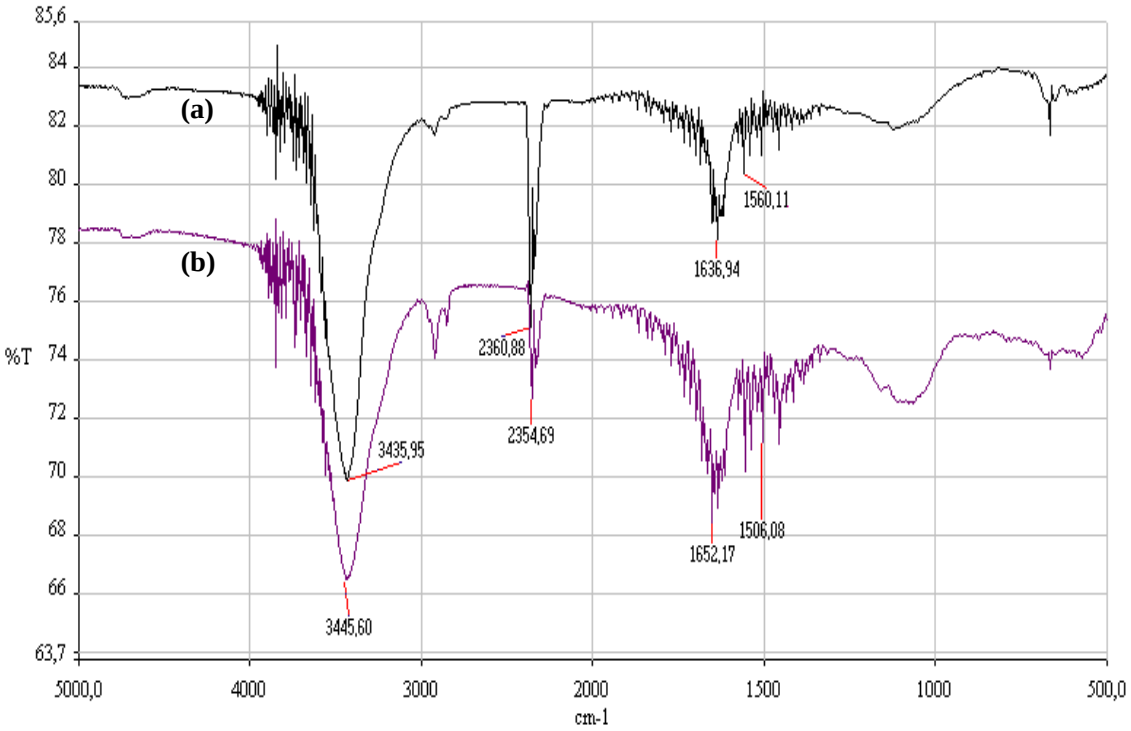

Figure 4.1.3. Infrared spectra of (a) FNDs, (b) FNDs coated with Rho-dcBSA-PEO(5000)$_{27}$ (**6**).

FTIR measurements

Figure 4.1.3a shows the FTIR spectrum of acid treated FNDs. Several distinct features appear at 3435 cm^{-1}, 1635 cm^{-1} in the spectral region. These two peaks can be assigned to the O-H stretch of the surface carboxyl groups and to the C=O stretching of the carboxylate anion. The associated hydrogen bonds between physically adsorbed water molecules are responsible for the broad absorption bands observed at 3000-3600 cm^{-1}.[87] Oxidized FNDs contain several carboxylic acid groups at their surface and therefore, they can interact with Rho-dcBSA-PEO(5000)$_{27}$ through electrostatic attraction forces between the surface-terminating anionic groups (-COO$^-$) and the positively charged, protonated amino groups (-NH$_3^+$) of the polypeptide shell. **Figure 4.1.3b** depicts the FTIR spectrum of the Rho-dcBSA-PEO(5000)$_{27}$ coated FNDs. Two absorption bands at 1652 and 1506 cm^{-1} are attributed to the amide I and amide II modes of the polypeptide backbone, respectively.[87,88] The significant increase in the intensity of the broad peak at 1070 cm^{-1} (C-N stretching of primary amine and C-O-C stretching from the high number of polyethylene glycol present in Rho-dcBSA-PEO(5000)$_{27}$ polypeptide hybrid) indicates the successful coating of FNDs with Rho-dcBSA-PEO(5000)$_{27}$.

Size measurements

The coating of FNDs with **5** should lead to an increase of the hydrodynamic radius of FNDs, which was studied by fluorescence correlation spectroscopy (FCS) (**Figure 4.1.4**). The diffusion time of only **5** is 0.3-0.7 ms; while after coating, the diffusion time of FNDs with **5** has increased to 7.2 ms. Slower diffusion times indicate a larger hydrodynamic radius due to the presence of the polypeptide shell around the FNDs.

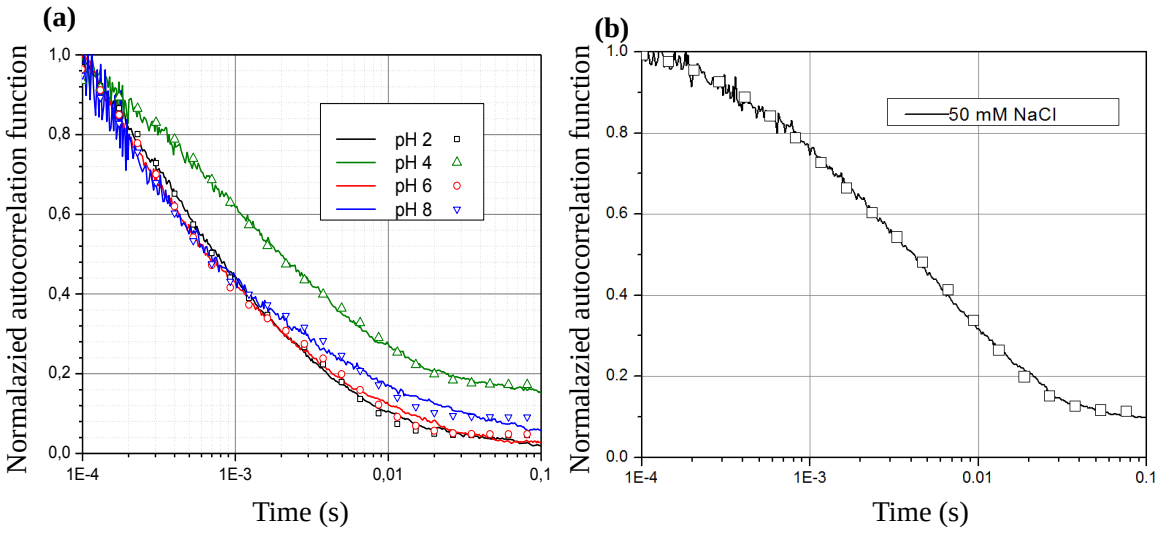

Figure 4.1.4. (a)Autocorrelation functions of **6** in solutions at different pH ranging from pH 2 to 8. (b) Autocorrelation function of **6** in 50mM NaCl solution. Lines are experimental data, symbols represent the exponential fit.

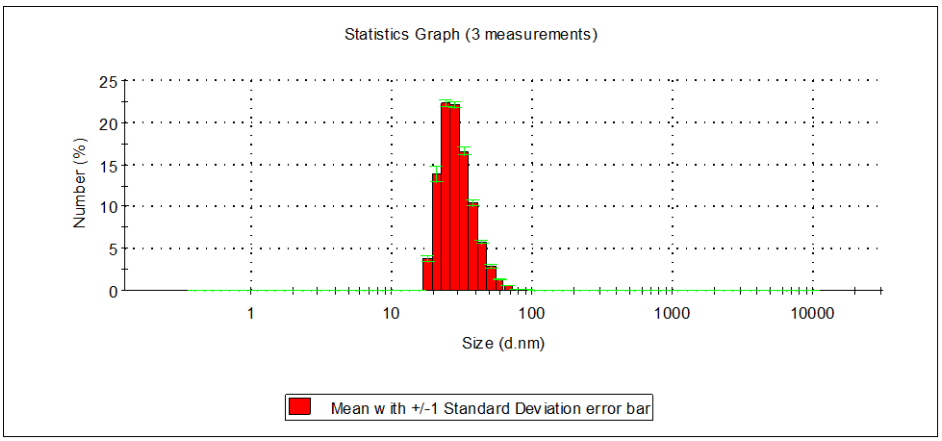

Figure 4.1.5. Number size distribution of only FNDs by DLS. The average hydrodynamic diameter of FNDs is 30.1±1.2 nm. The results were obtained after three independent measurements and each measurement consisting of ten individual runs.

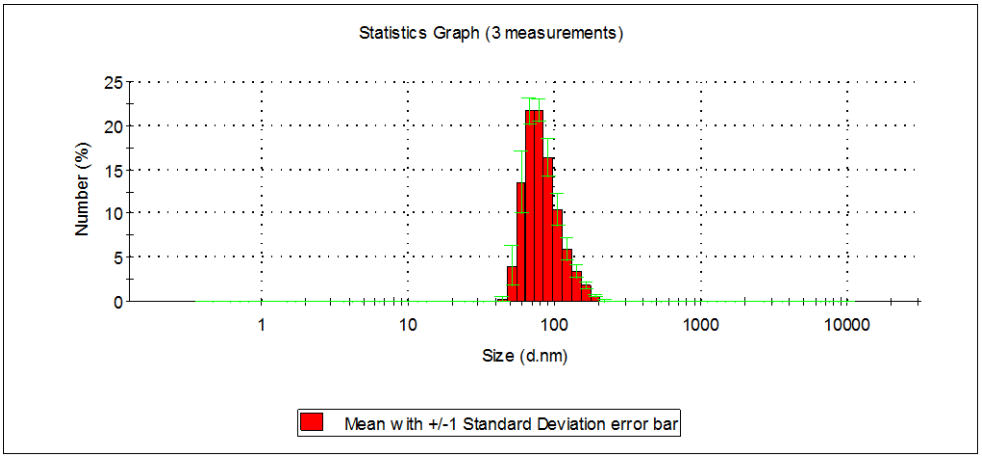

Figure 4.1.6. Number size distributions of Rho-dcBSA-PEO(5000)$_{27}$ coated FNDs (6) by DLS. The average hydrodynamic diameter of Rho-dcBSA-PEO(5000)$_{27}$ coated FNDs (6) is 84.5±3.8 nm. The results were obtained after three independent measurements and each measurement consisting of ten individual runs.

To confirm that the increase in hydrodynamic radius is not due to the presence of undesired large (<100 nm in diameter) agglomerates, I have analyzed the FNDs (**6**) coated with Rho-dcBSA-PEO(5000)$_{27}$ with transmission electron microscopy (TEM) (**Figure 4.1.7**). The TEM images show primary particles of average sizes of ~30 nm. TEM images of Rho-dcBSA-PEO(5000)$_{27}$ coated FNDs reveal well dispersed individual particles. Interestingly, upon drying onto the copper grid, Rho-dcBSA-PEO(5000)$_{27}$ coated FNDs did not flocculate and the individual particles are still visible. The difference in the radii obtained by DLS and TEM can be understood by considering the fact that in TEM only the core diamond structure is visible, while in DLS the total hydrodynamic diameter of FNDs coated with Rho-dcBSA-PEO(5000)$_{27}$ is measured. Contrast in transmission electron microscopy (TEM) is mainly produced by electron scattering at the specimen.[89] In TEM, only the core FNDs strongly scatter electrons and appear as dark spot.[89] While the protein shell around the diamond structure scatters only few electrons, it is mostly transparent to the electron beam and do not create large contrast, remains invisible in TEM.[89] DLS is measured in solution. The diameters obtained from DLS represent the total hydrodynamic diameter of FNDs coated with Rho-dcBSA-PEO(5000)$_{27}$. The large diameter in DLS measurement could be due to the presence of PEO chains in their extended architecture under the conditions of the DLS measurements, whereas they are collapsed in the dried state.

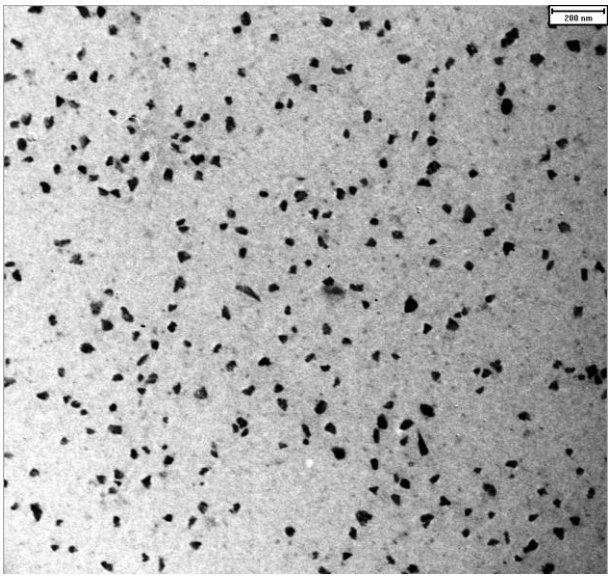

Figure 4.1.7. The TEM image of FNDs coated with Rho-dcBSA-PEO(5000)$_{27}$ (**6**). Scale bar 200nm.

Zeta Potential measurements

To determine the coating of the FNDs, the zeta potential was measured at pH 7.4. Uncoated, carboxylated FNDs bear a negative zeta potential of -43.3 mV due to the presence of several deprotonated carboxylic acid groups. Coating with Rho-dcBSA-PEO(5000)$_{27}$ (**5**) partially neutralizes the negative surface charges of the FNDs and the zeta potential of Rho-dcBSA-PEO(5000)$_{27}$-FND (**6**) increases to -9.5 mV. Therefore, this change of the zeta potential further implicates the successful coating of the FNDs by Rho-dcBSA-PEO(5000)$_{27}$.

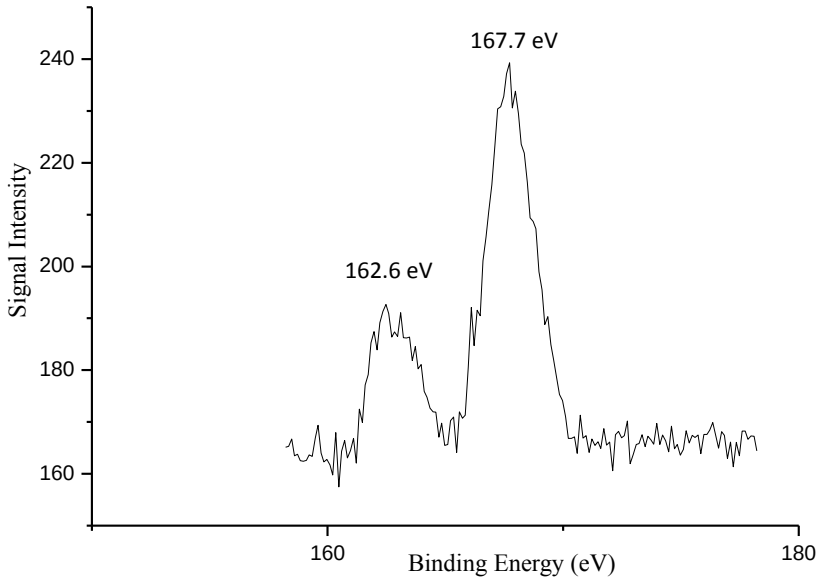

Figure 4.1.8. XPS S 2p core level spectrum of Rho-dcBSA-PEO(5000)$_{27}$ coated FNDs (**6**).

X-ray photoelectron spectroscopy (XPS) study

An X-ray photo electron spectroscopy study reveals the presence of two different types of sulfur atoms in the FNDs sample after coating with Rho-dcBSA-PEO(5000)$_{27}$ (**Figure 4.1.8**). One of them (S2p3/2 BE: 162.6 eV) is attributed to S (-II) sulfur, which arises from the protein backbone. The another (S2p3/2 BE: 167.7 eV) could be assigned to S(+VI) sulfur, which relates to sulfate (SO_4^{2-}) anions, which probably originate from the sulfuric acid used to remove graphitic carbon during the purification process.

Colocalisation of Rho-dcBSA-PEO(5000)$_{27}$ and FNDs on glass surface

To demonstrate successful coating of FNDs with **5**, co-localization experiments were performed. **Figure 4.1.9** reveals the confocal micrograph of the emission of Rho and NV centers of FNDs on a glass surface. The colocalized emission from the Rho-dcBSA-PEO(5000)$_{27}$ (green) and NV centers (red) confirms the successful coating of FNDs with Rho-dcBSA-PEO(5000)$_{27}$.

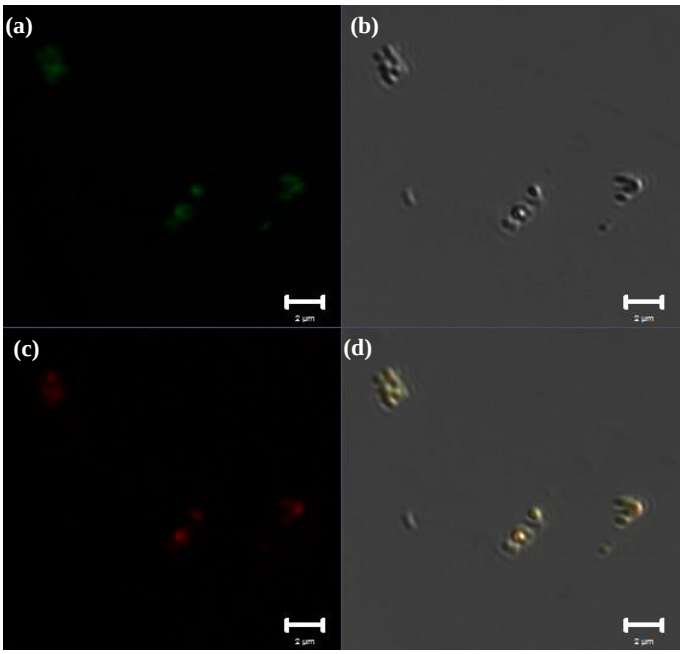

Figure 4.1.9. The sample solution was deposited on a glass coverslip and observed with the confocal microscope. (a) Green represents data acquired by the Rhodamine channel. (b) DIC image. (c) Red represents data acquired by the FNDs channel. (d) Overlay.

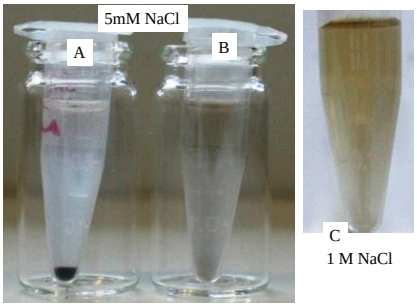

Figure 4.1.10. A) Photograph of FNDs solution in 5 mM NaCl. (B) Photograph of Rho-dcBSA-PEO(5000)$_{27}$ coated FNDs in 5 mM NaCl solution. (C) Photograph of Rho-dcBSA-PEO(5000)$_{27}$ coated FNDs in 1 M NaCl solution.

Stability of Rho-dcBSA-PEO(5000)$_{27}$ coated FNDs (6)

The stability of the FNDs solution strongly depends on the pH and solvent salt concentration. For bioimaging inside cells, the formation of stable solutions of FNDs at different pH and buffer media with high ionic strength is crucial.[90] The stability of Rho-dcBSA-PEO(5000)$_{27}$-FND (**6**) in solution was investigated based on their diffusion behaviour at a wide pH range of 2-8 and at high ionic strength such as in the presence of 50 mM NaCl by applying FCS. **Figure 4.1.4b** shows the autocorrelation curve for (**6**) at different pH and at 50 mM NaCl. The diffusion time of FNDs coated with Rho-dcBSA-PEO(5000)$_{27}$ at pH 2-8 were found in the range of 5.6 to 7.7 ms and of 9.6 ms in 50 mM NaCl solution indicating that no aggregate formation has occurred. The availability of just a single diffusion time for **6** indicates that large cluster formation of these functionalized FNDs is suppressed. The minor variation in the diffusion time and the diffusion coefficient over the pH range and even at very high ionic strength solution demonstrates the high colloidal stability of these FNDs (**Table 4.1.1**). Carboxylated FNDs without Rho-dcBSA-PEO(5000)$_{27}$ coating precipitate even in 5mM solution of NaCl within 30 minutes (**Figure 4.1.10A**), while Rho-dcBSA-PEO(5000)$_{27}$ coated FNDs (**6**) remain in solution for several months (**Figure 4.1.10B**). Even in 1M NaCl solution, **6** does not precipitate (**Figure 4.1.10C**). Most likely, the enhanced stability and the suppression of particle agglomeration could be due to the presence of both high numbers of primary amino groups and the long polyethylene oxide of Rho-dcBSA-PEO(5000)$_{27}$ compared to NDs stabilised by only PEO[64,91] or polylysine[36]. Precoating of the FNDs with Rho-dcBSA-PEO(5000)$_{27}$ helps to avoid nonspecific adsorption of the protein and other bio-molecules to the surface of FNDs, due to the presence of long polyethylene oxide (PEO) chain at the polypeptide backbone. Preventing nonspecific adsorption will increase the efficacy of the biosensors designed based on FNDs. The higher solubility and

colloidal stability of Rho-dcBSA-PEO(5000)$_{27}$ coated FNDs should allow avoiding the undesirable accumulation of FNDs at the cell surface and facilitate the cellular uptake and imaging studies.

Table 4.1.1. FCS data for 6 in solutions at different pH.

	DiffusionTime (milliseocond)	Diffusion coefficient (m^2/S)
pH 2	7.7	$1.8*10^{-12}$
pH 4	7.6	$1.8*10^{-12}$
pH 6	5.2	$2.6*10^{-12}$
pH 8	5.6	$2.5*10^{-12}$

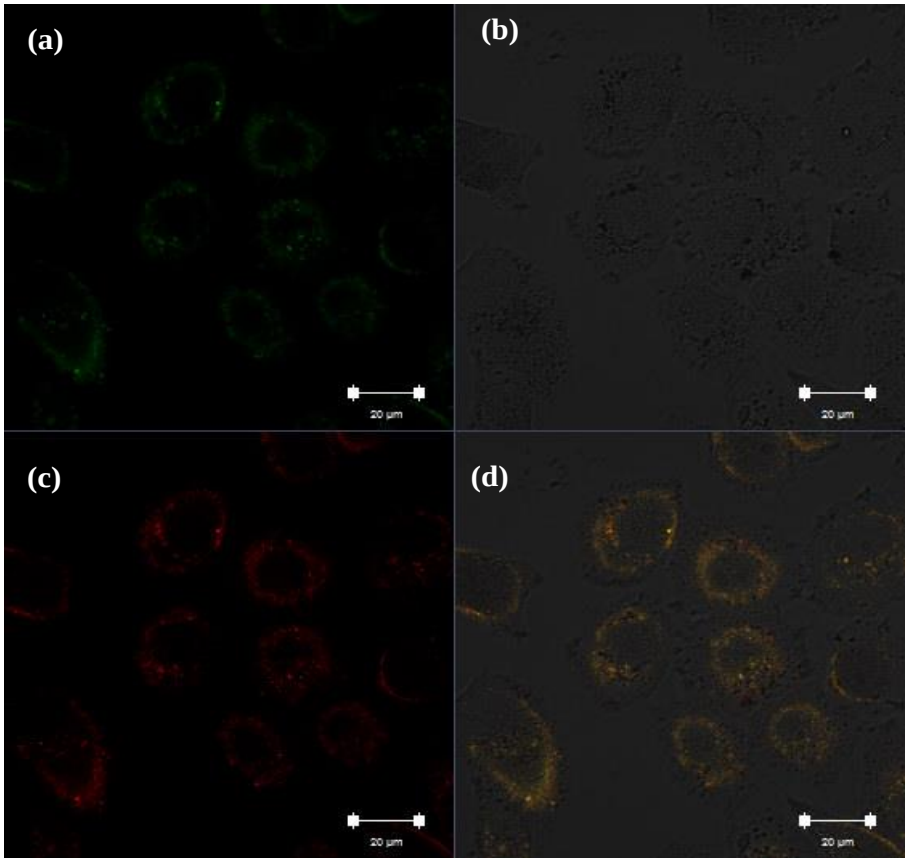

Figure 4.1.11. Confocal microscopy image of Hela cells incubated with Rho-dcBSA-PEO(5000)$_{27}$ coated FNDs (**6**). (a) Green represents data acquired by the Rhodamine channel. (b) DIC image. (c) Red represents data acquired by the FNDs channel. (d) Overlay. Image scanned using simultaneous scanning. The green and red spots overlap to such an extent that only yellow spots are visible in overlay.

Cellular uptake of Rho-dcBSA-PEO(5000)$_{27}$ coated FNDs (6)

To investigate the internalization and distribution Rho-dcBSA-PEO(5000)$_{27}$-FNDs into cells, HeLa cells are incubated with **6** at physiological buffer for 12 h. Rho-dcBSA-PEO(5000)$_{27}$ coated FNDs are uptaken by cells and traffic to the cytoplasm/perinuclear region (**Figure 4.1.11**). The distribution of **6** inside the cell is similar to the precursor protein cBSA-147.[34] Often, polymer coating dissociates from nanoparticles in intracellular compartments and the nanoparticles formed intracellular aggregates that are much larger in size than the isolated nanoparticles.[75,92-95] The premature release of cargos from polymer coated nanoparticles when interacting with cellular lipophilic membranes has been suggested due to the disruption of the polymer coatings from the nanoparticles.[96,97] Therefore it is also necessary to understand the intracellular fate of polymer coated FNDs. The intracellular fate of the Rho-dcBSA-PEO(5000)$_{27}$ coated FNDs has been visualized by colocalisation experiments of recording the emission intensities of both Rho and FNDs. Most importantly, the emission of the Rho chromophore of the copolymer shell and the FND remain colocalised inside the cells even after 24 h of incubation time (**Figure 4.1.11**). This result implies that the non-covalent electrostatic interaction between Rho-dcBSA-PEO(5000)$_{27}$ and FNDs is very strong so that the complex does not dissociate over the time inside the cell. Most probably, multiple noncovalent bonds between primary amines of Rho-dcBSA-PEO(5000)$_{27}$ and carboxylic acid of FNDs dramatically enhances the binding strength between FNDs and Rho-dcBSA-PEO(5000)$_{27}$ due to entropically favored cooperative effects. The intact coating of Rho-dcBSA-PEO(5000)$_{27}$ on FNDs has significance for the delivery of cancer therapeutics inside cells using polymer coated FNDs. These data will provide guidance for intracellular drug delivery using polymer coated FNDs.

Demonstration of multifunctionality of dcBSA-PEO(5000)$_{27}$ coated FNDs

For different biomedical applications, easy functionalization of the diamond materials is essential. As a proof of principle, in order to demonstrate access to the functional groups such as primary amines on the surface of dcBSA-PEO(5000)$_{27}$ coated FNDs, these residues have been reacted with Fluorescein isothiocyanate (FITC) and NHS activated Atto 520 (**scheme 4.1.2**). The isothiocyanates group of FITC form thioureas and NHS activated Atto 520 forms a stable amide bond upon reaction with primary amines on the surface of FNDs**.** FITC and Atto520 conjugated FNDs were also well uptaken by Hela cells and confocal laser scanning microscopy (CLSM) experiments show the colocalisation of the emission signal of the fluorescent dye and the FNDs. The colocalisation of FNDs and the fluorescent dyes confirms

the successful conjugation of FNDs and it is worthwhile to note that no precipitation or aggregation occurred during or after the bioconjugation reaction. Re-aggregation after the surface functionalization of FNDs is often observed[37] and the present results suggest that dcBSA-PEO(5000)$_{27}$ coated FNDs can in principle be functionalized with variety of biological entities and organic molecules to the FND surface in aqueous media under very mild conditions.

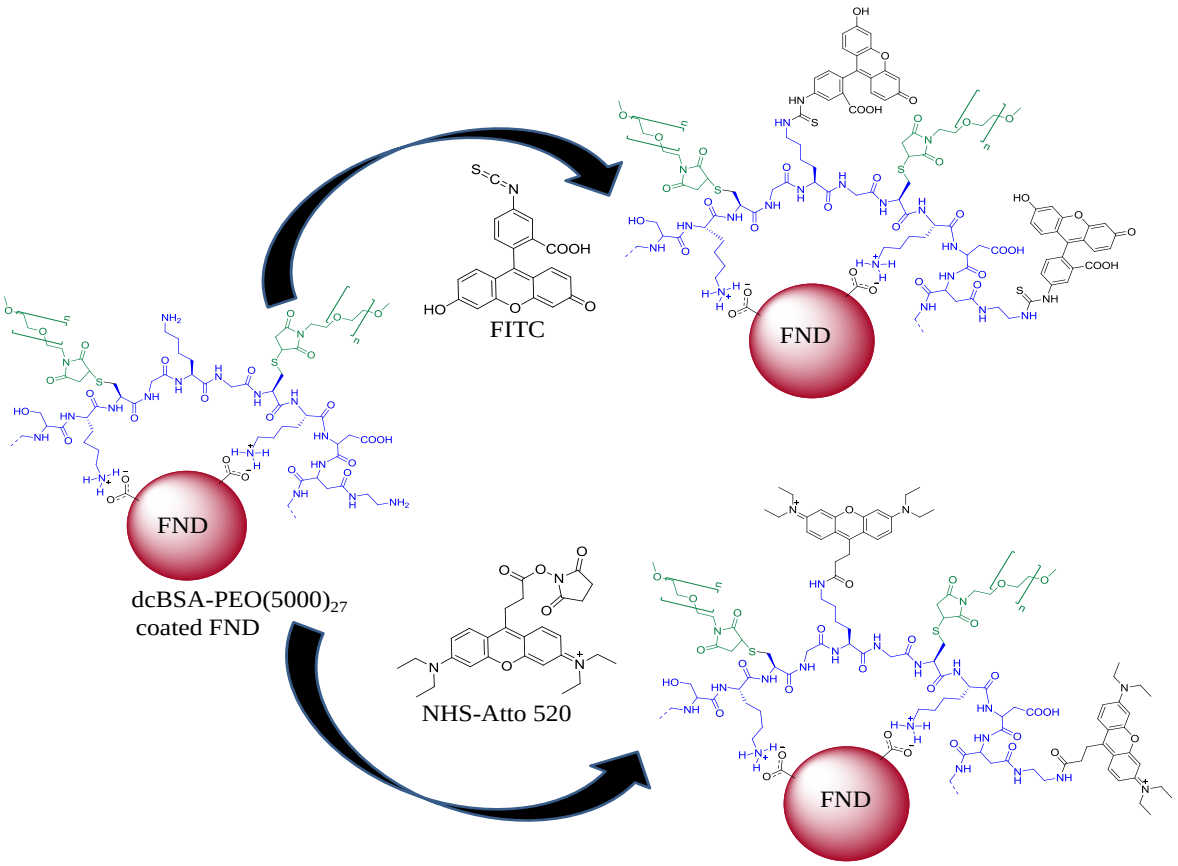

Scheme 4.1.2. Schematic representation of multifunctionality of dcBSA-PEO(5000)$_{27}$ coated FNDs.

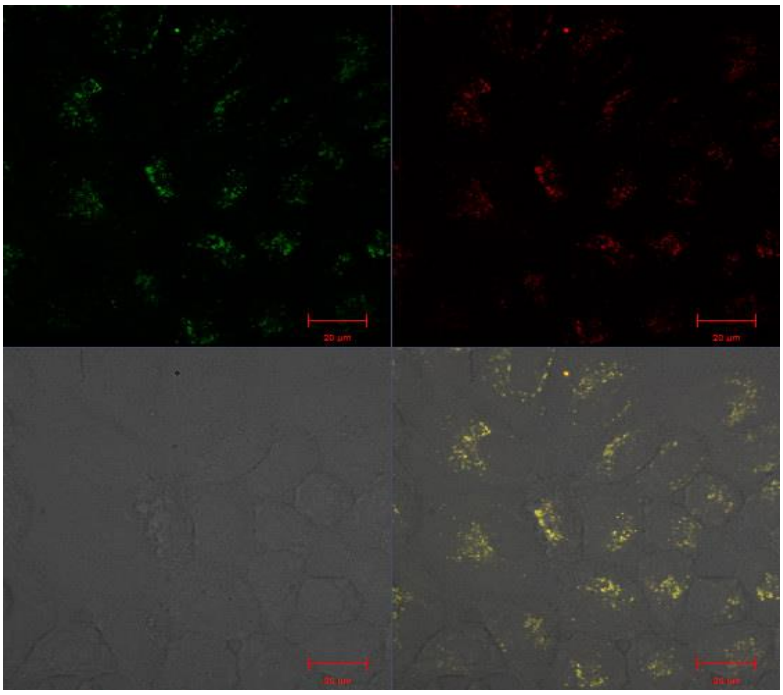

Figure 4.1.12. Confocal microscopy image of Hela cells incubated with FITC labeled dcBSA-PEO(5000)$_{27}$ coated FNDs. (a) Green represents data acquired by the FITC channel. (b) Red represents data acquired by the FNDs channel. (c) DIC image. (d) Overlay. Image scanned using simultaneous scanning.

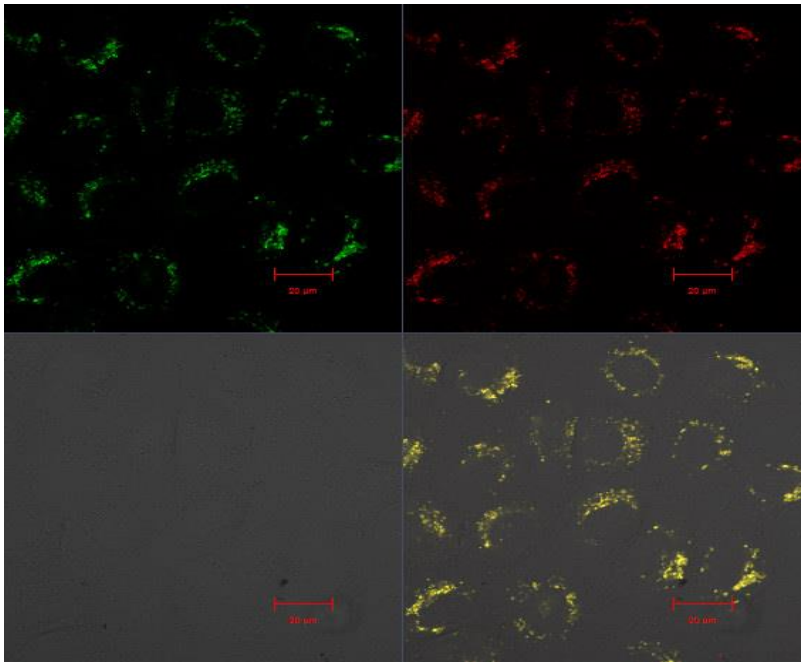

Figure 4.1.13: Confocal microscopy image of Hela cells incubated with Atto 520 labeled dcBSA-PEO(5000)$_{27}$ coated FNDs. (a) Green represents data acquired by the Atto520 channel. (b) Red represents data acquired by the FNDs channel. (c) DIC image. (d) Overlay. Image scanned using simultaneous scanning.

4.1.3. Conclusions

This work presents an important step towards the development of novel fluorescent biomarkers based on photostable diamond colour centers. FNDs have been coated successfully with a multifunctional, biocompatible, nontoxic[33] polypeptide copolymer, Rho-dcBSA-PEO$(5000)_{27}$. The successful coating of FNDs has been characterized by FTIR, XPS, DLS, zeta potential as well as colocalisation studies. The peptide-polymer-coating prevents long term aggregation of FNDs in aqueous solution. Rho-dcBSA-PEO$(5000)_{27}$ coating also abolishes the flocculation of FNDs at very high ionic strength as well as at a wide pH range even at very low pH. The high stability of the FNDs under physiological conditions offers the opportunity for *in vivo* administration, where it is required to monitor the FNDs over a months period after the injection.[98] The presence of PEO on the surface of the FNDs should also reduce opsonization and non-specific interactions with other serum proteins and suppress immunogenic response.[99] Colocalisation of Rho-dcBSA-PEO$(5000)_{27}$ and FNDs have also been shown inside the cell. Colocalisation of Rho-dcBSA-PEO$(5000)_{27}$ and FNDs indicate that Rho-dcBSA-PEO$(5000)_{27}$ and FNDs behave as a single entity inside the cell. Even though **5** and FNDs are not covalently bound, the presence of the strong electrostatic interactions between **5** and FNDs prevents dissociation inside the cell. The obtained results offer the opportunity to functionalize FNDs by simply modifying the dcBSA-PEO$(5000)_{27}$ shell. By this process, the challenges associated with nanodiamond precipitation could be avoided. The procedure reported herein offers a straight forward approach toward non-covalent surface functionalization of FNDs, which will have a great impact on enhancing the use of FNDs as markers for *in vivo* bioimaging, biomedicine and biosensing applications. Noteworthy, the side chains of the amino acids in the polypeptide backbone, such as primary amines from lysine, carboxylic groups from aspartic and glutamic acids, hydroxyl groups of serine, tyrosine and guanidine group of arginine offer the possibility of further covalent (e.g. via hydrazone linkers) functionalization of FNDs with drugs, DNA and tumor targeting agents. The rich surface functionality in combination with NIR fluorescence of FNDs make the nanosystem described herein an potential candidate for building up nanodiamond-based theranostics.

After successful coating of the FNDs with the denatured protein based multifunctional polypeptide and the development of a method for the stabilization of FNDs for cellular studies, the surface functionalization of FNDs will be further explored to address applications

in the field of sensor technology and diagnostics. FNDs are of high interest for detecting biomolecules *in vitro* and *in vivo* based on their unique magnetic properties. In the following section of this chapter, a first prototype will be developed by adsorbing the native metallo-protein ferritin at the surface of FNDs. The impact of the presence of ferritin on the on the relaxation time (T_1) and coherence time (T_2) of FNDs will be studied with the overall aim to establish a novel FNDs detection technology of native proteins in solution.

4.2. Detection of the Metallo-Protein Ferritin Using Color Centers in FNDs

Declraration: "Reprinted (adapted) with permission from *Nano Lett.* **2013**, *13*, 3305. Copyright 2013 American Chemical Society."

4.2.1. Introduction

Magnetic resonance imaging (MRI) is one of the most frequently used imaging tools in clinics, allowing diagnosis to be performed in a noninvasive and real-time manner.[100] Despite its innate high resolution, the low sensitivity of MRI often compromises the quality of diagnosis. The sensitivity of magnetic resonance imaging has recently been further improved to image single cells[101] and magnetic resonance force microscopy[102] has succeeded in detecting even single electrons[103]. However, this technique currently requires cryogenic temperatures, which limits most biological applications.[104] It is desirable to develop detection systems that allow ultrasensitive and rapid detection of single electron spin states under ambient conditions.[105]

Fluorescent nanodiamonds (FNDs) emit bright fluorescence at 550–800 nm due to imperfections called nitrogen-vacancy (NV) centers or color centers. It consists of a substitutional nitrogen atom with an adjacent vacancy (**Figure 4.2.1**) and has C_{3v} symmetry.[106] The N-V center has a large absorption cross section at the excitation wavelength, a short excited state lifetime τ = 11.6 ns[107] and high quantum efficiency ($\Phi \approx 1$)[108] suitable for single center detection. Two out of six electrons of the NV centre are unpaired, forming an electron spin triplet (S=1) in the electronic ground and first excited state. The paramagnetic electron ground state, making it accessible to optically detected

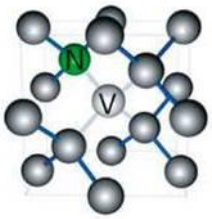

Figure 4.2.1. Structure of Nitrogen Vacancy (NV) center in diamond. (Image Ref[116])

magnetic resonance (ODMR).[109] Most importantly, the NV centre operates at room temperature and offers stable fluorescence even in small nanodiamonds,[110] long spin lifetimes,[111] excellent biocompatibility[112,113] as well as available quantum memory that can be encoded in proximal nuclear spins[114,115] Unlike, magnetic force microscopy NV center based single spin magnetometry also does not require magnetic field gradients. The use of a single diamond spin has allowed to map nanoscale magnetic field variations.[116] More recently, ambient nanoscale magnetic resonance detection of electronic spins of transition elements like Mn^{2+} have been reported by measuring the changes in the decoherence rate (T_2) of a single spin NV probe.[117] The nitrogen-vacancy (NV) colour centre in FNDs is a promising candidate for nanoscale magnetometry and imaging for extraordinary spatial resolution, field precision, linearity and directional sensitivity.[116,118-125]

Ferritins are a family of proteins that are found in many types of animals, plants and prokaryotes, with the primary function being iron storage. Each ferritin molecule is made of 24 subunits, which are self-assembled in a non-covalent fashion into a cagelike nanostructure.[126] Ferritin molecules are hollow protein shells that can store between 2500-4000 iron atoms.[127] Apoferritin is the protein shell, which is ca. 2 nm thick. The cavity inside apoferritin is ca. 8 nm in diameter and it contains a single-domain antiferromagnetic iron-oxyhydroxide-like core with uniaxial anisotropy and a magnetic moment of about 300 μB (resulting from a small fraction of uncompensated Fe^{3+} atomic spins).[128] Ferritin concentrations in serum are positively correlated with the total amount of iron stored in the body. Ferritin is critical to iron homeostasis and metabolism in mammals. Its alteration plays a significant role in anemia, such as iron aplastic anemia, chronic hemolytic anemia, thalassemia, hepatitis, hepatoma and chronic or acute hepatic injury.[129-131] Iron overload and overexpression of ferritin has been suggested to play a role in neurodegeneration in a

genetically engineered mouse model.[132] Hence, the determination of ferritin under physiological conditions to obtain pathological information is of great importance.

To date, various methods have been applied for ferritin detection, such as, electron microscopy,[133,134] atomic force microscopy (AFM) based techniques,[135-139] Western blots,[140] Radioimmunoassays (RIA)[141,142] and different immunoassays[143-147] are commonly used. However, these methods have some limitations. The vacuum environment of electron microscopy analysis and contact-mode and/or the vibrating motion of the samples in AFM imaging may lead to denaturation of the proteins.[134-136,148] The use of ^{125}I in radioimmunoassays requires handling and disposal of radioactive chemicals.[149] Most of the other reported detectors for ferritin use biochemical assays which require expensive specialized instruments for immunochromatography and reproducibility of electrochemistry immunoassays methods are still relatively poor.[145,146] The inductively coupled plasma mass spectrometry (ICP-MS) is also very powerful elemental detector to "screen" the presence of a given element in known or unknown large biomolecules and has also been used for detection of the iron content in ferritin.[150,151] However, the instrument itself is very expensive and prior to detection, the method needs to isolate ferritin from blood serum and also need harsh sample preparation like digestion with nitric acid to extract its iron content.[151] Therefore, the development of a new, simple, sensitive and non-invasive method for ferritin detection is very attractive for clinical applications.

Herein, first experiments for the implementation of FNDs as biological sensors will be demonstrated by immobilizing ferritin proteins at the FNDs surface and by investigating the influence of ferritin on the spin properties of single NV centers in FNDs. The metalloprotein ferritin has been introduced to the surface of carboxylate terminated FNDs by interactions with the amino groups of proteins and carboxylic acids of FNDs. Fourier transform infrared spectroscopy (FTIR), size measurements, zeta Potential, X-ray photoelectron spectroscopy (XPS), high resolution transmission electron microscopy (HRTEM) were used for the characterization of the FND-ferritin complexes (**scheme 4.2.1**). The iron (Fe^{3+}) ions in the protein molecule built a strongly fluctuating spin bath which couples to the electron spin of the NV. This interaction leads to shortening of both the electron spin coherence time (T_2) and relaxation time (T_1) by an order of magnitude, compared to the values for non-coated FNDs.

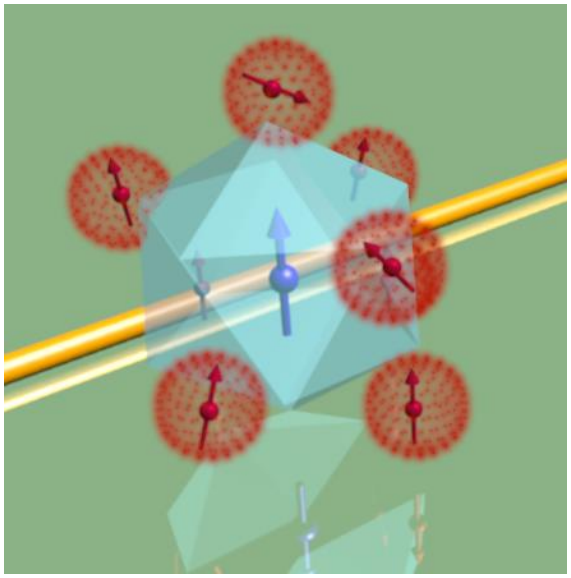

Scheme 4.2.1. Schematic diagram of the interaction between NV center and ferritin. The NV spin is represented in blue and the spin of ferritin in red. The yellow beam represents microwave radiation.

4.2.2. Results and Discussion

Functionalisation of FNDs with ferritin

Bioconjugation to nanoparticles can be performed actively (covalent bonds via chemical reactions) or passively (hydrophobic and/or electrostatic adsorption), after which unbound molecules must be separated.[152] A cost-efficient and simple bioconjugation technique between the nanoparticles and the protein is important, particularly for applications that require large amounts of the functionalized nanomaterials.[152] Furthermore, the covalent coupling of ferritin to FNDs via carbodiimide chemistry around pH 4-6 may induce conformation changes in protein molecules and can lead to denaturation of the protein.[153] Since it is well known that ferritin can dissociate and associate in a pH dependent manner and release iron from the core of the protein at low pH[152,154] and also it is sensitive to redox agents,[155,156] chaotropic agent like guanidine[157]. The outcome of the study of the interaction between FNDs and ferritin depends on the method of conjugation used. It is very important that the method of preparation of FND-ferritin complexes should preserve the native structure of ferritin.

Nanoscale magnetic imaging using the NV center, generally requires close proximity to the sample of interest, since the magnetic field from individual spins falls off with the distance

(r) ~ $1/r^3$.[118] It also means that bringing the NV center closer to the sample places, it is in a stronger field which therefore results in faster detection times and improved spatial resolution.[118] Therefore, it would be highly beneficial to establish a conjugation technique that allows adjusting the distance between the FNDs and ferritin within few nanometers. Keeping in mind all the requirements mentioned above, ferritin was attached to the FNDs surface by exploiting non-covalent interactions between FNDs and the biomolecule as described successfully in the first part (4.1) of this chapter. In a biological medium, FNDs interact with proteins, due to their nano-size and large surface-to-mass ratio and it is also known from the literature that oxidized FNDs are good adsorbents for proteins or polypeptides.[36] The adsorption proceeds mainly through electrostatic attraction forces between the surface-terminating anionic groups ($-COO^-$) and the positively charged amino groups ($-NH_3^+$) of the biomolecules. Previous studies have shown that the oxidized nanodiamond adsorb various biomolecules like proteins,[36,41,77-79] toxins,[80,81] antibodies,[82] hormones.[83] Ferritin was adsorbed to the surface of FNDs by incubating FNDs and ferritin in boric acid buffers at pH 8.5. At pH 8.5, the primary amino groups of ferritin remain positively charged and the surface terminating carboxylic acid of FNDs are negatively charged. The electrostatic attraction forces between the surface-terminating anionic groups ($-COO^-$) and the positively charged amino groups ($-NH_3^+$) facilitate the adsorption of ferritin on the surface of FNDs. Previously it has been observed that the proteins bound to nanoparticles depends on the concentrations of protein in the medium and it increases with increasing protein concentrations.[158] Therefore, to attach a maximum number of ferritin at the surface of FNDs and to make sure that the entire FNDs is covered by ferritin; ferritin was added 50 times in excess compared to FNDs.

Purification of FND-ferritin complexes from unbound free ferrtitin

After formation of the FND-ferritin complex it was observed by TEM that there were many unbound free ferritin molecules in the sample. This free ferritin in the solution can have an unwanted effect on FNDs based sensing. Therefore, it was necessary to separate unbound ferritin from the FND-ferritin complex. Centrifugation is one of the most important separation techniques widely used in colloid science and in cellular and molecular biology.[159] Centrifugal forces move particles radially from the axis of rotation and can separate these particles by size.[160] Since the FND-ferritin complexes have larger sizes than the ferritin only, it is expected that FND-ferritin sediments to the bottom of the centrifuge tube faster than the free ferritin. It is also very important adjust the rotation speed and time, so that only FND-

ferritin complex is able to sediment at the bottom of the centrifuge tube and that free ferritin will remain in the solution. It was found that 1000 rpm and 1 minute is optimal for the separation of FND-ferritin complexes from free ferritin. The FND-ferritin complex was purified from free ferritin by centrifugation and thorough washing with pure Milli-Q water after rotation cycle. The process was repeated for 5 times. The purification process was also monitored by TEM (**Figure 4.2.2**). TEM imaging (**Figure 4.2.2b**) showed that after washing with pure Milli-Q water for 5 times, the free ferritin was completely removed and bound ferritins remained still adsorbed to the surface of the FNDs. Adsorption of ferritin on the FNDs surface even after 5 times washing indicates high affinity of the ferritin towards the FNDs surface.

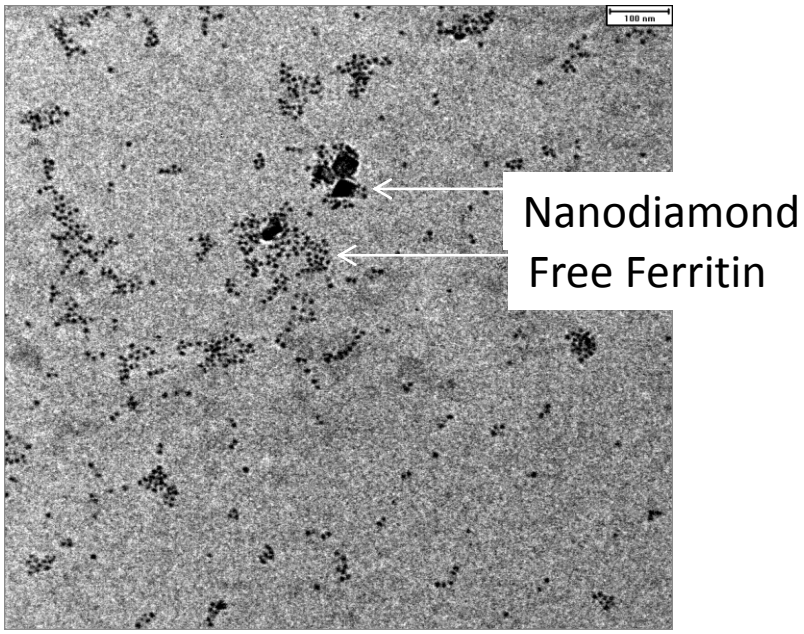

Figure 4.2.2a. TEM image of unpurified ferritin adsorbed FND. Scale bar 100 nm. "Reprinted with permission from *Nano Lett*. **2013**, *13*, 3305. Copyright 2013 American Chemical Society."

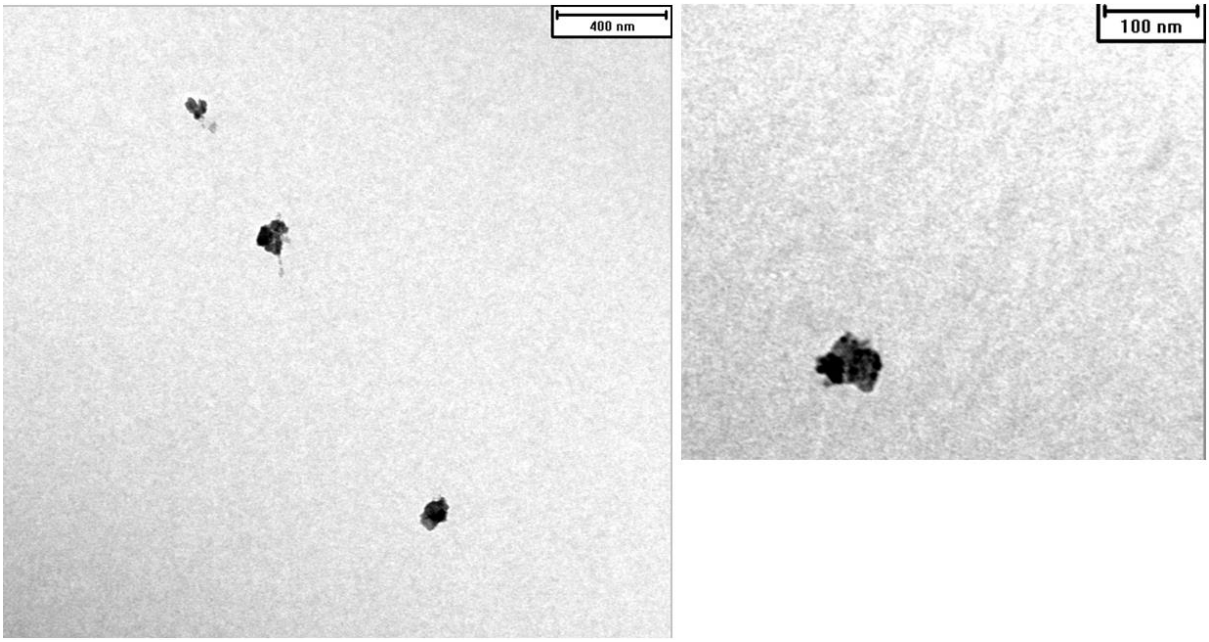

Figure 4.2.2b. TEM image of purified ferritin adsorbed FNDs. "Reprinted with permission from *Nano Lett*. **2013**, *13*, 3305. Copyright 2013 American Chemical Society."

Characterization of FND-ferritin complexes

The successful adsorption of ferritin on FNDs was confirmed by fourier transform infrared spectroscopy (FTIR), size measurement, zeta Potential, X-ray photoelectron spectroscopy (XPS), high resolution transmission electron microscopy (HRTEM).

Fourier transform infrared spectroscopy (FTIR) measurements

Figure 4.2.3a shows the FTIR spectrum of the FNDs. Several distinct features appear at 3435 cm^{-1} and 1635 cm^{-1} in the spectral region. These two peaks can be assigned to the O-H stretch of the surface carboxyl groups and to the C=O stretching of the carboxylate anions. The associated hydrogen bonds between physically adsorbed water molecules are responsible for the broad absorption bands observed between 3000-3600 cm^{-1}. FTIR was carried out to confirm that the protein has been attached to FND. **Figure 4.2.3b** shows the IR spectrum of the FND-ferritin complex. The signals at approximately 1654 $cm^{-}1$ and at 1534 cm^{-} correspond to the amide I and amide II bands, respectively, which relate to the peptide bonds of the protein ferritin. A broad absorption envelope in the low frequency region (700–400 cm^{-1}) was observed in the FND-ferritin spectra. The ferrihydrite peaks appear at 576 cm^{-1}.

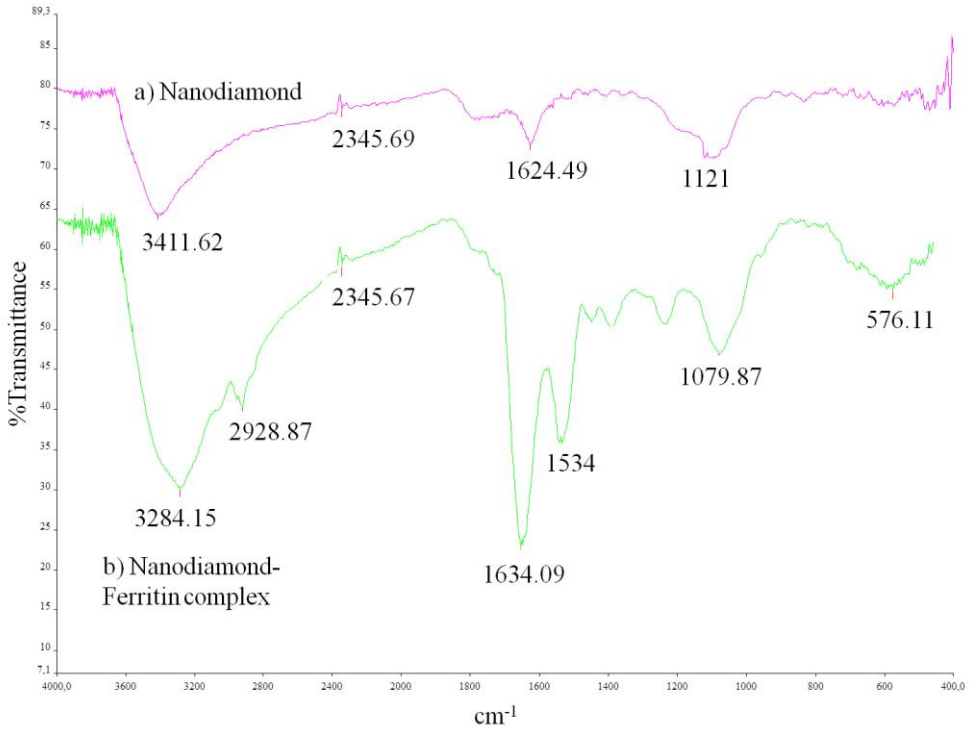

Figure 4.2.3. FTIR spectra of FND-ferritin complexes. "Reprinted with permission from *Nano Lett*. **2013**, *13*, 3305. Copyright 2013 American Chemical Society."

Size measurements

Dynamic light scattering (DLS) measurements

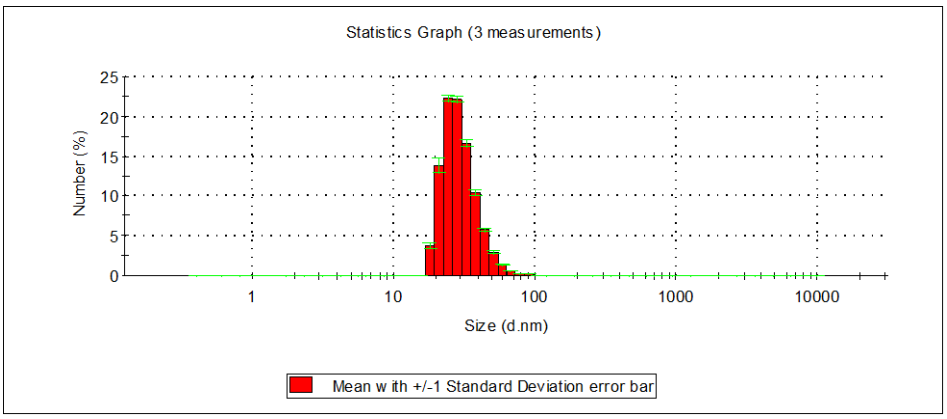

Figure 4.2.4a. Number size distributions of FNDs by DLS. The average hydrodynamic diameter of the FNDs is 30.1±1.2 nm. The results were obtained after three independent measurements. "Reprinted with permission from *Nano Lett.* **2013**, *13*, 3305. Copyright 2013 American Chemical Society."

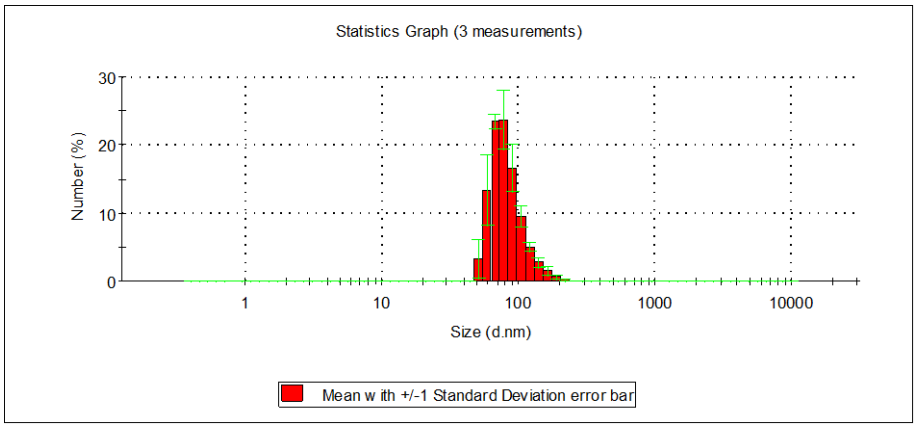

Figure 4.2.4b. Number size distributions of FND-ferritin complexes by DLS. The average hydrodynamic diameter is 83.8±2.7. The results were obtained after three independent measurements. "Reprinted with permission from *Nano Lett.* **2013**, *13*, 3305. Copyright 2013 American Chemical Society."

Dynamic light scattering (DLS) has been used to characterize the FND-ferritin complexes in solution. DLS measurements reveal that the FNDs have an average hydrodynamic diameter of about 30.1±1.2 nm (**Figure 4.2.4a**). After adsorption of ferritin, the hydrodynamic radius of the FND-ferritin complexes increases to an average of 84.5±3.8 nm (**Figure 4.2.4b**). The increase in the hydrodynamic radius reflects the contribution of the ferritin on the diamond surface. The large increase in the hydrodynamic radius may be due to partial aggregation of single FND-ferritin complexes as can be seen in TEM image **Figure 4.2.2b**. Most likely, a mixture of single and dimer FND-ferritin complexes were formed in solution and size of aggregated FND-ferritin complex was around~70-80 nm (**Figure 4.2.2b**).

Zeta Potential measurements

The FND-ferritin complexes have a more negative zeta-potential in comparison with either isolated FND or ferritin (-20.13 mV). Uncoated, carboxylated FNDs bear a negative zeta potential of about -40.9±0.7 mV due to the presence of several deprotonated carboxylic acid groups. After adsorption of ferritin on the FNDs, the zeta potential of the complex further decreased to -46.9±1.1 mV. Most probably due to presence of negatively charged ferritin on the surface of FNDs, the zeta potential of FND-ferritin is more negative than carboxylated FNDs.

X-ray photoelectron spectroscopy (XPS) study

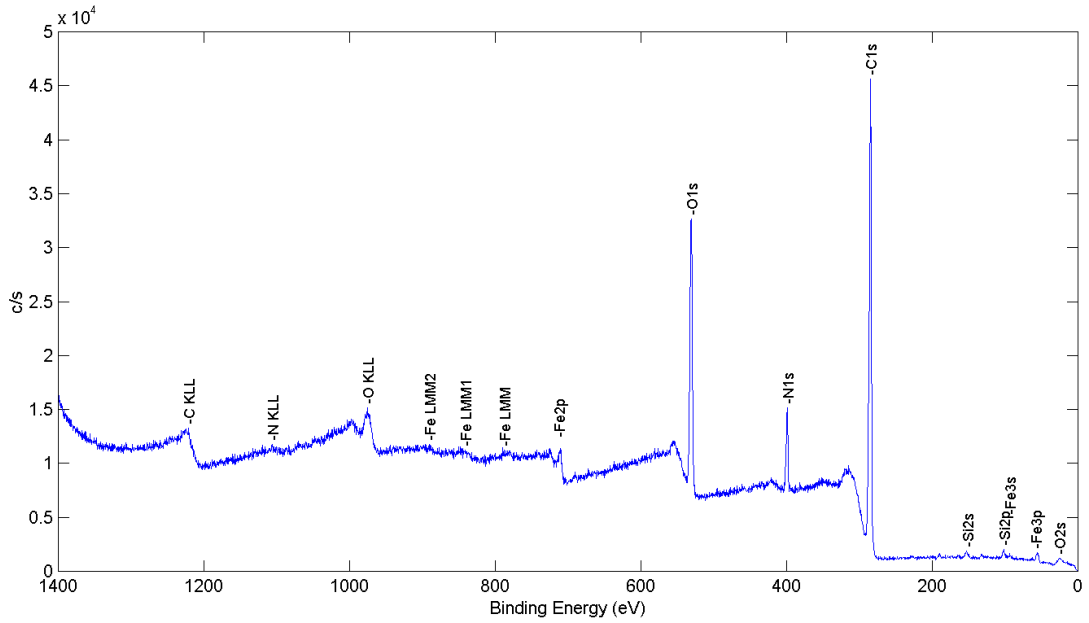

Figure 4.2.5. XPS spectra of FND-ferritin complex, showing the presence of Fe. "Reprinted with permission from *Nano Lett.* **2013**, *13*, 3305. Copyright 2013 American Chemical Society."

X-ray photoelectron spectroscopy (XPS) has been used to gain information about the iron content of the FND-ferritin complexes. An X-ray photo electron spectroscopy (**Figure 4.2.5**) study of FND-ferritin complexes reveals the presence of iron. The 2p transition was observed at 711eV peaks and 3s, 3p exhibit binding energy peak at 95 eV, 53 eV respectively.

High-Resolution Transmission Electron Microscopy (HRTEM)

High Resolution TEM (HRTEM) was utilized for the visualization and characterization of the FND-ferritin complexes. **Figure 4.2.6** shows the HRTEM image of a FND-ferritin complex. HRTEM imaging confirmed the adsorption of ferritin to the FNDs. Spherical, electron dense iron particles with an average size of about 6-8 nm can clearly be seen on the surface of the The HRTEM image was taken by zooming into one of the monomer of FND-ferritin complex. In the HRTEM image, the FNDs and the iron atoms on the surface of FND can be seen. Since the protein shell does not scatter enough electrons, it does not allow for sufficient contrast and hence it remains invisible in HRTEM.

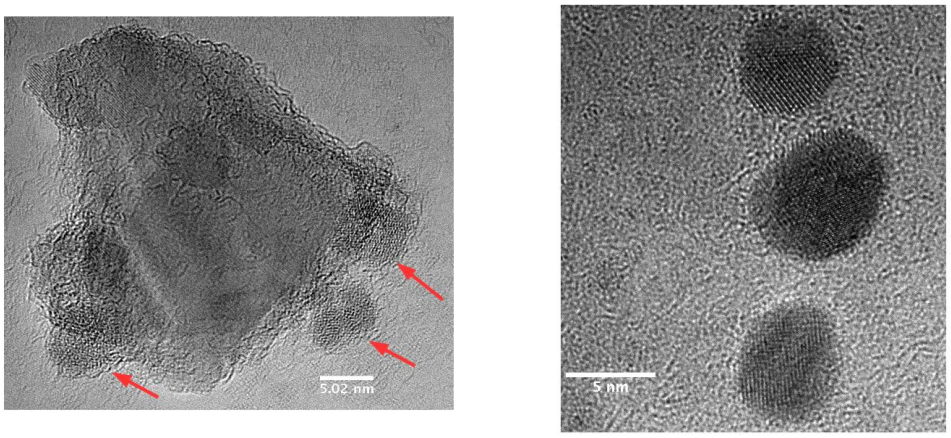

Figure 4.2.6. HRTEM images of ferritin molecules (right) and FND covered with ferritin (left). The red arrows indicate the position of the metalloprotein on the surface. "Reprinted with permission from *Nano Lett.* **2013**, *13*, 3305. Copyright 2013 American Chemical Society."

The optically detected magnetic resonance (ODMR) experiments

The optically detected magnetic resonance (ODMR) experiments have been performed using a home-built confocal microscope.[161] For the optical excitation of the NV centers, a laser beam of 532 nm is focused on the sample (glass cover slip) using an oil immersion objective (60x, NA=1,35). Microwaves for driving the electron spin have been provided by wires produced by standard photolithography on the substrate surface. The electron spin coherence time T_2 has been measured with the ODMR version of the Hahn echo pulse sequence,[162] for the relaxation time T_1 determination the adapted inversion recovery technique was used.[163] In total 64 nanodiamonds was investigated and divided into two groups – free FND (as received, group 1) and purified FND-ferritin complexes (group 2). As a negative control, the decoherence of NV immersed in water (group 1) was measured. The T_1 and T_2 times for both groups are plotted in **Figure 4.2.7** and **Figure 4.2.8** respectively.

In both experiments, the average value for group 2 is about seven times shorter compared to group 1. Upon adsorption of ferritin to the FNDs surface, dipolar coupling to the additional magnetic sources (S = 5/2 Fe^{3+}spins) alters the NV decoherence profile, providing new extrinsic decoherence channels (as opposed to the nitrogen and surface spin baths intrinsic to the FNDs). Importantly, measurements of the spin-echo profile before the addition of spin solution allows the initial decoherence sources to be characterised. By knowing the initial spin environment, measurements on the same single spin probes allow detecting changes in the local magnetic fields arising from the exposure to ferritin. This result confirms that the

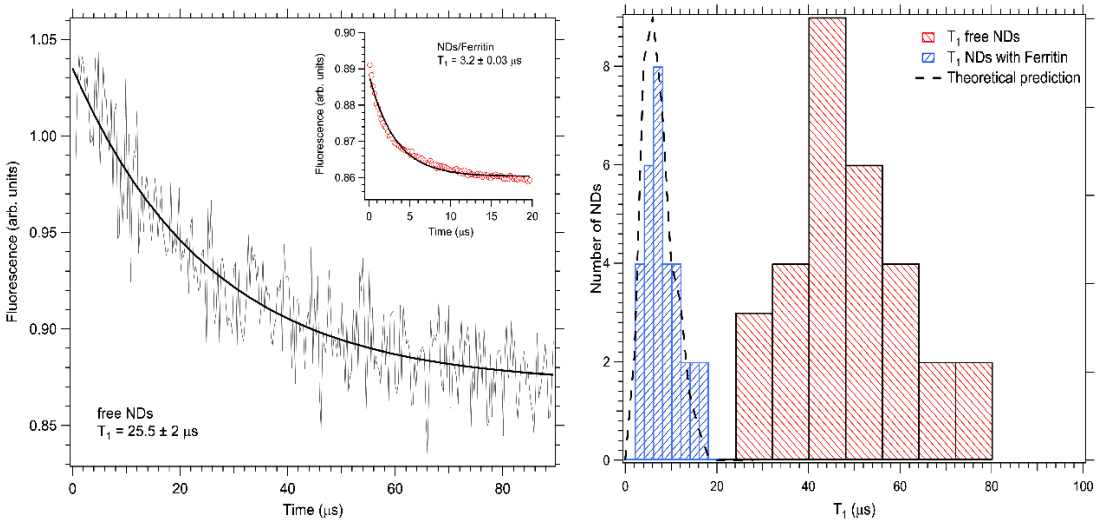

.

Figure 4.2.7. Measurement of the electron spin-lattice relaxation time T_1 of NV covered by FNDs from group 1 (left) and in FNDs from group 2 (left, inset). Statistical distribution of the T_1 for "free" FNDs (right, blue bars) and for coated FNDs (right, red bars). Decrease of T_1 for group 2 is clearly visible. The black dotted curve is a theoretical model using the fluctuation dynamics of the iron ions. "Reprinted with permission from *Nano Lett.* **2013**, *13*, 3305. Copyright 2013 American Chemical Society."

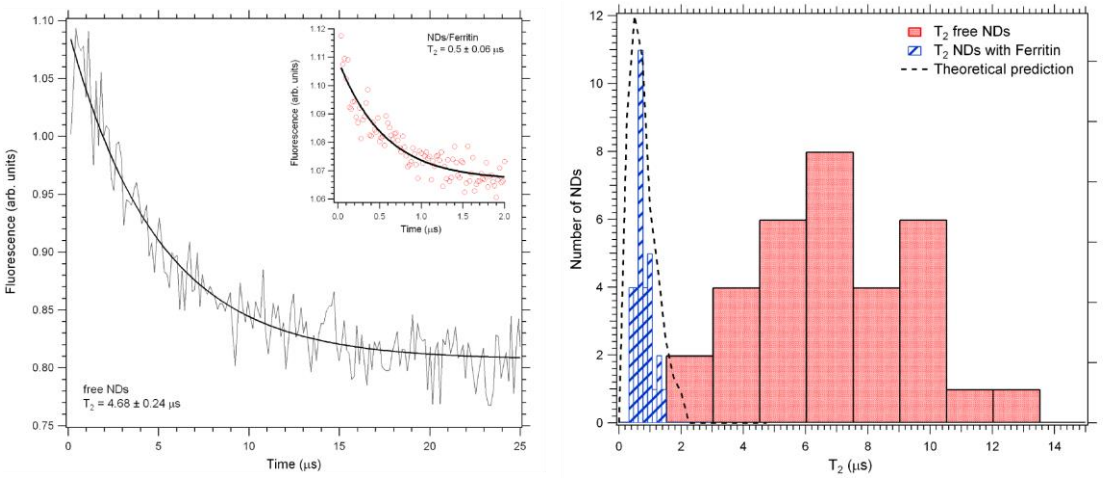

Figure 4.2.8. Electron spin Hahn echo decay for FNDs in group 1 (left) and group 2 (left, Inset). Again a decrease of T_2 for group is observed. The dotted line is a theoretical model. "Reprinted with permission from *Nano Lett.* **2013**, *13*, 3305. Copyright 2013 American Chemical Society."

presence of the ferritin molecules has a strong impact on the spin properties of NV, thus demonstrating the feasibility of FNDs as nano-scale magnetic field sensors. Theoretical models have been established in collaboration with Prof. Martin Plenio, Controlled Quantum Dynamics Group, Universität Ulm which can fully describe the observed effects.

The iron Fe^{3+} (electron spin 5/2) is stored as a ferrihydrite mineral $[FeO(OH)]_8[FeO(H_2PO_4)]$, which is attached to the inner wall of the apoferritin sphere. The mutual flip-flops of Fe^{3+} spins cause fluctuating magnetic fields acting on the NV inside the FNDs. This process has been modeled classically and analyzed in cooperation with the group of Prof. Martin Plenio, Controlled Quantum Dynamics Group, Universität Ulm. The iron spins exchange polarization randomly at a certain rate, which is related to the line width of the electron spin resonance spectrum of ferritin. The transversal component of this fluctuating field leads to the relaxation of the NV center and shorten the value of T_1. The noise spectrum at the frequency corresponding to the NV centers' zero field splitting (i.e. ω_o=2.87 GHz) gives the estimation of T_1 as $1/S^{\perp}$ ($\omega=\omega_o$). The value of T_2 is affected by the longitudinal component of the fluctuating field. The decay of the coherence in the spin echo experiment can be calculated from the longitudinal noise spectrum $S^{\parallel}(\omega)$ and the filter function of spin echo as

$$SE = \exp\left[-\chi(t)\right] = 8\int_0^{\infty} \frac{d\omega}{\pi} S^{//}(\omega) \sin^4\left(\frac{\omega t}{4}\right) \frac{1}{\omega^2}$$

The statistics of the numerical results are obtained from the simulation of a number of nano FNDs with 8 to 15 ferritins attached. The numerical results for T_1 and T_2 are shown as dashed lines in **Figure 4.2.1** and **Figure 4.2.8** respectively. The parameter of the iron spin exchange polarization rate is chosen as 2.1 GHz, which is corresponds to the reported spectral width of the ESR signal of ferritin.[164] There is a good agreement between the experimental results and the theoretical prediction.

Table 4.2.1. Summary of the effect of ferritin on NV center.

	FND	FND-ferritin
T_1	43.6 μS	23.2 μS
	FND	**FND-ferritin**
T_2	3.4 μS	0.62 μS

Conclusions

External spins (Fe^{3+}) have been introduced at the FNDs surface to detect their presence by measuring changes in the NV decoherence rate, T_1. Nanoscale magnetic resonance detection of spins extrinsic to the NV center, using T_1 and T_2 of NV spins have been demonstrated. NV spin-echo shed light on the surface spin dynamics of FNDs. FNDs sensing in principle offers certain advantages over more conventional immunoassays, such as it is non-invasive and does not need the use of expensive instruments or harsh sample preparation. The experimental demonstration of decoherence detection in biological environment underpins the considerable potential of nanoscale decoherence-based biosensing.

The potential impact of single-spin imaging of ferritin at room temperature can be far-reaching. The ferritin core composition significantly differs between physiological and pathological conditions. Although iron storage is the main role of ferritin, it has also been observed that ferritin can bind other atoms such as aluminum, zinc etc.[165] Many experimental evidences indicate a possible relationship between the presence of aluminium (Al) inside the ferritin core and the development of Alzheimer's disease (AD).[166] AD patients shows a low percentage of Fe and high content of Al in ferritin.[167] The metal content of ferritin may serve as biomarkers for neurodegenerative diseases, such as Alzheimer's or Parkinson's disease.[167] Therefore, it would be an important finding if Al is detected inside the ferritin core using NV center detection. Understanding the chemical structure of the ferritin core may also help to develop an early diagnosis method for the onset of degenerative diseases.

4.3. References

(1) Orrit, M. *J. Chem. Phys.* **2002**, *117*, 10938.
(2) Klar, T. A.; Jakobs, S.; Dyba, M.; Egner, A.; Hell, S. W. *Proc.Natl. Acad.Sci. USA* **2000**, *97*, 8206.
(3) Resch-Genger, U.; Grabolle, M.; Cavaliere-Jaricot, S.; Nitschke, R.; Nann, T. *Nat. Methods* **2008**, *5*, 763.
(4) Chang, Y. R.; Lee, H. Y.; Chen, K.; Chang, C. C.; Tsai, D. S.; Fu, C. C.; Lim, T. S.; Tzeng, Y. K.; Fang, C. Y.; Han, C. C.; Chang, H. C.; Fann, W. *Nat.Nanotechnol.* **2008**, *3*, 284.
(5) Fu, C. C.; Lee, H. Y.; Chen, K.; Lim, T. S.; Wu, H. Y.; Lin, P. K.; Wei, P. K.; Tsao, P. H.; Chang, H. C.; Fann, W. *Proc.Natl. Acad.Sci. USA* **2007**, *104*, 727.
(6) Schrand, A. M.; Huang, H. J.; Carlson, C.; Schlager, J. J.; Osawa, E.; Hussain, S. M.; Dai, L. M. *J. Phys.Chem. B* **2007**, *111*, 2.
(7) Jelezko, F.; Wrachtrup, J. *Phys. Status Solidi A* **2006**, *203*, 3207.
(8) Bradac, C.; Gaebel, T.; Naidoo, N.; Sellars, M. J.; Twamley, J.; Brown, L. J.; Barnard, A. S.; Plakhotnik, T.; Zvyagin, A. V.; Rabeau, J. R. *Nat. Nanotechnol.* **2010**, *5*, 345.

(9) Tisler, J.; Balasubramanian, G.; Naydenov, B.; Kolesov, R.; Grotz, B.; Reuter, R.; Boudou, J. P.; Curmi, P. A.; Sennour, M.; Thorel, A.; Borsch, M.; Aulenbacher, K.; Erdmann, R.; Hemmer, P. R.; Jelezko, F.; Wrachtrup, J. *Acs Nano* **2009**, *3*, 1959.
(10) Jelezko, F.; Wrachtrup, J. *J.Phys-Condens Mat.* **2004**, *16*, R1089.
(11) Gruber, A.; Drabenstedt, A.; Tietz, C.; Fleury, L.; Wrachtrup, J.; vonBorczyskowski, C. *Science* **1997**, *276*, 2012.
(12) Balasubramanian, G.; Chan, I. Y.; Kolesov, R.; Al-Hmoud, M.; Tisler, J.; Shin, C.; Kim, C.; Wojcik, A.; Hemmer, P. R.; Krueger, A.; Hanke, T.; Leitenstorfer, A.; Bratschitsch, R.; Jelezko, F.; Wrachtrup, J. *Nature* **2008**, *455*, 648.
(13) Dolde, F.; Fedder, H.; Doherty, M. W.; Nobauer, T.; Rempp, F.; Balasubramanian, G.; Wolf, T.; Reinhard, F.; Hollenberg, L. C. L.; Jelezko, F.; Wrachtrup, J. *Nat. Phys.* **2011**, *7*, 459.
(14) Maze, J. R.; Stanwix, P. L.; Hodges, J. S.; Hong, S.; Taylor, J. M.; Cappellaro, P.; Jiang, L.; Dutt, M. V. G.; Togan, E.; Zibrov, A. S.; Yacoby, A.; Walsworth, R. L.; Lukin, M. D. *Nature* **2008**, *455*, 644.
(15) Han, K. Y.; Willig, K. I.; Rittweger, E.; Jelezko, F.; Eggeling, C.; Hell, S. W. *Nano Lett.* **2009**, *9*, 3323.
(16) Han, K. Y.; Kim, S. K.; Eggeling, C.; Hell, S. W. *Nano Lett.* **2010**, *10*, 3199.
(17) Cai, J. M.; Jelezko, F.; Plenio, M. B.; Retzker, A. *New J. Phys.* **2013**, *15*, 013020.
(18) Dahoumane, S. A.; Nguyen, M. N.; Thorel, A.; Boudou, J.-P.; Chehimi, M. M.; Mangeney, C. *Langmuir* **2009**, *25*, 9633.
(19) Tu, J. S.; Perevedentseva, E.; Chung, P. H.; Cheng, C. L. *J.Chem.Phys.***2006**, *125*, 174713.
(20) Mochalin, V.; Osswald, S.; Gogotsi, Y. *Chem.Mater.***2008**, *21*, 273.
(21) Comet, M.; Pichot, V.; Siegert, B.; Britz, F.; Spitzer, D. *J. Nanosci. Nanotechnol.* **2010**, *10*, 4286.
(22) Krueger, A. *J.Mater.Chem.* **2011**, *21*, 12571.
(23) Jarre, G.; Liang, Y.; Betz, P.; Lang, D.; Krueger, A. *Chem.Commun.* **2011**, *47*, 544.
(24) Liang, Y.; Meinhardt, T.; Jarre, G.; Ozawa, M.; Vrdoljak, P.; Schöll, A.; Reinert, F.; Krueger, A. *J.Colloid Interf. Sci.* **2011**, *354*, 23.
(25) Wang, J.; Firestone, M. A.; Auciello, O.; Carlisle, J. A. *Langmuir* **2004**, *20*, 11450.
(26) Chang, I. P.; Hwang, K. C.; Ho, J. A.; Lin, C.-C.; Hwu, R. J. R.; Horng, J.-C. *Langmuir* **2009**, *26*, 3685.
(27) Chang, I. P.; Hwang, K. C.; Chiang, C.-S. *J.Am.Chem.Soc.* **2008**, *130*, 15476.
(28) Chen, L.-H.; Lim, T.-S.; Chang, H.-C. *J. Opt. Soc. Am. B* **2012**, *29*, 2309.
(29) Pichot, V.; Comet, M.; Fousson, E.; Baras, C.; Senger, A.; Le Normand, F.; Spitzer, D. *Diamond Relat.Mater.* **2008**, *17*, 13.
(30) Mitev, D.; Dimitrova, R.; Spassova, M.; Minchev, C.; Stavrev, S. *Diamond Relat.Mater.* **2007**, *16*, 776.
(31) Osswald, S.; Yushin, G.; Mochalin, V.; Kucheyev, S. O.; Gogotsi, Y. *J. Am. Chem.Soc.***2006**, *128*, 11635.
(32) Lim, T.-S.; Fu, C.-C.; Lee, K.-C.; Lee, H.-Y.; Chen, K.; Cheng, W.-F.; Pai, W. W.; Chang, H.-C.; Fann, W. *Phys.Chem.Chem.Phys.***2009**, *11*, 1508.
(33) Mochalin, V. N.; Gogotsi, Y. *J. Am.Chem.Soc.***2009**, *131*, 4594.
(34) Manus, L. M.; Mastarone, D. J.; Waters, E. A.; Zhang, X.-Q.; Schultz-Sikma, E. A.; MacRenaris, K. W.; Ho, D.; Meade, T. J. *Nano Lett.***2009**, *10*, 484.
(35) Ushizawa, K.; Sato, Y.; Mitsumori, T.; Machinami, T.; Ueda, T.; Ando, T. *Chem. Phys. Lett.* **2002**, *351*, 105.
(36) Huang, L. C. L.; Chang, H.-C. *Langmuir* **2004**, *20*, 5879.
(37) Mochalin, V. N.; Shenderova, O.; Ho, D.; Gogotsi, Y. *Nat. Nanotechnol.* **2012**, *7*, 11.

(38) Chao, J.-I.; Perevedentseva, E.; Chung, P.-H.; Liu, K.-K.; Cheng, C.-Y.; Chang, C.-C.; Cheng, C.-L. *Biophys. J.***2007**, *93*, 2199.
(39) Eidelman, E. D.; Siklitsky, V. I.; Sharonova, L. V.; Yagovkina, M. A.; Vul, A. Y.; Takahashi, M.; Inakuma, M.; Ozawa, M.; Õsawa, E. *Diamond Relat.Mater.* **2005**, *14*, 1765.
(40) Yuan, Y.; Chen, Y.; Liu, J.-H.; Wang, H.; Liu, Y. *Diamond Relat.Mater.* **2009**, *18*, 95.
(41) Tzeng, Y.-K.; Faklaris, O.; Chang, B.-M.; Kuo, Y.; Hsu, J.-H.; Chang, H.-C. *Angew. Chem. Int. Ed.* **2010**, *50*, 2262.
(42) Krueger, A.; Lang, D. *Adv. Func. Mater.* **2012**, *22*, 890.
(43) Zhang, B.; Li, Y.; Fang, C.-Y.; Chang, C.-C.; Chen, C.-S.; Chen, Y.-Y.; Chang, H.-C. *Small* **2009**, *5*, 2716.
(44) Hartmann, M.; Betz, P.; Sun, Y.; Gorb, S. N.; Lindhorst, T. K.; Krueger, A. *Chem. Eur. J.* **2012**, *18*, 6485.
(45) Krueger, A.; Stegk, J.; Liang, Y.; Lu, L.; Jarre, G. *Langmuir* **2008**, *24*, 4200.
(46) Presti, C.; Alauzun, J. G.; Laurencin, D.; Mutin, P. H. *Chem. Mater.* **2013**, *25*, 2051.
(47) Romanova, E. E.; Akiel, R.; Cho, F. H.; Takahashi, S. *J. Phys. Chem. A.* **2013**, DOI: 10.1021/jp403183x
(48) Zhong, Y. L.; Loh, K. P.; Midya, A.; Chen, Z.-K. *Chem. Mater.* **2008**, *20*, 3137.
(49) Barras, A.; Szunerits, S.; Marcon, L.; Monfilliette-Dupont, N.; Boukherroub, R. *Langmuir* **2010**, *26*, 13168.
(50) Basiuk, E. V.; Santamaría-Bonfil, A.; Meza-Laguna, V.; Gromovoy, T. Y.; Alvares-Zauco, E.; Contreras-Torres, F. F.; Rizo, J.; Zavala, G.; Basiuk, V. A. *Appl. Surf. Sci.* **2013**, *275*, 324.
(51) Cheng, J.; He, J.; Li, C.; Yang, Y. *Chem. Mater.* **2008**, *20*, 4224.
(52) Huynh, V. T.; Pearson, S.; Noy, J.-M.; Abboud, A.; Utama, R. H.; Lu, H.; Stenzel, M. H. *ACS Macro Lett.* **2013**, *2*, 246.
(53) Xu, G.; Zhang, W.; Wei, L.; Lu, H.; Yang, P. *Analyst* **2013**, *138*, 1876.
(54) Man, H. B.; Kim, H.; Kim, H.-J.; Robinson, E.; Liu, W. K.; Chow, E. K.-H.; Ho, D. *Nanomedicine: Nanotechnology, Biology and Medicine* **2013** DOI:10.1016/j.nano.2013.07.014.
(55) Mochalin, V. N.; Pentecost, A.; Li, X.-M.; Neitzel, I.; Nelson, M.; Wei, C.; He, T.; Guo, F.; Gogotsi, Y. *Mol. Pharm.* **2013** DOI: 10.1021/mp400213z.
(56) Zhang, X.; Wang, S.; Liu, M.; Hui, J.; Yang, B.; Tao, L.; Wei, Y. *Toxicol. Res.* **2013**, *2*, 335.
(57) Zhang, X.-Q.; Lam, R.; Xu, X.; Chow, E. K.; Kim, H.-J.; Ho, D. *Adv. Mater.***2013**, *23*, 4770.
(58) Li, Y.; Zhou, X.; Wang, D.; Yang, B.; Yang, P. *J. Mater.Chem.***2011**, *21*, 16406.
(59) Martín, R.; Álvaro, M.; Herance, J. R.; García, H. *ACS Nano* **2010**, *4*, 65.
(60) Chen, M.; Zhang, X.-Q.; Man, H. B.; Lam, R.; Chow, E. K.; Ho, D. *J.Phys. Chem. Lett.***2010**, *1*, 3167.
(61) Kim, H.; Man, H. B.; Saha, B.; Kopacz, A. M.; Lee, O.-S.; Schatz, G. C.; Ho, D.; Liu, W. K. *J. Phys.Chem. Lett.* **2012**, *3*, 3791.
(62) Alhaddad, A.; Adam, M.-P.; Botsoa, J.; Dantelle, G.; Perruchas, S.; Gacoin, T.; Mansuy, C.; Lavielle, S.; Malvy, C.; Treussart, F.; Bertrand, J.-R. *Small* **2011**, *7*, 3087.
(63) Boudou, J.-P.; David, M.-O.; Joshi, V.; Eidi, H.; Curmi, P. A. *Diamond Relat. Mater.***2013**, *38*, 131.
(64) Zhang, X.; Wang, S.; Fu, C.; Feng, L.; Ji, Y.; Tao, L.; Li, S.; Wei, Y. *Polym. Chem.* **2010**, *3*, 2716.
(65) Bumb, A.; Sarkar, S. K.; Billington, N.; Brechbiel, M. W.; Neuman, K. C. *J.Am.Chem.Soc.***2013**, *135*, 7815.

(66) Geidel, C.; Schmachtel, S.; Riedinger, A.; Pfeiffer, C.; Müllen, K.; Klapper, M.; Parak, W. J. *Small* **2011**, *7*, 2929.
(67) Ning, Y.; Zhang, H.; Han, J.; Yang, C.; Liu, Y.; Zhou, D.; Yang, B. *J. Mater. Chem.* **2011**, *21*, 6837.
(68) Liu, G.-Y.; Liu, X.-S.; Wang, S.-S.; Chen, C.-J.; Ji, J. *Langmuir* **2012**, *28*, 557.
(69) Chen, H.; Wu, X.; Duan, H.; Wang, Y. A.; Wang, L.; Zhang, M.; Mao, H. *ACS Appl.Mater.***2009**, *1*, 2134.
(70) Chen, K.; Xie, J.; Xu, H.; Behera, D.; Michalski, M. H.; Biswal, S.; Wang, A.; Chen, X. *Biomaterials* **2009**, *30*, 6912.
(71) Yang, M.; Chen, T.; Lau, W. S.; Wang, Y.; Tang, Q.; Yang, Y.; Chen, H. *Small* **2009**, *5*, 198.
(72) Chen, H. Y.; Abraham, S.; Mendenhall, J.; Delamarre, S. C.; Smith, K.; Kim, I.; Batt, C. A. *ChemPhysChem* **2008**, *9*, 388.
(73) Ashley, C. E.; Carnes, E. C.; Phillips, G. K.; Padilla, D.; Durfee, P. N.; Brown, P. A.; Hanna, T. N.; Liu, J.; Phillips, B.; Carter, M. B.; Carroll, N. J.; Jiang, X.; Dunphy, D. R.; Willman, C. L.; Petsev, D. N.; Evans, D. G.; Parikh, A. N.; Chackerian, B.; Wharton, W.; Peabody, D. S.; Brinker, C. J. *Nat. Mater.* **2011**, *10*, 389.
(74) Zou, P.; Yu, Y.; Wang, Y. A.; Zhong, Y.; Welton, A.; Galbán, C.; Wang, S.; Sun, D. *Mol.Pharm.* **2010**, *7*, 1974.
(75) Qi, L.; Gao, X. *ACS Nano* **2008**, *2*, 1403.
(76) Yezhelyev, M. V.; Qi, L.; O'Regan, R. M.; Nie, S.; Gao, X. *J. Am. Chem.Soc.* **2008**, *130*, 9006.
(77) Kong, X. L.; Huang, L. C. L.; Hsu, C. M.; Chen, W. H.; Han, C. C.; Chang, H. C. *Anal. Chem.***2004**, *77*, 259.
(78) Puzyr', A.; Pozdnyakova, I.; Bondar', V. *Phys. Solid State+* **2004**, *46*, 761.
(79) Nguyen, T. T.-B.; Chang, H.-C.; Wu, V. W.-K. *Diamond Relat.Mater.* **2007**, *16*, 872.
(80) Kuang-Kai Liu, M.-F. C., Po-Yi Chen, Tony J F Lee, Chia-Liang Cheng, Chia-Ching Chang, Yen-Peng Ho and Jui-I Chao *Nanotechnology* **2008**, *19*, 205102.
(81) Puzyr', A.; Purtov, K.; Shenderova, O.; Luo, M.; Brenner, D.; Bondar, V. *Dokl. Biochem. Biophys.* **2007**, *417*, 299.
(82) Purtov, K. V.; Petunin, A. I.; Burov, A. E.; Puzyr, A. P.; Bondar, V. S. *Nanoscale Res. Lett.***2010**, *5*, 631 .
(83) Shimkunas, R. A.; Robinson, E.; Lam, R.; Lu, S.; Xu, X.; Zhang, X.-Q.; Huang, H.; Osawa, E.; Ho, D. *Biomaterials* **2009**, *30*, 5720.
(84) Militello, V.; Vetri, V.; Leone, M. *Biophys. Chem.* **2003**, *105*, 133.
(85) Eisele, K.; Gropeanu, R. A.; Zehendner, C. M.; Rouhanipour, A.; Ramanathan, A.; Mihov, G.; Koynov, K.; Kuhlmann, C. R. W.; Vasudevan, S. G.; Luhmann, H. J.; Weil, T. *Biomaterials* **2010**, *31*, 8789.
(86) Wu, Y.; Pramanik, G.; Eisele, K.; Weil, T. *Biomacromolecules* **2012,** *13*, 1890.
(87) Lin-Vien, D. C., N. B.; Fateley, W. G.; Grasselli, J. G. *The Handbook of Infrared and RamanCharacteristic Frequencies of Organic Molecules*; Academic: Boston, MA., 1991.
(88) Cantor, C. R. S., P. R. *Biophysical Chemistry*; Freeman: San Francisco, CA, 1980; Part II, Chapter X.
(89) Flegler SL, H. J. J., Klomparens KL *Scanning and Transmission Electron Microscopy: An Introduction.*; W.H. Freeman and Company: New York 1993.
(90) Mei, B. C.; Oh, E.; Susumu, K.; Farrell, D.; Mountziaris, T. J.; Mattoussi, H. *Langmuir* **2009**, *25*, 10604.
(91) Wang, D.; Tong, Y.; Li, Y.; Tian, Z.; Cao, R.; Yang, B. *Diamond Relat.Mater.* **2013**, *36*, 26.

(92) Kneipp, J.; Kneipp, H.; McLaughlin, M.; Brown, D.; Kneipp, K. *Nano Lett.* **2006**, *6*, 2225.
(93) El-Sayed, I. H.; Huang, X.; El-Sayed, M. A. *Nano Lett.* **2005**, *5*, 829.
(94) Mallidi, S.; Larson, T.; Tam, J.; Joshi, P. P.; Karpiouk, A.; Sokolov, K.; Emelianov, S. *Nano Lett.* **2009**, *9*, 2825.
(95) Aaron, J.; Travis, K.; Harrison, N.; Sokolov, K. *Nano Lett.* **2009**, *9*, 3612.
(96) Kim, S.; Shi, Y.; Kim, J. Y.; Park, K.; Cheng, J. *Expert Opin. Drug Del.* **2010**, *7*, 49.
(97) Chen, H.; Kim, S.; Li, L.; Wang, S.; Park, K.; Cheng, J.-X. *Proc. Natl. Acad.Sci. USA* **2008**, *105*, 6596.
(98) Vaijayanthimala, V.; Cheng, P.-Y.; Yeh, S.-H.; Liu, K.-K.; Hsiao, C.-H.; Chao, J.-I.; Chang, H.-C. *Biomaterials* **2012**, *33*, 7794.
(99) Owens III, D. E.; Peppas, N. A. *Int. J. Pharm.* **2006**, *307*, 93.
(100) Cleary, K.; Peters, T. M. *Annu.Rev. Biomed. Eng.***2010**, *12*, 119.
(101) Aguayo, J. B.; Blackband, S. J.; Schoeniger, J.; Mattingly, M. A.; Hintermann, M. *Nature* **1986**, *322*, 190.
(102) Rugar, D.; Yannoni, C. S.; Sidles, J. A. *Nature* **1992**, *360*, 563.
(103) Rugar, D.; Budakian, R.; Mamin, H. J.; Chui, B. W. *Nature* **2004**, *430*, 329.
(104) Paul, G.; Sir Peter, M. *Rep. Prog. Phys.* **2002**, *65*, 1489.
(105) Gruber, A.; Dräenstedt, A.; Tietz, C.; Fleury, L.; Wrachtrup, J.; Borczyskowski, C. *Science* **1997**, *276*, 2012.
(106) Loubser, J. H. N.; Wyk, J. A. *Rep.Prog. Phys.* **1978**, *41*, 1201.
(107) Collins, A. T.; Thomaz, M. F.; Jorge, M. I. B. *J.Physics C Solid State* **1983**, *16*, 2177.
(108) G. Davies *Properties and Growth of Diamond*; INSPEC, The Institution of Electrical Engineers: London, 1994.
(109) Harley, R. T.; Henderson, M. J.; Macfarlane, R. M. *J. Phys. C Solid State* **1984**, *17*, L233.
(110) Bradac, C.; Gaebel, T.; Naidoo, N.; Sellars, M. J.; TwamleyJ; Brown, L. J.; Barnard, A. S.; PlakhotnikT; Zvyagin, A. V.; Rabeau, J. R. *Nat. Nanotechnol.* **2010**, *5*, 345.
(111) Balasubramanian, G.; Neumann, P.; Twitchen, D.; Markham, M.; Kolesov, R.; Mizuochi, N.; Isoya, J.; Achard, J.; Beck, J.; Tissler, J.; Jacques, V.; Hemmer, P. R.; Jelezko, F.; Wrachtrup, J. *Nat. Mater.* **2009**, *8*, 383.
(112) Fu, C.-C.; Lee, H.-Y.; Chen, K.; Lim, T.-S.; Wu, H.-Y.; Lin, P.-K.; Wei, P.-K.; Tsao, P.-H.; Chang, H.-C.; Fann, W. *Proc. Natl. Acad.Sci. USA* **2007**, *104*, 727.
(113) McGuinness, L. P.; YanY; StaceyA; Simpson, D. A.; Hall, L. T.; MaclaurinD; PrawerS; MulvaneyP; WrachtrupJ; CarusoF; Scholten, R. E.; Hollenberg, L. C. L. *Nat. Nanotechnol.* **2011**, *6*, 358.
(114) Jelezko, F.; Gaebel, T.; Popa, I.; Domhan, M.; Gruber, A.; Wrachtrup, J. *Phys. Rev. Lett.* **2004**, *93*, 130501.
(115) Dutt, M. V. G.; Childress, L.; Jiang, L.; Togan, E.; Maze, J.; Jelezko, F.; Zibrov, A. S.; Hemmer, P. R.; Lukin, M. D. *Science* **2007**, *316*, 1312.
(116) Balasubramanian, G.; Chan, I. Y.; Kolesov, R.; Al-Hmoud, M.; Tisler, J.; Shin, C.; Kim, C.; Wojcik, A.; Hemmer, P. R.; Krueger, A.; Hanke, T.; Leitenstorfer, A.; Bratschitsch, R.; Jelezko, F.; Wrachtrup, J. *Nature* **2008**, *455*, 648.
(117) McGuinness, L. P.; Hall, L. T.; Stacey, A.; Simpson, D. A.; Hill, C. D.; Cole, J. H.; Ganesan, K.; Gibson, B. C.; Prawer, S.; Mulvaney, P.; Jelezko, F.; Wrachtrup, J.; Scholten, R. E.; Hollenberg, L. C. L. *New J. Phys.* **2013**, *15*, 073042.
(118) Taylor, J. M.; Cappellaro, P.; Childress, L.; Jiang, L.; Budker, D.; Hemmer, P. R.; Yacoby, A.; Walsworth, R.; Lukin, M. D. *Nat. Phys.* **2008**, *4*, 810.

(119) Maze, J. R.; Stanwix, P. L.; Hodges, J. S.; Hong, S.; Taylor, J. M.; Cappellaro, P.; Jiang, L.; Dutt, M. V. G.; Togan, E.; Zibrov, A. S.; Yacoby, A.; Walsworth, R. L.; Lukin, M. D. *Nature* **2008**, *455*, 644.
(120) Degen, C. L. *Appl. Phys.Lett.* **2008**, *92*, 243111.
(121) Rondin, L.; Tetienne, J. P.; Spinicelli, P.; Savio, C. D.; Karrai, K.; Dantelle, G.; Thiaville, A.; Rohart, S.; Roch, J. F.; Jacques, V. *Appl. Phys. Lett.***2011**, *100*, 153118.
(122) Maletinsky, P.; Hong, S.; Grinolds, M. S.; Hausmann, B.; Lukin, M. D.; Walsworth, R. L.; Loncar, M.; YacobyA *Nat. Nanotechnol.* **2012**, *7*, 320.
(123) Nusran, N. M.; Momeen, M. U.; Dutt, M. V. G. *Nat. Nanotechnol.* **2012**, *7*, 109.
(124) Maertz, B. J.; Wijnheijmer, A. P.; Fuchs, G. D.; Nowakowski, M. E.; Awschalom, D. D. *Appl.Phys. Lett.* **2010**, *96*, 092504.
(125) Pham, L. M.; Sage, D. L.; Stanwix, P. L.; Yeung, T. K.; Glenn, D.; Trifonov, A.; Cappellaro, P.; Hemmer, P. R.; Lukin, M. D.; Park, H.; Yacoby, A.; Walsworth, R. L. *New J. Phys.* **2011**, *13*, 045021.
(126) Uchida, M.; Kang, S.; Reichhardt, C.; Harlen, K.; Douglas, T. *BBA-Gen Subjects* **2010**, *1800*, 834.
(127) Zhang, F.; Gates, R. J.; Smentkowski, V. S.; Natarajan, S.; Gale, B. K.; Watt, R. K.; Asplund, M. C.; Linford, M. R. *J.Am.Chem.Soc.***2007**, *129*, 9252.
(128) Simon, K. H. L.; John, R. C.; Wenrong, Y. *Nanotechnology* **2011**, *22*, 455501.
(129) Yoneda, M.; Nozaki, Y.; Endo, H.; Mawatari, H.; Iida, H.; Fujita, K.; Yoneda, K.; Takahashi, H.; Kirikoshi, H.; Inamori, M.; Kobayashi, N.; Kubota, K.; Saito, S.; Maeyama, S.; Hotta, K.; Nakajima, A. *Dig. Dis. Sci.* **2010**, *55*, 808.
(130) Shalitin, S.; Carmi, D.; Weintrob, N.; Phillip, M.; Miskin, H.; Kornreich, L.; Zilber, R.; Yaniv, I.; Tamary, H. *Eur. J. Haematol.* **2005**, *74*, 93.
(131) Knovich, M. A.; Storey, J. A.; Coffman, L. G.; Torti, S. V.; Torti, F. M. *Blood Rev.* **2009**, *23*, 95.
(132) Grabill, C.; Silva, A. C.; Smith, S. S.; Koretsky, A. P.; Rouault, T. A. *Brain Res.* **2003**, *971*, 95.
(133) Fernández, B.; Gálvez, N.; Sánchez, P.; Morales, J.; Santoyo, F.; Cuesta, R.; Domínguez-Vera, J. M. *Inorg. Chim. Acta* **2007**, *360*, 3951.
(134) Fujikawa, S.; Muto, E.; Kunitake, T. *Langmuir* **2007**, *23*, 4629.
(135) Daniels, S.; Ngunjiri, J.; Garno, J. *Anal. Bioanal. Chem.* **2009**, *394*, 215.
(136) Schön, P.; Görlich, M.; Coenen, M. J. J.; Heus, H. A.; Speller, S. *Langmuir* **2007**, *23*, 9921.
(137) Pakes, C. I.; George, D. P.; Ramelow, S.; Cimmino, A.; Jamieson, D. N.; Prawer, S. *J. Magn. Magn. Mater* **2004**, *272-276*, E1231-E1233.
(138) Tominaga, M.; Ohira, A.; Yamaguchi, Y.; Kunitake, M. *J.Electroanal.Chem.***2004**, *566*, 323.
(139) Ohnishi, S.; Hara, M.; Furuno, T.; Okada, T.; Sasabe, H. *Biophys. J.***1993**, *65*, 573.
(140) Liu, P.; Na, N.; Liu, T.; Huang, L.; He, D.; Hua, W.; Ouyang, J. *PROTEOMICS* **2011**, *11*, 3510.
(141) Manns, M., Meyerzumbuschenfelde, K. H., Hutteroth, T. H., Hess, G. *Clin. Exp. Immunol.* **1980**, *42*, 263.
(142) Pluygers EP, B. M., Baldewyns PE, Burion J.A. *Cancer Detect. Prev.* **1986**, *9*, 495.
(143) Shapiro, M. G.; Szablowski, J. O.; Langer, R.; Jasanoff, A. *J. Am.Chem. Soc.* **2009**, *131*, 2484.
(144) Muhsen, K.; Barak, M.; Shifnaidel, L.; Nir, A.; Bassal, R.; Cohen, D. *J. Pediatr.Gastr. Nutr.* **2009**, *49*, 262.
(145) Wang, X.; Tao, G.; Meng, Y. *Microchim.Acta* **2009**, *167*, 147.
(146) Zhang, X.; Wang, S.; Hu, M.; Xiao, Y. *Biosens. Bioelectron.* **2006**, *21*, 2180.

(147) Wang, S.-F.; Tan, Y.-M. *Anal.Bioanal.Chem.***2007**, *387*, 703.
(148) Dobson, J. *FEBS Lett.* **2001**, *496*, 1.
(149) Husák V, B. M. *Cas. Lek. Cesk.* **1979**, *118*, 117.
(150) Sanz-Medel, A.; Montes-Bayón, M.; Sánchez, M. L. F. *Anal. Bioanal. Chem.* **2003**, *377*, 236.
(151) Scott M. Smith, P. L. G. In *NASA Tech Briefs* Houston, Texas, 2003.
(152) Jääskeläinen, A.; Soukka, T.; Lamminmäki, U.; Korpimäki, T.; Virta, M. *Biotechnol. Bioeng.* **2009**, *102*, 1012.
(153) Saptarshi, S.; Duschl, A.; Lopata, A. *J. Nanobiotechnology* **2013**, *11*, 26.
(154) Lin, X.; Xie, J.; Zhu, L.; Lee, S.; Niu, G.; Ma, Y.; Kim, K.; Chen, X. *Angew.Chem.Int.Ed.* **2011**, *50*, 1569.
(155) Matioli, G. T.; Baker, R. F. *J.Ultra Mol. struc.R.***1963**, *8*, 477.
(156) Lipschitz, D. A.; Bothwell, T. H.; Seftel, H. C.; Wapnick, A. A.; Charlton, R. W. *Brit.J. Haematol.* **1971**, *20*, 155.
(157) Listowsky, I.; Blauer, G.; Englard, S.; Betheil, J. J. *Biochemistry* **1972**, *11*, 2176.
(158) Monopoli, M. P.; Walczyk, D.; Campbell, A.; Elia, G.; Lynch, I.; Baldelli Bombelli, F.; Dawson, K. A. *J. Am. Chem. Soc.* **2011**, *133*, 2525.
(159) Brakke, M. K.; Kenneth, M. S.; Max, A. L. In *Advances in Virus Research*; Academic Press: 1961; Vol. Volume 7, p 193.
(160) Kowalczyk, B.; Lagzi, I. n.; Grzybowski, B. A. *Curr.Opin. Colloid In.* **2011**, *16*, 135.
(161) Dolde, F.; Jakobi, I.; Naydenov, B.; Zhao, N.; Pezzagna, S.; Trautmann, C.; Meijer, J.; Neumann, P.; Jelezko, F.; Wrachtrup, J. *Nat. Phys.***2011**, *9*, 139.
(162) Jelezko, F.; Gaebel, T.; Popa, I.; Gruber, A.; Wrachtrup, J. *Phys.Rev.Lett.* **2004**, *92*, 076401.
(163) Schweiger, A. J., G. *Principles of Pulse Electron Paramagnetic Resonance* Oxford University Press: New York, 2001.
(164) Wajnberg, E.; El-Jaick, L. ; Linhares, M. P.; Esquivel, D. M. S. *J. Magn. Reson.* **2001**, *153*, 69.
(165) De Sole, P.; Rossi, C.; Chiarpotto, M.; Ciasca, G.; Bocca, B.; Alimonti, A.; Bizzarro, A.; Rossi, C.; Masullo, C. *Clin. Biochem.* **2013**, *46*, 89.
(166) Exley, C. *J. Inorg. Biochem.***1999**, *76*, 133.
(167) Gupta, V.; Anitha, S.; Hegde, M. L.; Zecca, L.; Garruto, R. M.; Ravid, R.; Shankar, S. K.; Stein, R.; Shanmugavelu, P.; Jagannatha Rao, K. S. *CMLS-Cell. Mol. Life S.* **2005**, *62*, 143.

Chapter 5. Summary and Outlook

In this thesis, innovative approaches have been introduced to prepare highly stable, multifunctional, biocompatible NIR emitting nanoprobes (AuNPs and FNDs) by coating the nanoprobes with polypeptide based copolymers. Protocols have been established to functionalise the NIR probes to stain particular cell organelle (nucleus) and for sensing of biomolecule (ferritin). Although the successes have been achieved in synthesis and applications of NIR probes, there are still several unexplored features that require further studies. In the following section the achievements of this thesis have been summarised and also the further directions have been proposed.

In this dissertation work the methods for preparation of monodisperse multifunctional copolymers from globular proteins have been developed. Copolymers with different polypeptide length, charge, secondary structure have been realised by using polyethyleneoxide (PEO) as a highly biocompatible and water soluble stabilizer. Instead of PEO it is in principle also possible to use other polymers, such as dendrimers or hydrophobic polymers as stabilizing agent. The use of a broader stabilizing agent would allow preparation of polypeptide copolymers with unique properties suitable for more diverse applications. For instance, using hydrophobic polymers as side chains might result in unique supramolecular aggregation properties or using dendrimers as side chains might lead to change in rigidity of the copolymers.

These copolymers have been used for preparation of highly stable ultrasmall NIR emitting AuNPs. It has been observed that AuNPs stabilised by copolymer with shorter backbone emits more hypsochromic. It would be interesting to prepare AuNPs with various lengths of copolymers and gain a clear understanding of the effect of length copolymers on the emission properties of AuNPs. This might lead to a method to prepare AuNPs with tunable emission wavelength.

These multifunctional biocompatible NIR emitting AuNPs prepared in this thesis can easily be conjugated to various drug and targeting molecule, such as folic acid, antibody for tumor selective drug delivery. NIR emitting fluorescent AuNPs for targeting cell nuclei have been constructed and the nuclear uptake has been shown in live intact cell. It can be anticipated that the NIR emitting AuNPs may be a promising starting point for the fabrication of multifunctional nanomaterials for the study of nucleus biology. It has been reported that a significant enhancement in the anticancer activity of the drug; if the drug is directly delivered to the cell nucleus.[1] Therefore construction of multifunctional AuNPs for nuclear-targeted

drug delivery system for cancer therapy would be interesting. The drug and NIR emitting AuNPs conjugate could be very helpful in studying the mechanism of action of drug. It is also worth trying this nuclear targeting NIR emitting AuNPs as a non-viral gene delivery agent. One of the bottlenecks for non-viral gene transfer is the nuclear transport of the DNA/vector complex. The ultra small NIR emitting nuclear targeting AuNPs have been developed in this thesis work could help to overcome the bottlenecks by delivering the gene to cell nucleus and improve the efficacy of gene therapy.

It has been shown that non-covalent polypeptide copolymer coating of FNDs prevents the aggregation of FNDs in biological media. The copolymer coated FNDs behave as a single entity inside the cell and they do not dissociate inside the cell. The obtained results offer the opportunity to functionalize FNDs by simply modifying the copolymer shell. Already in my lab the experiments regarding the functionalization of FNDs are in progess. Currently, copolymer coated FNDs have been covalently conjugated to anticancer agent, such as doxorubicin via an acid sensitive hydrazone linker and the pH sensitive release profile, toxicity of the drug is under study using different optical method, such as FCS, CLSM. Polypeptide copolymer coated FNDs have very attractive potential as nanoparticles based drug delivery system.

It has also been shown that the ferritin molecules have a strong effect on both coherence and relaxation time of the FNDs. The iron (Fe^{3+}) ions in the protein molecule built a strongly fluctuating spin bath which couples to the electron spin of the NV. This interaction leads to shortening of both the electron spin coherence time (T_2) and relaxation time (T_1) by an order of magnitude, compared to the values for non-coated FNDs. Iron overload, over expression of ferritin have been implicated for neurodegeneration in a genetically engineered mouse model.[2,3] Although ferritin has its main role in iron storage, several experimental evidences demonstrate that it is able to bind also *in vivo* other metals, such as aluminum and zinc.[4,5] Many experimental evidences indicate a possible relationship between the presence of Al inside the ferritin core and the development of Alzheimer's disease (AD).[6,7] AD patients show a low percentage of Fe and high content of Al in ferritin.[8] The metal content of ferritin serve as biomarkers for neurodegenerative diseases, such as Alzheimer’s, Parkinson’s etc. It would be practically useful to develop a new FNDs based detection method that can differentiate between various metal content (e.g., Fe^{3+}, Al^{3+}) inside the ferritin. This technique could be a valuable tool for the early diagnosis of onset of Alzheimer and follow-up of the diseases.

Detection of metalloenzyme by FNDs can also be extended to other metallo enzymes containing paramagnetic metal, such as manganese-containing superoxide dismutase (Mn-SOD or SOD2). Manganese-containing superoxide dismutase (Mn-SOD or SOD2), a specific antioxidant enzyme for superoxide, is a primary cellular defence enzyme involved in protecting cells from oxidative stress.[9] It would be highly interesting to study the effect of manganese in MnSOD on coherence and relaxation time of the FNDs. By observing the effect of change in oxidation state of manganese ($Mn^{2+} \leftrightarrow Mn^{3+}$) on coherence and relaxation time of FNDs, the mechanism of antioxidant activity of MnSOD can be studied.

References

(1) Pan, L.; He, Q.; Liu, J.; Chen, Y.; Ma, M.; Zhang, L.; Shi, J. *J.Am.Chem.Soc.* **2012**, *134*, 5722.
(2) Grabill, C.; Silva, A. C.; Smith, S. S.; Koretsky, A. P.; Rouault, T. A. *Brain Res.* **2003**, *971*, 95.
(3) Smith, M. A.; Harris, P. L. R.; Sayre, L. M.; Perry, G. *Proc.Natl. Acad.Sci.USA* **1997**, *94*, 9866.
(4) Fleming, J. T.; Joshi, J. G. *Neurobiol. Aging* **1991**, *12*, 413.
(5) Sakamoto, T.; Ogasawara, Y.; Ishii, K.; Takahashi, H.; Tanabe, S. *Neurosci. Lett.* **2004**, *366*, 264.
(6) Exley, C. *J.Inorg.Biochem.***1999**, *76*, 133.
(7) Gupta, V.; Anitha, S.; Hegde, M. L.; Zecca, L.; Garruto, R. M.; Ravid, R.; Shankar, S. K.; Stein, R.; Shanmugavelu, P.; Jagannatha Rao, K. S. CMLS-*Cell.Mol. Life S.* **2005**, *62*, 143.
(8) De Sole, P.; Rossi, C.; Chiarpotto, M.; Ciasca, G.; Bocca, B.; Alimonti, A.; Bizzarro, A.; Rossi, C.; Masullo, C. *Clin. Biochem.* **2013**, *46*, 89.
(9) Chan, P. H. *Stroke* **1996**, *27*, 1124.

Experimental Details

Materials

All chemical reagents were obtained from commercial suppliers and used without further purification unless otherwise noted. Human serum albumin (HSA), hen egg white lysozyme (LY), bovine serum albumin (BSA), trypsin inhibitor from *Glycine max* (Kunitz)**,** trypsin inhibitor from chicken egg white (Ovomucoid), dithiothreitol (DTT), *O*-(2-maleimidoethyl)-*O′*-methylpolyethylene(oxide)-5000 (PEO(5000)-MI), *N*-(2-aminoethyl)maleimide, 4,4′-dithiodipyridine (DPS), sinapinic acid (ultrapure, matrix substance) and horse spleen ferritin were purchased from Sigma-Aldrich. cBSA-147 (cBSA) was synthesized according to the previous report.[1] Hydrogen tetrachloroaurate (III) trihydrate (>99.9%), *N*-(3 dimethylaminopropyl)-*N′*-ethylcarbodiimide hydrochloride, *tris*(2-carboxyethyl)phosphine (TCEP), sorbitol, guanidine.HCl, guanidine.SCN, thioctic acid and *N*-hydroxysuccinimide were purchase from Alfa Aesar. $NaBH_4$ (98%) from Lancaster, Nuclear Localisation Sequence (NLS) (PKKKRKVEDPYC) from GL Biochemical Ltd, China and 4′,6-diamidin-2-phenylindole (DAPI) was purchased from Fluka. Dulbecco's modified eagle medium (DMEM) with glucose 4.5 g/L, fetal bovine serum (FBS) in standard quality (EU approved) from PAA Laboratories and MEM non-essential amino acids solution 10 mM (100×) from Invitrogen were used for cell culture. Fluorescent nanodiamonds were produced according to literature.[2] Deionized water was purified with a Milli Q plus system (Millipore) having a resistivity >18 mΩ/cm.

Instruments and General Procedure of Measurements

Dynamic Light Scattering (DLS)

The particle size and size distribution {polydispersity index (PDI)} were measured by DLS on a Nano-Zetasizer (Malvern Instruments) at 20 ºC under the scattering angle of 173º at 633 nm wavelength. Particle sizes are given as the average of three independent measurements. The dispersion was diluted with water in a glass cuvette before the measurement.

Zeta Potential Measurements

Zeta potential measurements were performed at room temperature using a Nano-Zetasizer (Malvern, UK). The nanoparticles were resuspended in 5 mM KCl at a concentration of 0.5 mg/mL. The pH was adjusted to 7 by diluted HCl or NaOH. The zeta potential was calculated from the electrophoretic mobility using the Smoluchowski equation[3] as the average values of three runs.

Transmission Electron Microscopy (TEM)

TEM measurements were performed on a Zeiss EM 10 microscope with an acceleration voltage of 80 kV. A total of 5 μL of the sample was placed on a 400-mesh carbon coated copper grid and air dried at room temperature.

UV-visible Absorption Spectroscopy

UV-visible spectra were recorded on a TECAN infinite M1000 microplate reader. Aqueous AuNPs solutions (300 μL) were analyzed in a 96 well μclear bottom black microplate (Greiner, Germany) at room temperature.

Fluorescence Spectroscopy

Emission spectra were recorded on a TECAN infinite M1000 microplate reader upon excitation at 365 nm. The aqueous AuNPs solutions (300 μL) were analyzed in 96 well μclear bottom black microplates (Greiner, Germany) at room temperature.

MALDI-ToF-MS Spectrometry

All MALDI-ToF-MS spectra of protein and peptide samples were recorded on Bruker Daltronics REFLEX III mass. The matrix for protein samples used in the experiments was a 1:1 (v/v) MeCN/H_2O (0.1 % TFA) mixture which was saturated with sinapinic acid (3-(4-hydroxy-3,5-dimethoxyphenyl)prop-2-enoic acid). In order to run a sample, 0.5 μl of the sample solution was pipetted on the metal microplate target, followed by 0.5 μl of the matrix solution and dried in air before analysis. All the MALDI-ToF MS spectra were analysed by "mmass" software.

Gel Filtration

Bio-Gel P30 from Bio-Rad was used for desalting column. 1 mL protein solution can be purified by 4 g of Bio-Gel P30 gel powder. First, 4 g of Bio-Gel P30 gel needed to be incubated in 15 mL of Milli Q water at RT overnight before use. Then, the gel was packed in a gel filtration column resulting in about 10 mL of the activated gel. MQ-water was applied to wash the column continuously until the elution was completely free of any impurities as assayed by UV determination. Later, 1 mL of protein solution was loaded on the column and eluted with Milli Q water. 0.5 mL per fraction were collected and assayed *via* UV absorption. Pure fractions were combined which is a protein solution in Milli Q water free of any salts and small molecules. Water was further removed *via* lyophilization to afford the lyophilized form of the proteins.

Fourier Transform Infrared Spectroscopy (FTIR)

IR spectra was measured over the wavelength range of 4000–400 cm^{-1} using the KBr disc method with a FT-IR spectrometer (Perkin Elmer Spectrum 2000). The dried nanoparticle

samples were mixed with KBr powder and pressed into pellets, which were then placed in an IR cell. The blank KBr spectrum provided the background for subtraction. Sample spectra were baseline-corrected and smoothed using the Nicoletinstrumental software (OMNICw) provided.

X-Ray Photoelectron Spectroscopy

Instrument: Physical Electronics "PHI 5800 ESCA System". Excitation with monochromatized Al K_α radiation (15 kV, 300 W); angle sample-analysator 45°; pass energy: 93.9 eV for survey scans, 5.85 eV for detail scans; fixed analyzer transmission (FAT)-mode. Neutralization with electron flood gun, C (1s) peak binding energy set to 284.8 eV. The samples were adsorbed on Si wafers. The information of all elements in thin films were gained from the survey scan spectrum of XPS. The detailed information of each element in the thin film were obtained from the narrow scan spectrum of XPS.

AKTA

ÄKTA Purifier FPLC and SuperoseTM 6 10/30 column were used for protein copolymer purification. 20 mM Tris, 150 mM NaCl (pH 7.4) buffer was used as eluent.

Sodium Dodecyl Sulfate Polyacrylamide Gel Electrophoresis (SDS PAGE)

Precast NuPAGE TA 3%-8% Gel and NuPAGE Bis-Tris 4%-12% Gel were purchased from Invitrogen and gel electrophoresis was performed in Invitrogen Novek^{TM} Mini-Cell.

Circular dichroism study

Circular dichroism (CD) spectra were measured on a JASCO J-810 spectropolarimeter.

Vivaspin centrifugal concentrators were purchased from GE healthcare.

Chapter 2. Preparation of Monodisperse, Multifunctional Polypeptide Copolymers

Preparation of dcBSA-PEO(5000)$_{28}$-(TA)$_{26}$ (2) and dHSA-PEO(5000)$_{27}$-(TA)$_{22}$ (4), (Scheme 2.1)

cBSA (cationised bovine serum albumin) or HSA (0.3 μmol) were dissolved in degassed urea-phosphate buffer (10 mL, 10 mM phosphate buffer, 5 M urea and 2 mM EDTA, pH 7.4) and stirred at room temperature for 15 min. TCEP (8.6 mg, 30 μmol) was added as a solid and the solution was stirred for additional 30 min under argon atmosphere. Then, PEO-5000-MI (154 mg, 31 μmol) was added and stirred under argon atmosphere for 3 hrs. After the attachment of the PEO chains, *N*-(2-aminoethyl)maleimide trifluoroacetate salt (8 mg, 31.5 μmol) was introduced and the solution was stirred for another 3 hrs under argon atmosphere

in order to react with the remaining thiol groups. Thereafter, the reaction mixture was purified by size exclusion FPLC (ÄKTA Explore, SuperoseTM 6 10/30 column, 20 mM Tris-HCl buffer with 150 mM NaCl, pH 7.4). The purified sample fraction corresponding to first protein peak was collected and concentrated by ultrafiltration. Subsequently, the product mixture was passed through a Bio-Gel P30 desalting column and lyophilized to afford as white solid. Yield-40%.

Preparation of dKunitz-PEO(5000)$_4$ (6) (Scheme 2.2)

5mg Kunitz was denatured using 5mL guanidine-Tris buffer (8M guanidine, 0.2 M NaCl, 1 mM EDTA, and 0.1 M Tris/HCl) stirring at 100^{0}C for 4 hour. TCEP (8.6 mg, 30 μmol) was added as a solid and the solution was stirred for additional 30 min under argon atmosphere. Then, PEO-5000-MI (154 mg, 31 μmol) was added and stirred under argon atmosphere for 3 hrs. Thereafter, the reaction mixture was purified by size exclusion FPLC (ÄKTA Explore, SuperoseTM 6 10/30 column, 20 mM Tris-HCl buffer with 150 mM NaCl, pH 7.4). The purified sample fraction corresponding to first protein peak was collected and concentrated by ultrafiltration. Subsequently, the product mixture was passed through a Bio-Gel P30 desalting column and lyophilized to afford as white solid. Yield-25%

Preparation of dLY-PEO(5000)$_8$ (8) (Scheme 2.3)

5 mg Lysozyme was denatured using 4 mL guanidine-Tris buffer (8M guanidine, 0.2 M NaCl, 1 mM EDTA, 0.1 M Tris/HCl, pH 8.5) by stirring at room temperature for 4 hour. Then the disulphide bonds of lysozyme were reduced by adding 1mL 1M DTT and stirring at room temperature for 24 h. After 24 h, the pH of the reaction mixture was adjusted to below 4 using HCl. DTT was separated manually by Sephadex G25 column using 0.1 M acetic acid as eluent. Then the solution was lyophilized to get *Denatured Lysozyme*. PEO-5000-MI (41mg, 8.2 μmol) was dissolved in degassed urea-phosphate buffer (10 mL, 10 mM phosphate buffer, 5 M urea and 2 mM EDTA, pH 7.4) and stirred at room temperature for 15 min. Then *Denatured Lysozyme* (5 mg, 0.34 mmol) was added and stirred under argon atmosphere overnight. Yield-30%.

Preparation of dOvomucoid-PEO(5000)$_{18}$ (10) (Scheme 2.4)

Ovomucoid was dissolved in degassed 10 M guanidine (pH-7.4) with 15% sorbitol and stirred at room temperature for 4h. TCEP (8.6 mg, 30 μmol) was added as a solid and the solution was stirred for additional 30 min under argon atmosphere. Then, PEO-5000-MI (154

mg, 31 μmol) was added and stirred under argon overnight. Thereafter, the reaction mixture was purified by size exclusion FPLC (ÄKTA Explore, SuperoseTM 6 10/30 column, 20 mM Tris-HCl buffer with 150 mM NaCl, pH 7.4). The purified sample fraction corresponding to first protein peak was collected and concentrated by ultrafiltration. Subsequently, the product mixture was passed through a Bio-Gel P30 desalting column and lyophilized to afford as white solid. Yield 35%.

Circular Dichroism Study

CD spectral measurements were performed on a JASCO J-810 spectropolarimeter. Rapid Scan Mode (RSM) CD spectrophotometer equipped with a temperature-jacketed cuvette holder was used. The entire instrument, including the sample chamber, was constantly flushed with argon gas during the operation. All measurements were done at 37^0C. For far-UV CD spectra, (195–245 nm), the protein concentration was 30–40 μg/ml. All solutions were filtered with a 0.20 μm pore nylon filter prior to recording the spectra. The cuvette pathlength was 1 mm. The protein solution was incubated for a minimum of 5 min to enable sufficient equilibration at 37^0C. CD data were analysed by DICHROWEB. (http://dichroweb.cryst.bbk.ac.uk/html/home.shtml)

Gel Permeation Chromatography

Gel permeation chromatography was recorded by Waters 515 HPLC pump, Waters 244 refractive index detector, PL Aquagel-OH 30/40/50 and PL Guard Column (Agilent). Pure water was used as solvent with a flow rate of 1 mL/min.

Chapter 3. 3.1. Highly Stable, Ultra Small, Multifunctional Near Infrared (NIR) Gold Nanoemitters for Bioimaging Application

Preparation of dcHSA-PEO(5000)$_{27}$-(TA)$_{22}$ (1), dcBSA-PEO(5000)$_{28}$-(TA)$_{26}$ (3) and dLY-PEO(5000)$_8$-(TA)$_8$ (5)

Denatured protein-PEO hybrid was dissolved in Milli-Q water (1 mL). Then, thioctic acid, activated by *N*-hydroxysuccinimide (NHS) (2.4 mg, 8 μmol) was dissolved in DMF (0.2 mL) and added to the protein-PEO hybrid solution. Then $NaHCO_3$ (0.2 mL, 5 mg/mL) solution in water was added to adjust pH to 8.5 and the reaction mixture was vigorously stirred or shaken overnight. The insoluble thioctic acid-NHS residue was filtered off after reaction. A clear solution was obtained and transferred to an ultrafiltration tube (Vivaspin 20, MWCO 30000),

washed 5-times with pure water and further purified through a Bio Gel P-30 desalting column.

Determination of number of thioctic acid attached to the copolymer

DPS test

The procedure for the DPS test has been reported previously.[4] Briefly, 4,4'-dithiodipyridine (DPS) is reduced by free –SH groups to form 4-thiopyridone with a unique absorption maximum at 325 nm. A stock solution of 2 mg/mL thioctic acid in 20 mM Tris buffer was prepared at pH 7.4. The stock solution was diluted to different concentrations by pure water to prepare the standard solution. 20 µL of the sample or the thioctic acid standard and 80 µL of freshly prepared 2% (w/v) $NaBH_4$ solution were added into Eppendorf tubes. The solution was cooled at 0^0C and incubated for 3 hours while shaking. After reduction, HCl (1 µL, 6 M) was added to adjust the pH to 1. Citrate buffer (50 µL, 1.5 M, pH 4.5) was added and the solution was vortexed until no gas formation was observed anymore. Then, aqueous solution of DPS (50 µL, 5 mM) was added and incubated for 1min. 200 µL of each solution were added to Greiner UV Star® Microplate 96 wells and the absorbance at 325 nm was recorded on a Tecan TM InfiniteM1000 microplate reader. The read-out was repeated 3 times on average. This assay is sensitive down to 1µg/mL thioctic acid with an excellent correlation.

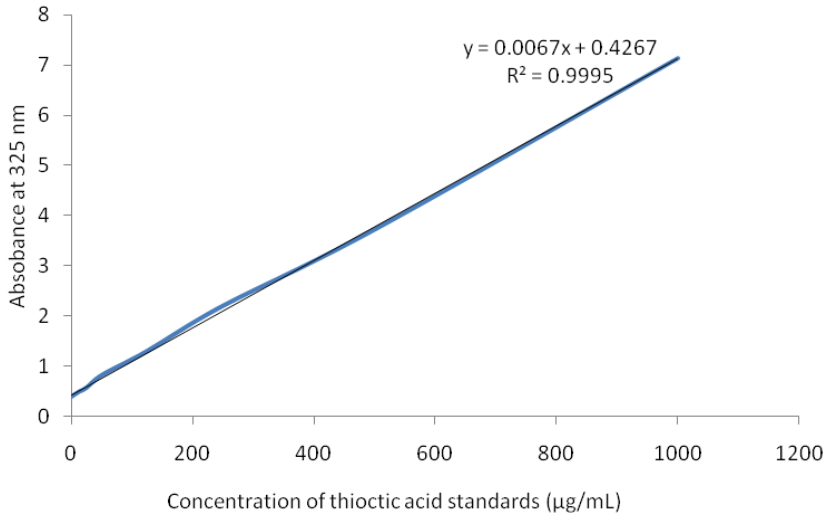

Figure 5.1. Calibration curve of DPS assay based on thioctic acid standard.

Table 5.1. Absorption at 325 nm for different concentrations of thioctic acid and PP-PEOs.

Conc. of TA (µg/mL)	1000	500	250	125	50	25	12.5	0
Absorbtion endpoint at 325 nm	7.127	3.715	2.193	1.292	0.81	0.56	0.48	0.381

Table 5.2. Absorption at 325 nm for different PP-PEOs

	dcBSA-PEO(5000)$_{28}$-(TA)$_{26}$	dHSA-PEO(5000)$_{27}$-(TA)$_{22}$	dLY-PEO(5000)$_{8}$-(TA)$_{8}$
Absorbtion endpoint at 325 nm	0.966	0.933	1.035

The number (x) of thioctic acids per PP-PEOs is calculated using the following expression

$$x = \left(\frac{\frac{V_1}{M_1}}{1000} \cdot c_1 \right) / \frac{m_2}{M_2}$$

V_1: Volume of PP-PEOs solution in water = 2 mL

M_1: Molecular weight thioctic acid (TA) = 206.33 g/mol

c_1: Concentration of thioctic acid (TA)

m_2: amount of PP-PEOs used = 6 mg

M_2: Molecular weight of PP-PEOs

General approach for stabilizing AuNPs by protein-derived copolymers:

$HAuCl_4*3H_2O$ (20 µL, 50.8 mM) and the respective copolymer were combined and the resulting mixture was diluted to 3.5 mL by distilled water. Thereafter, the mixture was stirred at room temperature for 1h. Then, 1 mL of a freshly prepared $NaBH_4$ (1 mg/mL) solution in chilled deionized water was added dropwise to the solution containing $HAuCl_4{\cdot}3H_2O$ and the

copolymer using a syringe pump. In all cases, ten times excess of $NaBH_4$ was used. Subsequently, the reaction mixture was stirred overnight. Separation of coated AuNPs from remaining free copolymer was achieved by passing through a Bio-Gel P30 desalting column. AuNPs were characterized by TEM and UV spectroscopy.

High Resolution Transmission Electron Microscopy of dcBSA-PEO(5000)$_{28}$-(TA)$_{26}$ coated AuNPs (**4f**)

A graphene substrate was fabricated *via* micromechanical cleavage and transferred to a Quantifoil grid. In order to reduce contamination on the substrate, graphene was annealed at 250°C for 5 minutes and then treated with H_2:O_2 ion plasma. Solutions of dcBSA-AuNPs (**4f**) were deposited by drop coating on graphene and investigated using an imaging-side aberration-corrected FEI TITAN 80-300 operated at 80kV acceleration voltage.

Calculation of the size distribution of dcBSA-PEO(5000)$_{28}$-(TA)$_{26}$ coated particle from AFM and FCS

AFM

10 µL of an aliquot of dcBSA-PEO(5000)$_{28}$-TA$_{26}$ coated AuNPs diluted 100 times (0.5 µM) was deposited onto a freshly cleaved mica surface and the solvent was removed by drying in air at room temperature. AFM measurements were performed with a Vecco Multimode 3 AFM using Olympus micro cantilevers with a spring constant of 1.7 N/m. AFM Images were recorded on different sample areas with a scan size of 10 µm and analyzed with a particle detection and analysis routine within the SPIP 5 (Image Metrology) image analysis software. The obtained histograms of the NP height distribution obtained from the analysis of the maximal height of more than 1000 particles were fitted with a Gauss curve.

FCS

A commercial CLSM-FCS setup manufactured by Carl Zeiss (Jena, Germany) consisting of the modules ConfoCor 2, LSM510 and an inverted microscope, model Axiovert 200 was used. In addition, a Zeiss C-Apochromat 40x/1.2 W water immersion objective was applied. The AuNPs were excited by an Argon laser and the emission was collected after filtering with a LP505 long pass filter. The eight-well, polystyrene chambered cover-glass (Lab-Tek, Nalge Nunc International) was used as a sample cell for the water solutions of (**4**). For each solution, a series of ten measurements with a total duration of five minutes was performed. The confocal observation volume was calibrated using a reference dye with a known

diffusion coefficient i.e. Rh6G. The measured autocorrelation curves were fitted with the model function given below in order to determine the hydrodynamic radii of **4** in independent measurements:

$$G(\tau) = 1 + \frac{1}{N}\left(1 + \frac{\tau}{\tau_D}\right)^{-1}\left(1 + \frac{\tau}{S^2\tau_D}\right)^{-1/2}$$

where N is the average number of fluorescent species in the observation volume *V*, τ_D is the lateral diffusion time and $S=z_0/\omega_0$ is the ratio of axial to radial dimension of *V*. The diffusion coefficient of the fluorescent species D can be determined as $D = \omega_0^2/4\tau$ and their hydrodynamic radius trough $R_H = k_B T/6\pi\eta D$ where *T* is the temperature, k_B the Boltzmann constant and η the viscosity of the solution. Average hydrodynamic radii (R_H) in the range of about 1-2 nm were found.

Cytotoxicity Assay

Onto a white 96 well plate 8000 A549 cells were plated per well and incubated overnight for attachment. The wells were 70–80% confluent on the day of experiment. Cells were then treated with 50 µL of 1 µM dcBSA-AuNPs (**4f**). Blank cells without treatment were used as positive control. After treatment, Cell-Titer Glo (Promega) cell viability assay kit was used to quantify the cell viability of the cell culture in each well, according to the manufacturer's manual.

Cellular Uptake Study

Transmission electron microscopy

Cells grown on 50 µm thick sapphire discs were cryo-fixed by high pressure freezing from the physiologically defined state, without prefixation in a Wohlwend HPF Compact 01 high pressure freezer (Engineering Office M. Wohlwend GmbH, Sennwald, Switzerland). Electron microscopy was performed on ultra-thin sections (70 nm) with a Jeol 1400 at an acceleration voltage of 80 kV.

Scanning Electron Microscopy

For scanning electron microscopy cells were chemically fixed with 2 % of glutaraldehyde and post fixed with 0.1 % osmium tetroxide, dehydrated in a graded series of propanol, critical point dried and coated by electron beam evaporation with 5 nm of carbon. Imaging of

the surface using secondary electrons and of the gold particles using the mass sensitive backscattered electron mode was performed.

Confocal Laser Scanning Microscopy (CLSM)

In an 8 well Lab-Tek Chambered Coverglass (Nunc) 25.000 A549 cells were seeded per well in DMEM and incubated overnight (37°C, 5% CO_2 and 95% humidity) for adhesion. The next day 50 µl of a 1 µM dcBSA-AuNPs **(4f)** were added to the cells and incubated for 24 h under standard conditions. Then the cells were washed twice with PBS. The supernatant was discarded and the cells were kept in 150 µl PBS with 2% Glucose and immediately determined by CLSM using a Zeiss LSM 710 setup. Optical excitation was carried out with a 405 nm laser beam. The fluorescence emission of the AuNPs was detected at 630-740 nm. To reduce unspecific background each picture was taken as an average of 4 scans.

3.2.Translocation of Near InfraRed (NIR) emitting Gold nanoparticles into the Cell Nucleus

Preparation of Thioctic Acid (TA) capped NIR emitting AuNPs (1)

80 µL 100 mM $HAuCl_4 \cdot 3H_2O$, 120 mg TA in 5 mL water at pH 12 were stirred for 1 h. Then 1 mL solution of $NaBH_4$ (1 mg/mL) in water was added to reduce the Au^{3+} to Au (0) and stirred overnight. Then the AuNPs solution was purified by dialysis (MWCO 1000).

Conjugation of 1 with NLS peptide (2)

The pH of the AuNPs solution was reduced very slowly to 6 by adding 1 M HCl dropwise. Then 1 mg NLS sequence was added to the reaction mixture and 5 mg EDC.HCl were added and stirred overnight. Then the AuNPs solution was purified by dialysis (MWCO 1000).

UV-Vis and fluorescence measurements

UV-vis absorption and fluorescence spectra were recorded on a TECAN Microplate Reader. 300 µL of the AuNPs solution were transferred to flat transparent bottom black 96 well plates and measurements were performed.

Nucleus Uptake Study

Cell Culture

A549 cells were seeded onto glass coverslips (13 mm diameter) at a density of $1*10^4$ cells per disk in 1 mL of complete medium. The medium used was 71% Dulbecco's Modified Eagles Medium (DMEM) (Sigma, U.K.), 17.5% Medium 199, 9% fetal bovine serum (FBS),

1.6% 200 mM L-glutamine, and 0.9% 100 mM sodium pyruvate. The cells were incubated at 37 °C in a 5% CO_2 atmosphere for 24 h. At this time point, the cells were incubated in complete medium supplemented with 0.05 mg mL^{-1} (1 μM) gold nanoparticles for 24 h more.

Staining with DAPI

DAPI (Fluka) was dissolved in Milli-Q to give a stock solution of 2 mg/mL, and it was stored at 4 °C in the dark. The working solution (10 μg/mL) was freshly prepared by diluting the stock solution in PBS. The cells were then stained with DAPI for 15 min at room temperature in the dark and rinsed with PBS before confocal microscopic analysis.

Confocal Laser Scanning Microscopy

In an 8 well Lab-Tek Chambered Coverglass (Nunc) 25.000 A549 cells were seeded per well in DMEM and incubated overnight (37°C, 5% CO_2 and 95% humidity) for adhesion. The next day 50 µl of a 1 µM AuNP solution were added an incubated for 24 h 37°C 5% CO_2. Then the cells were washed twice with PBS. The Supernatant was discarded and the cells were kept in 150 µl PBS + 2% Glucose and immediately determined by CLSM using a Zeiss LSM 710 setup. Optical excitation was carried out with a 405 nm laser beam. The fluorescence emission of the AuNPs was detected at 630-740 nm. To reduce unspecific background each picture was taken as an average of 4 scans. A 60× oil immersion objective and pinhole size of 110 μm were used for image capturing. Images were processed and analyzed using the ZEN software (Zeiss).

4.1. Stabilization of fluorescent nanodiamonds for cell studies by a polypeptide polymer coating

Acid Treatment of FNDs

The FNDs (10 mg) of average size of 30 nm, were boiled in a 18 mL mixture of concentrated sulfuric, hydrochloric acid and perchloric acids in a volume ratio (1:1:1) under reflux at 92 °C for 24 h in order to remove graphitic and organic impurities from the surface. The cleaning step involved neutralizing by repeated centrifugation (8 x 30 min at 10000 rpm), discarding the supernatant and suspending the sediment pellet in deionized water. After purification the FNDs were lyophilised and 6 mg solid FNDs were obtained (Yield - 60 %).

Preparation of BSA-Rho (2) (Scheme 4.1.1)

Mono-rhodamine labelled BSA was prepared according to the following procedure. To a solution of BSA (300 mg, 4.5 μmol) in 300 ml 50 mM phosphate buffer pH 7.4 1 ml of a freshly prepared aqueous solution of TCEP (1 mM, 1 mmol) , was added and the reaction mixture was stirred for 10 min at room temperature. Then, a solution of tetramethylrhodamine-5-maleimide (TMRh-MI, from Sigma-Aldrich, 4.3 mg) in DMSO (1 ml, 9 mmol, 200% excess) was added and the reaction mixture was stirred at RT for another 1 h under argon atmosphere. The non-reacted TMRh-MI was removed by ultrafiltration and size-exclusion chromatography (BioGel P 30, MQ water). The first colored layer was lyophilized to afford rhodamine monolabeled BSA as a bright pink solid (260 mg, yield 86%).

Preparation of cBSA-Rho (3) (Scheme 4.1.1)

cBSA-Rho was synthesized according to our previous report.[1] 150 mg (~2.25 μmol) of BSA was allowed to completely dissolve in 15 ml of degassed 2.5 M ethylenediamine-HCl solution (pH 4.75), followed by adding EDC (4 mmol, 621 mg) and stirring for 75 min. The reaction was then terminated by adding 1 ml acetate buffer (4 M, pH 4.75). After reaction, cBSA was washed twice with acetate buffer (4 M, pH 4.75) and 3 times with deionized distilled water using Vivaspin 20 (MWCO 30000) centrifugal concentrator and then lyophilized to obtain 154 mg cBSA-Rho as bright pink fluffy solid (yield: 94%).

Synthesis of Rho-dcBSA-PEO(5000)$_{27}$ (5) (Scheme 4.1.1)

Rho-cBSA (**3**) (10 mg, 0.15 μmol) was dissolved in degassed urea-phosphate buffer (10 mL, 10 mM phosphate buffer, pH 7.4, 5 M urea and 2 mM EDTA) and stirred at room temperature for 15 min. TCEP (4.3 mg, 15 μmol) was added as a solid, and the solution was stirred for additional 30 min under argon atmosphere. Then, PEO(5000)-MI (77 mg, 15.5 μmol) was added and the mixture was stirred under argon atmosphere for 3 hrs. After the attachment of the PEO chains, *N*-(2-aminoethyl)maleimide trifluoroacetate salt (8 mg, 31.5 μmol) was introduced and the solution was stirred for another 3 hrs under argon atmosphere. Thereafter, the reaction mixture was purified five times by ultrafiltration with 20 mM Tris-HCl buffer (pH 7.4, containing 150 mM NaCl, 2 mM EDTA) and then by size exclusion FPLC (ÄKTA Purifier, column, 20 mM Tris-HCl pH 7.4 buffer with 150 mM NaCl). The

purified sample fraction corresponding to the first protein peak was collected and concentrated by ultrafiltration. Subsequently, the product mixture was passed through a Bio-Gel P30 desalting column and lyophilized to yield Rho-dcBSA-PEO$(5000)_{27}$ as pink solid. The yield was 40%.

Adsorption of Rho-cBSA-PEO$(5000)_{28}$ to the surface of FNDs

0.5 mg Rho-cBSA-PEO$(5000)_{28}$ was dissolved in 100 mL boric acid solution (pH 8.5). 50 ml solution of 8 μg/mL FNDs solution in boric acid (pH 8.5) was added slowly to the Rho-cBSA-PEO$(5000)_{28}$ solution using a syringe pump over a period of 3h and stirred overnight. The reaction mixture was concentrated to 1 mL using Vivaspin 20 (MWCO 30000) centrifugal concentrator by centrifuging at 4000 rpm and used for further experiment.

Conjugation of dcBSA-PEO$(5000)_{27}$ coated FNDs with FITC (Scheme 4.1.2.)

0.1 mg of dcBSA-PEO$(5000)_{27}$ coated FND and 0.1 mg FITC were stirred for 24 h. Then the FNDs samples were purified by membrane dialysis (MWCO 3000) against water (six times, 1 L) for 3 days to remove unreacted small molecules and used for cell studies.

Conjugation of dcBSA-PEO$(5000)_{27}$ coated FNDs with Atto 520 (Scheme 4.1.2)

0.1 mg of dcBSA-PEO$(5000)_{27}$ coated FNDs in 5 mL of water and 0.1 mg Atto 520 NHS ester in 100 μL of DMSO were mixed and stirred for overnight at pH8. The pH was adjusted with N,N-diisopropylethylamine (DIEA). Then the FNDs samples were purified by membrane dialysis (MWCO 3000) against water (six times, 1 L) for 3 days to remove unreacted small molecules and used for cell studies.

4.2. Detection of the Metallo-Protein Ferritin Using Color Centers in FNDs

Adsorption of ferritin to the surface of FNDs

0.5 mg ferritin was dissolved in 100 mL boric acid solution (pH 8.5). 50 ml solution of 8 μg/mL FNDs solution in boric acid (pH 8.5) was added to the ferritin solution slowly using a syringe pump over a period of 3h. Then it was let stirr for overnight. The reaction mixture was concentrated to 1 mL (30000 MWCO) by centrifuge at 4000 rpm. Then the ferritin adsorbed nanodiamonds were separated from free ferritin by centrifugation at 1000 rpm for 1 minute. The nanodiamonds precipitated while ferritin remained in the solution. The

adsorption of ferritin on the surface of nanodiamonds and the separation of free ferritin was monitored by TEM images.

References

(1) Eisele, K.; Gropeanu, R. A.; Zehendner, C. M.; Rouhanipour, A.; Ramanathan, A.; Mihov, G.; Koynov, K.; Kuhlmann, C. R. W.; Vasudevan, S. G.; Luhmann, H. J.; Weil, T. *Biomaterials* **2010**, *31*, 8789.
(2) Chang, Y.-R.; Lee, H.-Y.; Chen, K.; Chang, C.-C.; Tsai, D.-S.; Fu, C.-C.; Lim, T.-S.; Tzeng, Y.-K.; Fang, C.-Y.; Han, C.-C.; Chang, H.-C.; Fann, W. *Nat. Nanotechnol.* **2008**, *3*, 284.
(3) von Smoluchowski, M. B. I. A. S. C. *Bull. Int. Aced. Sci. Cracovle* **1903**, 184.
(4) Hansen, R. E.; Østergaard, H.; Nørgaard, P.; Winther, J. R. *Anal. Biochem.* **2007**, *363*, 77.

Declaration of Cooperations

Chapter 2

The preparation and characterization of dcBSA-PEO(5000)28 and dHSA-PEO(5000)27 have been developed by Ms. Wu Yuzhou, Institute of Organic Chemistry III–Macromolecular Chemistry and Organic Materials, Universität Ulm and are part of her thesis and the synthesis have been repeated in this chapter.

Experiments with Ovomucoid and Kunitz have been accomplished together with Ms. Ayse Guenay under my supervision and based on my synthetic protocols and they were partly also included in her master's thesis, Institute of Organic Chemistry III–Macromolecular Chemistry and Organic Materials, Universität Ulm.

Chapter 3

High-resolution transmission electron microscopy (HRTEM) of AuNPs (**Figure 3.1.5.**) was performed by Gerardo Algara-Siller, Electron Microscopy Group of Materials Science, Universität Ulm.

Chapter 4

Experiments described in **chapter 4 (section 4.1)** have been accomplished together with Lars Boorberg, Institute of Organic Chemistry III–Macromolecular Chemistry and Organic Materials, Ulm University and they were included also within his master's thesis. The experimental protocols in the master's thesis were based on the intellectual property developed in this thesis.

High-resolution transmission electron microscopy (HRTEM) of nanodiamond ferritin complex (**Figure 4.2.6**) was performed by Gerardo Algara-Siller, Electron Microscopy Group of Materials Science, Universität Ulm. T_1, T_2 and FCS measurements were performed by Anna Ermakova, Institute for Quantum Optics, Universität Ulm and the theoritical calculations were performed by Dr. Jianming Cai, Controlled Quantum Dynamics Group, Universität Ulm.

Erklärung

Ich versichere hiermit, daβ ich die Arbeit selbständig angefertigt habe und keine anderen als die angegebenen Quellen und Hilfsmittel benutzt sowie die wörtlich oder inhaltlich übernommenen Stellen als solche kenntlich gemacht habe.

Ulm, den _____

Goutam Pramanik _____

Declaration of Originality

I hereby certify that, to the best of my knowledge, my thesis does not infringe upon anyone's copyright nor violate any proprietary rights and that any ideas, techniques, quotations, or any other material from the work of other people included in my thesis, published or otherwise, are fully acknowledged in accordance with the standard referencing practices.

Ulm, den _____

Goutam Pramanik_____

Acknowledgments

In my PhD thesis period, I received great supports—from my supervisor, from my family members, from my colleagues and from my friends. This is an unforgettable and very memorable period of time and it is a great pleasure here to take the opportunity to thank all the helping hands that had assisted me to achieve my thesis.

My utmost gratitude goes to my thesis supervisor—Prof. Dr. Tanja Weil for her great academic and personal supports throughout my thesis. I am very fortunate to have worked under her guidance. I attribute the level of my PhD degree to her encouragement and effort and without her, this thesis, would not have been completed or written.

I would like to express my sincere gratitude to Dr. Ulrich Zeiner and Dr. Christoph Meier for their help and innumerable discussions on various topics.

Gratitude is also extended to all our collaborators: Prof. Fedor Jelezko and the group members of Institute of Quantumoptik; Prof. Ute Kaiser and the group members of Electron Microscopy Group of Materials Science; Prof. Paul Walther and group members of Zentrale Einrichtung Elektronenmikroskopie; Prof. Theo Lasser and group members of Laboratoire d'optique biomédicale, EPFL.

My parents have been a great source of inspiration. My Parents is my pillar of strength and all my accomplishments would not have been possible without them.

I am very grateful to all OC III members for their generous helping hands.

Thank you all!

Curriculum Vitae

Personal Information

Name: Goutam Pramanik

Date of Birth: 3rd June1983 in India.

Place of Birth: Kharisha, India

Nationality: Indian.

Permanent Address

Vill-Kharisha, Post- Kolaghat, District- Purba Medinipur.

State- West Bengal, Country- India. PIN-721134.

Education

June, 2010 - Present

Doctoral study - University of Ulm, Germany.

Thesis title: "Near Infrared emitting Nanoemitters for Bioimaging Applications".

Supervisor: Prof. Dr. Tanja Weil.

January, 2009 - April, 2010

Master by Research - National University Of Singapore, Singapore.

Thesis title: "Towards Novel Naphthalene Based Near Infrared Dyes for Bioimaging Applications".

Supervisor: Prof. Dr. Tanja Weil.

August, 2006 - July, 2008

Master of Science (Chemistry) - Indian Institute Of Technology (IIT), Madras, India.

Thesis title: "Metallaboranes of Group VIII Transition Metals: SYNTHESIS AND THEIR REACTIVITY".

Supervisor: Prof. Dr. Sundargopal Ghosh.

August, 2002 - June, 2006

Bachelor of Science (Chemistry Hons.) - University Of Calcutta, India.

June, 2000 - May, 2002

Higher Secondary (X+2) - West Bengal Council of Higher Of Secondary Education.

June, 2000

Madhyamik (X) - West Bengal Board Of Secondary Education.

List of Publications

Published:

1. "Convenient Approach to Polypeptide Copolymers Derived from Native Proteins" Yuzhou Wu, **Goutam Pramanik**, Klaus Eisele and Tanja Weil - **Biomacromolecules**, 2012, 13, 1890 –1898. (Shared First Author)

2. "Detection of a Few Metallo-Protein Molecules Using Color Centers in Nanodiamonds" Anna Ermakova, **Goutam Pramanik**, Jianming Cai, Gerado Algara-Siller, Ute Kaiser, Tanja Weil, Yan-Kai Tzeng, Huan-Cheng Chang, Liam McGuinness, Martin Plenio, Boris Naydenov and Fedor Jelezko - **Nano Letters**, 2013, 13, 3305–3309.

Manuscript Submitted:

3. "High Performance, Ultrasmall Near Infrared (NIR) Gold Nanoemitters for Cell Imaging Applications" **Goutam Pramanik**, Yuzhou Wu, Gerardo Algara-Siller, Christoph Meier, Kaloian Koynov, Klaus Eisele, Paul Walther, Ute Kaiser and Tanja Weil.

4. "Stabilization of fluorescent nanodiamonds for cell studies by a polypeptide polymer coating" **Goutam Pramanik**, Anna Ermakova, Yuzhou Wu, Liam McGuinness, Boris Naydenov, Rolf Reuter, Joerg Wrachtrup, Fedor Jelezko and Tanja Weil.

5. "Self-assembly of Polypeptide Copolymers into Nanostructured Protein Coatings" Christoph Meier, Yuzhou Wu, **Goutam Pramanik**, and Tanja Weil.